Magnetospheric response to geomagnetic storms

Thesis submitted for the degree of Doctor of Philosophy

Timothy Charles Booth

Department of Physics and Astronomy

March 2017

'It does not matter how slowly you go as long as you do not stop'

-Confucius

Abstract

Timothy Booth: Magnetospheric response to geomagnetic storms

Geomagnetic storms are well observed phenomena that enhance the plasma of the inner magnetosphere to high energies. They are defined by the characteristic trace in indices that measure the variation of the north-south component of the Earth's magnetic field, such as the Dst or SYM-H. These indices are not purely measures of the symmetric ring current but include components of other current systems within the magnetosphere, primarily the tail and magnetopause currents. Using the methodology of *Asikainen et al.* [2010] the SMR index has been deconstructed to observe the evolution of the aforementioned current systems over the storm durations. *Reeves et al.* [2003] showed that only half of all storms caused an increase in the relativistic electron flux at geosynchronous orbit. For the remaining half the electron flux either does not change or decreases. It has been shown that the ring current decays faster for flux decrease storms than flux increase storms. Using a superposed epoch analysis, of geomagnetic indices and solar wind parameters, it has also been shown that although flux increase storms tend to have faster, less dense solar wind in the recovery phase of storms, it appears that it is the orientation of the IMF, which remains more southward in the recovery phase, that is the key parameter. This allows for the continued injection of plasma sheet particles into the inner magnetosphere. Further evidence to support this has been shown with the hydrogen and helium fluxes mirroring that of the electron flux. Finally, potential wave modes were evaluated over storm durations and potential acceleration mechanisms were noted as being more intense during flux increase storms than flux decrease storms; this is most likely due to the increase in the seed particles necessary for their generation.

Acknowledgements

I first of all would like to thank my supervisor Dr Darren Wright for his help and encouragement throughout this process. I would also like to thank Professor Steve Milan for assistance when Darren was unavailable. I am sincerely grateful to Dr Matt James for his assistance with coding in the early days and his continued humour, which made even the toughest days a little easier to bear.

In addition, I would like to thank Dr Timo Asikainen, Dr Emilia Kilpua and Professor Geoff Reeves for supplying the ancillary data for the determination of the relative current indices, storm drivers and relativistic electron flux changes, respectively.

This thesis would not have been completed if not for the continuing love and support of my family especially my mum, dad and fiancée. I would finally like to thank Country 105 CKRY Calgary, for providing the soundtrack that kept me motivated.

Table of Contents

Table of Tables

Table of Figures

CHAPTER 1

Introduction

[1.1]   Basics of Solar-Terrestrial Physics

The Sun is the ultimate source of energy within the solar system and as all subsequent interactions between the particles of the solar wind and the Earth's magnetosphere begin here so shall we. All information for this chapter was found in *Kivelson and Russell* [1995] and references therein, unless otherwise stated.

[1.1.1] The Sun

The Sun is not only an average star which sits within the main sequence on the Hertzsprung-Russell diagram, but is also unique amongst its peers for a very important reason; it is the closest star to Earth. It is a gravitationally bound sphere of plasma which comprises of ~90% hydrogen, ~10% helium and ~0.1% heavier elements such as oxygen, nitrogen and carbon [*Kivelson and Russell*, 1995]. The Sun's energy is produced from fusion reactions which convert five million tons of hydrogen to helium per second within its core. Outside the core there is the radiative zone. Radiation generated in the Sun's core takes millions of years to reach the surface due to the opacity of this region. The temperature of the Sun falls off rapidly such that convection becomes the dominant energy transport process in the outer quarter (by radius), this region is called the convection zone and stretches out to the Sun's surface. Extending outward from the surface of the Sun, is its atmosphere, which comprises of the photosphere, chromosphere and corona (Figure 1). As its name suggests, the photosphere emits the majority of the light and is granular in appearance, which indicates the top of convection cells within the convection zone [*Kivelson and Russell*, 1995].
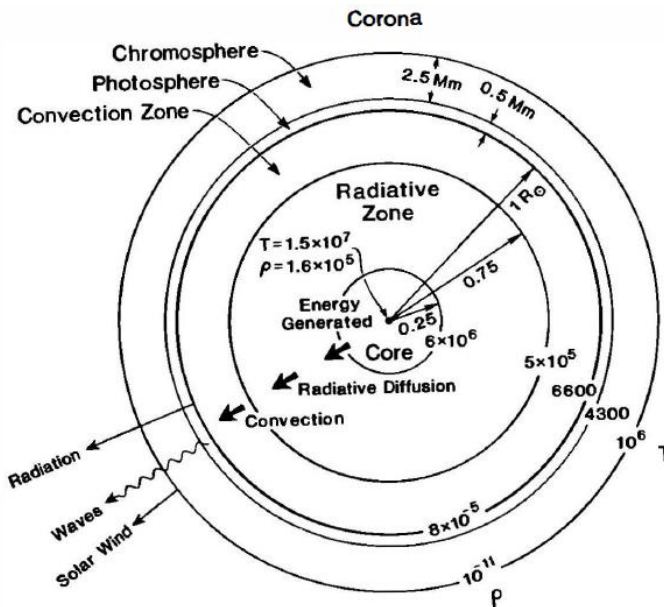
Figure 1: The structure of the Sun, reproduced from Kivelson and Russell [1995], p61

The Sun's magnetic field, originally thought to have minimal effect on the solar atmosphere, is now known to control the majority of its structure and dynamics. Coronagraphs, which use an occultation disk to obscure the main body of the Sun have shown the existence of coronal mass ejections preceding erupting prominences [*Simnet*, 2000]. In addition, soft x-ray images have shown bright and dark regions representing magnetic interactions, such as coronal loops, and coronal holes respectively [*Zeilik and Gregory*, 1998]. The interaction between the magnetic field of the Sun and the plasma in the solar atmosphere can be described by the equations of magnetohydrodynamics (MHD). These combine the equations of electromagnetism and fluid mechanics and are used to treat the plasma as a continuous medium rather than individual particles [*Kivelson and Russell*, 1995].

[1.1.2] The Solar Wind

Ionised particles, primarily hydrogen, continuously emanate from the Sun and, along with remnants of the solar magnetic field, form the solar wind. This solar wind is the result of the difference in gas pressure between the solar corona and the interstellar medium. This can be shown as follows by considering an isothermal solar atmosphere in hydrostatic equilibrium [*Kivelson and Russell,* 1995].

[1.1.2.1]   Solar Atmosphere Pressure Balance

Start with the MHD equation of motion of a plasma (Equation 1) and the ideal gas law (Equation 2) and assume spherical symmetry. Take the isothermal approximation such that the temperature of the plasma is a constant and equal to both the ion and the electron temperatures. Also assume that the number of electrons and ions are equal and as such the charge density is 0 implying that $\rho_q \boldsymbol{E}$ forces are also 0. It is also assumed that the velocities of both the ions and the electrons are equal and as such there is no charge separation and therefore no current in the plasma. This therefore implies that there are no $\boldsymbol{j} \wedge \boldsymbol{B}$ forces acting on the plasma. Using the ideal gas law (Equation 2) the total plasma pressure of the solar atmosphere can simply be written as a sum of the ion and electron partial pressures (Equation 3).

$$\rho_m \frac{d\boldsymbol{V}}{dt} = -\nabla P + \rho_m \boldsymbol{g} + \boldsymbol{j} \wedge \boldsymbol{B} + \rho_q \boldsymbol{E} \tag{1}$$

$$P = nkT \tag{2}$$

$$P = P_e + P_i = n_e k T_e + n_i k T_i = 2nkT \tag{3}$$

The mass density (ρ_m) of the solar atmosphere can be calculated as the sum of the electron and ion densities (Equation 4)

$$\rho_m = n_e m_e + n_i m_i = n(m_e + m_i) = 2n\langle m \rangle \tag{4}$$

where $\langle m \rangle \left(= \frac{1}{2}(m_e + m_i) \right)$ is the mean mass of the plasma. By substituting equation 4 into equation 2 the plasma pressure can be written as shown in equation 5.

$$P = \frac{\rho_m kT}{\langle m \rangle}, \text{ or } \rho_m = \frac{\langle m \rangle P}{kT}, \text{ as } n = \frac{\rho_m}{2\langle m \rangle} \tag{5}$$

Applying the assumptions to the MHD equation of motion of a plasma, equation 1 can be re written in the form of equation 6.

$$\rho_m \frac{d\mathbf{V}}{dt} = -\nabla P + \rho_m \mathbf{g} \tag{6}$$

where

$$\mathbf{V} = V(r)\hat{\mathbf{r}}, \nabla P = \frac{dP}{dr}\hat{\mathbf{r}}, \text{ and } \mathbf{g} = -g\hat{\mathbf{r}}$$

Thus the equation of motion in the $\hat{\mathbf{r}}$ direction can be written as shown in equation 7

$$\rho_m \frac{dV(r)}{dt} = -\frac{dP}{dr} - \rho_m g \tag{7}$$

From here we assume that the plasma is in hydrostatic equilibrium and as such the velocity is equal to 0. This implies that the left hand side (LHS) of equation 7 is also equal to zero and as such can be rewritten to form equation 8.

$$\frac{dP}{dr} = -\rho_m g \tag{8}$$

Substituting equation 5 into equation 8 gives equation 9.

$$\frac{dP}{dr} = -\frac{\langle m \rangle P}{kT} g \tag{9}$$

For the Sun the size of the atmosphere is thick in comparison to the size of the Sun and as such g will not be a constant but will instead vary with distance, r, from the centre of the Sun as given by equation 10.

$$g = \frac{GM_\odot}{r^2} \tag{10}$$

Where G is the gravitational constant and $M_\odot$ is the mass of the Sun. This modifies equation 9 to give equation 11.

$$\frac{dP}{dr} = -\frac{\langle m \rangle P}{kT}\frac{GM_\odot}{r^2} \tag{11}$$

Equation 11 can be solved to give the pressure, at some distant point r from the solar surface, by separating the variables and integrating both sides. This is shown below and leads to the variation of the pressure with radial distance as given in equation 12.

$$\frac{dP}{dr} = -\frac{\langle m \rangle P}{kT} \frac{GM_\odot}{r^2}$$

$$\frac{dP}{P} = -\frac{GM_\odot \langle m \rangle}{kT} \frac{dr}{r^2}$$

$$\int_{P_0}^{P(r)} \frac{dP}{P} = -\frac{GM_\odot \langle m \rangle}{kT} \int_{R_\odot}^{r} \frac{dr}{r^2}$$

$$[\ln P]_{P_0}^{P(r)} = -\frac{GM_\odot \langle m \rangle}{kT} \left[-\frac{1}{r} \right]_{R_\odot}^{r}$$

$$\ln P(r) - \ln P_0 = -\frac{GM_\odot \langle m \rangle}{kT} \left(-\frac{1}{r} + \frac{1}{R_\odot} \right)$$

$$\ln \left(\frac{P(r)}{P_0} \right) = -\frac{GM_\odot \langle m \rangle}{kT} \left(\frac{1}{R_\odot} - \frac{1}{r} \right)$$

$$P(r) = P_0 \exp \left(-\frac{GM_\odot \langle m \rangle}{kT} \left(\frac{1}{R_\odot} - \frac{1}{r} \right) \right) \tag{12}$$

From equation 12 it can clearly be seen that as r tends to infinity $P(r)$ does not tend to zero. Therefore, the pressure at infinity does not equal zero and the Sun cannot provide the pressure to be at hydrostatic equilibrium. If the pressure of the local interstellar medium is greater than the pressure at infinity, then the solar atmosphere could be in hydrostatic equilibrium. This is not the case and so the Sun continuously blows off its atmosphere due to this pressure difference and hence causes the solar wind.

The solar wind can be accelerated to supersonic speeds due to the gravitational force of the Sun falling off faster than the pressure gradient of the solar wind as shown above. The ratio of the bulk velocity to the thermal velocity is large for solar wind plasma and causes the particles to move faster than the sound speed of the plasma, which indicates that the solar wind is supersonic [*Kivelson and Russell*, 1995]. The solar wind is also the medium in which variations in solar activity are transmitted to planets within the solar

system, which in turn drives activity at those planets, such as geomagnetic storms at Earth. The solar wind also drags out the magnetic field of the Sun into interplanetary space due to the frozen in flux approximation originally proposed by Hannes Alfvén [*Alfvén*, 1942].

[1.1.2.2]   Frozen-In Flux Approximation
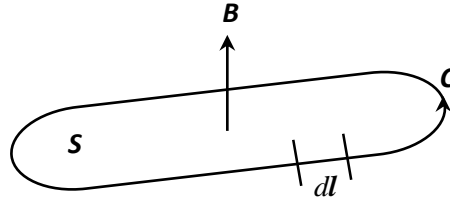
Figure 2: Schematic showing the configuration of the closed contour C in the proof of the frozen-in flux approximation

Consider a closed contour **C** that is made up of small segments $d\boldsymbol{l}$ which is not parallel to the magnetic field **B** and is moving with the plasma (as shown in Figure 2) then the magnetic flux ($\boldsymbol{\psi}$) through the surface **S** is given by equation 13.

$$\boldsymbol{\psi} = \int_S \boldsymbol{B} \cdot d\boldsymbol{S} \tag{13}$$

Figure 2 shows the configuration of the closed contour **C** at the initial time t_0. At any subsequent time t the change in the magnetic flux through the surface **S** is due to the change in the magnetic field with time and the change in the size of the surface. As such the time variation in the magnetic flux can be written as in equation 14.

$$\frac{d\boldsymbol{\psi}}{dt} = \frac{\partial \boldsymbol{\psi}_1}{\partial t} + \frac{\partial \boldsymbol{\psi}_2}{\partial t} \tag{14}$$

First we shall consider the change in the magnetic field with time through the constant surface **S**. The change in flux in this case can be written in the form of equation 13 as shown below. A substitution of Faraday's law (Equation 15) gives the change in magnetic flux as given by equation 16.

$$\frac{\partial \psi_1}{\partial t} = \int_S \frac{\partial \boldsymbol{B}}{\partial t} \cdot d\boldsymbol{S}$$

$$\nabla \wedge \boldsymbol{E} = -\frac{\partial \boldsymbol{B}}{\partial t} \Rightarrow \frac{\partial \boldsymbol{B}}{\partial t} = -\nabla \wedge \boldsymbol{E} \tag{15}$$

$$\frac{\partial \psi_1}{\partial t} = -\int_S \nabla \wedge \boldsymbol{E} \cdot d\boldsymbol{S} \tag{16}$$

The second part of the change in flux through the surface $\boldsymbol{S}$ is the change in the surface due to the motion of the plasma, which is moving with a bulk velocity of $\boldsymbol{V}$. As mentioned above contour $\boldsymbol{C}$ is moving with the plasma and is made up of individual elements $d\boldsymbol{l}$. If we consider a single line element as shown in Figure 3 over time it sweeps out an area which is additional to the original surface. At time t_0 the line element $d\boldsymbol{l}$ is given by the dotted line and at a later time ($t_0 + dt$) the line element is given by the solid line. The grey shaded area is the new area which is additional to that of the original surface $\boldsymbol{S}$ and as such the magnetic flux through this area must be added to the flux through surface $\boldsymbol{S}$.
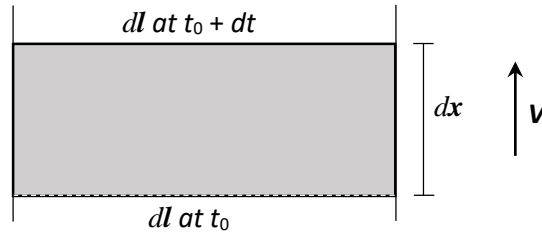
Figure 3: Schematic showing the area swept out between time t_0 and $t_0 + dt$ by a line element, dl, of the closed contour C.

The new area ($d\boldsymbol{A}$), shown as the grey area in Figure 3 between t_0 and $t_0 + dt$, is simply the cross product of $d\boldsymbol{x}$ and $d\boldsymbol{l}$ as the direction of the surface normal is perpendicular to both $d\boldsymbol{x}$ and $d\boldsymbol{l}$. $d\boldsymbol{x}$ can be simply calculated by multiplying the velocity by the change in time and therefore the area swept out by $d\boldsymbol{l}$ per unit time is given by equation 17.

$$d\boldsymbol{A} = d\boldsymbol{x} \wedge d\boldsymbol{l}$$

$$d\boldsymbol{x} = \boldsymbol{V}dt \Rightarrow d\boldsymbol{A} = dt(\boldsymbol{V} \wedge d\boldsymbol{l})$$

$$\frac{d\boldsymbol{A}}{dt} = \boldsymbol{V} \wedge d\boldsymbol{l} \tag{17}$$

The total magnetic flux through this new area is the integral around the complete contour of the magnetic field multiplied by the change in area with time (Equation 18).

$$\frac{\partial \boldsymbol{\psi}_2}{\partial t} = \int_C \boldsymbol{B} \cdot \frac{d\boldsymbol{A}}{dt} = \int_C \boldsymbol{B} \cdot \boldsymbol{V} \wedge d\boldsymbol{l} \tag{18}$$

Using the trigonometric identities $A \cdot B \wedge C = A \wedge B \cdot C$ and $A \wedge B = -B \wedge A$ equation 18 can be rewritten to form equation 19. Stokes' theorem states that the surface integral of the curl of a function is equal to that of the line integral of a function around the closed path which bounds that surface, as given by equation 20. We can thus apply Stokes' theorem to equation 19 to give equation 21.

$$\frac{\partial \boldsymbol{\psi}_2}{\partial t} = -\int_C \boldsymbol{V} \wedge \boldsymbol{B} \cdot d\boldsymbol{l} \tag{19}$$

$$\int_C \boldsymbol{F} \cdot d\boldsymbol{l} = \int_S \nabla \wedge \boldsymbol{F} \cdot d\boldsymbol{S} \tag{20}$$

$$\frac{\partial \boldsymbol{\psi}_2}{\partial t} = -\int_S \nabla \wedge (\boldsymbol{V} \wedge \boldsymbol{B}) \cdot d\boldsymbol{S} \tag{21}$$

Substituting equations 16 and 21 into equation 14 gives the functional form of the change in the magnetic flux with time (Equation 22).

$$\frac{d\boldsymbol{\psi}}{dt} = -\int_S \nabla \wedge \boldsymbol{E} \cdot d\boldsymbol{S} - \int_S \nabla \wedge (\boldsymbol{V} \wedge \boldsymbol{B}) \cdot d\boldsymbol{S} \tag{22}$$

Space plasmas are collisionless and as such the conductivity tends to infinity. This implies that the idealised Ohm's law equation (Equation 23) may only be satisfied if the bracketed terms are equal to zero (Equation 24). Using this fact, a substitution can be made for the $\boldsymbol{V} \wedge \boldsymbol{B}$ term in equation 22, and by doing so it can be shown that the change in magnetic flux with time ($\frac{d\boldsymbol{\psi}}{dt}$), through the surface $\boldsymbol{S}$, is equal to zero (Equation 25)

$$j = \sigma(E + V \wedge B) \tag{23}$$

$$E + V \wedge B = 0 \Rightarrow V \wedge B = -E \tag{24}$$

$$\int_S \nabla \wedge (V \wedge B) \cdot dS = -\int_S \nabla \wedge E \cdot dS$$

$$\frac{d\psi}{dt} = -\int_S \nabla \wedge E \cdot dS + \int_S \nabla \wedge E \cdot dS = 0 \tag{25}$$

Equation 25 has shown that the magnetic flux through a surface remains constant in time. This is true for any closed contour which has a significant implication, which is that the magnetic field lines must move with the plasma. In other words, the field is 'frozen in' to the plasma, which gives us the frozen-in-flux approximation. This is best though of by considering equation 14. If the plasma moves in such a way that contour contracts (i.e. $\frac{\partial \psi_2}{\partial t}$ reduces) then the magnetic field strength must increase such that $\frac{\partial \psi_1}{\partial t}$ exactly cancels out the change in $\frac{\partial \psi_2}{\partial t}$. This makes sense if the field lines are considerd as frozen in because any contraction in the contour will force the field lines closer together and closer field lines implies a greater field strength. The opposite is also true that a reduction in field strength should be observed if the contour expands (i.e. field lines are further apart).

Spacecraft observations, such as that of Wind, ACE and SOHO which are situated in orbit of the L1 point have provided detailed observations of the solar wind and its characteristics at a distance of close to 1AU. Typically, the solar wind has a proton density of 6.6 cm^{-3}, an electron density of 7.1 cm^{-3}, a dynamic pressure of 2.9 nPa, and a flow speed of 450 kms^{-1} [*Kivelson and Russell*, 1995]. Changes in solar activity, however, cause these values to be extremely variable and this drives geomagnetic activity.

Magnetised planetary bodies create their own cavity within the solar wind which denies plasma of solar wind origin direct access to regions in which a planetary magnetic field dominates. The solar wind dynamic pressure defines the shape of the magnetosphere

compressing the dayside and elongating the nightside into a long tail (Figure 4) [*Seki et al.*, 2015]. The size of the magnetosphere is defined by a balance between the dynamic pressure of the solar wind and the magnetic pressure of the Earth's magnetic field. As such enhancements in the dynamic pressure, due to enhanced solar activity, causes the magnetosphere to shrink and vice versa (See section [1.1.3.1]).
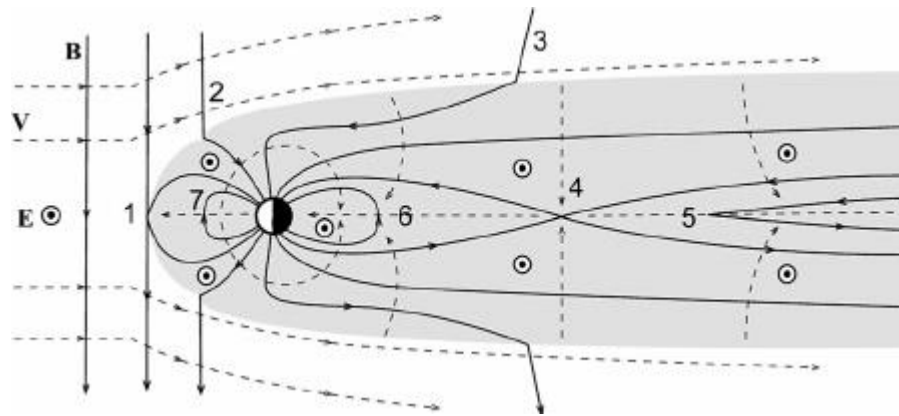
Figure 4: Schematic of the Earth's magnetosphere and the stages of the Dungey cycle, as numbered 1-7. Reproduced from Seki et al. [2015]

The solar wind travels faster than the sound speed of the plasma and must therefore undergo an abrupt change as it experiences the magnetosphere as an obstacle to its flow. In order to flow around the Earth's magnetosphere, the solar wind must be slowed to subsonic speeds. As such a shock forms around the magnetosphere and takes the shape of a symmetrical paraboloid of revolution centred about the Sun-Earth line [*Kivelson and Russell*, 1995]. Initially, the presence of a shock was unexpected as solar wind plasma is collisionless. Collisions are usually a requirement of shocks as they allow for the dissipation and heating that are needed for shock formation. Instead the solar wind electric and magnetic fields are able to alter the motion of the particles and provide the dissipation usually provided by collisions [*Kivelson and Russell*, 1995].

[1.1.3] The Earth

The Earth is a magnetised planet that has a natural magnetic field, which is mostly dipolar and is caused by the geodynamo. This is due to the convection caused by the buoyancy forces which develop as the result of a cooling Earth and the solidification of

iron onto the inner core [*Glatzmaier and Roberts*, 1996]. As discussed above, the magnetisation of a planet causes the existence of a cavity within the solar wind in which the magnetic field of the planet dominates. The size and the dynamics of the magnetosphere are controlled by the propagating solar wind and the strength of the intrinsic field. The dynamic pressure controls the size of the magnetosphere through pressure balance, with the sub-solar magnetopause located at a distance where the ram pressure of the solar wind is equalled by the magnetic pressure of the terrestrial magnetic field [*Kivelson and Russell*, 1995].

[1.1.3.1]   Magnetopause Standoff Distance

The magnetopause standoff distance can be approximated by assuming that the plasma pressure within the magnetosphere is negligible and that there is no magnetic pressure associated with the solar wind. Equation 26 shows the magnetic pressure of the Earth's magnetic field equal to the ram pressure of the solar wind. The latter can be simply described as the momentum change of a particle reflected at the magnetopause (1st term on the RHS of equation 26) multiplied by the number of particles crossing the boundary (2nd term on the RHS of equation 26).

$$\frac{B_{MP}^{2}}{2\mu_0} = 2mV \times nV \tag{26}$$

The magnetic field strength at the magnetopause can be approximated as double that of the natural dipole field (B_D). This is due to the current at the magnetopause creating inducing a magnetic field that enhances the natural dipole inside the magnetopause and cancels the IMF outside the boundary (for northwardly direct IMF). It is therefore possible to rewrite equation 26, giving equation 27 , where *nm* is simply the mass density ρ_m.

$$\frac{(2B_D)^2}{2\mu_0} = 2\rho_m V^2 \tag{27}$$

The magnetic field strength of a dipole field falls off as r^3 and as such the dipole field strength at the distance of the magnetopause (R_{MP}) can be written as shown in equation 28, where B_{EQ} and $R_\oplus$ are the dipole field strength at the surface and the radius of the Earth respectively.

$$B_D = B_{EQ} \left(\frac{R_\oplus}{R_{MP}}\right)^3 \tag{28}$$

Equation 28 can now be substituted into equation 27 and rearranged, as shown below, to get the approximation of the standoff distance of the subsolar point of the magnetopause (Equation 29).

$$\frac{\left(2B_{EQ}\left(\frac{R_\oplus}{R_{MP}}\right)^3\right)^2}{2\mu_0} = 2\rho_m V^2$$

$$\frac{2B_{EQ}^2}{\mu_0}\left(\frac{R_\oplus}{R_{MP}}\right)^6 = 2\rho_m V^2$$

$$B_{EQ}^2 \left(\frac{R_\oplus}{R_{MP}}\right)^6 = \mu_0 \rho_m V^2$$

$$\left(\frac{R_{MP}}{R_\oplus}\right)^6 = \frac{B_{EQ}^2}{\mu_0 \rho_m V^2}$$

$$R_{MP} = R_\oplus \left(\frac{B_{EQ}^2}{\mu_0 \rho_m V^2}\right)^{\frac{1}{6}} \tag{29}$$

Substituting in typical values for the mass density of the solar wind (ρ_m), the solar wind speed (V) and the surface magnetic field strength at the equator (B_{EQ}) into equation 29 the distance to the magnetopause on the dayside can be calculated as approximately 10 R_E. One of the mechanisms that controls the dynamics of the magnetosphere in a more indirect way is through the regulation of the energy flux into the magnetosphere via reconnection. This is controlled by the solar wind IMF field strength, orientation and the solar wind velocity [*Paulikas and Blake*, 1978; *Reeves et al.*, 2011; *Milan et al.*, 2012; *Kilpua et al.*, 2015].

[1.1.3.2]   Magnetic Convection

Magnetic convection within the magnetosphere, occurs when the IMF is oriented so that it lies in the opposite direction to the Earth's dipole field [*Dungey* 1961]. This causes magnetic reconnection of the field lines, on the dayside, thus coupling the magnetic field of the Sun to that of the Earth (#1, Figure 4). The terrestrial magnetic field is then dragged from the dayside to the nightside (#2-3, Figure 4) until the build-up of magnetic flux triggers reconnection in the tail (#4, Figure 4) and the release of a plasmoid tailward and out of the system (#5, Figure 4). This closes the terrestrial magnetic field which is returned to the dayside via the inner magnetosphere (#6-7, Figure 4). On short timescales the rate of reconnection on the nightside may, and is often, not equal to the rate of reconnection on the dayside [*Milan et al.,* 2012]. This leads to an imbalance and a gradual 'storage' of magnetic flux on the nightside which builds up before being suddenly released. This sudden release of magnetic flux defines a substorm, which injects plasma from the plasma sheet into the near Earth region. Substorms and storms, although different, are intrinsically linked as they are both driven by the same processes. This is demonstrated by the fact that substorms are always observed during storms, especially during the main phase when they are most intense [e.g. *Gonzalez et al.*, 1994; *Taylor et al.,* 1994; *Gonzalez et al.*, 1999; *Anderson et al.*, 2015].

Due to the dipolar nature of the Earth's magnetic field it increases in strength as particles travel along the field line. This will act to slow the particles in this direction, eventually returning them back to the equator in a process called magnetic mirroring [*Kivelson and Russell*, 1995]. These particles also drift around the Earth due to the change in field strength along the gyration of the particles. In weaker fields, the particles will have greater gyroradii than when they are in stronger fields, causing them to drift (Section [1.1.3.5]). The combination of these two effects can trap particles, following injection via substorms, on complete drift orbits and thus create the radiation belts originally discovered by Van Allen [*Kivelson and Russell*, 1995].

[1.1.3.3] Plasma Regions

Although the magnetosphere is treated as a vacuum, to a first approximation, in the pressure balance method of determining the standoff distance of the subsolar point, this is far from the case. The magnetosphere is in reality filled with a variety of plasma populations each occupying distinct regions of space (Figure 5 and Figure 11) [*Kivelson and Russell*, 1995]. The major populations include the plasmasphere, the plasma sheet, the tail lobes, the mantle and the plasma sheet boundary layer. The tail lobes are thought to lie on open field lines and have low density plasma, typically below 0.1 cm^{-3}. The ions in this region are thought to be of ionospheric origin and are often observed moving away from the Earth [*Kivelson and Russell*, 1995].
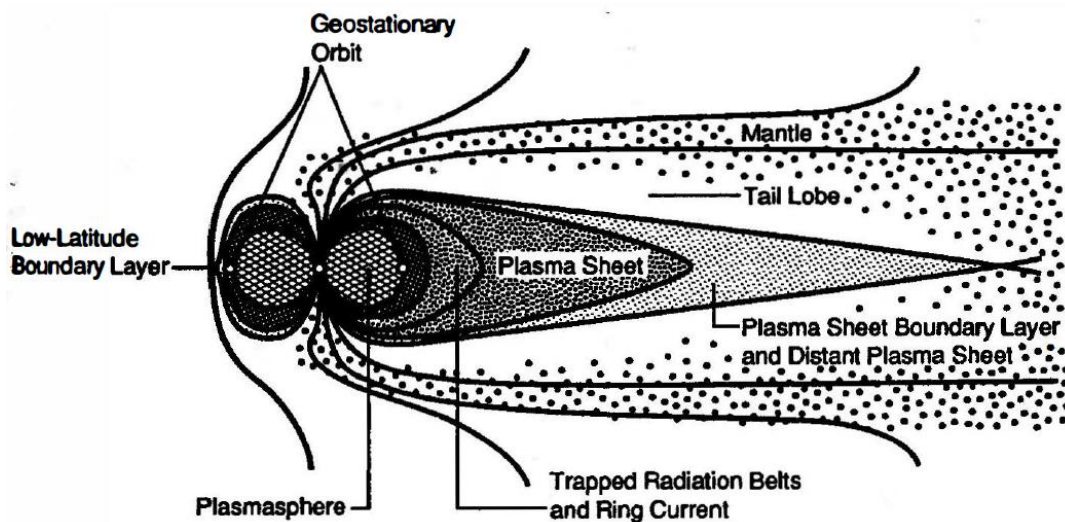
Figure 5: Two dimensional representation of the major plasma regions of the magnetosphere, reproduced from Kivelson and Russell [1995], p291. Geostationary orbit is located at a distance of 6.6R$_E$.

The plasma sheet boundary layer is thought to be on closed field lines and contains low density plasma (0.1 cm^{-3}), which typically flows along the field lines with flow velocities of a few hundred kms^{-1}. This region occupies the space between the tail lobes and the central plasma sheet [*Kivelson and Russell*, 1995]. The plasma sheet is situated on closed field lines and comprises of hot plasma with typical densities of 0.1 cm^{-3} to 1 cm^{-3}. During geomagnetically quiet times the plasma sheet is primarily composed of H$^+$ ions of solar wind origin, however during more active periods there is a higher concentration of O$^+$ ions indicating an ionospheric source [*Kivelson and Russell*, 1995]. The inner edge of the

plasma sheet typically corresponds to the outer edge of the radiation belts which lies around geostationary orbit (~6.6 R_E), at midnight local time [*Kivelson and Russell*, 1995]. This boundary tends to move closer to the Earth during substorms [*Cao et al.*, 2011].

Moving closer to the Earth the radiation belts and the ring current exist between around 1.5 and 6 R_E. They contain particles that are trapped on closed field lines and complete full orbits of the Earth. The particle number and energy densities vary along the field lines with both maximising near the equator due to particles being lost from the system at low altitudes [*Kivelson and Russell*, 1995]. The radiation belts comprise of high energy ions, primarily H^+, and electrons (>0.1 MeV and >1 MeV respectively). Both the proton and electron radiation belts occupy the same spatial location, however there exists a slot region in the electron radiation belt where fluxes minimise at around L = 2.2 R_E [*Kivelson and Russell*, 1995]. It is thought to occur due to pitch angle scattering of electrons by plasmaspheric hiss waves [*Lyons and Thorne*, 1973; *Albert*, 1994; *Abel and Thorne*, 1998]. It was originally thought that the ring current was solely comprised of H^+ ions with energies between a few 10s keV to ~100 keV but, similarly to the plasma sheet, O^+ ions of ionospheric origin were found to be as significant a contributor to the energy density; specifically, at energies below 50 keV [*Kivelson and Russell*, 1995].

The final region that will be introduced is the plasmasphere. This is a region which typically occupies a similar spatial region of the magnetosphere as the radiation belts. The plasmasphere is a region of colder (~1 eV), denser plasma which is dominated by co-rotation [*Kivelson and Russell*, 1995]. During quiet times this region can extend out beyond L = 5 due to weaker convection, however, during storm times, when convection is strong, the plasmasphere is eroded to lower L shells as plasma is lost to the magnetopause via dayside plumes [*Moldwin et al.*, 2002].

The plasmasphere is then gradually refilled, over several days, following the enhanced activity by the polar wind. The plasmapause is defined as the edge of the plasmasphere and is observed as a rapid decrease in the proton density along its radial profile [*Kivelson and Russell*, 1995]. Its location varies depending on the strength of magnetospheric convection, which is enhanced during periods of increased geomagnetic activity. The

plasmasphere contains a bulge on the duskside, due to the weaker flow speed of plasmaspheric plasma in this region as co-rotation and convection processes act in opposite directions [*Kivelson and Russell*, 1995].

[1.1.3.4]   Motion of Individual Particles

The charged particles which make up a plasma are subject to electric and magnetic forces. The Lorentz force (F_L), as described by equation 30, is the force experienced by a particle with charge q and velocity v in an electric field E and magnetic field B.

$$F_L = q(E + v \wedge B) \tag{30}$$

From this equation a few basic parameters of the motion of charged particles can be inferred. To do this we shall consider the case of a moving particles in a constant magnetic field and without the presence of an electric field. The initial conditions will assume a Cartesian co-ordinate system with the magnetic field directed along the z axis ($B = B\hat{z}$) and the velocity of the particle described by the sum of its components in each of the three axes ($v = v_x\hat{x} + v_y\hat{y} + v_z\hat{z}$). Applying these assumptions to equation 30 with the fact that $F = ma$, where m is simply the mass of the particle and $a \left(= \frac{dv}{dt} \right)$ is the acceleration of the particle, gives the solution as described by equation 31

$$m\frac{dv}{dt} = q(v \wedge B)$$

$$\frac{dv}{dt} = \frac{q}{m}\left(v_y B\hat{x} - v_x B\hat{y}\right) \tag{31}$$

Equation 31 can be split to give the acceleration of the particle in each direction of the Cartesian co-ordinate system as given in equations 32 - 34

$$\frac{dv_x}{dt} = \frac{qB}{m}v_y \tag{32}$$

$$\frac{dv_y}{dt} = -\frac{qB}{m}v_x \tag{33}$$

$$\frac{dv_z}{dt} = 0 \tag{34}$$

Equation 34 implies that v_z is a constant, which also means that the component of the velocity along the field line is a constant as $v_z = v_\parallel$. Concentrating on equation 32 a second order differential equation can be created to solve for v_x by differentiating it and substituting equation 33 into the resulting formula, giving equation 35.

$$\frac{d}{dt}\frac{dv_x}{dt} = \frac{d}{dt}\frac{qB}{m}v_y \Rightarrow \frac{d^2v_x}{dt^2} = \frac{qB}{m}\frac{dv_y}{dt}$$

$$\frac{d^2v_x}{dt^2} = \frac{qB}{m}\left(-\frac{qB}{m}v_x\right) = -\left(\frac{qB}{m}\right)^2 v_x \tag{35}$$

Using equation 35 a solution for v_x can be found. The form of equation 35 suggests that a solution for v_x is of the form of a cosine wave. Equation 36 shows the form of the solution used here.

$$v_x = v_\perp \cos(\Omega t) \tag{36}$$

Below shows that equation 36 is a solution to equation 35 and produces an interesting result suggesting that the particles have an angular frequency of Ω, which is called the gyrofrequency and is given by equation 37.

$$v_x = v_\perp \cos(\Omega t) \Rightarrow \frac{dv_x}{dt} = -\Omega v_\perp \sin(\Omega t)$$

$$\frac{d^2v_x}{dt^2} = -\Omega^2 v_\perp \cos(\Omega t) = -\Omega^2 v_x$$

Therefore, equation 36 is only as solution of equation 35 if equation 37 is true

$$-\left(\frac{qB}{m}\right)^2 v_x = -\Omega^2 v_x$$

$$\Omega = \frac{qB}{m} \tag{37}$$

Using this solution, it is possible to find the form of v_y by substituting the differential of v_x into equation 32.

$$\frac{dv_x}{dt} = -\Omega v_\perp \sin(\Omega t)$$

$$-\Omega v_\perp \sin(\Omega t) = \frac{qB}{m} v_y = \Omega v_y$$

$$v_y = -v_\perp \sin(\Omega t) \tag{38}$$

From equations 36 & 38 it can be shown that the magnitude of the velocity in the x-y plane is simply the velocity perpendicular to the magnetic field.

$$\left(v_x{}^2 + v_y{}^2\right)^{\frac{1}{2}} = \left((v_\perp \cos(\Omega t))^2 + (-v_\perp \sin(\Omega t))^2\right)^{\frac{1}{2}}$$

$$= \left(v_\perp{}^2(\cos^2(\Omega t) + \sin^2(\Omega t))\right)^{\frac{1}{2}}$$

$$= (v_\perp{}^2)^{\frac{1}{2}} = v_\perp$$

Finally, the trace of the particle as it moves with time can be shown to be a circle if the velocities are integrated (Equations 39 & 40).

$$x = \int v_x dt = \int v_\perp \cos(\Omega t)\, dt = \frac{v_\perp}{\Omega} \sin(\Omega t) + x_0 \tag{39}$$

$$y = \int v_y dt = \int -v_\perp \sin(\Omega t) dt = \frac{v_\perp}{\Omega} \cos(\Omega t) + y_0 \tag{40}$$

The functional form of x and y are simply the equation of a circle starting at point (x_0, y_0) and with a radius given by equation 41. This radius defines the gyroradius of the particle and is dependent of the charge of the particle. This means that ions and electrons gyrate in different directions which allows for charge separation under specific conditions and creates the large scale currents within the magnetosphere. These currents are discussed in greater detail in section [1.1.3.5] below.

$$r_g = \frac{v_\perp}{\Omega} = \frac{mv_\perp}{qB} \tag{41}$$

[1.1.3.5]   **Current Systems**

The motion of the electrons and ions, that constitute both solar wind and magnetospheric plasma, when they encounter different magnetic regions, establishes a variety of current systems. Ionospheric current systems such as the solar dynamo and substorm electrojet are connected to the more distant magnetosphere via field aligned currents (Figure 11) [*Kivelson and Russell*, 1995]. Additional currents within the magnetosphere are shown in Figure 11. These include the ring current, magnetopause current and tail current, which are the current systems of interest. Charge separation of ions in the inner magnetosphere is due to the formation of two different drifts, gradient drift and curvature drift [*Kivelson and Russell*, 1995]. Gradient drift is due to the change in the magnetic field strength over the distance of one gyration. As equation 41 shows the gyroradius is inversely proportional to the strength of the magnetic field. Therefore, as the magnetic field strength increases the gyroradius decrease. As positive and negative charges gyrate in opposite directions they also drift in opposite directions as shown in Figure 6, this causes a charge separation and thus a current (*j*) to develop.
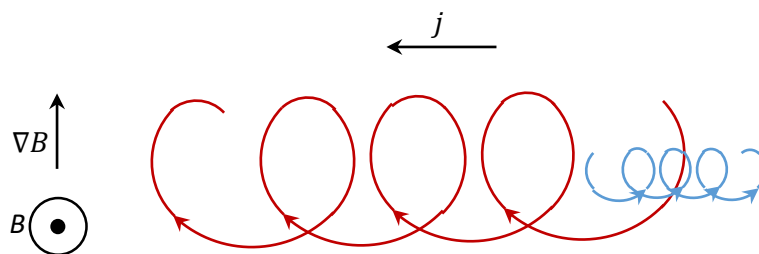
Figure 6: A schematic showing the effects of a non-uniform magnetic field over the size of a particle gyration. In the stronger magnetic field (top) the gyroradius of both ion (red) and electron (blue) is smaller than in the weaker magnetic field (bottom). This causes charge separation and therefore a current (j) to develop.

Curvature drift occurs due to the fact that the field lines are curved. Figure 7 shows the configuration of a curved field line along which a particle may travel. If the curvature of the field line is large over a gyration, then the particle will experience a centrifugal force over the gyration orbit. This force acts in the direction of the radius of curvature (R_C) and can be written as a function of the velocity along the field line and R_C (Equation 42).
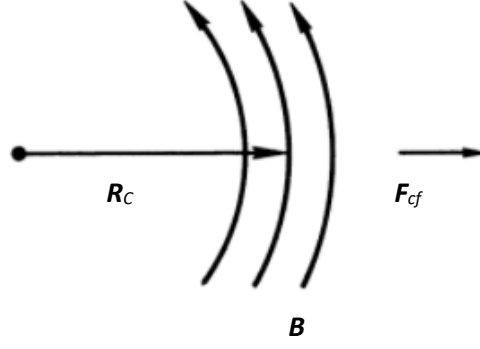
Figure 7: The configuration of the magnetic field lines, which cause the particles gyrating along them to experience a centrifugal force (F_{cf}) in the direction of the radius of curvature (R_C). Reproduced from Chen [1974] p.26

$$F_{cf} = \frac{mv_\parallel^2}{R_C}$$

$$\boldsymbol{F}_{cf} = F_{cf}\widehat{\boldsymbol{R}_C} \text{ and } \boldsymbol{R}_C = R_C\widehat{\boldsymbol{R}_C}$$

$$\therefore \boldsymbol{F}_{cf} = \frac{mv_\parallel^2}{R_C^2}\boldsymbol{R}_C \tag{42}$$

The Lorentz force (Equation 30) can be used to calculate the functional form of the drift velocity ($\boldsymbol{v}_D$), however instead of the force in an electric field ($q\boldsymbol{E}$) the centrifugal force ($\boldsymbol{F}_{cf}$) is used as shown in equation 43. As can be seen from Figure 7 this force acts only perpendicular to the magnetic field ($\boldsymbol{F}_{cf_\perp} = \boldsymbol{F}_{cf}$) and as such equation can be written in terms perpendicular to the magnetic field (Equation 44).

$$\boldsymbol{F}_L = \boldsymbol{F}_{cf} + q(\boldsymbol{v} \wedge \boldsymbol{B}) \tag{43}$$

$$m\frac{d\boldsymbol{v}_\perp}{dt} = \boldsymbol{F}_{cf} + q(\boldsymbol{v}_D \wedge \boldsymbol{B}) \tag{44}$$

Here we assume that the perpendicular velocity is constant such that the left hand side of equation 44 is zero as given by equation 45. The following expression can be found for the drift velocity (Equation 49) by taking the cross product of equation 46 with the magnetic field vector and using the vector identity shown in equation 47. The dot product between the drift velocity and the magnetic field in equation 48 is zero as the drift velocity is perpendicular to the magnetic field.

$$0 = \boldsymbol{F}_{cf} + q(\boldsymbol{v}_D \wedge \boldsymbol{B}) \tag{45}$$

$$-\boldsymbol{F}_{cf} = q(\boldsymbol{v}_D \wedge \boldsymbol{B}) \tag{46}$$

$$-\frac{1}{q}\left(\boldsymbol{F}_{cf} \wedge \boldsymbol{B}\right) = (\boldsymbol{v}_D \wedge \boldsymbol{B}) \wedge \boldsymbol{B}$$

$$(\boldsymbol{A} \wedge \boldsymbol{B}) \wedge \boldsymbol{C} = \boldsymbol{B}(\boldsymbol{C} \cdot \boldsymbol{A}) - \boldsymbol{A}(\boldsymbol{C} \cdot \boldsymbol{B}) \tag{47}$$

$$\therefore (\boldsymbol{v}_D \wedge \boldsymbol{B}) \wedge \boldsymbol{B} = \boldsymbol{B}(\boldsymbol{B} \cdot \boldsymbol{v}_D) - \boldsymbol{v}_D(\boldsymbol{B} \cdot \boldsymbol{B}) = -\boldsymbol{v}_D B^2 \tag{48}$$

$$-\frac{1}{q}\left(\boldsymbol{F}_{cf} \wedge \boldsymbol{B}\right) = -\boldsymbol{v}_D B^2$$

$$\boldsymbol{v}_D = \frac{1}{q}\frac{\left(\boldsymbol{F}_{cf} \wedge \boldsymbol{B}\right)}{B^2} = \frac{m v_\parallel^2}{q R_C^2}\frac{(\boldsymbol{R}_C \wedge \boldsymbol{B})}{B^2} \tag{49}$$

The right hand side of Equation 49 is found by substituting in equation 42 for the centrifugal force. Equation 49 shows that the drift velocity is perpendicular to both the magnetic field and the centrifugal force or radius of curvature. Not only this but it is charge dependant which means that the electrons and ions drift in opposite directions. This causes charge separation and a current to develop, which acts in the same direction as the current caused by the gradient drift discussed above.

Particles are almost always subject to both gradient and curvature drift simultaneously, and the inner magnetosphere is no exception. The configuration of the dipole of the Earth as shown in Figure 8 below where the magnetic field points out of the page and the field strength increase in the radial direction towards the planet and the radius of curvature of the field lines is directed in the outward radial direction. Due to this configuration the ions (red) and electrons (blue) can drift in complete orbits in opposite directions thus forming the ring current. The ring current is made of higher energy particles as the gyroradius, which is greater for higher energy particles, must be of a sufficient size such that the change in the magnetic field strength and the curvature of the field lines over a single gyration is non-negligible.
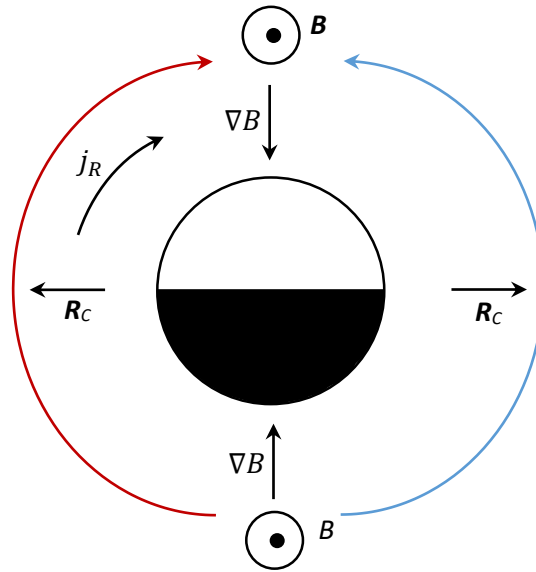
Figure 8: Configuration of the dipole field which causes the ions (red) and electrons (blue) to drift in opposite directions around the planet and thus form the ring current (j_R).

The ring current is established due to the combination of both of the above gradient and curvature drift of ions and electrons which orbit the Earth in opposite directions. The ring current is enhanced following injections from the plasma sheet via substorms. This circular current induces a magnetic field in the opposite direction to that of the Earth's natural dipole [*Daglis et al.*, 1999].

On the dayside the magnetopause current exists due to the reflection of solar wind protons and electrons as they enter the region of space dominated by the Earth's magnetic field Figure 9. To first approximation the solar wind can be thought of as not having a magnetic field. This is appropriate, if the IMF is assumed to be northward, close to the magnetopause as the magnetic field induced by the magnetopause current acts in the opposite direction to the IMF and so cancels out. In addition, the magnetic field of the Earth is strengthened as the magnetopause current induces a magnetic field in the same direction as the natural dipole field. For this reason, the magnetic field at the magnetopause is taken as twice the natural dipole field at that distance, as was used in the derivation of the magnetopause standoff distance (Section [1.1.3.1]) The particles complete half a gyration and then return to the solar wind. The current system is established due to the ions and electrons gyrating in opposite directions and acts in the direction opposite to that of the ring current [*Kivelson and Russell*, 1995].
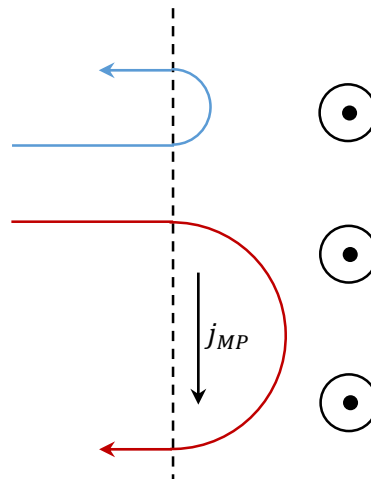
Figure 9: Schematic showing the configuration which produces the magnetopause current (j_{MP}). Electrons (blue) and ions (red) complete half gyration inside the magnetopause before returning to the solar wind. The orientation of the diagram is as though looking from above such that inside the magnetopause is to the right and the current flows from dawn to dusk as shown in Figure 11 below.

The tail current is formed on the nightside, as the Earth's plasma and field lines are dragged anti-sunward. This current is labelled as the neutral sheet current in Figure 11 and closes the magnetopause current in the tail [*Kivelson and Russell*, 1995]. This current is set up in the region where the magnetic field lines have been dragged into a non-dipolar configuration as is shown to the right hand side of number 6 in Figure 4 [*Kivelson and Russell*, 1995]. In this configuration the magnetic field north of the magnetic equatorial plane is directed in the opposite direction to the magnetic field in the southern hemisphere. As Figure 10 shows both ions (red) and electrons (blue) gyrate in opposite directions in each hemisphere due to the oppositely directed magnetic field (Equation 37). This allows for an interesting solution at the magnetic equator for particles which experience both magnetic configurations in a single gyration. These particles will gyrate in one direction for half of the orbit and the other direction when they cross into the oppositely directed magnetic field region. This will cause the electrons and ions to move in opposite directions and thus form a current as shown in Figure 10. This current acts in the same direction as the ring current on the nightside and thus will also induce a magnetic field that will act in the opposite direction to that of the Earth's natural dipole.
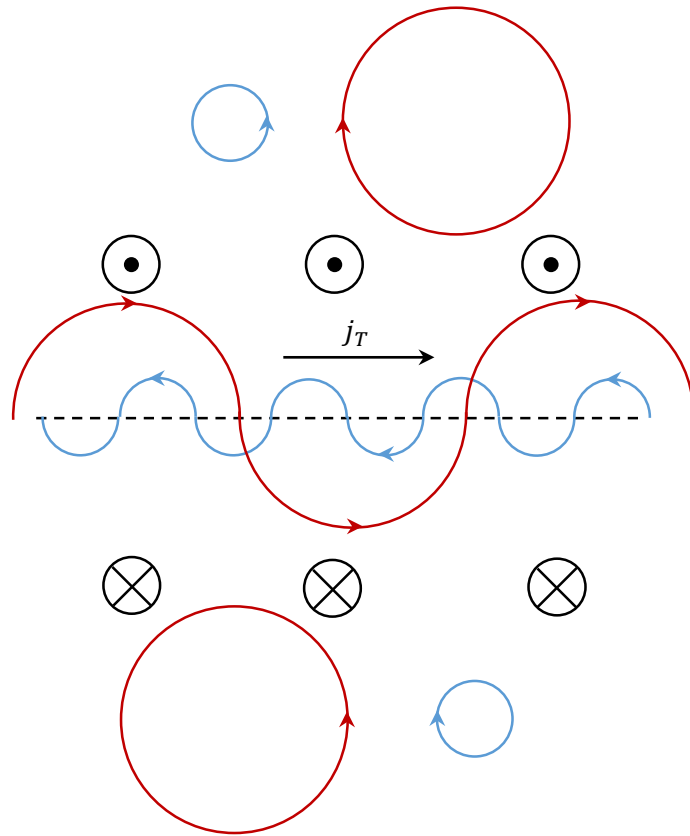
Figure 10: Schematic showing the configuration required for the formation of the tail current (j_T). Ions (red) and electrons (blue) with gyrate in opposite directions in both hemispheres. This leads to a solution along the boundary of the two magnetic field configurations where the particles complete a half gyration in either hemisphere. This in turn leads to charge separation and the formation of a current which acts in the same direction as the ring current on the nightside.
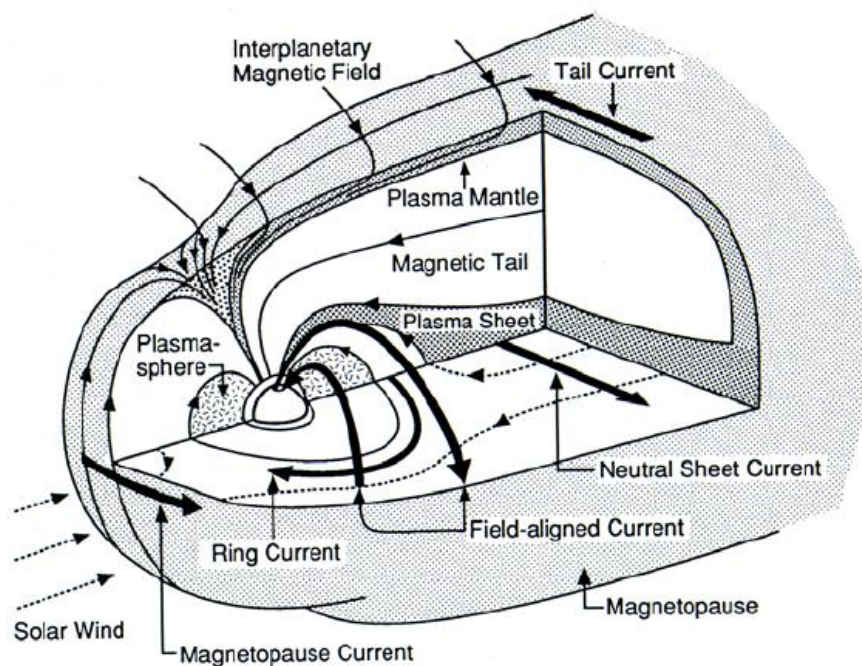
Figure 11: Three dimensional representation of the major plasma regions and current systems of the magnetosphere, reproduced from Kivelson and Russell [1995], p22

[1.1.3.6]   Geomagnetic Storms

Geomagnetic storms are extraordinary enhancements in the ring current caused by the southward orientation of the IMF for a significant period of time. Southward IMF can drive strong magnetic convection and is often due to discrete solar wind structures such as coronal mass ejections (CMEs) or co-rotating interaction regions (CIRs). Enhanced convection drives the injection of ions into the inner magnetosphere from the solar wind via the magnetospheric plasma sheet [*Kivelson and Russell*, 1995]. Geomagnetic storms induce large amplitude currents, such as the ring current. Hence there is a measureable, and prolonged, depletion in the Earth's natural dipole followed by a slow recovery over several days. This characteristic depletion in measured by several indices, such as the Dst index. Historically a measurement of -50 nT is required for the identification of a storm [*Gonzalez et al.*, 1994; *Kivelson and Russell*, 1995]. Geomagnetic storms will be discussed in greater detail in the following chapter.

[1.2]   Motivation

Acceleration of magnetospheric plasma to relativistic energies and its subsequent precipitation can cause serious and irreparable damage to satellites, due to spacecraft charging, lethal injury to astronauts caused by particle and radiation damage to cells [*Kivelson and Russell*, 1995]. The enhancement of magnetospheric current systems, which occurs during storms, induce variations in the Earth's magnetic field. Faraday's Law implies that these variations will generate a surface electric field, which can drive geomagnetically induced currents (GIC) [*Pulkkinen et al.,* 2017]. These GICs can overload power transformers and cause widespread blackouts, such as in Québec during March 1989. Not all storms, however, cause an increase in the flux of high energy particles [e.g. *Reeves et al.*, 2003]. The reason for this is unknown with the solar wind velocity [e.g. *Reeves et al.*, 2011; *Kilpua et al.*, 2015] and the solar wind density [e.g. *Lyatsky and Khazanov*, 2008] both thought to have some part in the modulation of high energy particle flux.

[1.3]   Aim

The aim of this thesis is to identify the mechanisms which cause different responses of the magnetosphere to geomagnetic storms. This will be done through the use of indices such as the SMR and AE indices as well as first hand observations of the plasma properties from the Cluster spacecraft.

During quiet times the ring current is composed of protons, which originate from the solar wind, whereas during storm times the composition of the ring current is dominated by the O^+ ions of ionospheric origin which maximises at the end of the main phase [*Daglis et al.,* 1999]. This change in composition can then dictate the decay processes that dominate during the recovery phase [*Daglis*, 2001]. The fluxes of different species at different energies will be observed using the Cluster data to observe whether there is any significant difference between the different types of storm.

The injection of seed particles into the inner magnetosphere during storms, can drive the excitation of wave modes, which in turn can resonantly interact with the trapped plasma population [e.g. *Daglis et al.*, 1999]. Plasma waves can both accelerate and deplete the plasma within the magnetosphere [e.g. *Shprits et al.*, 2008]. Low energy particles (~10-100 keV) can excite waves which then propagate within the magnetosphere and encounter higher energy particles [e.g. *Meredith et al.*, 2000]. These can resonantly interact with the waves, causing them to be damped and thus increase the energy of the particle due to conservation of energy [*Horne and Thorne*, 1998]. Specific wave modes will be targeted and their amplitude and location will be observed using data from the Cluster spacecraft to pinpoint the mechanisms which dominate during the different types of storm

CHAPTER 2

Literature Review

[2.1] Introduction

This chapter will discuss the current knowledge surrounding the development and mechanisms associated with geomagnetic storms in order to provide a context for the research presented in the subsequent chapters. It will start with a general overview of what a geomagnetic storm is before discussing the current theories associated with the energisation and loss processes which result in the precipitation of high energy particles.

[2.2] What is a Geomagnetic Storm?

A geomagnetic storm is defined by the enhancement of trapped particles in the inner magnetosphere resulting from the interaction of discrete solar wind structures with the magnetosphere [*Chapman*, 1918; *Chapman et al.*, 1963; *Gosling*, 1990; *Gonzalez et al.*, 1994]. The energisation of the particles within the inner magnetosphere can be observed on the ground as a reduction in the north-south component of the Earth's magnetic field. *Chapman* [1918] used ground magnetometers to show that these reductions occurred during periods of significant auroral activity. Although the precise mechanisms for particle acceleration are still not fully understood [e.g. *Daglis et al.*, 1999; *Daglis and Kozyra*, 2002] the solar wind structures that encounter the magnetosphere, such as coronal mass ejections (CMEs) and co-rotating interaction regions (CIRs) are the ultimate cause of the observed enhancements [*Kivelson and Russell*, 1995]. CMEs and CIRs are pockets of turbulent solar wind that disrupt the equilibrium that exists between the magnetosphere and the steady state solar wind, which often possess a region of southward IMF orientation. If this is orientation is sufficiently long lasting then a geomagnetic storm is likely to occur, due to enhanced coupling between the solar wind and the magnetosphere via reconnection [e.g. *Dungey*, 1961; *Petschek*, 1964].

[2.2.1] Reconnection

Reconnection is one of the pillars of solar terrestrial physics and describes how the solar wind interacts with the magnetosphere (see section [1.1.3.2]). The magnetic fields of the Earth and Sun are joined via reconnection on the dayside, which drives the convection of magnetic field lines within the magnetosphere [*Dungey,* 1961]. This process may be able to transfer around 10% of the solar wind energy into the magnetosphere [*Gonzalez et al.,* 1989], whereas processes associated with viscous interactions, which may occur during periods of northward IMF, are less efficient by approximately an order of magnitude [*Tsurutani et al.,* 1992]. The rate at which this occurs (Φ_D) is balanced on the nightside, Φ_N, where the process is reversed. These rates are equal when averaged over a sufficiently long period but over shorter durations need not be [*Milan et al.,* 2012]. They are linked to the change of open magnetic flux content of the magnetosphere by Faraday's law (Equation 50) which states that the change of magnetic flux is equal to the integral of the electric field around the open-closed field line boundary (OCB) [*Siscoe and Huang,* 1985; *Cowley and Lockwood*, 1992; *Milan et al.,* 2007].

$$\frac{dF_{PC}}{dt} = \Phi_D - \Phi_N = \oint \vec{E} \cdot \overrightarrow{dl} \tag{50}$$

Milan et al. [2012] examined specific events (when Φ_N = 0) to determine the functional form of the dayside reconnection rate, measured in volts, based upon solar wind parameters (Equations 51 & 52) improving on previous functions [e.g. *Newell et al.,* 2007; *Vasyliunas et al.,* 1982].

$$\Phi_D = L_{eff}(V_x)V_x B_{yz} \sin^{\frac{9}{2}}\left(\frac{1}{2}\theta\right) \tag{51}$$

$$L_{eff}(V_x) = 3.8R_E \left(\frac{V_x}{4 \times 10^5}\right) \tag{52}$$

where $L_{eff}(V_x)$ is the size of the merging gap, over which reconnection can take place, R_E is the radius of the Earth in m, V_x is the solar wind velocity given in ms^{-1}, B_{yz} is the magnitude, in Tesla, of the IMF in the y-z plane and θ is the clock angle (defined as the angle between the IMF y and z components (=tan^{-1}(B_y, B_z)). This coupling function produces values for the dayside reconnection rate comparable to the cross polar cap potential, as measured by SuperDARN [*Milan et al.*, 2012].

[2.2.2] Properties of Geomagnetic Storms

Geomagnetic storms are defined by intense global disturbances in the Earth's magnetic dipole field. This is due to the energisation of ring current particles (~10-300 keV) at a distance of between 2 and 7 R_E [*Daglis et al.,* 1999]. They are identified by their reduction in geomagnetic indices to below a given threshold, historically -50nT, and comprise of three distinct phases, the initial phase, the main phase and the recovery phase [*Gonzalez et al.*, 1994]. The initial phase is defined by the arrival of a CME or CIR and is typically observed as a small increase in the surface magnetic field strength which is mirrored by geomagnetic indices. These structures are associated with increased solar wind density and ram pressure causing a reduction in the stand-off distance of the subsolar point. The arrival of a sustained period of southwardly oriented IMF drives increased dayside reconnection and the injection of large amounts of energy (~10^{15} J) signalling the start of the main phase [*Kozyra et al.*, 1998]. Enhanced dayside reconnection will lead to the injection of particles, via substorms, following nightside reconnection. This enhances the ring current which induces a magnetic field oppositely directed to the Earth's natural dipole and is observed as a rapid decrease in geomagnetic indices [*Gonzalez et al.*, 1994]. If there is a reduction in the dayside driving due to lower solar wind velocity or less southward IMF then the recovery phase begins [*Gonzalez et al.*, 1994]. Geomagnetic indices will be observed to return to pre-storm levels over the ensuing days as ring current particles are removed by charge exchange, coulomb collisions or resonant wave particle interactions [e.g. *Horne and Thorne,* 1998; *Daglis et al.*, 1999].

The traditional detection of a storm by its minimum Dst value is somewhat arbitrary. *Anderson et al.* [2015] showed that geomagnetic storms with a minimum Dst value of greater than -50nT can also produce both enhancement and depletions of the relativistic electron flux. This indicates that storm time acceleration and loss processes are more complex than first thought as they must be independent of geomagnetic activity.

Enhanced convection, which drives the energisation of the ring current, requires a sustained period of southward IMF, up to as long as several hours [*Russell et al.*, 2000]. Indeed, longer durations of southward IMF have been shown to produce more intense storms [*Gonzalez et al.,* 1994; *Echer et al.*, 2008; *Milan et al.*, 2009]. Shorter durations (<20mins) of southward IMF can cause ring current energisation via individual substorm injection of plasma but this is quickly dissipated [*Burton et al.* 1975]. During the main phase of storms, when convection is high, *Liemohn et al.* [2001] showed that open drift paths account for up to 90% of the energy flow in the magnetosphere. This implies the formation of an asymmetric ring current as particles are not trapped but drift through the inner magnetosphere ony once before being lost [*Liemohn et al.*, 2001]. This has been regularly observed by the IMAGE spacecraft [*Daglis and Kozyra*, 2002].

During the recovery phase of storms, geomagnetic indices slowly increase back to pre-storm values over a period of days. This may be observed as a two-step process with a more rapid recovery observed during the early recovery phase. This could be due to plasma density decreases, particle outflow or magnetospheric particle redistribution [*Daglis and Kozyra*, 2002]. Alternatively, *Hamilton et al.* [1988] showed that the charge exchange lifetimes of O^+ are consistent with a rapid ring current decay during the early recovery phase. The concentration of ring current O^+ ions can dominate during the main phase, and have been shown to mirror the changes of geomagnetic indices index during storms [*Kozyra et al.*, 2000]. Observed compositional changes in the low energy plasma in the inner magnetosphere indicates that charge exchange is an important loss mechanism [e.g. *Kistler et al.*, 1989; *Kistler et al.*, 1999; *Jordanova et al.*, 2001]. In fact, *Kozyra et al.*, [2000] suggested that it dominates during the late recovery phase, explaining the slow decay, of the trapped ring current particles, over several days.

Both acceleration and loss processes are enhanced during geomagnetic storms. These competing processes cause substantial variations in the relativistic electron flux of the outer radiation belt [*Meredith et al.*, 2003c]. Acceleration processes do not always dominate, in fact flux increases are only observed for ~50% of all storms [*Reeves et al.*, 2003]. The other 50% of storms are equally split, either producing a flux change of less than a factor of 2 from pre- to post-storm or causing a dramatic flux decrease [*Onsager et al.*, 2002; *Reeves et al.*, 2003].

Unsurprisingly, geomagnetic storms are more likely to occur around solar maximum, when CMEs and CIRs are more common, than solar minimum [*Gonzalez et al.*, 1994]. The main peak of geomagnetic activity generally occurs slightly after solar maximum during the declining phase due to persistent high speed stream driven CIRs [e.g. *Sugiura*, 1980; *Legrand and Simon*, 1991]. A second peak in geomagnetic activity a couple of years before solar maximum has also been observed [*Gonzalez et al.*, 1990]. In addition to the solar cycle dependence of geomagnetic activity there is also a semi-annual variation whereby storms are more likely to occur around the equinoxes than solstices. *Russell and McPherron* [1973] suggested that this phenomenon was caused by an increase in the effective southward component of the IMF during equinox.

[2.2.2.1]   The Russell-McPherron Effect

Russell and McPherron [1973] showed that during equinox there is a geometric effect that increases the amount of southward IMF, and thus the geoeffectiveness, of disctrete solar wind structures during these periods. Figure 12 shows the geometry of the IMF for the Russell-McPherron effect during March equinox. The Earth is below the solar ecliptic plane and so the magnetic field of the Sun is pointed toward the Sun (left hand schematic). In the GSE co-ordinate system the x-axis is directed toward the Sun, the y-axis is directed in the opposite direction to the orbital velocity of the Earth (V_O) and the z-axis is orthoganol to the solar ecliptic plane. The March equinox IMF orientation can thus be translated into the GSE X-Y plane as shown on the right hand side of Figure 12. This gives a component of the IMF in the negative Y_{GSE} direction.
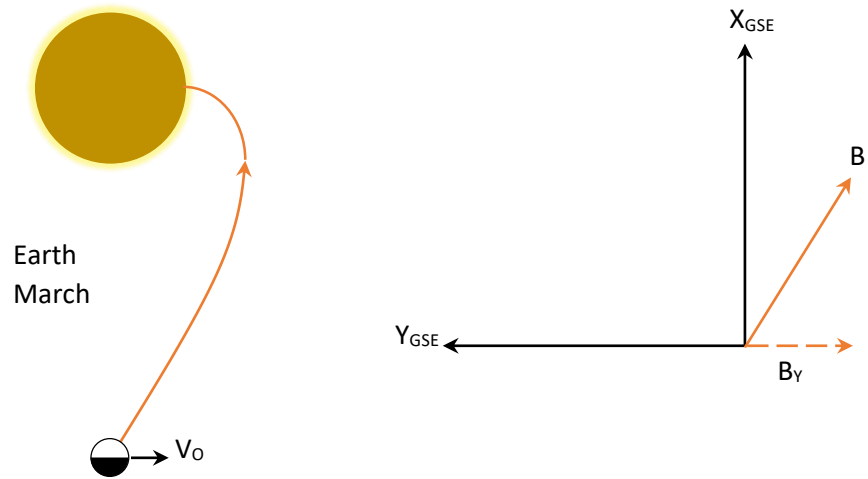
Figure 12: The orientation of the IMF (orange) at March equinox (left) and its translation into GSE X-Y plane (right). In the left hand diagram, the IMF is pointed toward the Earth indicating that the Earth is below the solar ecliptic plane.

Figure 13 shows the B_Y component of the IMF in Figure 12 in the GSM Y-Z plane. During equinox the rotation axis of the Earth is in the GSE Y-Z plane, whereas during solstice the rotation axis is in the GSE X-Z plane, therefore at a particular time the Earth's magnetic dipole axis (i.e. the GSM z-axis) will also lie in the GSE Y-Z plane. This therefore means that there is a component of the IMF B_Y which acts in the negative Z_{GSM} direction (i.e. in the opposite direction to the Earth's dipole field (B_{YZ} in Figure 13)) and acts in addition to the IMF B_Z component.
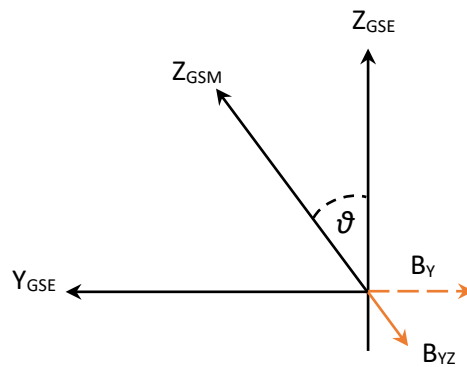
Figure 13: Schematic showing that during equinox when the magnetic dipole axis lies in the GSE Y-Z plane there is a component of B_Y that acts in the negative Z_{GSM} direction, which is independent of the B_Z orientation of the IMF.

The Russell-McPherron effect therefore gives a greater geoeffectiveness of any solar wind structure, with this IMF polarity, during equinox than during solstice [*Russell and McPherron*, 1973]. This is because of the angle between the Earth's dipole axis and the Z_{GSE} axis (ϑ in Figure 13) when projected in the GSE Y-Z plane. This angle maximises at equinox and is zero at solstice. Figure 12 & Figure 13 show the IMF orientation for the March equinox, during the October equinox the Z_{GSM} axis will be projected in the negative Y_{GSE} direction, therefore this effect will only occur if the IMF B_Y component is positive. This can occur if the IMF is directed away rather than toward the Sun.

[2.2.3] Solar Wind Drivers

As discussed above CMEs and CIRs are important and efficient drivers of geomagnetic activity [e.g. *Gosling*, 1990; *Gosling and Pizzo*, 1999]. *Kilpua et al.* [2015] defined four driving structures that cause geomagnetic activity (Figure 14). They identified three separate interactions with CMEs depending on their speed and direction. All CMEs consist of ejecta which propagates through the solar wind. If the ejecta of a CME travels faster than the ambient solar wind, then draped magnetic flux tubes will create a sheath region as the ejecta catches up with the upstream plasma. CIRs are formed when faster streaming solar wind catches up with slower solar wind ahead of it. As the fast solar wind cannot pass the slow solar wind an interface region is produced at the boundary of the two (S4, Figure 14) [*Kilpua et al.*, 2015].
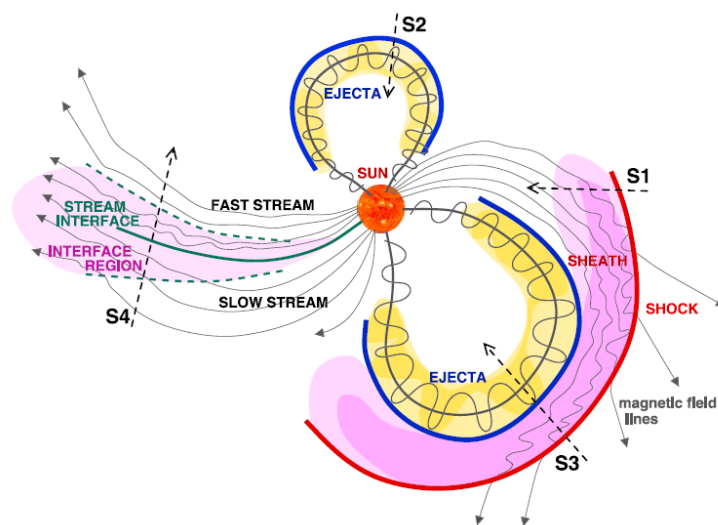
Figure 14: Schematic of solar wind structures and substructures reproduced from Kilpua et al. [2015]. S1 is defined as a sheath only CME, S2 is defined as an ejecta only CME, S3 is a sheath plus ejecta CME and S4 shows a CIR.

Borovsky and Denton [2006] showed that CMEs and CIRs are distinctly different and although they both drive geomagnetic activity the exact mechanisms which occur may also be different. The magnetosphere reacts differently to each driving structure. CIR driven storms have been shown to almost always produce ring current and radiation belt flux enhancements while this only occurs about half the time for CME driven storms [*Miyoshi and Kataoka*, 2005]. They also found that the ring current is located closer to the earth during CME driven storms due to stronger convection and so these storms are generally observed as being more intense than CIR driven storms. Conversely, the ring current of CIR driven storms decays less quickly, which has been attributed to continuous substorm injections during the recovery phase [*Tanskanen et al.*, 2005] which could provide the source particles for the observed flux enhancements. *Reeves et al.* [2011] noted that the high speed solar wind during the declining phase of solar cycles is more likely to produce enhanced relativistic electron fluxes than the same speed of solar wind during times of solar maxima. This implies that the coherent nature of CIRs may be more effective at producing relativistic electron flux enhancement than other solar wind structures (e.g. CMEs) supporting the conclusion of *O'Brien et al.* [2001]. As Figure 14 shows both CMEs and CIRs contain substructures which each have distinct solar wind properties. Therefore, the effect that each of these regions have on the magnetosphere and its plasma populations will be different [e.g. *Huttunen and Koskinen*, 2004; *Yermolaev et al.*, 2009; *Hietala et al.*, 2014; *Kilpua et al.*, 2015].

Kilpua et al. [2015] concluded that post-storm relativistic electron flux variations are dependant on the pre-storm flux, the specific properties of the driving structure and the solar wind speed following said structure. They showed that high density substructures (e.g. ejecta or interface regions) can efficiently deplete the relativistic electron flux due to magnetopause shadowing. This mechanism can remove previosly trapped particles via the magnetopause as the high density substructures cause increased convection and the compression of the dayside magnetopshere [*Li et al.,* 1997; *Li and Temerin*, 2001; *Onsager et al.*, 2007]. Post-storm relativistic electron flux increases due to the continued injection of particles, via substorms, were observed to be associated with the fast solar wind following the driving structure [*Tanskanen et al.*, 2005; *Kilpua et al.*, 2015].

Contrary to the conclusion of *Kilpua et al.* [2015] pre- and post-storm geosynchronous relativistic electron fluxes have been shown to be uncorrelated with each other, as both increases and decreases in flux have been observed to occur for any pre-storm flux and any strength of storm [*Reeves et al.*, 2003].

[2.3]   Solar Wind – Magnetosphere Interaction

As discussed above, the ultimate cause of observed space weather is the interaction of the solar wind with the magnetosphere. General trends between solar wind parameters, such as velocity and density, and the relativistic electron flux in the outer radiation belts have been well documented [*Paulikas and Blake*, 1978; *Lyatsky and Khazanov*, 2008; *Reeves et al.*, 2011]. Despite this, it is not possible to make specific predictions due the changing dominance of acceleration, transport and loss mechanisms on timescales which vary from seconds to days and differ from event to event [*Baker et al.*, 2013; *Baker et al.*, 2014; *Turner et al.*, 2014].

Paulikas and Blake [1978] showed a strong correlation between the solar wind velocity and radiation belt electron fluxes, which even persisted during periods of disturbed solar wind. It has also been shown that fast solar wind structures, such as interplanetary shocks, can drive flux increases without the requirement for enhaced convection driven by southward IMF [e.g. *Blake et al.*, 1992; *Li et al.*, 1993; *Li et al.*, 2003]. Conversely, *Weigel et al.* [2003] showed that few electron flux enhancements are preceded by extreme solar wind speeds (>600 kms^{-1}). *Reeves et al.* [2011] revisited the work done by *Paulikas and Blake* [1978]. They found that the previosly observed non-linear, triangle shaped distribution was a persistant feature in their updated data over multiple solar cycles (Figure 15). Specific events do not always follow this long term trend and in some cases an anti-correlation between the solar wind velocity and relativistic electron flux is observed [*Paulikas and Blake*, 1978]. This may be due to the effect of other solar wind properties on the relativistic electron flux.
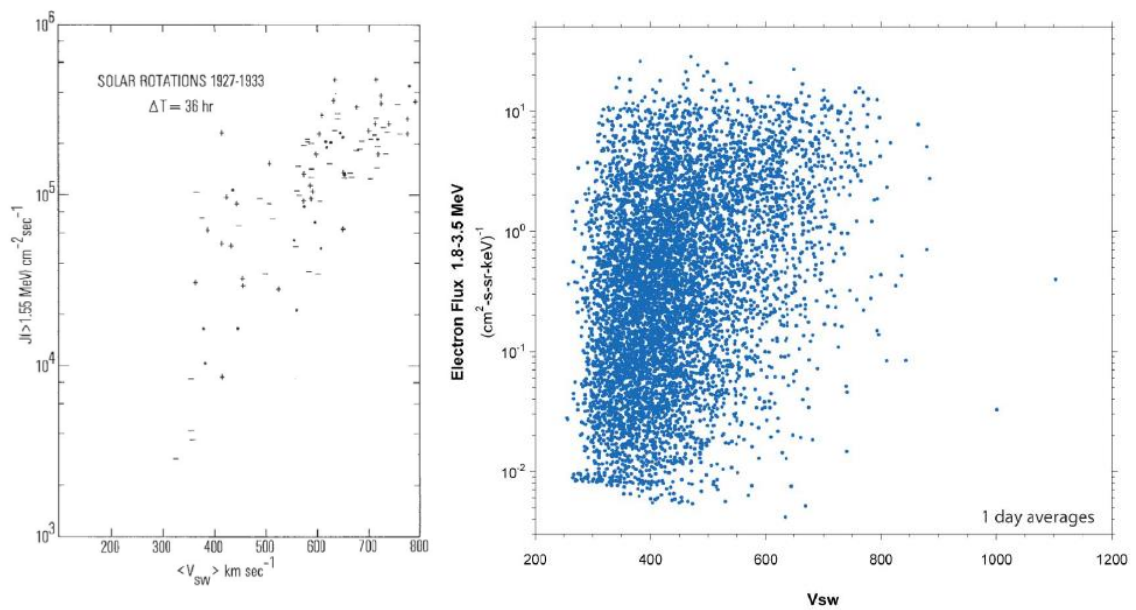
Figure 15: The typical triangle distribution as originally reported by Paulikas and Blake [1978] (left) and reproduced using an extended data set by Reeves et al. [2011] (right). Plots reproduced from Reeves et al. [2011]

There is not a simple linear relationship between the enhancement of relativistic electron flux and increased solar wind velocity [*Baker et al.*, 2004]. Fast solar wind can produce high relativistic electron fluxes whilst slow solar wind can produce a range of flux values as seen in the long term data (Figure 15) [*Paulikas and Blake*, 1978; *Reeves et al.*, 2011]. This distribution is persistent even when a lag of between 0 and 3 days is applied to the data (Figure 16). Noticeably fewer low velocity high flux days are observed for a lag of 2 days suggesting that the acceleration and transport of electrons takes a couple of days to respond to the enhanced solar wind velocity (Figure 16) [*Reeves et al.*, 2011]. Similarly to the lag observed for the enhacement of electron flux, by regions of fast solar wind, it may remain elevated for several days following the end of this driving. This explains the existance of the low velocity high flux days in the data [*Reeves et al.*, 2011]. Both the time lag and the rate of decay of relativistic electron flux can vary from event to event and therefore only partially explains the observed distribution [*Reeves et al.*, 2011]. A similar distribution to the one observed for the relativistic electron flux is also observed for lower energy electrons which may provide the source population for the relativistic electron distribution [*Reeves et al.*, 2011].
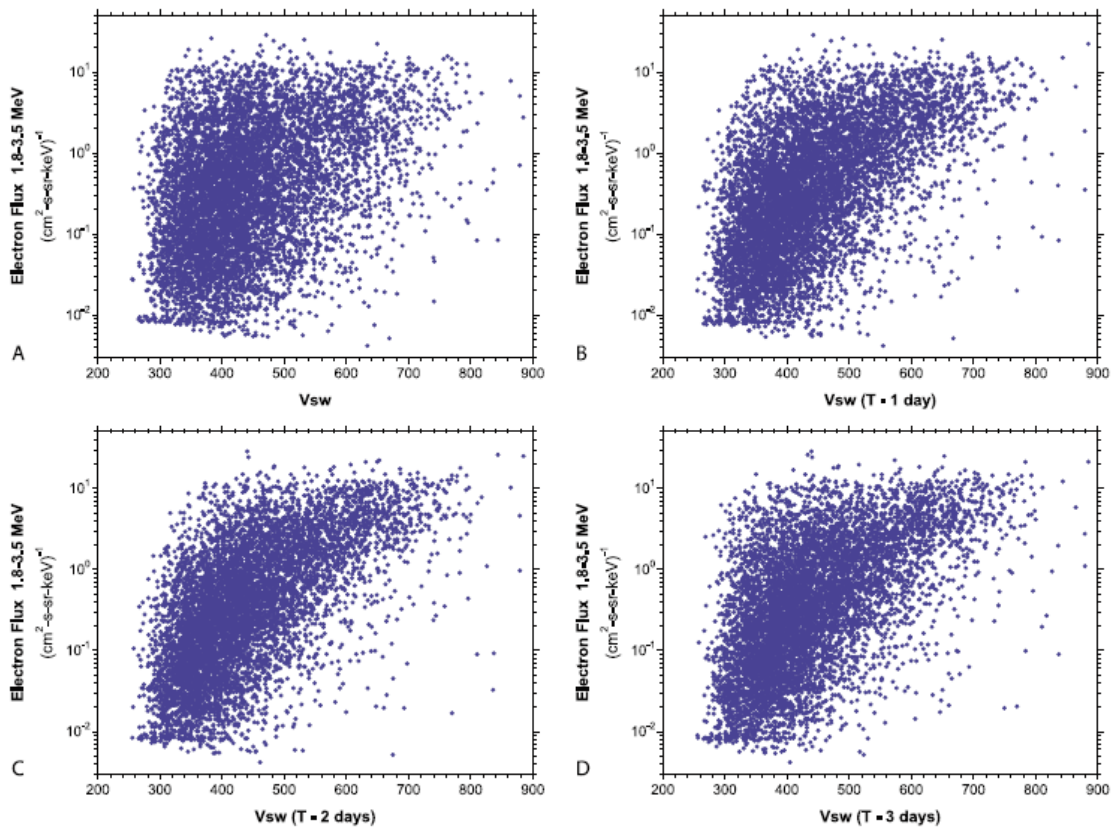
Figure 16: Persistence of the triangle distribution after a lag of 0 to 3 days is applied. Plots reproduced from Reeves et al., 2011.

Following the re-examination of the solar wind velocity relationship originally observed by *Paulikas and Blake* [1978] it was concluded [*Reeves et al.*, 2011] that there is no solar wind velocity threshold that produces a more effective enhancement of the electron flux. Therefore fast solar wind is not a neccesary condition for the acceleration of electrons to relativistic energies [*Reeves et al.*, 2011]. The relationship between the solar wind velocity and the relativistic electron flux was observed by *Reeves et al.* [2011] to become more scattered at solar maximum and more ordered during the declining phase of the solar cycle. This may indicate that the specific type of solar wind driver is more important than the solar wind velocity in the enhancement of the relativistic electron flux at geosynchronous orbit [e.g. *Kilpua et al.*, 2015].

Other solar wind parameters, such as the solar wind density, also reportedly control the flux of relativistic electrons at geosynchronous orbit [*Lyatsky and Khazanov*, 2008]. It was found that there was a stronger linear anti-correlation between the solar wind density and the electron flux than the positive correlation between the flux and the solar wind velocity [*Lyatsky and Khazanov*, 2008]. This was still found to be the case when the solar wind velocity effect was negligible. It is important to note that although the correlation coefficient is greater for the solar wind density relationship the distribution, like for the solar wind velocity, is non-linear and so the use of a linear model comparison may not be appropriate.

Lyatsky and Khazanov [2008] propose two mechanisms that could explain the observed relationship. The first is magnetopause shadowing, which (as described in section [2.2.3]) can cause the loss of particles to the magnetopause during periods of high solar wind density. This would therefore not occur during periods of low solar wind density, allowing for greater flux values to be observed. Although this mechanism could explain the observed relationship it was less favoured by *Lyatsky and Khazanov* [2008] due to the poor correlation between the solar wind pressure and relativistic electron flux enhancements. The second mechanism is dependent on the correlation between the densities of the solar wind and plasma sheet [*Borovsky et al.*, 1998]. The magnetosphere has been shown to be strongly sheilded when the ratio between the conductances of the magnetosphere and ionosphere is much greater than 1 [*Lyatsky et al.*, 2006]. Enhanced sheilding implies weaker convection and therefore lower fluxes as fewer particles would be injected into the inner magnetosphere. *Lyatsky et al.* [2006] defined the magnetospheric conductance as 0.5nV, where n is the density of the magnetospheric energetic ion population and V is the volume of the flux tubes with a unit cross section at the ionosphere. Therefore. as the solar wind density increases the value of n would increase [*Borovsky et al.*, 1998] leading to enhanced sheilding and lower fluxes. This led *Lyatsky and Khazanov* [2008] to conclude that the solar wind density was a more important parameter than the solar wind velocity for controlling the flux of relativistic electrons at geosynchronous orbit.

As previously mentioned geomagnetic storms are caused by the interaction between the solar wind and the magnetosphere and can produce enhancements in the relativitic electron flux [e.g. *Reeves et al.*, 2003]. Many acceleration, transport and loss mechanisms, such as radial diffusion and plasma wave excitation, are enhaced during storms and indeed scale with storm intensity [*Anderson et al.*, 2015]. It may therefore be expected that the relativistic electron flux would also be greater following more intense storms; however, this realtionship is not so simple [*Reeves et al.*, 2003]. It has been shown that the most intense storms are no more likely to cause flux enhancements than 'micro-storms' and both enhancements and depletions in the electron flux can occur for any size of storm [*Reeves et al.*, 2003; *Anderson et al.*, 2015].

A requirement of geomagnetic storms is a prolonged period of southwardly oriented IMF. It may therefore be more reasonable to discuss the electron flux enhancements with regards to this solar wind parameter rather than just the occurrence of storms. Not only does southward IMF drive storms it has also been shown [*Miyoshi and Kataoka*, 2008; *McPherron et al.*, 2009] to be a controlling factor during periods of high speed solar wind. *Li et al.* [2005] observed this by comparing the time delay of electron enhancements following the arrival of high speed streams. They found that if the average IMF orientation was southward then flux enhancements occurred quicker. This was attributed to the Russell-McPherron effect, which can increase the geoeffectiveness of solar wind structures (as shown in section [2.2.2.1]) [*Russell and McPherron*, 1973].

Electron flux enhancements have been discussed as a product of fast solar wind [e.g. *Paulikas and Blake*, 1978], low solar wind density [e.g. *Lyatsky and Khazanov*, 2008] and also as a result of geomagnetic storms, which in turn require extended periods of southward IMF [e.g. *Baker et al.*, 1998b; *Reeves et al.*, 2003]. Confusion as to which is the controlling factor is due to the correlation between all of the aforementioned parameters. For example, during the recovery phase of storms, when the relativistic electron flux is often enhanced, the solar wind is typically fast flowing and rarefied.

Miyoshi and Kataoka [2008] observed that high speed streams which contained southward IMF produced the largest relativistic flux enhancements. In addition, *Li et al.* [2011b] observed that these flux enhancements always occurred with at least some level of geomagnetic activity leading them to conclude that the orientation of the IMF not the solar wind speed was the controlling factor. This shows that the response of the magnetosphere to solar wind driving is still not fully understood.

[2.4]   Plasma Sources and Losses

There are ultimately two sources that can fill the plasma regions of the Earth's magnetosphere. Hydrogen ions are supplied by both the solar wind and the ionosphere to the plasmasphere, plasma sheet and the ring current regions. The ionosphere also supplies significant amounts of heavier ions, e.g. oxygen, to these regions [*Kivelson and Russell*, 1995]. Geomagnetic storms significantly alter the composition of these regions. Plasma will be energised, redistributed and removed from the magnetosphere due to the enhancement of acceleration, transport and loss processes [e.g. *Turner et al.*, 2014].

[2.4.1] Plasma Source Regions

The below discussion is focused on the variations in the hot plasma populations of the magnetosphere and the mechanisms that cause them; however, it is worth noting that the nightside magnetosphere also contains a significant population of cold plasma. Combined measurements of ion velocities and densities taken whilst spacecraft were in eclipse have shown that the flux of the cold plasma may be as large as that of the hot plasma [*Akasofu*, 1981; *Seki et al.*, 2003; *Hirahara et al.*, 2004; *Engwall et al.*, 2009a; *Engwall et al.*, 2009b; *André et al.*, 2010]. *André et al.* [2015] showed that, out to about 15 R_E, low energy ionospheric ions are always observed in the lobes.

[2.4.1.1]   Ionosphere

Ionospheric outflow, driven by ambipolar diffusion, supplies heavy ions to the magnetosphere. These outflows have been shown to provide a significant proportion of the equatorial plasma, especially during periods of enhanced solar activity content, such that oxygen ions become the dominant ring current species, [*Liao et al.*, 2012].

[2.4.1.2]   Plasmasphere

Ionospheric outflow from sub auroral latitudes fills the closed filed lines of the inner magnetosphere to create a region of cold and dense plasma that co-rotates with the Earth [*Carpenter*, 1962; *Kotova*, 2007]. This region is the plasmasphere which is predominantly comprised of H^+ ions [*Darrouzet et al.*, 2009]. *Chappell* [1982] and *Roberts et al.* [1987] reported a population of heavy ions just inside the plasmapause. More recently, *Grew et al.* [2007] showed that the ratio $H^+:He^+:O^+$ was approximately 82:15:3 within the plasmapause and that the oxygen ion content dramatically increased, by as much as 60%, outside of the plasmasphere. The boundary of the plasmasphere is defined by a sharp drop in the total plasma density, which can be as much as two orders of magnitude, and is located close to the inner edge of the radiation belts [*Li et al.*, 2006]. The contrast in plasma density either side of the plasmapause is dependent on geomagnetic activity. During active periods this boundary is observed as a sharp discontinuity in plasma density while during less active periods it is more diffuse [*Darrouzet et al.*, 2013]. This is due to the continued outflow of ionospheric plasma until the gas pressure along the field lines has been equalised [*Park*, 1970; *Kotova*, 2007]. The balance between convection and co-rotation defines the size of the plasmasphere. The enhancement of convection during periods of increased geomagnetic activity causes the plasmasphere to shrink. The expansion of the plasmasphere following these periods may have an effect on the evolution of the ring current [*Horne and Thorne*, 1998; *Thorne*, 2010; *Chen et al.*, 2012].

[2.4.1.3]   Plasma Sheet

The plasma sheet is a nightside reservoir of hot plasma with typical densities of between 0.1 cm^{-3} and 1 cm^{-3}. It is a closed filed line region, the inner edge of which corresponds to the outer edge of the radiation belts and is magnetically connected to the auroral regions [*Cao et al.*, 2011]. During active times the plasma sheet composition changes to include a high concentration of O$^+$ ions [*Kivelson and Russell*, 1995]. This may be due to the direct supply of ionospheric ions via the auroral regions during the substorm expansion phase [*Akasofu*, 1981; *Gazey et al.*, 1997]. It is though that, during geomagnetic storms, up to 80% of O$^+$ in the plasma sheet could be supplied by this process [*Daglis and Axford*, 1996; *Sauvaud et al.*, 2004]. *André et al.* [2015] concluded that plasma is energised as it traverses the plasma sheet due to the reduction of the occurrence of low energy plasma in this region. Indeed, **E∧B** drift has been shown to energise O$^+$ ions that passe through the plasma sheet [*Orsini et al.*, 1990; *Hirahara et al.*, 1994]. Injected plasma sheet particles will form the symmetric ring current during the recovery phase of storms [*Daglis and Kozyra*, 2002].

[2.4.1.4]   Ring Current

The ring current is formed by the charge separation, caused by the gradient-curvature drift, of ~10-100keV ions and electrons injected into the inner magnetosphere from the plasma sheet [*Daglis et al.*, 1999]. It was originally though that the ring current existed as two spatially distinct regions [e.g. *Akasofu and Chapman*, 1972]. The oxygen dominated inner belt (2-4 R_E) was thought to only occur during geomagnetic storms decaying quickly following the end of the main phase [e.g. *Lui et al.*, 1987]. The outer belt (>4 R_E) was thought to be a more persistant feature dominated by H$^+$ ions [e.g. *Williams*, 1985; *Hamilton et al.*, 1988]. *Tverskaya et al.* [2003] suggested that the electrons formed a single belt, the location of which seems to be dependent on the strength of the storm.

Enhanced convection during the main and early recovery phases of geomagnetic storms cause particles to be injected onto open drift paths suggesting that the ring current is highly asymmetric [*Daglis and Kozyra*, 2002]. As convection eases particles are injected onto closed drift paths allowing them to make complete drift orbits and thus form the symmetric ring current. During storm times O^+ ions dominate the ring current, the exact processes that allow for this are unclear; however, injection of O^+ from the enhanced storm time plasma sheet population may provide at least a part of the solution [*Welling et al.*, 2015]. The acceleration and loss of plasma during geomagnetic storms are dependent on the location and composition of the ring current [*Daglis*, 2001]. The evolution of the ring current must therefore be understood if one is to understand the wider processes at play in the magnetosphere during geomagnetic storms.

[2.4.2] Acceleration Mechanisms

The solar wind cannot directly produce the observed radiation belt fluxes, due to its low density [*Li et al.*, 1997]. Instead, geomagnetic activity drives multiple acceleration process that can energise particles on short timescales throughout the magnetosphere [*Iles et al.*, 2002]. These processes are dependent on location, phase of the storm and even IMF orientation [*Blake et al.*, 1997; *Kilpua et al.*, 2015] and have been shown to drive the observed enhancements of relativistic electron flux [*Reeves et al.*, 2003]. It has been shown that there are at least nine different processes that can increase the relativistic electron population [*Friedel et al.*, 2002]. They also show that a seed population of electrons, which can be provided by injection via substorms, is required for all of these mechanisms. Although geomagnetic activity will enhance electron fluxes, significant variations during quiescent periods have also been shown to exist [e.g. *Schiller et al.*, 2014; *Su et al.*, 2014].

[2.4.2.1]   Radial Diffusion

Radial diffusion is an important acceleration mechanism for the energisation of electrons during the main and recovery phases of geomagnetic storms [*Vennerstrøm*, 1999; *Mathie and Mann*, 2000a]. Drift-resonant interactions with ULF waves, during the main phase, can cause particles to diffuse inward to regions of greater magnetic field strength. This will cause the acceleration of particles as they conserve their adiabatic invariants [*Mathie and Mann*, 2001; *Barker et al.*, 2005; *Shprits et al.*, 2005; *Li et al.*, 2009]. During the recovery phase, inward motion can be provided by the conservation of the third adiabatic invariant as the ring current decays, which will again lead to the adiabatic acceleration of particles [*Mathie and Mann*, 2000a].

Betatron acceleration, driven by radial diffusion, was originally thought to be the dominant energisation mechanism for magnetospheric electrons [Schulz and Lanzerotti, 1974]. Although radial diffusion can provide the acceleration of particles it cannot account for the observed MeV electron flux variations during the recovery phase [*Horne*, 2002]. This is supported by the observations of flat-topped pitch angle populations [*Horne et al.*, 2003b], the energy dependence, with time, of the spectra of energetic particles [*Summers et al.*, 2002] and the length of time required for inward movement [*Miyoshi et al.*, 2003]. This implies the need for additional local acceleration processes [*Brautigam and Albert*, 2000].

[2.4.2.2]   Substorms

Substorms have been discussed as a product of magnetic convection (see Section [1.1.3.2]). The result of these events is the injection of particles deep into the magnetosphere [*Mauk*, 1986]. If the injection rate is of the order of the particle gyroperiod non-adiabatic acceleration will occur [*Seki et al.*, 2015]. The symmetric ring current can be formed via this mechanism as plasma sheet particles are accelerated and injected onto closed drift paths [*Gonzalez et al.*, 1994]. Substorms may also provide an acceleration mechanism which can reproduce the observed dominance of energetic O^+ in the ring current during storms [*Delcourt*, 2002]. Substorms reorganise the magnetic

configuration of the tail magnetosphere via reconnection [*Möbius et al.*, 1986]. The dipolarisation of these field lines induces an electric field which preferentially accelerates the heavy ion species to energies of a few hundred keV [*Ipavich et al.*, 1984; *Nosé et al.*, 2000].

Substorms can also indirectly accelerate electrons to relativistic energies. Unstable plasma populations can be created via the substorm injection of 100 keV particles into the inner magnetosphere during periods of enhanced convection [*Reeves et al.*, 2011]. This can drive the amplification of wave modes which in turn can resonate with the electron population accelerating them up to relativistic energies [*Lyatsky and Khazanov*, 2008]. This provides another link between the generation of MeV electrons and the orientation of the IMF [*Horne and Thorne*, 1998].

[2.4.2.3]   Wave-Particle Interactions - Acceleration

Resonant interactions with plasma waves has been shown to both accelerate and deplete magnetospheric plasma populations [e.g. *Shprits et al.*, 2008]. Later in this chapter (Section [2.5] onwards) the properties and generation mechanisms for several different plasma waves will be discussed in detail. In this section, and the equivalent plasma loss section ([2.4.4.5]), the effect of these waves on the plasma, rather than the waves themselves, will be discussed.

As noted above there are several processes that can cause the enhancement of both ion and electron fluxes. This will destabilise the equilibrium state of the magnetosphere and provide the free energy for the generation of wave modes [*Reeves et al.*, 2003; *Thorne et al.*, 2013]. These wave modes can propagate throughout the magnetosphere and energise newly injected particles, especially during the main phase of storms [*Gonzalez et al.*, 1989]. It has be shown that both ULF and VLF waves can accelerate electrons to relativistic energies on the timescale of hours [*Horne and Thorne*, 1998; *Summers et al.*, 1998; *Elkington et al.*, 1999].

Periods of elevated relativistic electron flux have been observed to correspond with peaks in ULF power [*Baker et al.*, 1998b; *Rostoker et al.*, 1998]. This may suggest that drift-resonant interactions with ULF waves, which violate all three adiabatic invariants, are key in accelerating electrons to relativistic energies [*Summers and Ma*, 2000b; *Green and Kivelson*, 2001]. These interactions can transfer the wave energy to the newly injected seed electrons during storms times [*Baker et al.*, 1998a]. The highest relativistic electron fluxes have been shown to occur when there is powerful ULF wave activity during the recovery phase of storms [*Green and Kivelson*, 2001; *O'Brien et al.*, 2003]. *O'Brien et al.* [2003] concluded that drift-resonant interactions with ULF pulsations are the main mechanism for the energisation of electrons to relativistic energies, following inward transport via radial diffusion [*Engebretson et al.*, 1998; *Ukhorskiy et al.*, 2006]. ULF waves have been shown to be generated by Kelvin-Helmholtz instabilities, which are a product of the velocity discontinuity at the magnetopause [*Mathie and Mann*, 2000b].

Another mechanism for the energisation of electrons in the magnetosphere is the gyro-resonant interaction with VLF wave modes, such as whistler mode chorus waves [*Meredith et al.*, 2001; *Meredith et al.*, 2002; *Bortnik and Thorne*, 2007; *Tu et al.*, 2009]. Wave particle interactions with chorus mode waves have been shown to trigger efficient stochastic energy diffusion of seed electrons by breaking the conservation of the second adiabatic invariant [*Summers et al.*, 1998; *Shprits et al.*, 2006c]. It has been shown that this mechanism is at least as effective as radial diffusion for the local energisation of trapped electrons to relativistic energies within the radiation belts [*Horne and Thorne*, 1998; *Summers and Ma*, 2000a; *Chen et al.*, 2007]. During storms times it has been suggested that gyro-resonant interation with whistler mode chorus waves is the process that reflates the relativistic electron flux following the main phase drop out [*Miyoshi et al.*, 2003; *Onsager et al.*, 2002; *Green and Kivelson*, 2004]. It has been shown [*Li et al.*, 2007; *Shprits et al.*, 2008] that this acceleration mechanism can explain the observed 2-day delay in relativistic electron flux enhancement that was discussed in section [2.3] [e.g. *Baker et al.*, 1990; *Baker et al.*, 1994; *Reeves et al.*, 2011].

Gyro-resonant interactions with VLF waves can also accelerate ions within the magnetosphere. During the main phase of storms, it is believed that electromagnetic ion cyclotron (EMIC) waves, which are commonly observed at the duskside plasmapause, can accelerate O^+ ions in the direction perpendicular to the magnetic field [*Thorne and Horne*, 1997]. EMIC waves have been observed to strongly interact with high energy electrons with small pitch angles [*O'Brien et al.*, 2008; *Shprits et al.*, 2008]. At higher pitch angles EMIC waves are less able to accelerate electrons as the threshold resonant energy rises from to above 1 MeV [*Horne and Thorne*, 1998].

Whistler mode hiss waves can cause the energy diffusion of plasmaspheric electrons; however, this process was observed to be negligible when compared to loss via pitch angle scattering [*Abel and Thorne*, 1998; *Li et al.*, 2007].

[2.4.3] Transport Mechanisms

Substorm injection and inward radial diffusion not only accelerate particles but also transport plasma from the plasma sheet into the inner magnetosphere. This can provide the necessary conditions for the excitation of wave modes [*Thorne et al.*, 2013]. This is shown by the convection driven transport of seed electrons with energies of a few hundred keV, which are required for the generation of whislter mode chorus waves [*Li et al.*, 1997; *Friedel et al.*, 2002]. Not only this but it has been shown that radial diffusion is effective in transporting electrons that have been accelerated via resonant interactions with whistler mode chorus waves from the outer to the inner magnetosphere [*O'Brien et al.*, 2003; *Li et al.*, 2007; *Thorne et al.*, 2007].

[2.4.4] Loss Mechanisms

Plasma in not just accelerated during a geomagnetic storm. *Li et al.* [2007] showed that loss processes occur on similar and even shorter timescales than acceleration processes. During the main phase, as convection increases, the plasmasphere is eroded by the removal of plasma to the magnetopause [*Walsh et al.*, 2014]. The speed that this occurs can lead to the formation of plasmaspheric tongues [*Lemaire*, 2001; *Dandouras et al.*,

2005], shoulders [*Sandel et al.*, 2003; *Pierrard et al.*, 2008] and dayside drainage plumes [*Goldstein et al.*, 2003; *Welling et al.*, 2015]. It is not only the plasmasphere that is eroded during storm times, observations have shown the main phase removal of high energy electrons before they are replenished during the recovery phase [*Kilpua et al.*, 2015]. It has been suggested that fully adiabatic processes such as the 'Dst effect' [*Kim and Chan*, 1997] can account for the observed change. Although this may reproduce the flux drop-out at geosynchronous orbit, it cannot explain why these fluxes remain supressed for a quarter of all observed events [*Reeves et al.*, 2003]. It was therefore suggested that additional processes which cause real loss of particles from the magnetosphere must also be present during storms [*Green and Kivelson*, 2004].

[2.4.4.1]   The Dst Effect

As mentioned above the 'Dst effect' has been shown to account for the observed reduction in the geosynchronous relativistic electron flux during the main phase of storms, and can also affect high energy ions [*Kim and Chan*, 1997]. During the main phase of storms, the enhanced ring current induces a magnetic field which acts to reduce the magnetic field strength of the Earth. If this occurs slowly compared to the particles drift period, then they will diffuse outward to conserve the magnetic flux enclosed by their drift shell. If this coincides with a compression of the magnetopause then particles may be lost from the system [*Kim and Chan*, 1997].

[2.4.4.2]   Plasmaspheric Wind

Plasma interchange motion driven by the difference between centrifugal, pressure gradient and gravitational forces [*André and Lemaire*, 2006; *Pierrard et al.*, 2009] causes the loss of plasmaspheric plasma to the outer magnetosphere [*Lemaire and Schunk*, 1992; *Welling et al.*, 2015]. It was estimated by *Lemaire and Schunk* [1992] that the plasmasphere should take a maximum of 2.5 days to refill following the main phase of an intense storm; however, observations have shown that this, in fact, takes between 4 and 8 days [*Banks et al.*, 1971; *Obana et al.*, 2010]. A loss process, such as the

plasmaspheric wind, could explain the difference in these refilling times. More direct evidence for this mechanism was given by *Dandouras* [2013] who reported the net outward flow of plasmaspheric ions for all MLT and levels of geomagnetic activity.

[2.4.4.3]   **Coulomb Scattering**

Precipitation via coulomb scattering is due to the change in pitch angle caused by the interaction between the electric fields of two charged particles [*Daglis et al.,* 1999]. This process can remove ions from the inner edge of the ring current, where it overlaps with the high density plasmasphere, during the recovery phase of storms [*Fok et al.*, 1991; *Gonzalez et al.*, 1994].

[2.4.4.4]   **Charge Exchange**

Charge exchange is an important loss process at low altitudes whereby energetic magnetospheric ions strip an electron from the neutral atoms of the geocorona [*Daglis et al.,* 1999]. This neutralises the energetic particle causing it to no longer be trapped by the magnetic field. This mechanism becomes less important in the outer magnetosphere as the density of neutral atoms decreases with altitude [*Daglis et al.,* 1999]. Charge exchange is also less effective for the removal of high energy hydrogen ions as the collisional cross section is dependent on both energy and mass [*Smith and Bewtra*, 1978; *Daglis et al.*, 1999]. This implies the need for additional loss processes such as via gyro-resonant wave-particle interactions.

[2.4.4.5]   **Wave-Particle Interactions - Loss**

Plasma waves are generated from the flux enhancement of ions and electrons during storm times. It was suggested that, due to the limited MLT regions these waves occur in, collisional loss process would still dominate the decay of the symmetric ring current during the recovery phase [*Jordanova et al.*, 1998]. It has been shown that gyro-resonant wave-particle interactions with plasma waves can remove ring current particles from the inner magnetosphere on timescales much shorter than those

associated with coulomb scattering and charge exchange [e.g. *Cornwall et al.*, 1970; *Feldstein et al.*, 1994]. Observations have shown that, during storm times, energetic particle flux depletions are associated with increased chorus, hiss [*Smith et al.*, 1974; *Li et al.*, 2007] and EMIC wave power [*Clausen et al.*, 2011; *Chen et al.*, 2014]. Gyro-resonant interactions with these waves violates the first two adiabatic invariants causing the pitch angle scattering of energetic particles [e.g. *Lorentzen et al.*, 2000; *Millan et al.*, 2002; *Thorne et al.*, 2005b]. During the main phase of storms, the drift orbit of high energy electrons causes them to enter different regions of the magnetosphere, thus allowing them to be scattered by different wave modes [*Shprits et al.*, 2006a].

EMIC waves, with peak amplitudes of up to 10 nT, can cause the pitch angle scattering of relativistic particles into the loss cone [e.g. *Thorne and Kennel*, 1971; *Meredith et al.*, 2003c]. The timescale for this interaction can be of the order of 1 hour during the main phase of storms, which is shorter than that of collisional processes [e.g. *Albert*, 2003]. Resonant interactions with EMIC waves have been observed to scatter ring current ions into the loss cone [*Cocke and Cornwall*, 1967] leading *Cornwall et al.* [1970] to propose this mechanim is the dominant ring current loss process. Loss of ring current particles via scattering by EMIC waves has been shown to increase the Dst index by 10 nT/hr during the recovery phase of storms [*Kozyra et al.*, 1997]. Pitch angle scattering via EMIC waves has also been observed to efficiently remove relativistic electrons during periods of enhanced geomagnetic activity [*Thorne and Kennel*, 1971; *Li et al.*, 2007; *Shprits et al.*, 2008]. Enhanced EMIC wave power during the recovery phase may explain why the relativistic electron flux is observed to decrease over the duration some storms [e.g. *Onsager et al.*, 2002; *Green and Kivelson*, 2004].

Following the end of the main phase as the plasmasphere expands pitch angle scattering via gyro-resonant interactions with whistler mode hiss waves becomes more important [*Onsager et al.*, 2002; *Green and Kivelson*, 2004]. Once the plasmasphere expands past the drift orbits of relativistic electrons, chorus wave driven acceleration will cease allowing loss via plasmaspheric hiss to dominate [*Meredith et al.*, 2006].

Outside of the plasmasphere whistler mode chorus waves can, not only energise electrons, but also pitch angle scatter them into the loss cone forming the diffuse and discrete aurora [e.g. *Selesnick and Blake*, 2000; *Albert*, 2002; *Summers and Thorne*, 2003; *Newell et al.*, 2009; *Thorne et al.*, 2010]. Gyro-resonant interactions with whistler mode chorus waves at high latitudes have been suggested as the cause of observed MeV microburst precipitation [*Lorentzen et al.*, 2001; *Horne and Thorne*, 2003]. The source location of these microbursts has been found to be just outside the dawnside plasmasphere, which is consistent with the preferred location for chorus wave generation [*Nakamura et al.*, 2000; *O'Brien et al.*, 2004; *Thorne et al.*, 2005b].

[2.5]   Wave modes

The wave modes have been discussed above from the point of view of their effect on the magnetospheric plasma populations. This section will go into more detail on their properties, location and generation mechanisms.

During storms it is now thought that gyro-resonant interactions with magnetospheric plasma waves is at least as important as other acceleration and loss processes [e.g. *Chen et al.*, 2007]. Gyro-resonance can both generate and damp waves in the magnetosphere [*Horne and Thorne*, 1998]. For the generation of waves it is widely accepted that a seed population of ~10-100 keV particles is required [e.g. *Friedel et al.*, 2002]. Enhanced convection during storm times can provide an increase in these particles, via substorm injection from the plasmasheet [*Daglis et al.*, 1999]. Gyro-resonance will occur if Equation 53 is satisfied. This simply states that when a harmonic of the particle gyrofrequency, corrected for relativistic effects, matches the Doppler corrected wave frequency, energy can be transferred between the two.

$$\omega - k_\parallel v_\parallel + \frac{n|\Omega_j|}{\gamma} = 0 \tag{53}$$

In the above equation ω is the wave frequency, $k_{\parallel}$ and $v_{\parallel}$ are the wavenumber and velocity parallel to the magnetic field respectively, n is the harmonic number Ω_j is the particle gyrofrequency and γ is the Lorentz factor ($=(1 - v^2/c^2)^{-\frac{1}{2}}$).

During periods of enhanced geomagnetic activity temperature anisotropies in the equatorially mirroring H^+ and electron populations can drive the generation of EMIC and whistler mode waves respectively [*Horne and Thorne*, 1998]. EMIC waves are thought to provide an important acceleration mechanism for O^+ ions [*Thorne and Horne*, 1997] but are unable to effectively accelerate electrons [*Horne and Thorne*, 1998]. Scattering via whistler mode hiss waves is an important loss mechanism within the high density region of the plasmasphere and are thought to be the dominant loss mechanism for the creation of the slot region in the electron radiation belt [*Smith et al.*, 1974; *Meredith et al.*, 2004; *Li et al.*, 2007]. In the lower density regions outside the plasmasphere, whistler mode chorus waves can interact with both high (MeV) and lower (keV) energy electrons and are thought to be important for both acceleration and loss [*Li et al.*, 2007]. Each of these wave modes dominate in different regions of the magnetosphere at the same time. A good example of this is shown in Figure 17, which is reproduced from *Meredith et al.* [2004], and shows the change in wave spectral intensity over one orbit of the CRRES spacecraft.
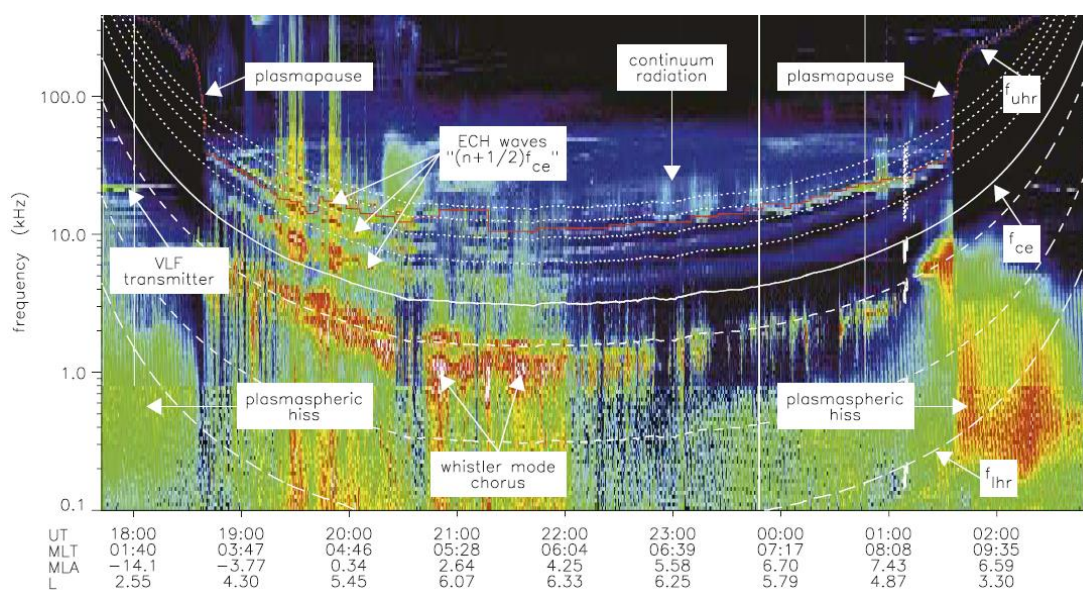
Figure 17: Reproduced from Meredith et al. [2004] and shows the wave spectral intensity observed on CRRES during orbit 119

[2.5.1] EMIC Waves

There are three bands of EMIC waves with frequencies between 0.2 and 5 Hz [e.g. *Bossen et al.*, 1976] split at each of the main magnetospheric ion gyrofrequencies (H^+, He^+, O^+) [*Horne and Thorne*, 1993]. Observations of EMIC waves show that their ubiquitous distribution at low L becomes significantly more dependant on MLT moving away from the Earth [*Wang et al.*, 2015]. The most intense EMIC waves have been found to occur within 10° of the magnetic equator at L>7 between 12 and 18 MLT, which corresponds to the region where hot and cold plasma converge [*Anderson et al.*, 1990; *Fraser et al.*, 1996; *Thorne et al.*, 2005a]. This led *Chen et al.* [2009] to conclude that cold plasmaspheric plasma was required for the generation of EMIC waves.

The generation mechanism for EMIC waves is thought to be ion temperature anisotropies caused by the interaction between the substorm injected hot ions of the ring current and the cold ions of the plasmasphere [e.g. *Horne and Thorne*, 1994; *Anderson et al.*, 1996; *Daglis et al.*, 1999; *Halford et al.*, 2010]. The growth rate of EIMC waves is then controlled by the temperature anisotropy and plasma composition [*Kozyra et al.*, 1984; *Horne and Thorne*, 1998]. Continued EMIC wave amplification will only occur if the temperature anisotropy remains above a certain threshold; however, generated EMIC waves will pitch angle scatter the ion population to reduce this anisotropy [*Mauk and McPherron*, 1980]. Reduced EMIC wave power has been observed in regions with a high O^+ content [*Kozyra et al.*, 1997; *Daglis et al.*, 1999]. Distribution function variations due to ULF waves [*Rasinkangas and Mursula*, 1998] and solar wind pressure intensifications [*Olson and Lee*, 1983; *Usanova et al.*, 2008] have also been suggested as alternative generation mechanisms for EMIC waves.

EMIC waves are thought to provide an important loss mechanism during the recovery phase of storms when wave power is expected to be strongest [*Halford et al.*, 2010]. This is due to a combination of plasmaspheric expansion via the ambipolar diffusion of cold ionospheric plasma [*Carpenter*, 1966] and the injection of hot plasma sheet plasma onto closed drift paths close to the Earth [*Reeves and Henderson*, 2001]. As such the two populations are more likely to occupy the same region of the magnetosphere,

increasing the probability of temperature anisotropies required for the generation of EMIC waves [*Chisham*, 1996; *Cao et al.*, 2011]. *Clausen et al.* [2011] observed that EMIC waves are most intense at the start of the recovery phase, following the end of dayside driving. They also show evidence for the correlation between dense solar wind regions and increased EIMC wave power.

[2.5.2] Hiss Waves

Whistler mode hiss waves are observed as broadband emissions with frequencies between ~100 Hz and 2 kHz and have been found to be most prevalent inside the high density plasmasphere [e.g. *Thorne et al.*, 1973; *Smith et al.*, 1974; *Meredith et al.*, 2004]. Resonant interactions between electrons and these waves are thought to be the cause of the slot region in the electron radiation belt [*Lyons and Thorne*, 1973; *Albert*, 1994; *Abel and Thorne*, 1998].

The generation mechanism for whistler mode hiss waves is thought to be the electron cyclotron instability of newly injected electrons (>40 keV) near the geomagnetic equator close to L=4 [*Kennel and Petschek*, 1966; *Muzzio and Angerami*, 1972]. Observed variations in the wave power with geomagnetic activity is consistent with this process [*Thorne et al.*, 1979; *Cornilleau-Wehrlin et al.*, 1993]. For regions where the wave frequency is small compared to the electron gyrofrequency, such as the plasmasphere, the functional form of the hiss wave growth rate (γ) is given by equation 54 [*Smith et al.,*1974].

$$\gamma = \pi\Omega A\eta \tag{54}$$

Where Ω is the electron gyrofrequency, A is the pitch angle anisotropy, and η is the fractional concentration of resonant electrons. Compressions of the magnetosphere and a change in the location of the plasmasphere will alter A and η respectively and thus cause variations in the growth rate of plasmaspheric hiss [e.g. *Owens and Frank*, 1968].

During periods of enhanced convection such as during the main phase of storms, the plasmasphere is compressed and so despite the increase of source particles hiss wave power remains muted [*Smith et al.*, 1974]. During the recovery phase the plasmasphere expands out past the drift paths of the source electrons. This leads to an increase in η and therefore a rapid increase in the amplitude of hiss waves, up to an order of magnitude greater than during quiet times [*Smith et al.*, 1974]. Ring current evolution will thus be dominated by the loss of electrons due to pitch angle scattering via gyro-resonant interactions with whistler mode hiss [*Meredith et al.*, 2006; *Li et al.*, 2007; *Meredith et al.*, 2007].

[2.5.3] Chorus Waves

Whistler mode chorus waves are observed as discrete non-linear rising and falling tones on the dawnside in the low density regions outside the plasmasphere [e.g. *Miyoshi et al.*, 2003]. These waves are found in two distinct bands in the frequency range of between 0.2 and 0.8 of the electron gyrofrequency (f_{ce}) [e.g. *Li et al.*, 2007] (Equation 55).

$$f_{ce} = \frac{|\Omega|}{2\pi}, \text{and } |\Omega| = \frac{B|q|}{m} \tag{55}$$

Lower band (0.2-0.5 f_{ce}) chorus intensity has been shown to peak at 0.34 f_{ce}, while upper band (0.5-0.8 f_{ce}) intensity peaks near 0.53 f_{ce} [e.g. *Tsurutani and Smith*, 1974; *Tsurutani and Smith*, 1977; *Koons and Roeder*, 1990].

The preferential location for enhancements in chorus wave power was discussed by *Meredith et al.* [2003a]. By observing the ratio between the electron plasma frequency (f_{pe}) and the electron gyrofrequency as well as chorus wave intensities they found a definite dawnside bias. In general, although they observed chorus waves in all MLT regions, they found that chorus wave intensities were greatest in regions where the f_{pe}/f_{ce} ratio was low. Typically, this occurs in low density regions outside of the plasmasphere [e.g. *Horne et al.*, 2003b]. Between 2100 and 0600 MLT peaks in chorus

wave power are found to be limited to a narrow range of latitudes within 15° of the magnetic equator. This latitude range expands to 30° of the magnetic equator between 0600 and 1500 MLT [*Meredith et al.*, 2003a]. This variation has been attributed to the uneven distribution of Landau damping effects caused by the population of keV electrons [*Thorne and Horne*, 1994; *Meredith et al.*, 2003b; *Bortnik et al.*, 2006] as previously observed by *Tsurutani and Smith* [1977].

These observations support a generation mechanism of first order cyclotron resonance with newly injected ~10-100 keV anisotropic plasma sheet electrons near the loss cone [*Kennel and Petschek*, 1966; *Horne and Thorne*, 2003; *Thorne et al.*, 2005a; *Li et al.*, 2007]. The energy gained by the waves, from the diffusion of these electrons into the loss cone, can then be used to accelerate >100 keV electrons with equatorial pitch angles up to relativistic energies [*Summers et al.*, 1998; *Horne et al.*, 2003a]. This acceleration process is thought to act on timescales of about 1 day and is able to reproduce the observed flat-topped pitch angle distributions and electron flux enhancements during the recovery phase of storms [*Meredith et al.*, 2002; *Horne et al.*, 2003a; *Horne et al.*, 2003b].

As the generation mechanism requires the injection of anisotropic seed electrons from the plasma sheet, which can be provided during storms, the intensity of chorus waves is likely to be dependent on geomagnetic activity [*Arnoldy and Chan*, 1969]. The required anisotropic population can also be created from the existing electron population by the driving of adiabatic processes, such as drift shell splitting [*Schulz and Lanzerotti*, 1974], due to compression of the magnetosphere [*Gary and Wang*, 1996].

The mechanim for the amplification of whistler mode chorus waves [e.g. *Kennel and Petschek*, 1966] may suggest that the intensity of chorus wave emission is directly correlated with the rate of ~10-100 keV electron precipitation. Using observations *Chen et al.* [2014] followed this line of reasoning to derive an equation that links these two parameters for all local times (Equation 56).

$$j(L, MLT) = B_w{}^2(L, MLT) \times P \times [(L-3)^2 + 0.03] \qquad (56)$$

where $j(L, MLT)$ is the precipitating electron flux in units of #/cm^2/s/sr and $B_w{}^2(L, MLT)$ is the chorus wave intensity in units of pT^2. The universality of equation 56 is limited by the adjustable fitting parameter (P), which is affected by variations in the pitch angle diffusion coefficient [*Gary and Wang*, 1996; *Chen et al.*, 2014]. *Chen et al.* [2014] note that for their data set a value of P~200 is suitable but this will not be the case for different events and data sets.

During storms times, when convection compresses the plasmasphere to inside the drift orbits of the ring current particles, gyro-resonant interactions with whistler mode chorus waves can provide an important acceleration and loss mechanism [*Horne and Thorne*, 1998; *Summers et al.*, 1998]. Enhancements in chorus wave intensity can drive both the acceleration of electrons within the ring current [e.g. *Meredith et al.*, 2002; *Meredith et al.*, 2003a; *O'Brien et al.*, 2003] and the electron precipitation that forms the aurorae [e.g. *Ni et al.*, 2008; *Nishimura et al.*, 2010] across a wide range of L and MLT.

[2.6]   Summary

In this chapter the current understanding of the driving of the magnetosphere by discrete structures in the solar wind has been discussed. Both CIRs and CMEs contain the necessary conditions to initiate geomagnetic storms and cause the enhancement of both large scale current systems and the flux of high energy particles. There are, significant differences between these two main types of solar wind structure [e.g. *Borovsky and Denton*, 2006]. CIRs are thought to be more likely to cause enhancements in the relativistic electron flux [e.g. *O'Brien et al.*, 2001] while CMEs tend to drive more intense geomagnetic storms [e.g. *Miyoshi and Kataoka*, 2005].

Reeves et al., [2003] showed that not all geomagnetic storms will increase the relativistic electron flux at geosynchronous orbit. The reason why one storm enhances the flux and another depletes it is still open to question. The relationship between the solar wind velocity and density and this flux is well known with higher velocity and lower density solar wind more likely to produce higher fluxes [*Paulikas and Blake*, 1978; *Lyatsky and Khazanov*, 2008]. Recently, *Kilpua et al.* [2015] suggested that the velocity of the solar wind following an event is the key factor in whether a specific event will cause a flux increase or not. These hypotheses will be evaluated in subsequent chapters.

The competition between acceleration and loss mechanisms, which are all enhanced during periods of increased geomagnetic activity [e.g. *Turner et al.*, 2014], is likely to determine the eventual change in the observed electron flux. VLF waves can be excited by ansotropies in the enhanced storm time plasma populations [e.g. *Friedel et al.*, 2002]. Gyro-resonant interactions with these waves can cause the acceleration and loss of plasma within the magnetosphere due to their ability to violate all three adiabatic invarients [e.g. *Shprits et al.*, 2008]. Variations in the intensity of EMIC, hiss and chorus waves as well as the flux of different plasma populations over the duration of geomagnetic storms will all be evaluated in the following data chapters.

CHAPTER 3

Instrumentation

[3.1]   Introduction

Statistical analysis of magnetospheric phenomena require the use of a broad range of instruments that provide effective coverage of the magnetosphere both spatially and temporally. The key data set used here is that of the Cluster spacecraft, which covers the magnetosphere. The ACE and Wind datasets, provided in the combined OMNI data, also provides the upstream solar wind conditions and geomagnetic indices. In addition, ancillary data is also used from the LANL spacecraft. The instruments, and their limitations, which provide the data used in the following chapters are outlined here. All information for this chapter was found in the instrumentation papers referenced at or near the end of each paragraph, and references therein, unless otherwise stated. The periods of interest and the data coverage provided by each of the contributing spacecraft are shown in Figure 18.
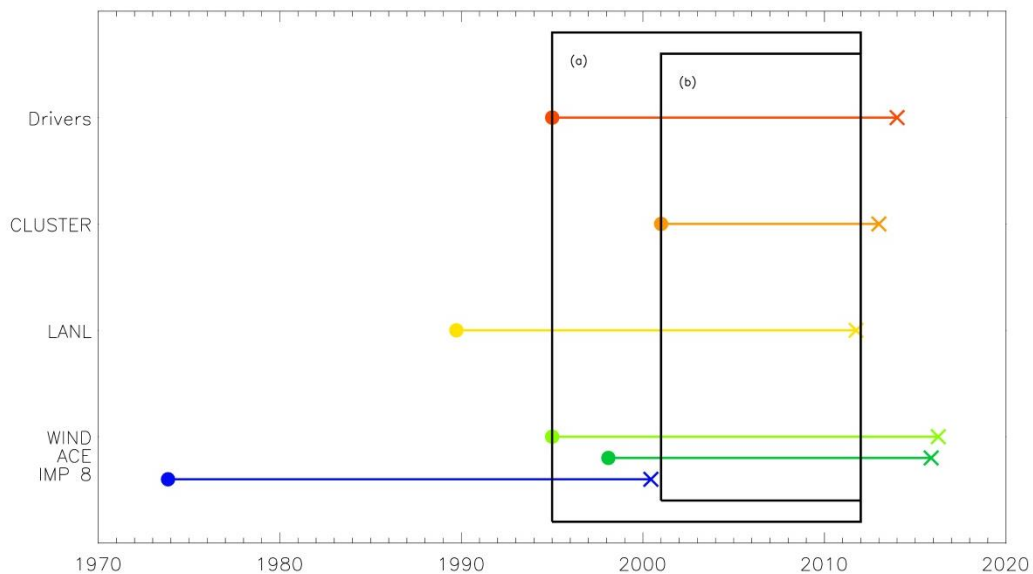
Figure 18: Shows the operational time periods for all the spacecraft of interest and highlights the periods of interest which will be analysed in the following data chapter 2 (a) and data chapters 1&3 (b). Note that 'Drivers' refers to the solar wind structures as identified by Kilpua et al. [2015].

[3.2]   Cluster

The Cluster spacecraft are a constellation of satellites that are designed to study the different magnetospheric processes over a wide range of scale sizes and in three dimensions [*Credland et al.*, 1997; *Escoubet et al.*, 1997]. This is achieved by positioning the spacecraft in a tetrahedral configuration and varying the separation distance over the lifetime of the mission. Each of the four spacecraft are identical and fly 11 instruments to measure the magnetic field strength, plasma population and electromagnetic wave power to name a few. These instruments are contained in a spin stabilised cylindrical housing that measures 1.3m in height and 1.45m in radius [*Credland et al.*, 1997; *Escoubet et al.*, 1997]. From disastrous beginnings Cluster has become a key tool in furthering the knowledge and understanding of the magnetosphere and has taken detailed plasma and field measurements that span over more than one solar cycle.

Cluster orbits the Earth every 57 hours in an elliptical polar orbit fixed with respect to the Sun with a perigee of 4 R_E and an apogee of 19.6 R_E [*Escoubet et al.*, 1997]. As shown in Figure 19 over the duration of a year Cluster will experience all regions of the magnetosphere as the orbit is observed to precess around the Earth [*Credland et al.*, 1997; *Escoubet et al.*, 1997]. The most favourable orbital orientation for this work is when the spacecraft remain in the magnetosphere for the duration of their orbit (e.g. red orbit Figure 19). All data when the spacecraft is within the magnetosphere on closed field lines will be used even if this is just a part of the whole orbit.
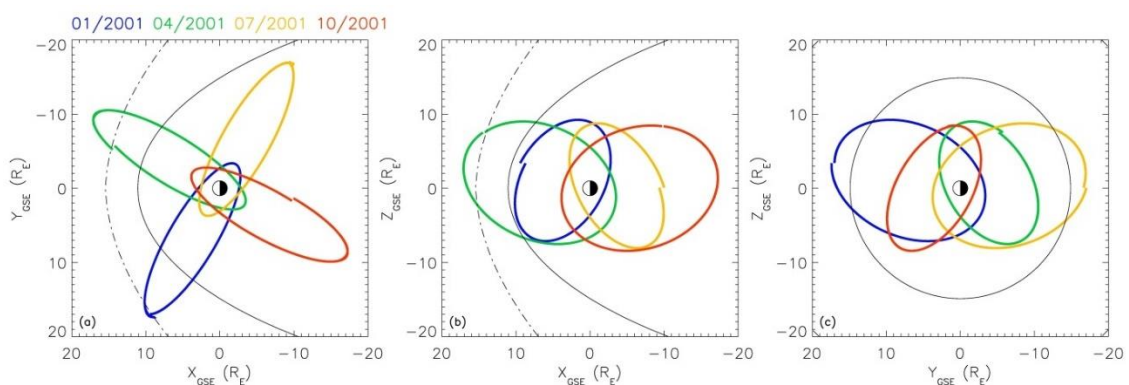
Figure 19: Shows the observed precession of the orbit of the Cluster 3 spacecraft over the duration of a year in intervals of three months in the (a) XY-, (b) XZ- and (c) YZ-planes.

The suite of instruments on board each of the Cluster spacecraft makes them the ideal tool for the simultaneous observation of plasma and wave enhancements which are likely to occur during periods of enhanced geomagnetic activity. As a result, 4 of the 11 instruments, will be utilised in subsequent data analysis (for further details see [*Credland et al.*, 1997; *Escoubet et al.*, 1997]).

[3.2.1] FGM

The fluxgate magnetometer (FGM) provides measurements of the strength of the magnetic field at the location of the spacecraft [*Escoubet et al.*, 1997]. *Balogh et al.* [1997] explain that the FGM instrument is comprised of two tri-axial fluxgate magnetometers one inboard and one outboard, located 1.5m and at the end of one of the two 5.2m radial booms respectively. They show that this configuration allows for the high resolution measurements of the magnetic field. The aim of the FGM instrument is to provide data which can be using in conjunction to the other Cluster instruments in providing a detailed analysis of complex magnetospheric processes and their spatial and temporal evolution in three dimensions (for further details see [*Balogh et al.*, 1997]).

[3.2.2] CIS

Magnetospheric ion distributions are primarily observed via the Cluster ion spectrometry (CIS) instrument. CIS comprises of two sensors, the time of flight ion composition and distribution function analyser (CODIF) and the hot ion analyser (HIA) [*Escoubet et al.*, 1997]. *Reme et al.* [1997] discuss how these sensors operate over a similar energy range, 0 to $40keVq^{-1}$ and $5eVq^{-1}$ to $32keVq^{-1}$ respectively; however, CODIF is able to resolve the main constituent ion populations (H^+, He^+, He^{++} and O^+) whereas HIA is better for taking measurements of the solar wind. The key scientific aim of the CIS instrument is to provide high resolution and accurate measurements of the ion distributions in order to evaluate dynamics of the magnetised plasma structures throughout the magnetosphere (for further information see [*Reme et al.*, 1997]).

The CODIF sensor is best suited for resolving the plasma properties of the inner magnetosphere and as such is the sensor used in this work. Unfortunately, the CIS instrument has been plagued with issues since launch. The instrument on Cluster 2 has never worked and the instruments on Cluster 1 and Cluster 3 both had to be switched off after developing faults which could not be corrected. The CIS instrument on Cluster 4 is the only instrument that has worked correctly for the duration of the mission so far.

[3.2.3] PEACE

The electron distributions are measured by the plasma electron and current experiment (PEACE) instrument, via the use of two sensors positioned on opposite sides of the spacecraft [*Escoubet et al.*, 1997]. The low energy electron analyser (LEEA) primarily measures electrons from 0.7 to 10eV but can take measurements of the electron distribution up to 30keV. The high energy electron analyser (HEEA) covers the full energy range (0.7eV to 30keV) with a geometric factor which is five times that of the LEEA [*Escoubet et al.*, 1997]. The PEACE instrument is designed to provide velocity and electron distribution measurements to determine the processes, such as energisation and scattering, which can modify the electron distributions and their sources [*Johnstone et al.*, 1997].

[3.2.4] STAFF

A three-axis search coil magnetometer and a spectrum analyser constitute the spatio-temporal analysis of field fluctuation (STAFF) instrument is able to identify the source of plasma waves [*Escoubet et al.*, 1997]. The former is able to measure the magnetic element of electromagnetic fluctuations up to 4kHz and the latter is able to execute correlation analyses between the components of these fluctuations [*Escoubet et al.*, 1997]. *Cornilleau-Wehrlin et al.* [1997] show that the STAFF instrument is important in characterising the waves that occur within the magnetosphere. Combining the measurements from all four spacecraft provides a high time resolution, three dimensional evaluation of the magnetic field variations (for more information see [*Cornilleau-Wehrlin et al.*, 1997]).

[3.3]   LANL

The data set used in the characterisation of the geomagnetic storms [*Reeves et al.*, 2003] during the period of interest (Figure 18) is an extended version of that of [*Reeves et al.*, 2011]. This data set is produced by combining the daily averages of the fluxes, measured by the energetic spectrometer for particles instrument (ESP), across all seven spacecraft linearly scaled to the reference spacecraft 1989-046.

Meier et al. [1996] explain that the ESP instrument is capable of measuring the energetic spectra of high energy electrons (0.7MeV to 10MeV) through the use of a bismuth germanate crystal optically coupled to a thick plastic scintillator. Shielding of the detector is provided by half an inch of aluminium which prevents electrons with energies below 6 MeV from entering the detector. A small area of reduced thickness in both elements of the detector provides a window through which the majority of electrons are detected (for further details see [*Meier et al.*, 1996]).

[3.4]   OMNI

Ancillary data was downloaded from NASA/GSFC's Operating Missions as a Node on the Internet (OMNI) data set which provides the solar wind conditions and geomagnetic indices. The ultimate source of energy which drives the processes of the magnetosphere at all times, to varying degrees, is the Sun and the perpetual outward flow of solar wind plasma. It is therefore important to understand the properties of the solar wind in order to fully comprehend the cause of observed differences which can occur over the duration of geomagnetic storms. Spacecraft are able to provide in situ data by orbiting the L_1 Lagrange point [*Lagrange*, 1772], ~1.5 million km upstream of the Earth. This data is then time delayed to the bow-shock nose, based on the flow speed of the solar wind, in order to provide accurate arrival times of solar wind structures.

Since the early 1980s there has been a continuous measurement of the solar wind, originally by IMP-8 alone then later by WIND and ACE as well (Figure 18). These satellites are capable of providing data at a time resolution of 1 minute. Below is a brief overview of the ACE and WIND satellites as they provide the majority of the data over the time period of interest (1995-2011 inclusive, Figure 18).

[3.4.1] Wind

The key instrument upon the ACE and WIND spacecraft is the magnetometer which continuously measures the IMF in three dimensions. *Lepping et al.* [1995] explain that the main aim of the magnetic field investigation instrument (MFI) on board WIND is to supply accurate high resolution measurements of the IMF across eight discrete ranges between ±4nT and ±65,536nT. This is achieved by using two boom-mounted, tri-axial fluxgate magnetometers, which can accurately remove the spacecraft magnetic field from the measurements (for further information see [*Lepping et al.*, 1995]).

The solar wind velocity, density and temperature measurements are obtained from the three dimensional observations of the ion distribution function observed by the Faraday cup part of the solar wind experiment (SWE) instrument on board the WIND spacecraft [*Ogilvie et al.*, 1995]. SWE is capable of measuring the plasma properties of the solar wind by utilising suite of five instruments. The two Faraday cups are ideal for measuring the supersonic plasma of the solar wind (for further details see [*Ogilvie et al.*, 1995]).

[3.4.2] ACE

The advanced composition explorer (ACE) spacecraft consists of ten instruments, four of which are used in the monitoring of the solar wind by providing data for the real time solar wind experiment (RTSW) [*Chiu et al.*, 1998; *Zwickl et al.*, 1998]. The key data sets for the parameterisation of the solar wind are produced by the magnetic field experiment (MAG) and solar wind electron, proton and alpha monitor (SWEPAM) instruments on board the ACE spacecraft. A brief description of both instruments is outlined below.

The MAG instrument is the reconditioned WIND MFI instrument which was modified to interface with the different hardware on board the ACE spacecraft. As discussed by *Smith et al*, [1998], the main aim of the ACE magnetometer is to provide highly accurate three dimensional IMF measurements. The instrument comprises of a couple of tri-axial fluxgate magnetometers which are positioned 4.19 m from the centre of the spacecraft on opposite booms (for further details see [*Lepping et al.*, 1995; *Smith et al.*, 1998]).

The SWEPAM instrument is comprised of reconditioned flight spares from the "solar wind over the poles of the sun" instrument from the joint NASA/ESA Ulysses mission [*Bame et al.*, 1992]. SWEPAM is able to measure a complete spectrum of the solar wind every 64s and transmits this data to the ground [*McComas et al.*, 1998]. The data is then processed in order to obtain the solar wind temperature, density and velocity (for further information see [*Bame et al.*, 1992; *McComas et al.*, 1998]).

[3.5] Geomagnetic Indices

The geomagnetic indices (Dst, SYM-H, Dcx and SMR) all measure the variation in the magnetic field strength of the Earth's dipole field, which is attributed to the enhancement of the ring current in the inner magnetosphere. They are used to identify geomagnetic storms by their characteristic trace in these indices, which must pass a given threshold. Historically, a Dst threshold of -50nT has been used as a distinction between storm and non-storm periods; however, this is somewhat arbitrary and does not take into account the underlying physics. The Dst index varies between +100nT and -600nT at its extremes with quiet times defined by a Dst value of 0nT [*Gonzalez et al.*, 1994]. Although the Dst index was designed such that 0nT would indicate quiet times both the analysis of Magsat data during quiet days in 1979 and the median Dst value between 1976 and 1986 suggest that the quiet time threshold is actually between -10 and -20 nT [*Gonzalez et al.*, 1994]. To make things more complicated *Anderson et al.* [2015] showed that 'micro-storms' (Dst > -50 nT) can cause extremely similar variations in geosynchronous relativistic electron flux to larger (Dst < -50 nT) geomagnetic storms suggesting that 'micro-storms' are not more representative of substorms as originally proposed [*Gonzalez et al.*, 1994].

The Dst index was originally introduced by *Sugiura* [1963] and has been the goto geomagnetic index for the identification of geomagnetic storms and the study of ring current dynamics. It is calculated from the combined mesurements of the north-south component of the surface magnetic field strength taken by four magnetometer stations. The locations of these stations were chosen to provide good longitudinal coverage with little contamination from the equatorial electrojet and region 1 and 2 currents [*Sugiura*, 1963]. The index is produced from the raw measurements by first removing the secular and solar quiet variations [*Sugiura et al.*, 1991] before dividing by the cosine of the magnetic latitude of the magnetometer stations. An hourly global index is produced by taking the average of all four stations and is proportional to the total energy carried within the ring current as shown by the Dessler-Parker-Sckopke relationship (Equation 57) [*Dessler and Parker*, 1959; *Sckopke*, 1966].

$$\frac{D_{st}^{*}(t)}{B_0} = \frac{2E(t)}{E_M} \tag{57}$$

$E(t)$ is the energy of the ring current, at a given time t, and E_M (~8x10^{17} J) is the total magnetic energy of the Earth's external magnetic field [*Carovillano and Siscoe*, 1973]. B_0 is the average surface field strength at the equator and $D_{st}^{*}(t)$ is the induced magnetic field strength of the ring current. $D_{st}^{*}(t)$ is the corrected Dst index following the removal of magnetopause current contributions as given by Equation 58 [e.g. *Burton et al.*, 1975; *Feldstein*, 1992].

$$D_{st}^{*} = D_{st} - bP^{1/2} + c \tag{58}$$

Where P is the solar wind pressure, b is a constant of proportionality and c corresponds to the contribution of the quiet time solar wind pressure; b and c have typical values of 0.2 nT/(eVcm^{-3})$^{1/2}$ and 20 nT respectively [*Gonzalez et al.*, 1994]. Equation 59 shows that the change in D_{st}^{*} over the duration of a storm can be thought of as the competition between the rate of energy injection into the ring current, related to $Q(t)$, and the rate of ring current decay (τ), which is due to a combination of loss processes [*Burton et al.*, 1975].

$$\frac{dD_{st}^*(t)}{dt} = Q(t) - \frac{D_{st}^*(t)}{\tau} \qquad (59)$$

The SYM-H index has become more prevalent in recent research due to its 1-minute time resolution, which allows for the observation of fine structures within the storm time magnetosphere [e.g. *Boteler et al.*, 1998; *Häkkinen et al.*, 2002; *Weigel et al.*, 2002; *Wanliss and Reynolds*, 2003; *Campbell*, 2004; *Hutchinson et al.*, 2011]. The SYM-H index is calculated from the data of 6 out of 10 ground magnetometer stations. The better quality data from four pairs of stations are combined with the data from two other stations (Honolulu and Memambetsu) that are always used. Once the stations have been selected the background and solar quiet magnetic fields are removed from the raw measurements [*Wanliss and Showalter*, 2006]. The SYM-H index is then rotated into a magnetic dipole co-ordinate system and, similarly to the Dst index, a latitude correction is made for each station before the values are averaged into a single index. The main differences between the SYM-H and Dst indices is the time resolution and the baseline calculation method, which is more accurately determined for the Dst index [*T. Iyemori et al.,* http://swdcwww.kugi.kyoto-u.ac.jp/aeasy/asy.pdf; *Wanliss and Showalter*, 2006]. Wanliss and Showalter [2006] evaluated the absolute difference between the two indices for different levels of geomagnetic activity. They found that this difference was of the order of 10 nT for quiet periods increasing, but remained less than 20 nT for the most active times (Figure 20). This ultimately led *Wanliss and Showalter* [2006] to recommend the use of the SYM-H index as a de facto high resolution Dst index.
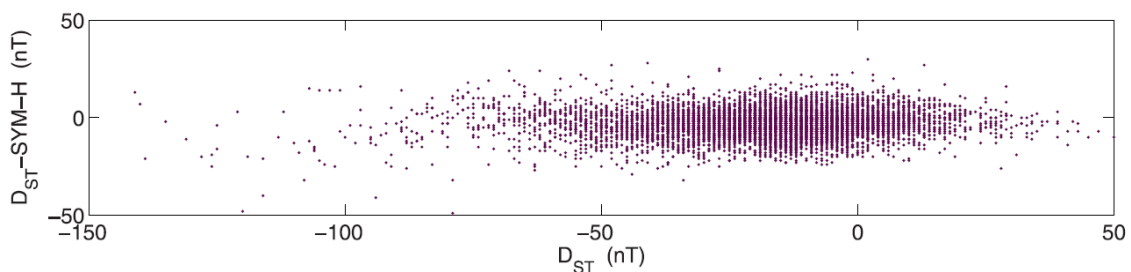
Figure 20: Reproduced from Wanliss and Showalter [2006] and shows the deviation between the SYM-H and Dst indices, for 1984, increasing as Dst becomes more negative

Although variations in these geomagnetic indices are thought of as being solely driven by ring current energisation, some issues still remain as to the level of contamination from other current systems in both the SYM-H and Dst indices [e.g. *Zhao et al.*, 2015]. *Greenspan and Hamilton* [2000] observed that the ring current may only account for between 40% and 70% of the Dst index. In fact, *Skoug et al.* [2003] reported a time period during which the Dst index was almost entirely driven by the tail current. Conversely, *Strangeway* [2000] suggested that non ring current contributions to the Dst index are small or cancel out due to the observation that it is strongly correlated with 100 eV - 32 keV oxygen ions.

In addition to the contamination of other current systems, the relatively few number of ground stations used to calculate the Dst index has led some [e.g. *Karinen et al.*, 2002] to call into question its accuracy. *Cliver et al.* [2001] found a 5.3 nT semi-annual variation in the index, unrelated to the occurrence of geomagnetic storms. Others reported systematic and random errors, including the induction effects due to the difference in ground conductivity at each station not being removed [e.g. *Baumjohann*, 1986; *Mursula and Karinen*, 2005; *Mursula et al.*, 2008; 2011].

Karinen and Mursula [2005] attempted to reconstruct the Dst index by following the original derivation method [*Sugiura*, 1963; *Sugiura et al.*, 1991] in order to extend the data by a full solar cycle back to 1932. Instead they were forced to revise the derivation due to missing information on some of the exact processing methods, such as the treatment of data gaps. In so doing they were able to eliminate some of the errors in the Dst index, creating a better representation of the storm time magnetic field variations, which they called the Dcx index [*Karinen and Mursula*, 2006].

The SMR index is constructed from 98 low and mid-latitude magnetometers and, like all geomagnetic indices, is fundamentally a measure of the variations of the north-south component of the magnetic field. These 98 stations are simply all of the magnetometer stations that contribute to the SuperMAG project and have a magnetic latitude of below ±50°, the locations of which are shown in Figure 21. The SYM-H and Dst (and hence Dcx) indices are similar measures of this magnetic variation but use fewer stations, 6 out of

10, and 4 respectively. The SMR indices are produced by removing artefacts both manually and automatically, resampling the data into minute cadence if necessary, and by rotating the measurements into a common co-ordinate system [*Newell and Gjerloev*, 2012]. An automated two-step process is used to subtract the baseline from the magnetic field measurements and thus remove yearly and Sq current contributions (for more information see [*Gjerloev*, 2012]). The values are then divided by the cosine of the magnetic latitude of each of the stations before being averaged to produce four separate local time indices which cover six hours of local time centred at local times of 00, 06, 12 and 18. A global SMR index, independent of the number of stations within each local time sector, is produced by taking the average of the four local time indices (for more information see [*Newell and Gjerloev*, 2012]).
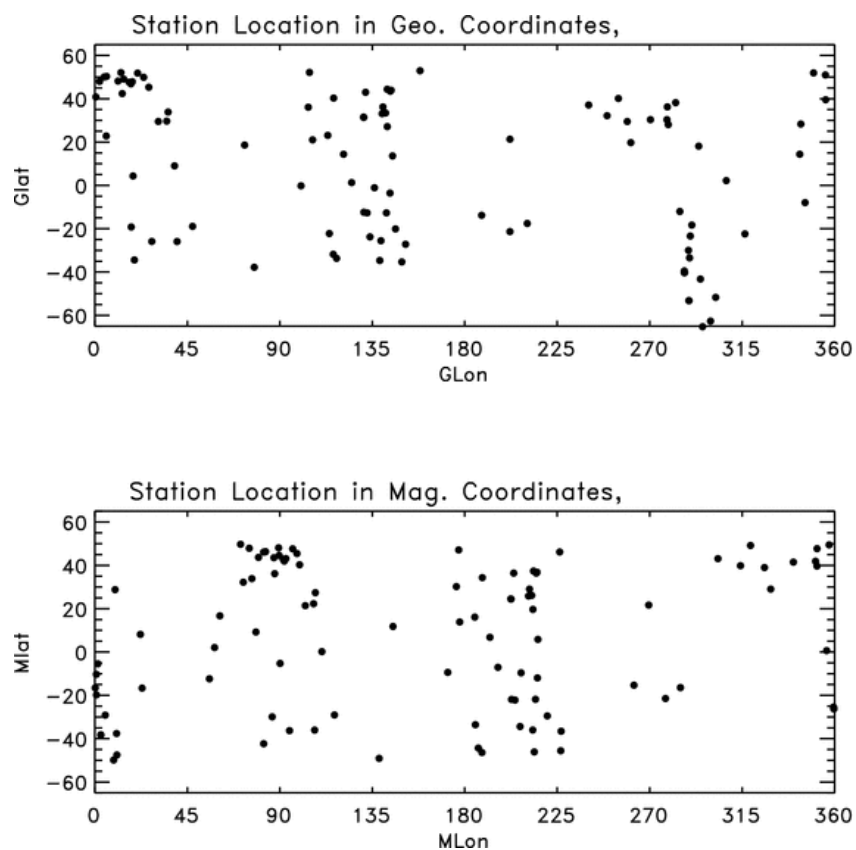
Figure 21: The locations of all the magnetometer stations contributing to the production of the SMR index, shown in both geographic (top) and magnetic (bottom) latitude and longitude. Reproduced from Newell and Gjerloev [2012]

CHAPTER 4

The Time Evolution of Magnetospheric Currents Derived from a New Storm Time Index

[4.1]   Introduction

Indices provide an important method for determination of global variations between different geomagnetic storms. These variations describe global characteristics of geomagnetic storms without direct measure of the plasma environment. This chapter will discuss the use of the Dcx and SMR indices in the identification and characterisation of geomagnetic storms. It will be shown that the SMR and Dcx indices are closely related with the main difference between the two being the time resolution. As with all geomagnetic indices the SMR and Dcx indices are not solely a representation of the ring current but include contributions from additional current systems. Following the methodology of *Asikainen et al.* [2010] the functional forms of the ring, tail and magnetopause current contributions will be updated the SMR, rather than Dcx, index. Finally, the time evolution of these current systems, for all storms and specific subsets, will be evaluated using a superposed epoch analysis.

[4.2]   Determinations of Current Indices

Asikainen et al. [2010] defined the Dcx index as a combination of the magnetopause, tail and ring currents and developed a model based on solar wind parameters so that each contribution could be analysed separately from the main index. The contribution of the tail current to the Dcx index was shown by *Asikainen et al.* [2010] to be dependent upon the so called MT-index such that as this latitude increased the strength of the tail current decreased [*Sergeev et al.*, 1993]. The MT-index was defined by *Sergeev and Gvozdevsky* [1995] as the invariant latitude of the isotropic boundary of 100 keV protons

reduced to magnetic midnight. This definition has been altered slightly [*Asikainen et al.*, 2010] by using a different proton population as described below, but is still fundamentally the latitude of the isotropic boundary. The isotropic boundary is the sharp change in particle distributions from isotropic, on highly curved tail field lines to anisotropic corresponding to particles on more dipolar field lines [*Sergeev et al.*, 1993; *Asikainen et al.*, 2010]. This change in the isotropy of the observed particle distribution has been shown to occur due to an increase in the scattering efficiency when the curvature of the field line on which particles are trapped becomes less than 8 times the particle gyroradius [*Sergeev and Tsyganenko*, 1982]. *Asikainen et al.* [2010] used the two orthogonal detectors of the MEPED detector (see [*Seale and Bushnell*, 1987; *Evans and Greer*, 2000] for detailed descriptions of the instrument) on-board the NOAA/POES low altitude satellites to identify the location of the isotropic boundary on an hourly basis. This was done by using corrected [*Asikainen and Mursula*, 2011] MEPED, 16 second averaged, 120keV - 250keV proton data and setting two criteria which must be met in order for a positive identification of the boundary. The first criterion is that the count rates in the 0° and 90° detectors satisfy the following inequality for a minimum of two consecutive measurements.

$$\left| \frac{I_0 - I_{90}}{I_0 + I_{90}} \right| < 0.3 \tag{60}$$

where I_0 and I_{90} are the count rates for the 0° and 90^0 detectors respectively. Secondly the count rate of the 0° detector must be above 5 cts·s^{-1}. The isotropic boundary location shows a significant MLT dependence being more poleward in the morning and evening sectors than at midnight [*Sergeev et al.*, 1993; *Sergeev and Gvozdevsky*, 1995; *Asikainen et al.*, 2010]. The MT-index is produced by removing the local time dependence of the isotropic boundary for both northern and southern isotropic boundaries and then averaging the values for all locations detected in each UT hour.

The values of the MT index were provided [Timo Asikainen, personal communication, 14th December 2015], for the years 2001-2011 inclusive, however, the processing methodology used to create these values, as described above, are different from that

used by *Asikainen et al.* [2010]. It is therefore necessary to re-evaluate the relationship and relative contribution of the three current systems. The current indices can be evaluated with respect to the SMR index by showing that this index can be used as a de facto high resolution Dcx index (Section [4.3]). Figure 22 shows the plot of the average SMR index against the Dcx index, similarly to the relationship between the SYM-H and Dst indices [*Wanliss and Showalter*, 2006] a high correlation is observed. The magnetic field measured by the SuperMAG magnetometer stations contains contributions from the ring current, magnetopause currents and tail currents as well as additional current systems within the magnetosphere and ionosphere [*Gjerloev*, 2012]. Therefore, the SMR index produced from these measurements will also contain contributions from these current systems. Similarly to the Dcx index [*Asikainen et al.*, 2010], it can thus be written as a summation of these current systems (with contributions from other systems combined within the constant, c).

$$SMR = SMR_{RC} + SMR_T + SMR_{MP} + c \qquad (61)$$
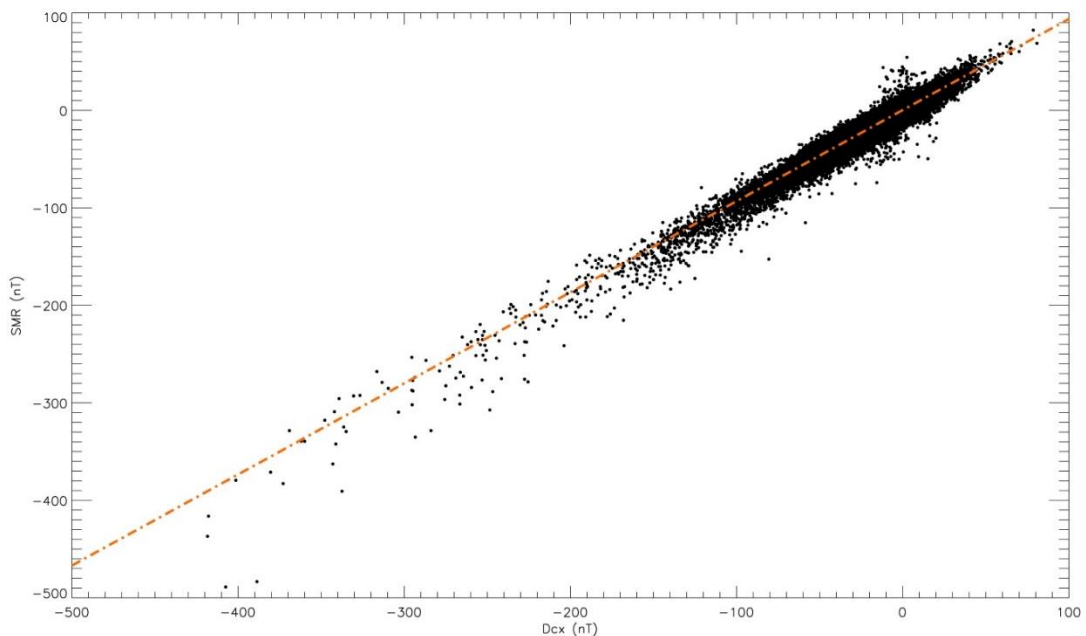
Figure 22: SMR index (hourly average) vs the Dcx index shows the expected high correlation between the two indices.

Table 1: Correlations and linear model coefficients for the relationship between the SMR index and Dcx index. SMR hourly values determined from three different methods, (a) average across the hour, (b) the first value of the hour, (c) the midpoint value within the hour

Case		Linear Fit (model SMR = (m*Dcx) +c)		Spearman's Rho	Pearson's R
		m	c		
a)	Average	0.935±0.0007	0.362±0.0149	0.920	0.962
b)	Initial Value	0.933±0.0008	0.347±0.0169	0.905	0.951
c)	Midpoint Value	0.938±0.0007	0.396±0.0159	0.913	0.957

[4.3]   Dcx vs SMR

In order to establish whether it is plausible to use the SMR index as a high resolution version of the Dcx index the two are compared in a similar manner to that conducted by *Wanliss and Showalter* [2006] between the Dst and SYM-H indices. Table 1 shows the correlation coefficients and linear fit model parameters for the relationship between the SMR and Dcx indices. As *Wanliss and Showalter* [2006] discussed for SYM-H, there are similarly 60 SMR values for every value of the Dcx index, as such we take a similar view to *Wanliss and Showalter* [2006] and evaluate the coefficients for three different methods of calculating the SMR index for each hour. In order to directly compare the Dcx and SMR indices the resolution of the SMR index has to be reduced to match that of the Dcx index. The first method, case (a) (equivalent to case 3 [*Wanliss and Showalter*, 2006]), is simply the average of the 60 SMR index values over the duration of the hour. This value provides the highest correlation in both Spearman's ρ and Pearson's R and will be used as the hourly SMR value going forwards. The coefficients for the SMR, as taken at the start of the hour (b (= Case 1)), and at the midpoint of the hour (c (=Case 2)) are slightly lower that of the average SMR but also show a high correlation with the Dcx index. Unlike the relationship between the SYM-H and Dst index there appears to be no distinct change in the gradient around -300 nT. Table 1 shows the linear model and correlation fit for all three cases. Comparing the values for the linear model within Table 1 above to that of Table 2 within [*Wanliss and Showalter*, 2006] we find that the average gradient of all three of the line a little farther from the perfect (=1.0) relationship between the two indices (=0.935) than that between the Dst and SYM-H indices above -300nT (=0.968) and closer to this value than for the Dst and SYM-H indices below -300nT (=0.776). The average constant value is much closer to zero

(=0.368) than for the relationship between the Dst and SYM-H indices both above (= -2.37) and below (= -48.5) -300 nT. Although there is no apparent change in gradient at the lowest SMR index values, the difference between the two indices is more apparent.

Figure 23 shows the difference between the Dcx and SMR indices for two different years. As can be seen the two indices are extremely similar, as is highlighted in the middle plots. The largest differences between the two indices occur during the most intense storms (such as during the Halloween storm of 2003, and another large storm earlier in the month). During these times the residuals (middle plots) are greatest, close to 100nT and 50nT respectively and are clearly extreme outliers when compared to the rest of the year, over which the residual generally lies between ±20nT. When compared to a less geomagnetically active year, such as during 2007 (right hand side Figure 23) in which neither index drops below -80nT the two indices are much better confined with residuals rarely reaching beyond ±10nT. The bottom plots demonstrate this point effectively with the larger residuals clearly located at the more extreme levels of enhanced geomagnetic activity.
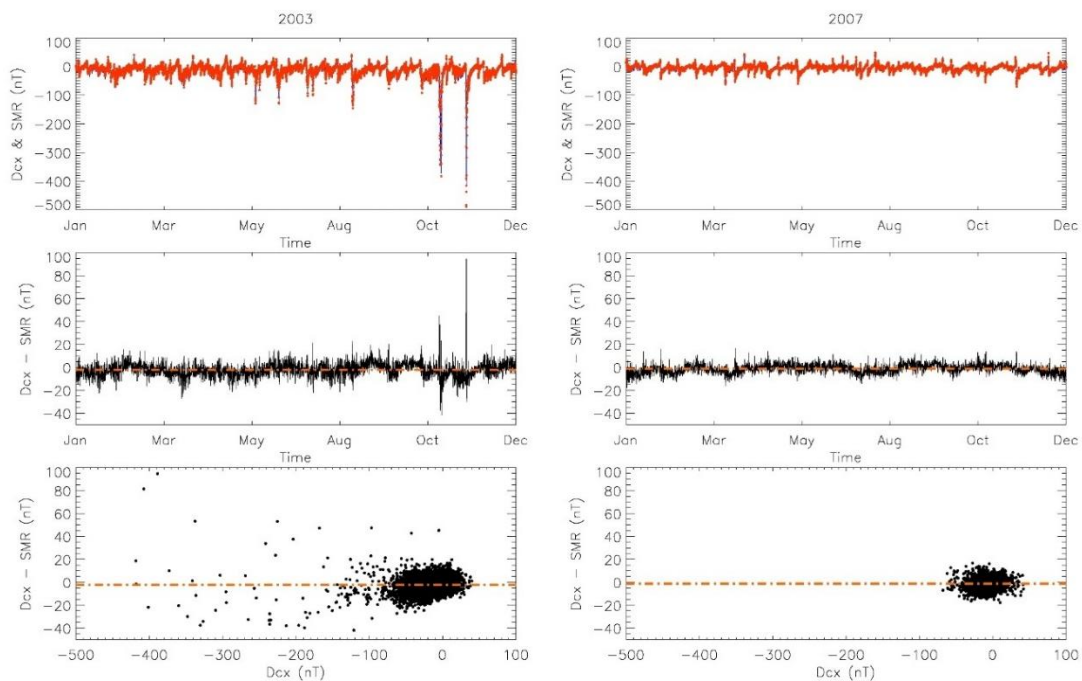
Figure 23: Plots of the variations in Dcx (blue line) and hourly averaged SMR (red circles) indices over time (top) for a typical "active" year (during solar maximum) (left) and a "quiet" year (during solar minimum (right). Also shown are the residuals (Dcx – SMR) over the duration and how they vary with time (middle) and the residuals with Dcx value (bottom)

Wanliss and Showalter [2006] split the relationship between the SYM-H and Dst indices into two linear fits, either side of -300nT in the SYM-H indices, based on visual examination of the data. In order to observe any potential change in gradient with the change in Dcx index a local linear regression analysis has been performed. This analysis technique evaluates the model parameters (in this instance SMR = (m*Dcx) + c) for a sliding window of Dcx. Points closer to the centre of the window provide a better approximation of the model parameters as such a tricube weighting function (Equations 62 & 63) is used. This function reduces the effect of outliers on the fit for each window by assigning each point, within a window, a weighting based on its proximity to the centre of the window. The closer to the centre the higher the weighting.

$$w(z) = \left(1 - \left|\left(2\frac{z-z_0}{Win}\right)^3\right|\right)^3, \text{ for } 2\frac{|z-z_0|}{Win} \leq 1 \tag{62}$$

$$w(z) = 0, \text{ for } 2\frac{|z-z_0|}{Win} > 1 \tag{63}$$

where z is the value of the Dcx index, z_0 is the Dcx value of the centre of the window and *Win* is the size of the window. This analysis uses 100 equally spaced windows of size 50nT between Dcx values of -420 and 80 such that the centres of each of the windows were at Dcx_i = -420 + 5i, where i indicates the window number between 0 and 100, for each of the differently calculated SMR hourly values. A robust least-squares regression is then performed using the bisquare weighting function [*Draper and Smith*, 1998] to minimise the effects of outliers over each of the windows. The bisquare weights are calculated in the following manner

$$w(e) = \left[1 - \left(\frac{e}{k}\right)^2\right]^2, \text{ for } |e| \leq k \tag{64}$$

$$w(e) = 0, \text{ for } |e| > k \tag{65}$$

where e is the residual, from the fit, and k is defined as

$$k = \frac{4.685 \times MAR}{0.6745} \tag{66}$$

where MAR is the median of absolute residuals.

Figure 24, reproduced from *Nurunnabi et al.* [2013], shows the difference between the tricube and bisquare functions. The tricube function produces a flatter top such that a wide range of points close to the centre point (x) are all given high weightings, before falling off rapidly for points further away. In this analysis x for the tricube weighting function is the centre of each of the Dcx windows. The bisquare weighting is narrower at the top which only gives those points that are very close to the centre point a high weighting. In this analysis x for the bisquare weighting is the value of the fit at each point within the Dcx window.

The reason for the two different weighting functions is that within each window more points are wanted with higher weights initially so the tricube function is used to give each point their weighting before constructing the first model fit. The bisquare function is then used to constrain the fit once the first model has been made.
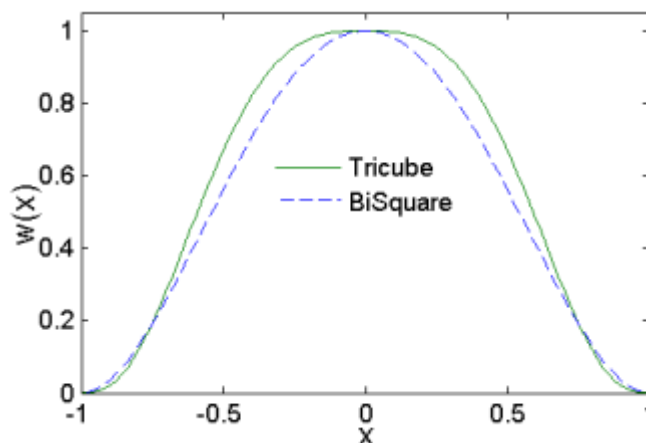
Figure 24: Tricube (green) and bisquare (blue dashed) weight functions. The weight W(X) is dependent on how far the value is from the centre point X. Reproduced from [Nurunnabi et al., 2013]

Initially each point in the Dcx window is plotted and a straight line is fit to the data weighted by the tricube function (Equations 62 & 63). The next step is then to evaluate the fit, this is done by weighting each point by its distance from the fit. This gives the residual from which a weighting for each point can be calculated using the bisquare weighting function (Equations 64 - 66). This weights points higher if they are closer to the fit and lower if they are further away. After multiplying the bisquare weight by the tricube weight each point has a different weight based on its proximity to both the centre of the Dcx window and the model fit. The fit is then re-run with the new weightings and a new model is produced. This therefore changes the values of the residuals of each of the points and as such the bisquare weightings. The old bisquare weightings are then discarded and the fit is run again with the new weightings. This is done iteratively until the weighting of each point remains constant. This value is then taken as the value of the model parameters for that window and assigned to the average Dcx value of the window. The window is then shifted by a step and the process is then rerun such that the values of the model parameters are evaluated as the Dcx changes from the most negative to the most positive values within the dataset.

Figure 25 and Figure 26 demonstrate that, unlike between the Dst and SYM-H [*Wanliss and Showalter*, 2006], the Dcx and SMR indices have an almost constant gradient and intercept value and therefore fits a single linear model well. Large variations within the gradient and intercept are observed at the most and least geomagnetically active periods where the counting statistics are poor (red points Figure 25) and thus the errors are large. The apparent oscillation in the data, specifically at the most negative values is an artefact of the local linear regression technique. These can result from random noise points in the dataset, which are more common for the extreme values of the Dcx index. The effect of a single noise point is spread out over a large range due to the overlap in the windows. As before the average gradient and intercept for all three cases are similar, and are very close to one and zero respectively (Table 2). Figure 26 shows the weighted means of both the gradient (=0.884±0.0004) and intercept (=0.086±0.004) of the linear model, for case (a), over-plotted on the local linear regression, for windows where the number of measurements exceeded 10. As can be seen from these plots, for the most extreme geomagnetic conditions, both the gradient and intercept are poorly

constrained; however, for moderate and quiet periods become well defined. The dip in the gradient around 0 is puzzling but may be due to the fact that these windows include both positive and negative numbers and as can be seen from the residuals (Figure 27) the SMR index is less negative at negative values of the Dcx and less positive at positive values of the Dcx. These also include the points that appear quite noisy around 0 in Figure 22.
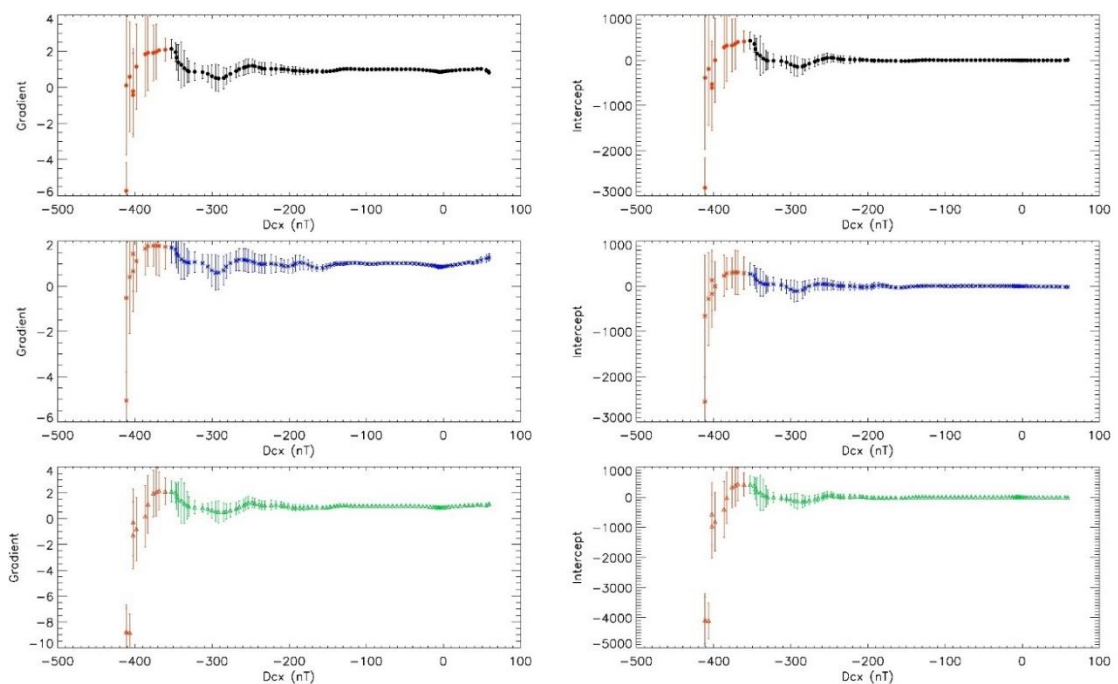
Figure 25: Gradient and Intercept changes with Dcx value for differently calculated SMR values (cases a-c, Table 1). The top panels (black) are for case (a), middle panels (blue) for case (b), and bottom panels (green) for case (c). The red points are plotted as an indication of those gradients and intercepts that were calculated from windows with poor observation statistics (n≤10)
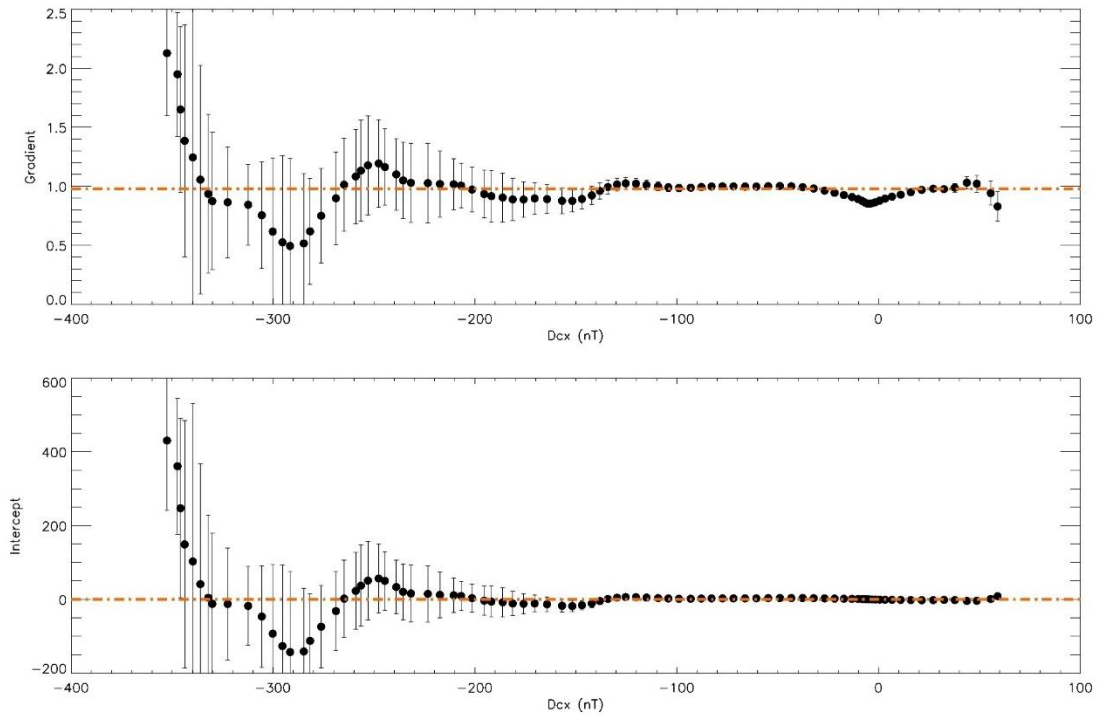
Figure 26: Enhanced view of the upper panels of Figure 25 for points with good observation statistics (n>10). The over-plotted orange line denotes the weighted mean of the all of the points.

Table 2: Shows the weighted means and standard deviations of the local linear regression gradients and intercepts analysis for all three cases of determining the hourly SMR value

Case	Local Linear Regression Weighted Mean		Local Linear Regression Standard Deviation	
	Gradient	Intercept	Gradient	Intercept
a) Average	0.884±0.0004	0.086±0.004	0.244	76.337
b) Initial Value	0.881±0.0005	0.089±0.005	0.205	53.397
c) Midpoint Value	0.888±0.0004	0.105±0.005	0.262	80.329

As Figure 26 shows, the greatest variations in both the linear model parameters are observed at the highest and lowest Dcx values. The weighted means of the local linear regression analysis show an improvement in model parameters for the intercept for all cases. This is despite a large standard deviation observed for the intercept across all parameters. This is likely due to the large absolute value of the gradients observed at the lowest values of Dcx, which will produce large absolute value of the intercepts. This, however, is observed to average to close 0 across all Dcx windows. The weighted means of the gradients for all cases are a poorer fit than observed in Table 1 but are a more reliable measure of the linear model parameters due to the more robust process involved in the weighting during the local linear regression technique. Figure 27 shows the mean and median residuals (Dcx – SMR) between the Dcx and SMR indices. *Wanliss*

and Showalter [2006] found that the difference between the SYM-H and Dst indices was on average less than 10nT for quiet times and that this increased to less than 20nT for the most disturbed conditions. Despite this the SYM-H index was recommended as the de facto high resolution Dst index. As Figure 27 shows the residuals remain within 5nT of the Dcx index for all but the most extreme geomagnetic activity and remains below 15nT at all times. The RMS deviation between the two indices was found to be 5.4nT and was calculated from all of the data points including during periods of the most extreme geomagnetic activity. This supports the findings from the local linear regression analysis as shown in Figure 27 and is less than the average residuals between the Dst and SYM-H indices. Combined with the close linear fit between the two indices it is suggested that, similar to *Wanliss and Showalter* [2006], the SMR index should be used as the de facto high resolution Dcx index.
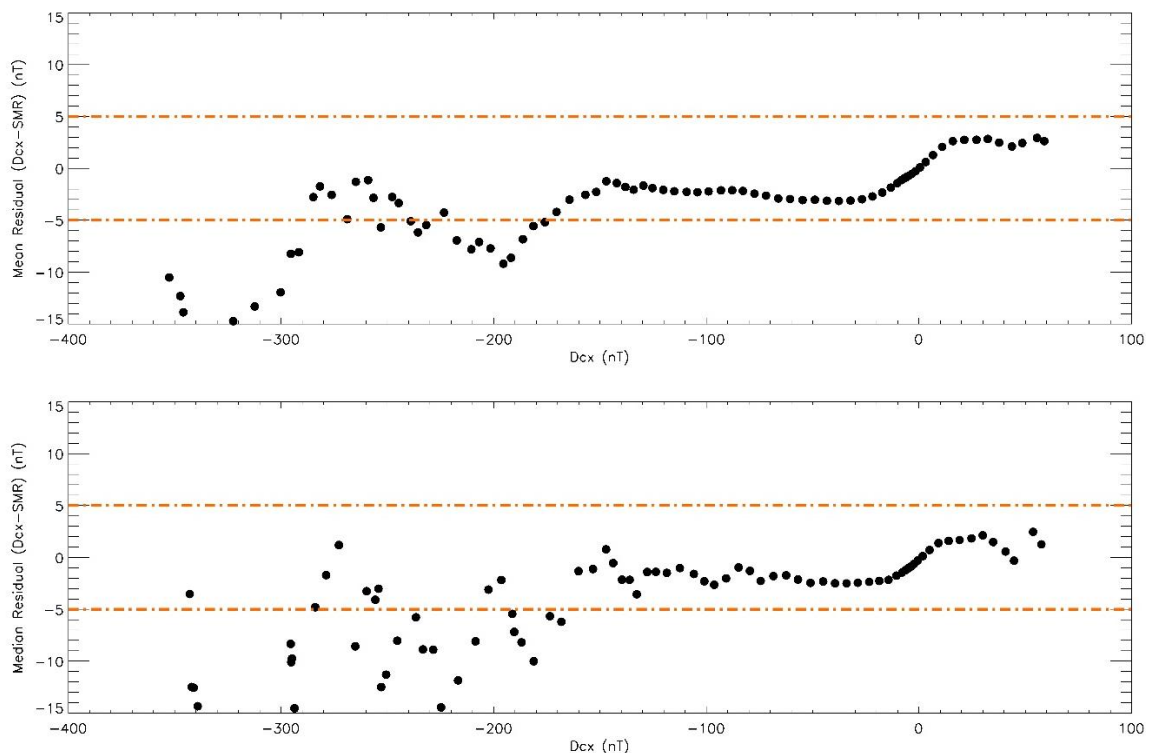
Figure 27: Mean and median residuals between the Dcx and SMR indices for case (a)

[4.4]   Current Indices

Now it has been established that the SMR index can be used as a high resolution Dcx index, the hourly averaged SMR data are used to calculate the functional forms of the tail current, magnetopause current and ring current contributions to the SMR index. These functional forms are a proof of concept that the current contributions can be extracted from the SMR. This may therefore lead to the production of the individual current indices at a higher resolution and separately for the four different local times. This is briefly explored at the end of the chapter but the hourly resolution data is suitable for the superposed epoch analysis. We follow the method detailed by *Asikainen et al.* [2010], which uses the weighted local linear regression technique, as outlined above, on a multivariate linear model to calculate the differential of the indices. This is then numerically integrated to understand how the index varies with respect to its measurable parameters. It is then possible to fit a model to the integrated form in order to describe the change in each of the modelled current systems with time.

Similarly to *Asikainen et al.* [2010], we start with the energy balance equation of the form proposed by *Burton et al.* [1975] to describe the time evolution of the ring current (equation 67).

$$\frac{dSMR_{RC}(t)}{dt} = Q(t) - \frac{SMR_{RC}(t)}{\tau(t)} \tag{67}$$

where Q indicates the contribution to the induced magnetic field due to the injection of energy into the ring current and is given in nT·hr^{-1} and τ is a function of several types of loss processes which describe the decay time of the ring current. τ is dependent upon the particle species, energy, pitch angle and L value and can vary from greater than 10 hours (such as during the recovery phase of storms) to a few hours (more common in the main phase) depending upon the strength of the geomagnetic storm. Indeed, *Gonzalez et al.* [1989] and *Prigancová and Feldstein* [1992] suggested that decay times of less than an hour may be appropriate for the most intense storms. Similarly to *Asikainen et al.* [2010], we assume that the tail index (SMR$_T$) is solely a function of the

MT index, the magnetopause index (SMR$_{MP}$) is solely a function of the square root of the solar wind dynamic pressure, and that Q and τ are functions of both the solar wind dynamic pressure and the solar wind electric field. By substituting equation 61 into equation 67 and applying the chain rule it is possible to obtain the time evolution of the SMR index as a function of the current systems of interest:

$$\frac{dSMR}{dt} = Q + \frac{c}{\tau} - \frac{SMR}{\tau} + \frac{SMR_{MP}}{\tau} + \frac{SMR_T}{\tau} + \frac{dSMR_T}{dMT}\frac{dMT}{dt} + \frac{dSMR_{MP}}{d\sqrt{P_{SW}}}\frac{d\sqrt{P_{SW}}}{dt} \quad (68)$$

It is possible to numerically obtain the values of the tail and magnetopause currents and the energy injection rate and decay time using observed values for the solar wind dynamic pressure, electric field and the MT index via the local linear regression technique. The data used to complete this analysis covers the time period from 2001 to 2011 inclusive and hence both the most and least active times of solar cycle 23. IMF data was sourced from the OMNI high resolution dataset, which provides measurements of the upstream solar wind conditions that are then projected to the bow shock nose, on a time resolution of one minute. The temporal resolution of the data was limited by the MT indices which can only be produced several times per hour once sufficient measurements of the latitude of the isotropic boundaries had been observed. This required that that OMNI data be reprocessed by taking an hourly average. The values of MT index were provided by Timo Asikainen [Private Communication, 14th December 2015] and originate from 120-250keV proton measurements made by the MEPED detector on-board the NOAA 15-18 satellites as described in section [4.2]. A three-point running mean was applied to the raw values of the MT indices in order to reduce the variance within each hourly window, which reduces the effect of rapid tail current dynamics on time scales of less than one hour.

[4.4.1] Tail Current

The tail current is assumed to be solely described by the location of the isotropic boundary, as defined by the MT index. As such the lowest latitudes of the isotropic boundary are expected for the largest tail current. The data is therefore confined to periods where the SMR index is less than -30 nT which covers weak to the most intense geomagnetic activity. *Asikainen et al.* [2010] also showed that the overall correlation is also slightly improved if the data from the quietest periods are removed from this stage of the analysis.

To evaluate the contribution of the tail current from within the SMR index a multivariate local linear regression is performed to determine the value of the coefficients of equation 68 in windows which vary in MT. For clarity equation 69 shows the individual parameters as inputs and outputs from the multivariate linear fit. The model has four main parts, the response variable (green), the explaining variables (blue), the model gradients (orange) and the model constant (purple).

$$\frac{dSMR}{dt} = -\frac{1}{\tau}SMR + \frac{dSMR_T}{dMT}\frac{dMT}{dt} + \frac{dSMR_{MP}}{d\sqrt{P_{SW}}}\frac{d\sqrt{P_{SW}}}{dt} + Q$$
$$+ \frac{(SMR_{MP} + SMR_T + c)}{\tau}$$

(69)

The model requires four input variables (green & blue); these can be estimated using the midpoint approximation, equations 70 - 72. Once each of the input variables are estimated they are binned in 120 equally sized windows from the minimum (=55°) to the maximum (=75°) value of the MT index within the reduced storm time data set (SMR ≤ -30nT), such that the local regression windows are centred at $MT_i = 55 + 0.1667i$. In this context *i* denotes the bin number between 0 and 120. The same window width as used by *Asikainen et al.* [2010], with a size of 3°, was chosen and each value within this window is weighed based on their relative distance from the window centre using the tricube weighting method outlined in (equations 62 & 63).

$$\frac{dSMR_i}{dt} = \frac{SMR_{i+1} - SMR_{i-1}}{2} \qquad (70)$$

$$\frac{dMT_i}{dt} = \frac{MT_{i+1} - MT_{i-1}}{2} \qquad (71)$$

$$\frac{d\sqrt{P_{SW}}_i}{dt} = \frac{\sqrt{P_{SW}}_{i+1} - \sqrt{P_{SW}}_{i-1}}{2} \qquad (72)$$

The robust bisquare linear regression weighting to deal with outliers was also employed (equations 64 - 66) and the model was run iteratively until the model parameters (orange & purple) remained unchanged. The result of this analysis provides a description of the model parameters as a function of the MT index. Most of these parameters can be discarded at this point as their variation with the MT index has no application in this analysis; however, the key result of this analysis is the variation of $dSMR_T/dMT$ as a function of the MT index. Figure 28 shows the output of the local linear regression analysis (left) and its integrated form (right). The MT values assigned to each point are that of the average MT value of each window. Windows with poor observational statistics were not included within the analysis. This included any window in which the number of observations was below 10 or if the standard deviation was above 1. Figure 28 effectively shows that the largest derivatives are observed for the lowest values of the MT index and hence large tail currents occur for periods where an isotropic boundary is observed at low latitudes, i.e. during periods of intense geomagnetic activity. This translates across to the integral form (right of Figure 28) which was created using the trapezium approximation with the boundary condition that the tail current contribution to the SMR index tends to 0 nT for an observed value of the MT index of 80.4° (corresponding to the maximum value of the MT index within the dataset and hence the quietest conditions).
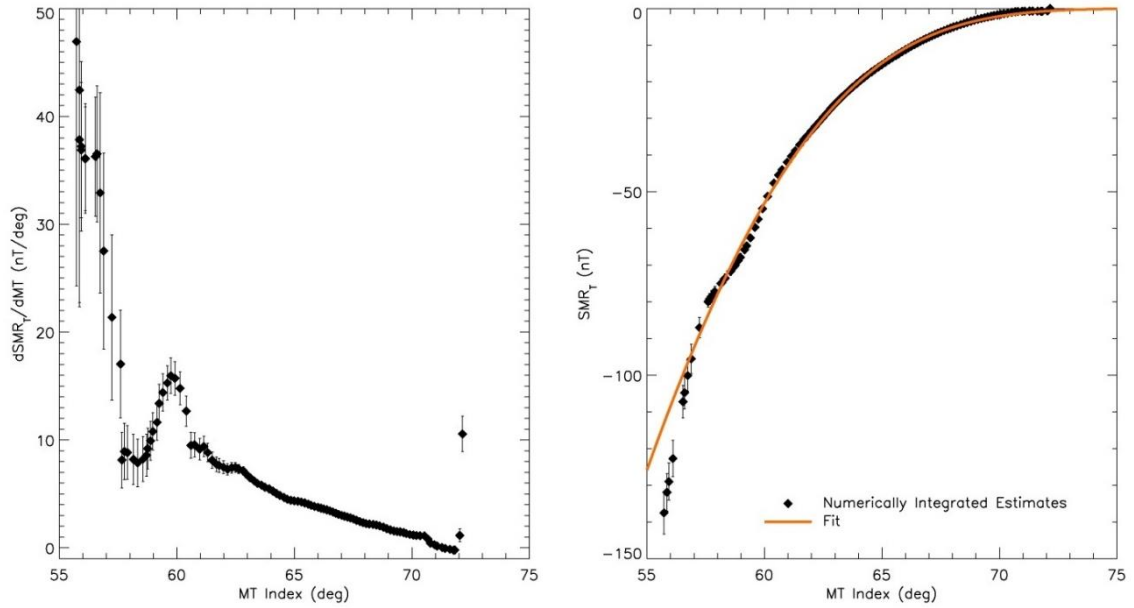
Figure 28: Local linear regression analysis output. The estimated derivative of SMR_T as a function of the MT index is shown on the left and the numerical integration of the left hand plot with the most appropriate fit is shown on the right.

The orange line over-plotted on the right hand side of Figure 28 is the best fit for the data and was created by fitting a weighted curve based on the error in the estimated values of the SMR_T index. This therefore forces the fit to be a better description of the estimates that have a lower error associated with them. The functional form of the fit was taken from *Asikainen et al.* [2010] as a starting point and then iterated until the chi squared statistic minimised, resulting in a final expression which provides a good fit to the data.

$$SMR_T = -3.562 \times 10^{10} \left(\frac{1}{\cos^2 MT} + 6.217 \right)^{-8.745}, \text{ for } MT \leq 80.4°$$

(73)

$$SMR_T = 0, \text{ otherwise}$$

It was found that the best fit was produced when the cos[-2] dependence of the MT index was set as a fixed parameter. This is also physically reasonable as, previously noted by *Asikainen et al.* [2010], this corresponds to an L value of a dipolar field line with invariant latitude of MT. A similarly large variation in the tail current is observed, when compared to that of *Asikainen et al.* [2010]; however, the most negative values are approximately 20nT greater than those previously estimated.

[4.4.2] Magnetopause Current

It is now possible to evaluate the tail current contribution for all times from the observed hourly MT index by using equation 73. This allows for the next stage of the analysis to be completed by removing the tail current contribution from the hourly SMR data. This modifies equation 61 in the following way:

$$(SMR - SMR_T) = SMR_{RC} + SMR_{MP} + c \qquad (74)$$

Where SMR – SMR$_T$ is treated as a single variable such that it is possible to combine equations 74 and 67 to create a linear model in the same form as equation 69, and use this to evaluate the contribution of the magnetopause currents to the system.

$$\frac{d(SMR - SMR_T)}{dt} = -\frac{1}{\tau}(SMR - SMR_T) + \frac{dSMR_{MP}}{d\sqrt{P_{SW}}}\frac{d\sqrt{P_{SW}}}{dt} + Q$$
$$+ \frac{(SMR_{MP} + c)}{\tau} \qquad (75)$$

Similarly to equation 69, equation 75 shows the model input parameters, as the response variable (green) and explaining variables (blue), and the model output parameters as the gradients (orange) and intercept (purple). Thus by taking windows of $\sqrt{P_{SW}}$ it is possible to analyse how the derivative of the magnetopause current contribution and hence, after numerical integration, how the magnetopause current contribution to the SMR index varies with the square root of the solar wind dynamic pressure. Again any derivatives are estimated using the midpoint approximation and data was binned into 80 equally sized windows of 2 nPa$^{1/2}$ in the range of 0 to 8 nPa$^{1/2}$. The magnetopause currents have a greater effect during geomagnetically quiet periods than during storms, which are dominated by the ring and tail currents. The data was thus confined to periods during which the hourly SMR index remained above -30 nT.

Figure 29 shows the result of the local linear regression analysis (left) and its integrated form (right). Again the estimates are assigned the average value of the solar wind dynamic pressure within each window, with windows containing poor observational statistics removed from the analysis. Numerical integration was completed using the trapezium approximation and the boundary condition that the magnetopause current should equal zero at a solar wind pressure of 0 nPa.
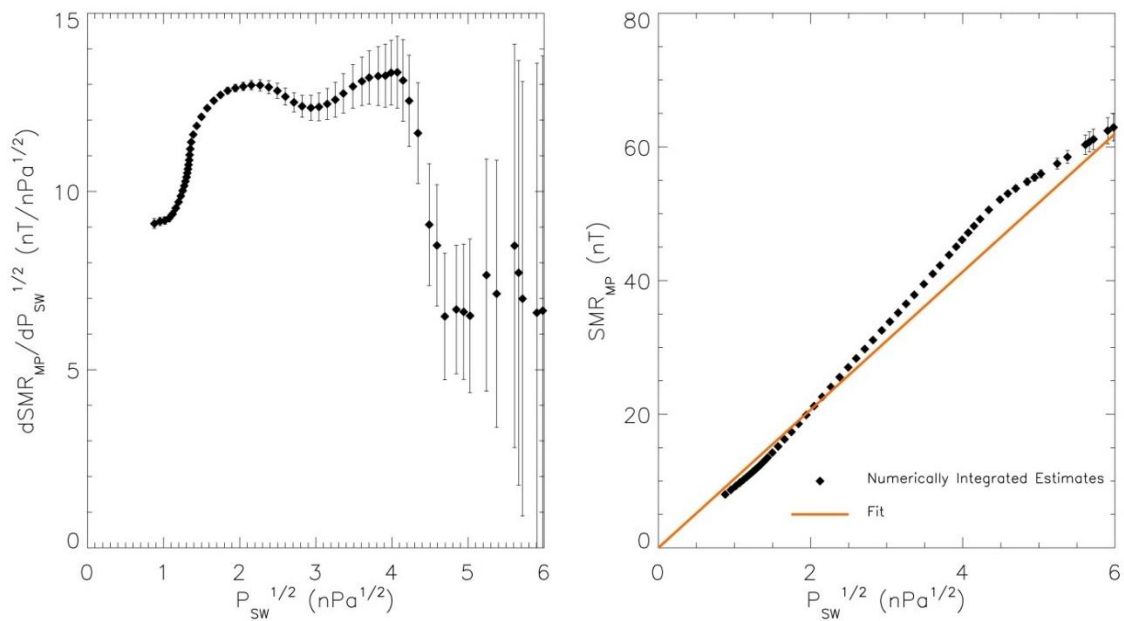
Figure 29: Local linear regression analysis of the contribution of the magnetopause currents on the SMR index. The estimated derivative of SMR_{MP} as a function of the square root of the solar wind dynamic pressure is shown on the left and its numerical integration with the best fit linear model is shown on the right.

A linear model for the variation of the magnetopause current with the square root of the solar wind dynamic pressure was assumed based on previous studies [e.g. *Burton et al.*, 1975; *O'Brien and McPherron*, 2000; *Asikainen et al.*, 2010]. The linear model over-plotted on the right hand side of Figure 29 is a poorer fit to that obtained by *Asikainen et al.* [2010]. The physical constraint of the model to pass through the origin forces the fit to be less than optimal. However, the formation of the magnetopause current, by the reflection of incident solar wind ions and electrons at the magnetopause following their encounter with the terrestrial field (Section [1.1.3.5]), would suggest that this constraint is appropriate.

The magnetopause current should therefore be a constant feature which flows in the opposite direction to the ring current and thus has a positive effect on the value of the overall SMR index. Alternatively, in order to obtain a better fit either the linear model or boundary condition assumption may be unsuitable when using the SMR index, instead of the Dcx index as previously used by *Asikainen et al.* [2010]. There are three possible corrections which could be made. The first of these would be to adopt a new model and retain the boundary condition. From visual inspection of the variation in the derivative of the SMR_{MP} parameter there appears to be two discontinuities, one near 1.5 $nPa^{1/2}$ and one close to 4.5 $nPa^{1/2}$. It therefore follows that the magnetopause current may be better described by three linear models (left hand side Figure 30). Secondly if the boundary condition is an incorrect assumption then a better fit can be obtained for the majority of the estimates with a single linear model and a new assumption that the magnetopause current has no effect upon the SMR index below a certain threshold of the solar wind dynamic pressure (right hand side Figure 30). Finally, a halfway measure between the two in which both original assumptions are rejected could also model the observed changes in the gradient of the magnetopause current. This would represent a threshold pressure to be required such that the fit did not pass through the origin and also a saturation of the magnetopause current at high solar wind pressure described by as second linear fit to above 4.5$nPa^{1/2}$ (centre Figure 30).

Figure 30 clearly shows that all of the new models are a much better representation of the estimated SMR_{MP} values. The description of the data is poor with the single linear model at the largest values of $\sqrt{P_{SW}}$ whereas the double and triple linear models were designed to be a better description of this region of the parameter space and as such perform much better in this region. Physically, this discontinuity might be thought of as reduction in the sensitivity of the SMR index to the magnetopause currents at the largest values of the solar wind dynamic pressure such that changes in the solar wind from a high pressure baseline has less effect than the same change in pressure at lower values. Additionally, the assumption that the magnetopause current contribution is a linear function of the square root of the solar wind pressure is extremely simple and assumes a planar magnetospheric model.

The reduction in the gradient at high P_{sw} values may also be due to the enhancement of the tail current from the compression of the tail lobes and could indicate the limitation of the assumption of the tail current being solely a function of the MT index. All models of the magnetopause current were evaluated and used to construct the energy injection and decay rates and it was found that the best fits of these parameters were obtained when using the double linear model (centre panel Figure 30).

The right hand side of Figure 29 yields a fit such that the constant of proportionality between the square root of the solar wind pressure and the contribution of the magnetopause current to the SMR index as outlined in equation 76. This is modified by the adoption of the new model such that the evolution of the magnetopause current contribution to the SMR index is more accurately described by the expression outlined in equations 77.

$$SMR_{MP} = (10.327 \pm 0.006)\sqrt{P_{SW}} \qquad (76)$$

$$SMR_{MP} = 0, \text{ for } \sqrt{P_{SW}} < 0.318$$

$$SMR_{MP} = (12.360 \pm 0.016)\sqrt{P_{SW}} - 3.929 \text{ , for } 0.318 < \sqrt{P_{SW}} < 4.490 \qquad (77)$$

$$SMR_{MP} = (7.180 \pm 0.540)\sqrt{P_{SW}} + 19.957, \text{ for } \sqrt{P_{SW}} > 4.490$$

The values of 12.360 and 7.180 for the constant of proportionality between the square root of the solar wind pressure and the contribution of the magnetopause current to the SMR index is in the same range as the values previously found (16 nT/nPa$^{1/2}$ [*Burton et al.*, 1975], 7.26nT/nPa$^{1/2}$ [*O'Brien and McPherron*, 2000], and 11.84nT/nPa$^{1/2}$ [*Asikainen et al.*, 2010]).
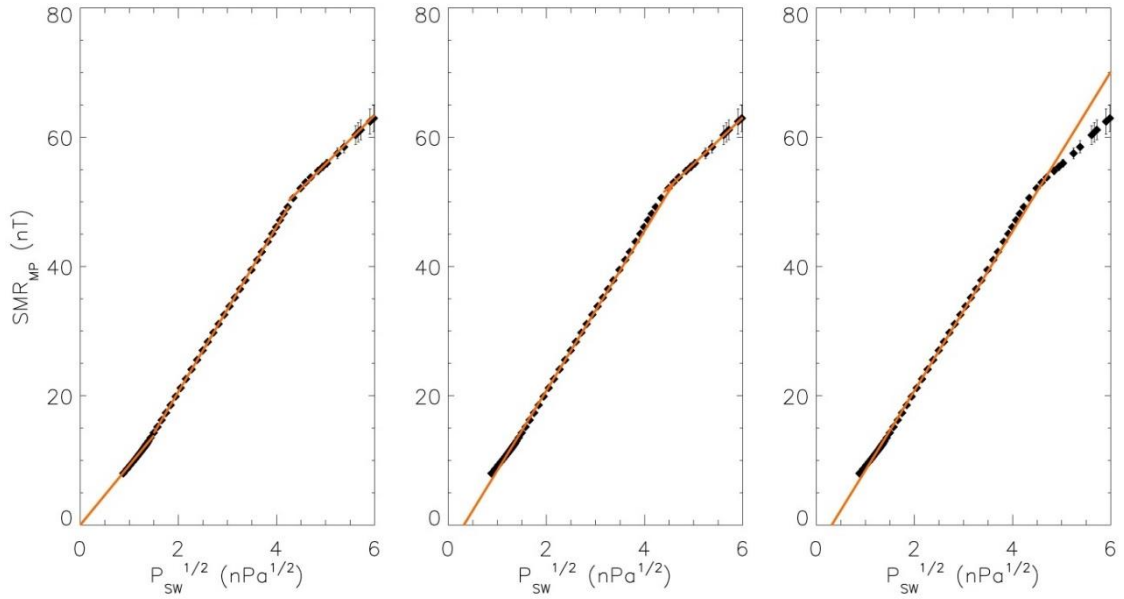
Figure 30: Alternative models which provide a better description of the variation of the magnetopause current with changes in the solar wind dynamic pressure. Left is the triple linear model with the boundary condition fixing the intercept value, centre is the double linear model with no boundary condition, and right is the single linear model without the boundary condition.

[4.4.3] Ring Current

In the previous two sections the tail and magnetopause currents have been characterised and their contribution to the SMR index evaluated. It is thus possible to evaluate both current contributions for all times and subsequently remove them from the overall SMR index. This modifies equation 61 to produce equation 78, which can then be used to produce a linear model of the remaining unknown variables (equation 79). It is then possible to evaluate the energy injection rate and decay time of the ring current by completing a final local linear regression analysis.

$$(SMR - SMR_T - SMR_{MP}) = SMR_{RC} + c \tag{78}$$

$$\frac{d(SMR - SMR_T - SMR_{MP})}{dt} = -\frac{1}{\tau}(SMR - SMR_T - SMR_{MP}) + Q + \frac{c}{\tau} \tag{79}$$

Similarly to equations 69 & 75, equation 79 shows the model input parameters, as the response variable (green) and explaining variables (blue), and the model output parameters as the gradient (orange) and intercept (purple). In this final model however both outputs will be used to evaluate the evolution of the energy injection rate and the decay time as a function of $E_{SW}P_{SW}^{1/6}$ [*Asikainen et al.*, 2010]. The data was binned in 200 equally sized windows of 2 mVm^{-1}nPa$^{1/6}$ between ±20 mVm^{-1}nPa$^{1/6}$. Again the window size used by *Asikainen et al.* [2010] produced the best fit of the data. The outputs of the local linear regression analysis are related to the decay and injection rates in the following way.

$$\tau = -\frac{1}{\beta_1} \tag{80}$$

$$Q = \beta_0 - \frac{c}{\tau} \text{ for } E_{SW}P_{SW}^{1/6} \geq 0 \tag{81}$$

$$Q = 0, \text{ otherwise}$$

$$c = \beta_0\tau = -\frac{\beta_0}{\beta_1} \text{ for } E_{SW}P_{SW}^{1/6} < 0 \tag{82}$$

Where β_0 and β_1 are the intercept (purple in equation 79) and gradient (orange in equation 79) values from the local linear regression analysis respectively. Figure 31 shows the decay time estimates from the local linear regression analysis. As previously noted by *Asikainen et al.* [2010] when the solar wind electric field, and thus the $E_{SW}P_{SW}^{1/6}$ parameter is negative, corresponding to northward IMF, there is no distinct pattern to the data and each of the points have a large associated error. As such the decay time, for all negative values of the solar wind electric field, is taken as a constant equal to the median value of the estimated decay times over this region of parameter space. For positive values of the electric field, corresponding to southward IMF the decay time reduces quickly from around 35 hours to slightly below 5 hours and has been suggested to be due to more ions being injected onto open drift past such that they are lost to the magnetopause within one drift period. It has also been suggested that the ring current

is forced closer to the earth during these periods and thus loss via coulomb collisions and charge exchange increases [*O'Brien and McPherron*, 2000]. Decay times can also be affected by an increase in the generation of plasma waves, which can cause pitch angle scattering and thus the removal of particles from the ring current as they are scattered into the loss cone [e.g. *Mauk and McPherron*, 1980; *Feldstein et al.*, 1994; *Horne and Thorne*, 2003].
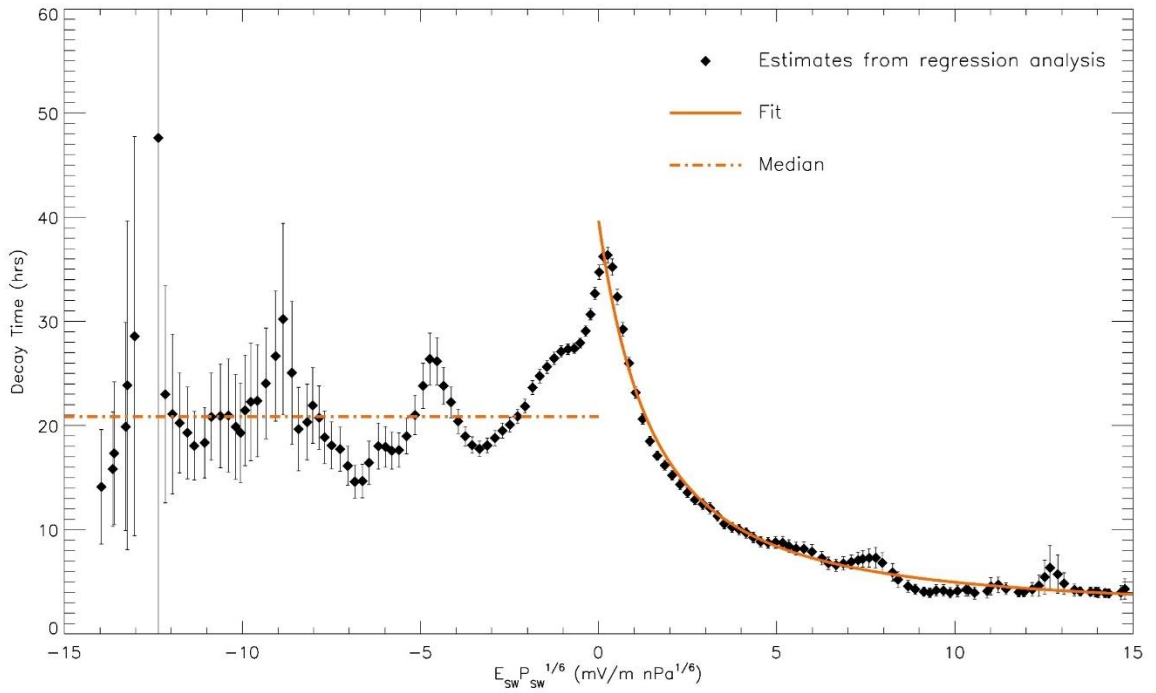
Figure 31: Ring current decay time estimates as a function of $E_{SW}P_{SW}^{1/6}$

The functional form originally suggested by *O'Brien and McPherron* [2000] and used successfully to describe the decay time for positive values of the solar wind electric field by *Asikainen et al.* [2010] also provides a good fit to the estimated decay times shown in Figure 31. This produces the following two expressions for the decay time depending on whether the $E_{SW}P_{SW}^{1/6}$ parameter is positive or negative.

$$\tau = 1.692 \exp\left(\frac{16.279}{5.160 + E_{SW}P_{SW}^{1/6}}\right), \text{ for } E_{SW}P_{SW}^{1/6} \geq 0$$

(83)

$$\tau = 20.833, \text{ otherwise}$$

In order to estimate the functional form of the energy injection rate Q, it is necessary to first evaluate the value of the constant c. To do this equation 81 is rearranged for the case where the electric field is negative, i.e. where $Q = 0$. This produces equation 82 from which the average value of the constant can be calculated from all of the windows for which the electric field is negative. This yields the value of 5.635 nT. It is now possible to use equation 81 for the case where the solar wind electric field is positive, the result of which is shown in Figure 32. Also plotted are the calculated estimates of the energy injection rate for negative values of the solar wind electric field as a sanity check as these values should be constantly very close to zero due to the method for calculating the constant value. Figure 32 effectively shows that the value of the constant is correct; it thus becomes possible to fit the estimated Q values for positive solar wind electric field. Again the functional form used by *Asikainen et al.* [2010] is used as the initial model which is then evaluated and modified in a stepwise fashion until the chi squared value minimises. This yields the following functional forms of the energy injection rate.

$$Q = -1.777\left[E_{SW}P_{SW}^{1/6}\right]^{1.254}, \text{ for } E_{SW}P_{SW}^{1/6} \geq 0$$

$$(84)$$

$$Q = 0, \text{ otherwise}$$
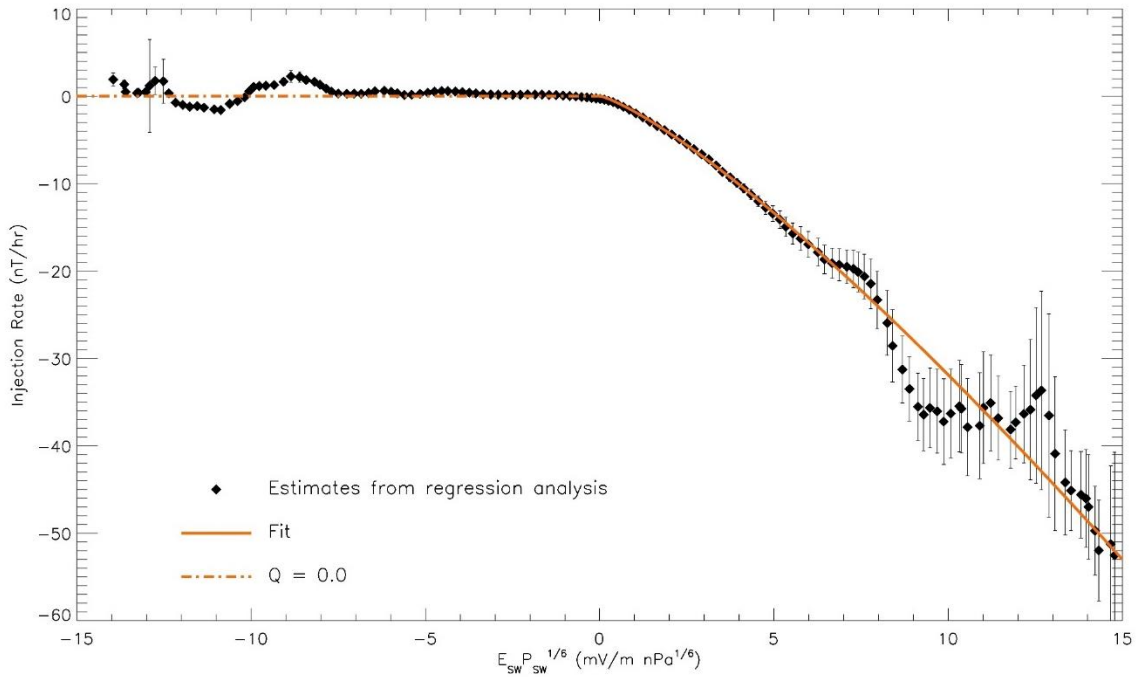
Figure 32: Ring current energy injection rate estimates as a function of $E_{SW}P_{SW}^{1/6}$

Asikainen et al. [2010] found that their expression for the energy injection rate over estimated the value for the most extreme events, such that they introduced a lower limit to the injection rate of -140 nT/hr, which corresponded to a $E_{SW}P_{SW}^{1/6}$ value of approximately 40. Here the threshold again corresponds to a $E_{SW}P_{SW}^{1/6}$ value of 40 and is set at -180 nT/hr, as calculated from Equation 84. Setting this the threshold at this value maximises the correlation between the modelled and measured SMR indices, by reducing the overestimate of the model for the most active periods.

The hourly contribution of the ring current to the SMR index can now be evaluated using the Runge-Kutta algorithm (Equations 85 - 89) in which the values are numerically calculated at each time step based on the evolution of the ring current which is described by equation 67 [*Burton et al.*, 1975]. In these equations h is the step length, in this case 1, and the Q and τ values at the half time steps are calculated by linearly interpolating between the corresponding values at time steps t and t+1. The initial condition (i.e. at t=0) is calculated by rearranging equation 61 for SMR_{RC} and using the values of the other current systems at t=0 calculated above.

$$SMR_{RC}(t+1) = SMR_{RC}(t) + \frac{1}{6}(k_1 + 2k_2 + 2k_3 + k_4) \qquad (85)$$

$$k_1 = h\left(Q(t) - \frac{SMR_{RC}(t)}{\tau(t)}\right) \qquad (86)$$

$$k_2 = h\left(Q(t+0.5h) - \frac{SMR_{RC}(t) + 0.5k_1}{\tau(t+0.5h)}\right) \qquad (87)$$

$$k_3 = h\left(Q(t+0.5h) - \frac{SMR_{RC}(t) + 0.5k_2}{\tau(t+0.5h)}\right) \qquad (88)$$

$$k_4 = h\left(Q(t+h) - \frac{SMR_{RC}(t) + k_3}{\tau(t+h)}\right) \qquad (89)$$

In order to evaluate the validity of the model the SMR index is reproduced by calculating each of the current contributions from the measured parameters as described in the sections above and substituting them into equation 61. Each of the hourly data points are then plotted against the corresponding measured value (Figure 33). This shows that the model is a good approximation of the measured values and thus it is appropriate to use to describe the evolution of the different currents within the magnetosphere. *Asikainen et al.* [2010] found that their model tended to overestimate the level of geomagnetic activity for the most active periods (i.e. reproduce lower values of the Dcx index than measured). This is observed within the reproduction of the SMR index as shown in Figure 33 although to a lesser extent and there is also an underestimation of the most extreme events (SMR < -400 nT), which is not observed by *Asikainen et al.* [2010]. The overall correlation between the modelled and measured SMR indices is 0.90 and if a linear model is fit to the data it provides a close approximation to a 1:1 relationship with gradient and intercept values of 1.04 and 3.18 respectively. The RMS deviation of the indices is 9.63 nT which also indicates that the model is a good approximation of the measured SMR values and is able to reproduce the measured values across the full range of geomagnetic activity.
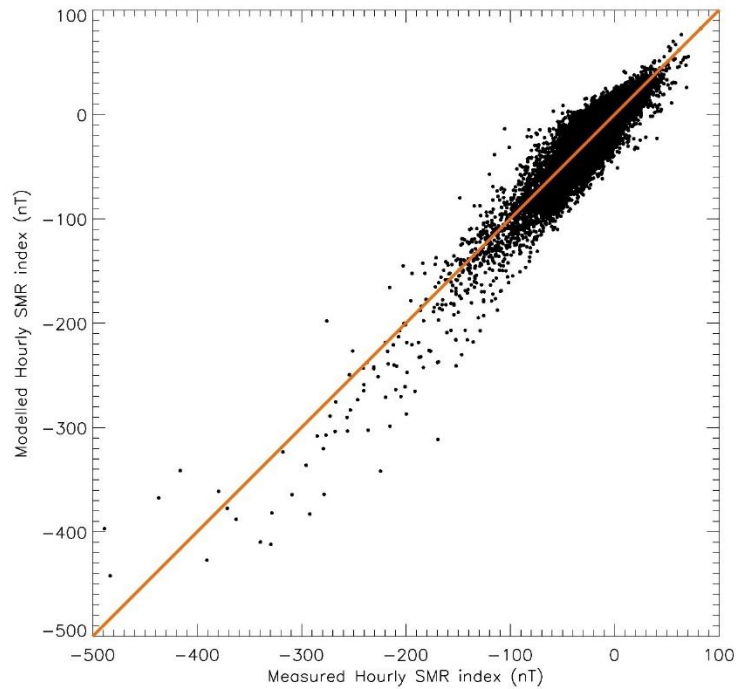
Figure 33: Modelled hourly SMR index versus the measured hourly SMR index. Over plotted is the line of unity which is indicative of a perfect fit.

[4.5]   Applying the Model

Now that the ring current, tail current and magnetopause current systems have all been re-evaluated, following the change in detection method of the isotropic boundary, it is possible to use them to examine the evolution of the current systems over the duration of different types of storm. To do this a superposed epoch analysis technique was used for the different types of storm that were observed and defined by the change in the relativistic electron flux as measured by the EPS instrument on board the LANL series of spacecraft (Section [3.3]).

Figure 34 shows the superposed epoch analysis of the current indices for all storms that were detected between 2001 and 2011 inclusive. These indices are plotted over the day either side of the minimum value of the SMR index and hence the end of the main phase of the storms, which defines the 0 epoch. Figure 34 shows that the average main phase of all detected storms includes enhancements in all current systems.

The magnetopause current appears to begin to decrease around an hour prior to the end of the main phase. In addition, the tail current also begins to level off before the end of the main phase. This may suggest that it takes on average one hour for changes in the solar wind to cause a noticeable change in the ring current and less than an hour for there to be an effect in the tail current. Interestingly the tail current appears to initially decay faster than the ring current index suggesting that the initial rapid recovery in the SMR index, which is also observed in all other indices (i.e. Dst and SYM-H indices), is due to the reduction in the tail and magnetopause current intensities rather than the ring current. Additionally, the ring current appears to remain significantly enhanced for the duration of the epoch analysis and does not show the two step recovery which has previously been attributed to the rapid removal of high energy oxygen from the ring current in the early recovery phase [e.g. *Akasofu and Chapman*, 1972; *Williams*, 1985; *Lui et al.*, 1987; *Hamilton et al.*, 1988].
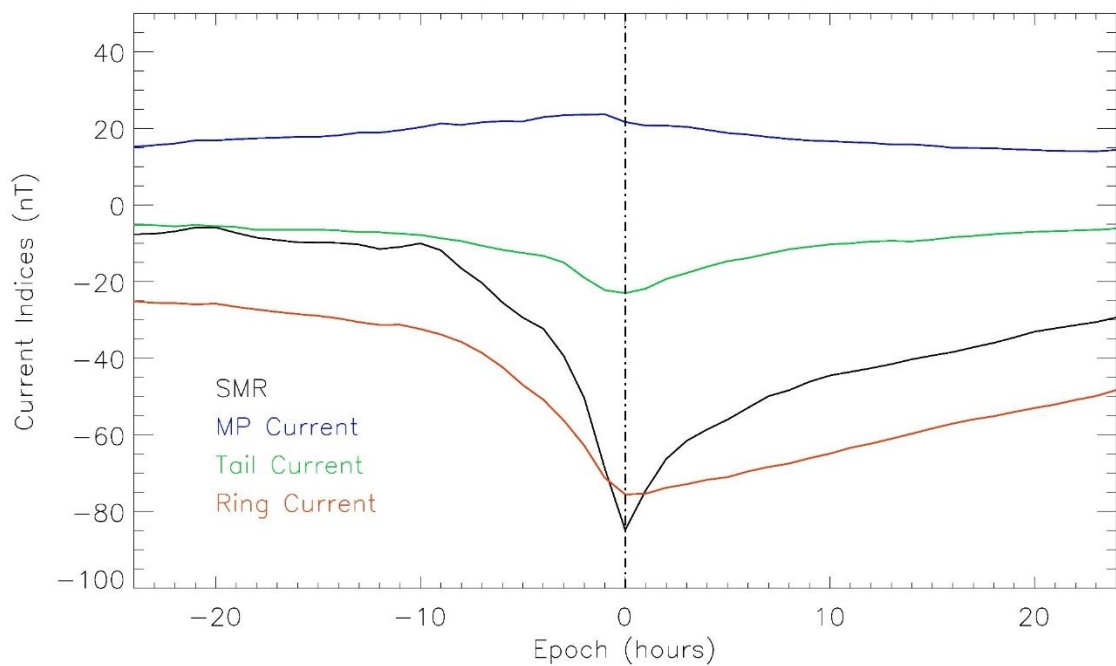
Figure 34: Upper panel shows the superposed epoch analysis of the three main current systems, ring current (Red), tail current (green) and magnetopause current (blue) as well as the SMR global index (black) for all of the 184 identified storms between 2001 and 2011.
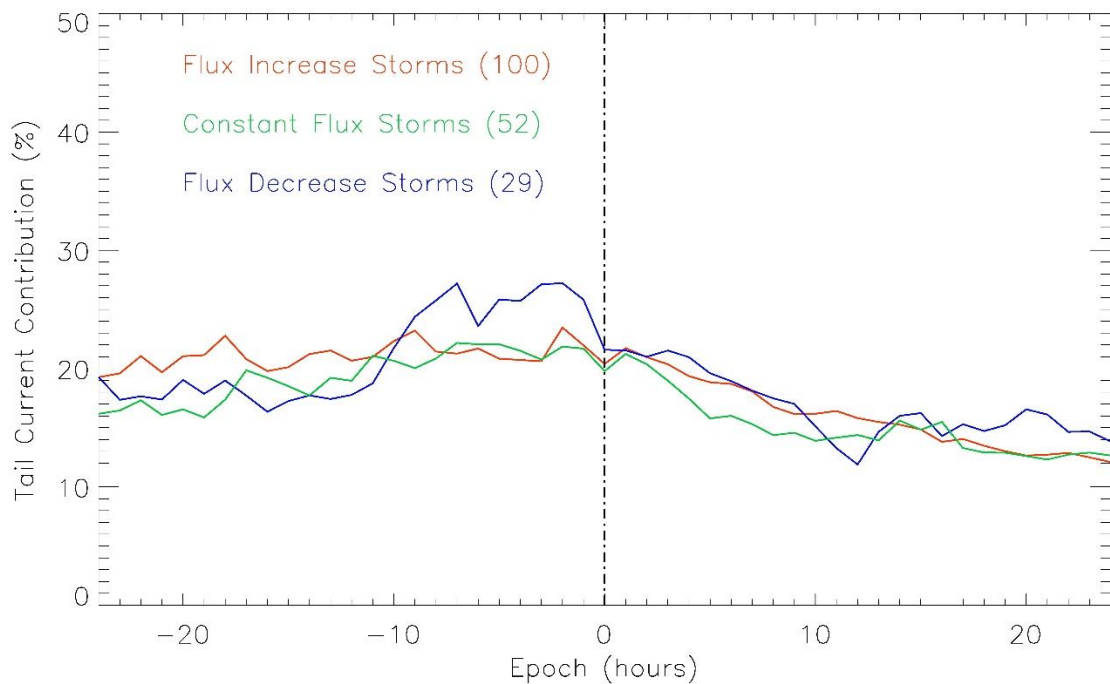
Figure 35: The tail current contribution to the pressure corrected SMR index for flux increase (red), decrease (blue) and constant flux (green) storms. The number in brackets indicates the number of events within each category.

Greenspan and Hamilton [2000] suggested that the ring current may only account for between 40% and 70% of the Dst index. Similarly, the tail current was shown by *Asikainen et al.* [2010] to comprise around 34% of the pressure corrected Dcx index, which was slightly larger than the 25% previously reported by *Turner et al.* [2000]. Figure 35 shows the tail current contribution to the pressure corrected SMR index (i.e. SMR – SMR$_{MP}$ – constant), and clearly shows that the tail current contribution remains relatively stable (apart from flux decrease storms) during the pre-storm and main phase at around 20% suggesting that the tail current is enhanced to the same extent of the ring current during this period as the strength of both current systems increase dramatically especially towards the end of the main phase, as indicated by the decrease in the contribution to the SMR index for both currents in Figure 34.

Figure 35 shows the variation in the tail current contribution broken down by the change in the relativistic electron flux over the duration of the storm as defined by *Reeves et al.* [2003], which will be discussed in more detail in the subsequent chapter. Following the cessation of dayside driving the tail current contribution shows a significant, and sustained, decrease to below 15%. As Figure 35 shows there is significant divergence for flux decrease storms as compared to the other types of storm. This can either be interpreted as an enhancement in the tail current strength, thus increasing its relative contribution to the pressure corrected SMR index, or a decrease in the strength of the ring current. This is most prevalent during the main phase (between -10 and 0 epoch). The tail current contribution begins to decrease, for all storms but most prevalently for decreasing storms, before the end of the main phase again suggesting that changes within the solar wind take around an hour to be felt by the ring current.

Figure 36 shows the tail current (top) and the ring current (bottom) for flux increase (red) flux decrease (blue) and constant flux (green) storms. Flux increase and constant flux storms have a similar evolution of the tail current, apart from during the late main phase during which the tail current and ring current strengthen more rapidly for flux increase storms. With respect to the ring current the flux decrease storms show a weaker ring current pre-main phase than both flux increase and constant flux storms. Constant flux storms have the strongest ring current pre-main phase but it does not become as enhanced as for the flux increase and decrease storms by the end of the main phase (epoch 0.0). Most strikingly, Figure 36 shows that the tail and ring currents for the flux decrease storms decay much more rapidly than for flux increase and constant flux storms, during the early recovery phase. Also observed, for flux decrease storms only, is a two-step recovery in the ring current. This may indicate a greater abundance of oxygen in the ring current for these types of storm, as suggested by [*Daglis et al.,* 1999] due to the more rapid decay of O^+ ions in comparison to H^+ ions. A more rapid reduction of the strength of the ring current for decreasing storms suggests that loss mechanisms are more dominant in the ring current for these types of storm. This can be achieved by either additional loss mechanisms, or a removal of the conditions required for the continued enhancement of the ring current.
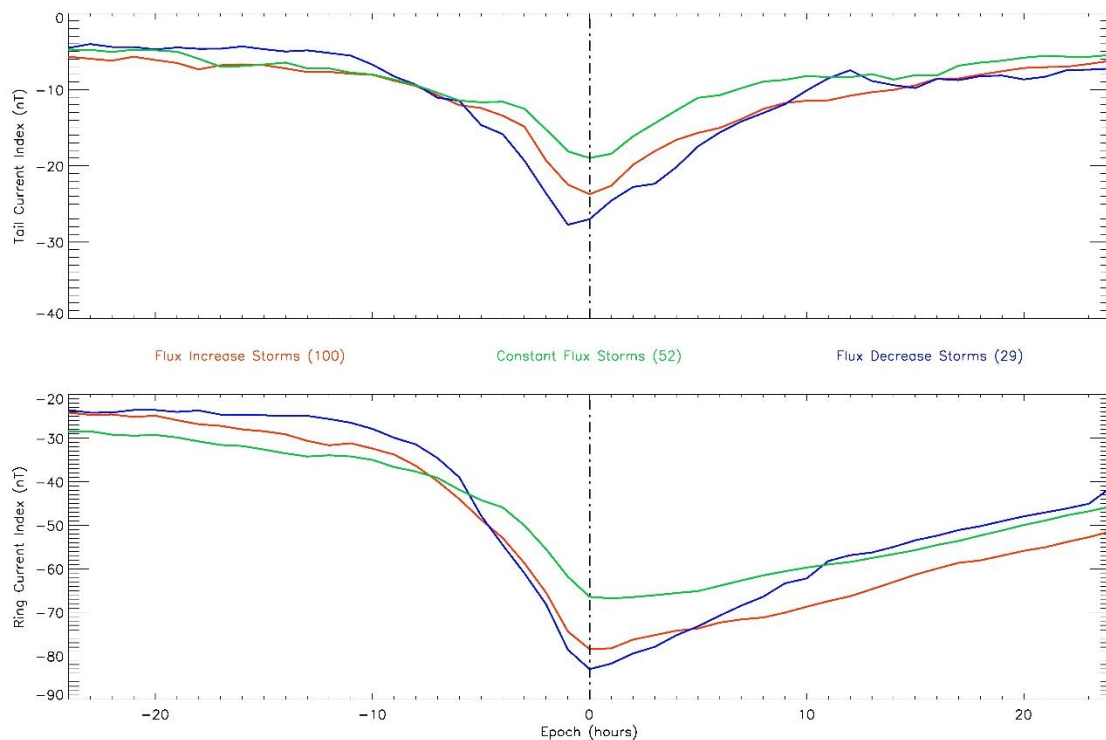
Figure 36: Shows the evolution of the tail current (top) and ring current (bottom) over the 48 hours centred on the minimum of the SMR index for the different types of storm. The number in brackets indicates the number of events within each category.

Another interesting comparison is between storms which are driven by different solar wind structures. *Kilpua et al.* [2015] identified four different types of solar wind driver. These are CIRs, and three different types of CME; Sheath driven, Ejecta driven and Sheath+Ejecta driven (Figure 14). Sheath driven storms are caused when the CME ejecta is travelling sufficiently fast that it produces a leading sheath, but the ejecta is not directed towards the Earth such that the magnetosphere only experiences the edge of the CME (i.e. sheath only). Sheath plus ejecta storms are the same type of fast moving CMEs as with the sheath only events however these events are directed towards the Earth in such a way that the magnetosphere is impacted by the ejecta as well as the sheath. Ejecta only events are CMEs directed towards the Earth but are not sufficiently fast to cause the formation of a leading sheath. Figure 37 shows the tail current contribution to the SMR index, which again shows a greater contribution pre-storm and during the main phase than during the recovery phase which again suggests the tail current decays much quicker than the ring current following the cessation of the dayside driving.
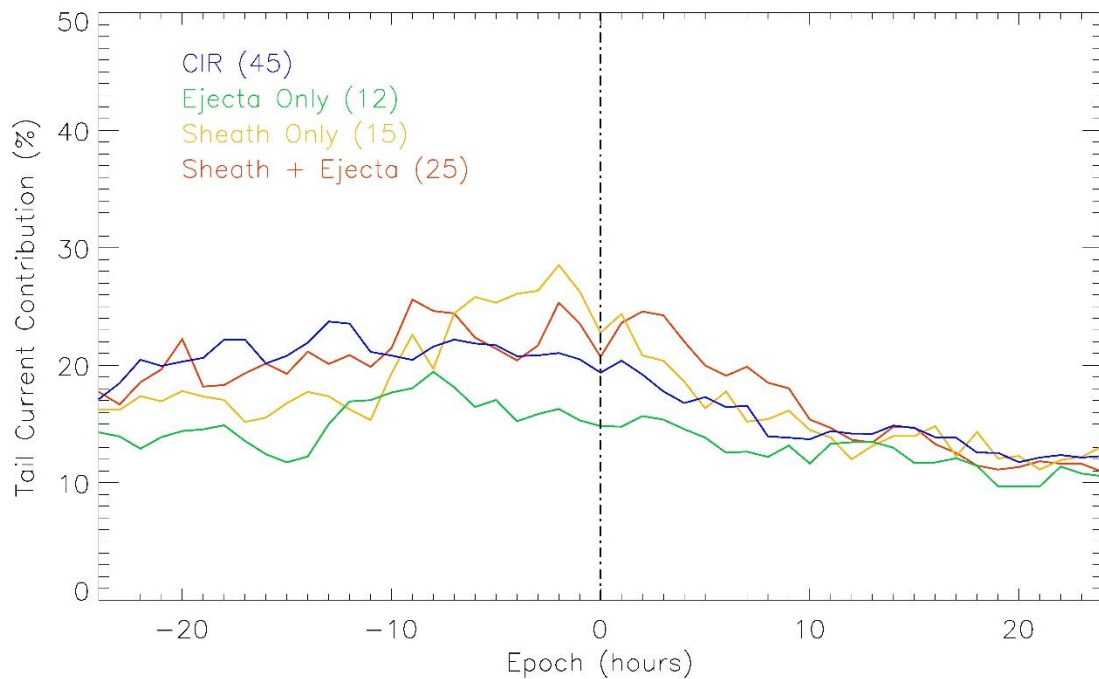
Figure 37: The tail current contribution to the pressure corrected SMR index for CIR driven (blue), Ejecta only driven (green), Sheath only (yellow) and Sheath plus Ejecta driven (red) storms. The number in brackets indicates the number of events within each category.

Figure 38 shows that the tail current is primarily enhanced towards the end of the main phase and also decays quickly at the start of the recovery phase. Interestingly it also shows that the CIR driven storms are more likely to produce weak storms, while the faster CMEs produce the stronger storms. The tail current seems to be controlled more by the occurrence of a sheath, with both sheath only and sheath plus ejecta storms causing an enhancement in the tail current to a similar magnitude despite the ring current being significantly more enhanced for sheath plus ejecta CMEs. Figure 38 also shows that the ring current remains at its most enhanced level for longer during storms which are driven by ejecta, and tend to peak slightly after the minimum value of the SMR index. Following this the enhanced ring current for all CME driven storms appears to decay more rapidly than the CIR driven ring current. The reason may be that high speed streams typically contain Alfvén waves, where the IMF B_Z oscillates and continuously feeds energy into the magnetotail for as long as the solar wind stream persists. This pulsating energy input leads to enhanced substorm activity and energetic particle injections into the inner magnetosphere [*Tanskanen et al.*, 2005]. These injections can maintain the ring current level, producing the observed slow decay rate.
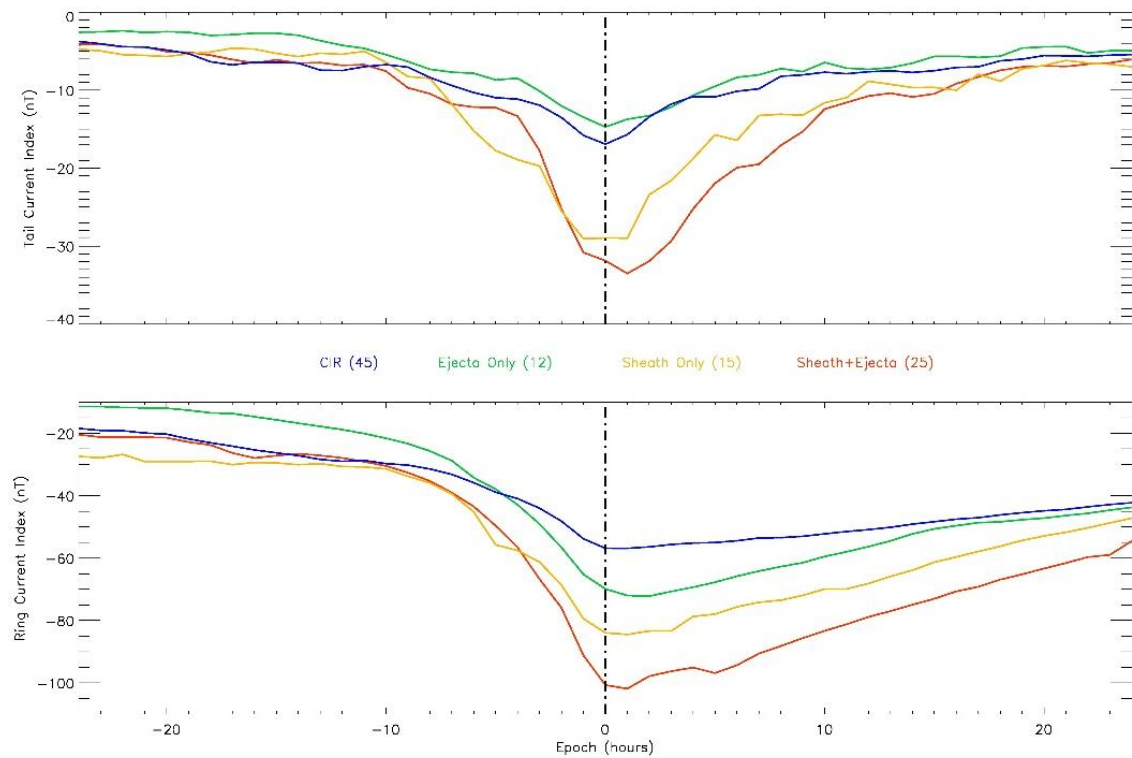
Figure 38: The evolution of the tail current (top) and ring current (bottom) for the four different driver types. CIR driven (blue), Ejecta only driven (green), Sheath only (yellow) and Sheath plus Ejecta driven (red) storms. The number in brackets indicates the number of events within each category.

[4.6] Conclusion

Following the method outlined by *Asikainen et al.* [2010] it has been shown that the magnetopause, tail and ring current contributions within the SMR index can be distilled from the overall index by using measurements of the isotropic boundary and the solar wind dynamic pressure and electric field. It has also been shown that the SMR index is a good description of the Dcx index, and the only major difference between the two is the improved time resolution of the SMR index. The current indices have been evaluated with respect to the hourly averaged SMR index. An attempt to improve the time resolution of these indices to the minute cadence of the raw SMR data was made but an assumption used in the analysis caused the minute variability to only be observed in the tail current index. As such it was felt that the hourly current indices were a better representation of the large scale current systems.

A superposed epoch analysis was carried out using the hourly indices, which showed that the tail current is usually around 30% of the pressure corrected SMR index, which falls following the end of the dayside driving as the ring current persists for an extended period of time, and does not show a rapid decay following the end of the main phase. In contrast the tail current enhancements decay much faster taking around half a day following the end of the main phase, to return to pre-storm levels. Additionally, flux decrease and flux increase storms have a more enhanced ring current than constant flux storms, which may suggest that constant flux storms are more likely to occur when the dayside driving is weaker. The ring current and tail currents are also observed to decay at a much greater rate for flux decrease storms than either constant flux or flux increase storms. This may indicate a more abrupt end to dayside driving for flux decrease storms with less energy fed into the magnetosphere during the recovery phase thus allowing the ring current to decay at a greater rate. It could also indicate a different composition of the ring current potentially suggesting a greater concentration of heavier ions for flux decrease storms, which are more easily scattered due to their larger collisional cross-sections.

CHAPTER 5

Analysis of the Cause of Storm Time Electron Flux Variations

[5.1] Introduction

The ultimate source of the variability of the magnetosphere is the solar wind and the different structures and properties it possesses. It is well established that these parameters significantly alter the evolution of the magnetosphere during both quiet and active periods with the solar wind velocity, solar wind density and orientation of the IMF all being shown to be significantly correlated with the driving of the magnetosphere and the enhancement of the terrestrial plasma environment [e.g. *Paulikas and Blake*, 1978; *Lyatsky and Khazanov*, 2008; *Reeves et al.*, 2011; *Milan et al.*, 2012]. This chapter will review previously observed relationships between the solar wind and the relativistic electron fluxes, evaluating them specifically for storm periods where the evolution of the electron flux is known. It will be shown that these relationships are not observed for flux decrease storms. A superposed epoch analysis will show the simultaneous evolution of a wider number of parameters, including the AE index, clock angle and dayside reconnection rate, than used in previous studies. This will ultimately lead to the identification of a new paradigm for the cause of storm time relativistic electron flux variations.

Gonzalez et al. [1994] defined a geomagnetic storm as "intervals of time when a sufficiently intense and long-lasting interplanetary convection electric field leads, through a substantial energisation in the magnetosphere-ionosphere system, to an intensified ring current sufficiently strong to exceed some key threshold of the quantifying Dst index". The threshold for the identification of storms is usually taken as -50nT [*Gonzalez et al.*, 1994], but the classification of storms by intensity is a difficult question as many different authors have different definitions for weak, moderate and intense storms.

Sugiura and Chapman [1961] suggested threshold values of -50nT < *Dst* ≤ -30nT for weak storms, -100nT < *Dst* ≤ -50nT for moderate storms and *Dst* ≤ -100nT for intense ('great') storms. These threshold values were also used by *Gonzalez et al.* [1994]. However, *Vijaya Lekshmi et al.* [2011] used threshold values of -100nT ≤ *Dst* < -50nT for their weak ('moderate') storms, -250nT ≤ *Dst* < -100nT for their moderate ('major') storms and *Dst* ≤ -250nT for their intense ('super') storms. Yet another definition was used by *Hutchinson et al.* [2011] who defined the three different storm strengths as 'weak' (−150nT < SYM-H ≤ −80nT), 'moderate' (−300nT < SYM-H ≤ −150nT) and 'intense' (SYM-H ≤ −300nT). *Hutchinson et al.* [2011] used SYM-H as a high resolution Dst, index as supported by *Wanliss and Showalter* [2006]. To add to the confusion *Anderson et al.* [2015] have shown that storms which have a minimum Dst of greater than -50nT produce a similar response in the relativistic electron flux when compared to the more classically defined storms.

This suggests that the definition of storms by their minimum Dst index is somewhat arbitrary and does not address the underlying physics sufficiently to classify periods as either geomagnetically active or quiet. In this chapter the storms and their drivers were identified by *Kilpua et al.* [2015], by using the classical identification method, i.e. using a Dst threshold of -50nT. The drivers of the storms were identified from the solar wind data and classified as CIRs, CMEs, multiple storms or storms for which the driving solar wind structure was unclear. The CME category was sub-divided into three different types, ejecta only, sheath only, and sheath plus ejecta, depending on the structures of the CME, which were encountered by the magnetosphere. Figure 39 shows the distribution of the identified storms by year, between 1995 and 2011. The top panel indicates the occurrence of storms which produce and increase, decrease or no change in the relativistic electron flux from pre to post-storm as defined by *Reeves et al.* [2003] (See section [2.3]). The bottom panel indicates the occurrence of storms driven by specific solar wind structure. Omitted from this figure are multiple storms and those for which the driving solar wind structure could not be resolved. Although the storms which fall into these categories have been omitted, the expected distribution of storm occurrence can clearly be seen.

Storm occurrence can be seen to maximise slightly ahead of solar maximum (as indicated by the peak in the yearly average sunspot number), as previously observed by *Gonzalez et al.* [1990], with CMEs more prevalent during this period. There is also a peak in storm occurrence during the declining phase (2005-2006), which appears to be due to an increase in the number of CIR driven storms. This is expected due to the increased occurrence of regular high speed streams, and their corresponding solar wind pressure and density enhancements, during this phase of the solar cycle [*Li et al.*, 2011b].
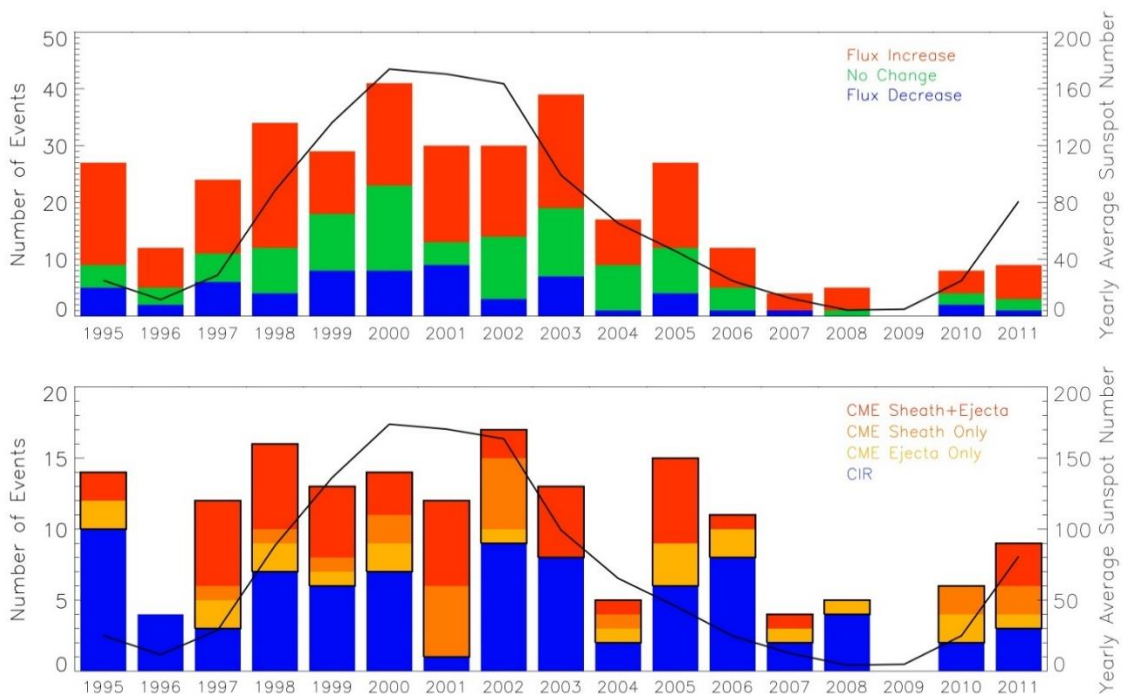
Figure 39: Breakdown of the occurrence of storms with a minimum Dst value of ≤ -50nT as identified by Kilpua et al. [2015]. Top panel shows all storms, coloured according to their resultant flux change: increase (red), no change (green) or decrease (blue). The bottom panel shows the subset of storms broken down by their solar wind structure: CIR driven storms are shown in blue, CME driven storms include all storms encompassed within the boxes with a black outline and are broken down into Ejecta only (yellow), Sheath only (orange) and Sheath plus Ejecta (red). Over-plotted is the yearly averaged sunspot number.

[5.1.1] Data Set

Geoff Reeves [personal communication, 13th August 2014] supplied an extended version of the daily averaged 1.8 - 3.5 MeV electron flux from the Los Alamos National Laboratory (LANL) space environment monitors. The data available covers the time period from the 22nd September 1989 to the 28th November 2011 inclusive. The data were averaged over all local times in order to reduce the diurnal variation in the observed intensity, caused by the asymmetry of the geomagnetic field. The data still contains some variation in the measurements between the different satellites; for more details on the reasons for this, as well as more detailed explanation of the averaging process used to produce the daily averaged electron flux values, please refer to [*Reeves et al.*, 2011]. Solar wind parameters were downloaded from the Goddard Space Flight Centre's OMNI web service at a resolution of one minute. The storm list of *Kilpua et al.* [2015] was used due to the identification of the solar wind structures that drive them, although the precise times for each of the storm phases have been updated as determined by the SMR index. Combined, the period of observations used here covers the years from 1995 to 2011 and includes a solar maximum, during which CMEs are most common, and a declining phase, during which regularly occurring high speed streams dominate, as can be seen in Figure 39.

[5.2] Storm time occurrence

The dates of the identified storms plotted in Figure 39 are identified by the end of the main phase and the commencement of the recovery phase; this is characteristically defined by the minimum value of the defining index (e.g. SYM-H, Dst, Dcx or SMR) over the duration of the storm. This is slightly different from the identification of the date of the storm by *Vijaya Lekshmi et al.* [2011] who use the end of storm onset as the date of the storm. The choice to use the minimum SMR value instead of the end of the initial phase of the storm to define the date of the storm was taken due to the ease of identification of the minimum index value in comparison to the relatively difficult identification of the end of the initial phase of the storm.

Interestingly a secondary periodicity is observed if the storm occurrences are plotted as a monthly time series. When a fast Fourier transform is taken of this periodicity a significant peak around a period of 6.0 months is revealed. When plotting the monthly distribution of the detected storms between 1995 and 2011 (Figure 40) there are peaks observed around March and October for all the detected storms (top panel) as well as the driver specific (CIR (middle panel) and CME (bottom panel)) driven storms. There is no apparent difference between the storms apart from the slight tendency for CME driven storms to occur during September rather than October. This is however, insignificant as there is only one more storm during September when compared to October. This is a well-known phenomenon, where geomagnetic storms are more likely to occur during the equinoxes than during the solstices. Different explanations have been suggested for this phenomenon such as the Russell-McPherron effect, (Section [2.2.2.1]) [*Russell and McPherron*, 1973], the equinoctial hypothesis, in which the orientation of the Earth's roatation axis modulates the effectiveness of southward IMF in driving geomagnetic activity [e.g. *Arnoldy,* 1971; *Gonzalez et al.*, 1994; *Newell et al.*, 2001; *Vijaya Lekshmi et al.*, 2011], the simple merging model [*Petschek,* 1964] and a Kelvin-Helmholtz driven model [*Boller and Stollov*, 1970]. The top panel of Figure 39 also shows that there is no significant difference in the occurrence of flux increase storms in comparison to those that cause flux decreases or no change in the flux as defined by *Reeves et al.* [2003], with all occurrences peaking close to the equinoxes and reaching a minimum nearer the solstices. The occurrence of more apparent peaks in the flux increase storms when compared to the other types of storm is most likely due to the higher likelihood, and therefore the greater number, of flux increase storms. *Reeves et al.* [2003] found that approximately 50% of storms caused an increase in the relativistic electron flux at geosynchronous orbit with no change and flux decreases both occurring approximately 25% of the time. Similar occurrence rates are found in this study, from the change in daily averaged electron fluxes, with flux increase storms occurring 54% of the time, constant flux 28% and flux decrease 18% of the time. Although this is slightly different from that observed by *Reeves et al.* [2003] it is most likely due to the use of the daily averaged flux rather than the hourly averaged flux used by *Reeves et al.* [2003]. The daily average flux was used as the hourly averaged flux data were not available.
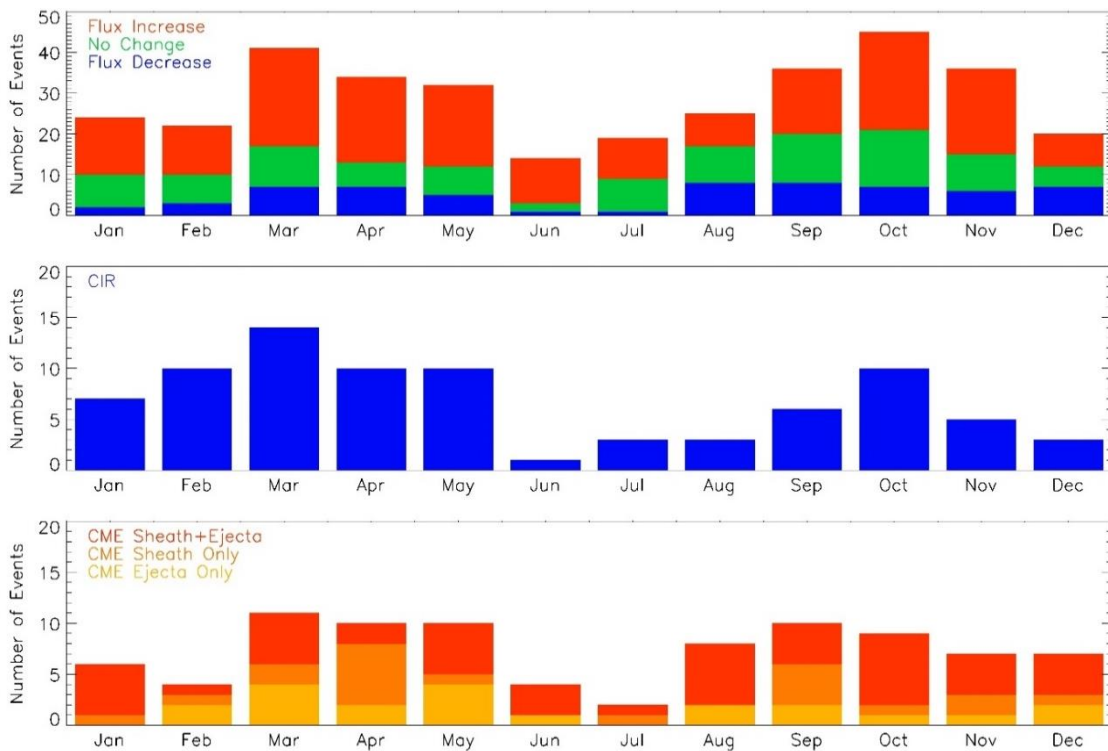
Figure 40: Top panel shows the monthly distribution of all storms broken down by their relativistic electron flux change. Flux increase storms are shown in red, flux decrease, blue, and constant flux storms are shown in green. The centre panel shows the monthly distribution of storms driven by CIRs and the bottom panel shows the monthly distribution of CME driven storms, broken down into the three sub-classes. Sheath plus ejecta are shown in red, sheath only driven storms in orange and ejecta only storms in yellow.

As indicated by *Russell and McPherron* [1973] and *Svalgaard* [2011], each of the different hypotheses of the cause of the observed semi-annual variation also produces very different universal time (UT) dependencies. *Vijaya Lekshmi et al.* [2011] reported the apparent UT dependence of the onset of the main phase around UT midnight as being as significant as that of the semi-annual variation. They used data from all storms between 1985 and 2005 and found that this variation was shown to be especially significant for large storms with a minimum Dst of between -100nT and -250nT. The observed main phase onset times for all of the storms identified by *Kilpua et al.* [2015], as well as those which are specifically driven either by CIRs or CMEs are plotted in Figure 41. The main phase onset times were taken by visually inspecting the SMR trace and identifying the time at which the index began to decrease rapidly to its minimum value.

Figure 41 shows that when the main phase onset is plotted for all identified geomagnetic storms no midnight preference is observed, in contrast to the findings of *Vijaya Lekshmi et al.* [2011]. It could be argued that there are peaks in the onset times around 04 and 19 UT and a potential third peak around 11 UT, most apparent in the top panel of Figure 41 but also visible in the occurrence times for CME driven storms. The reason for this could be that there isn't a relationship between the main phase onset and universal time; however, theory suggests that a UT dependence should be expected. Another explanation could be the difference in selecting the exact start of the main phase which must be done manually with this method. Additionally, there are inherent differences between the two indices used, and although the SMR index is ultimately a high resolution measure of the average north-south magnetic field variation and should thus be similar to the Dst index, it will not be exactly the same, which could lead to discrepancies in the determination of the main phase onset. Indeed, it has been shown that there are systematic errors associated with the Dst index which could cause the incorrect identification of the onset of the main phase especially when combined with the low time resolution of the index.

The Dcx index is a corrected Dst index and the SMR index is shown to be a good representation of the Dcx index at a higher time resolution in Chapter 4 Section [4.3], and thus the main phase onset times identified here may be more accurate than those found by *Vijaya Lekshmi et al.* [2011]. Another possibility for the difference when compared to *Vijaya Lekshmi et al.* [2011] is the total number of storms detected (=351), which is fewer than that of the 584 detected by *Vijaya Lekshmi et al.* [2011] who detected storms over the duration of two solar cycles. When the storms are constrained to those only driven by distinct drivers this number drops significantly giving a total of 82 CIR driven storms and 88 CME driven storms. Notably there is again no real difference between the type of storms and the universal time onset of the main phase, with flux increase, constant flux and flux decrease storms all being produced across all universal times, with the only exception being that there are no, constant flux storms at 07 UT.
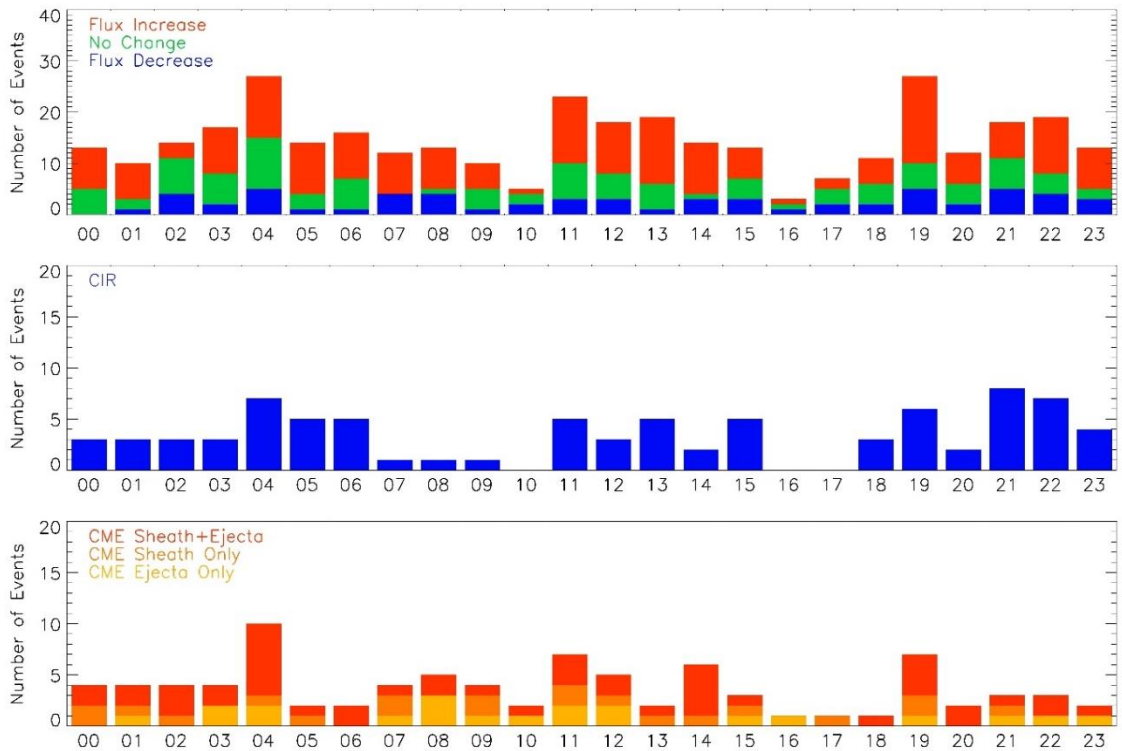
Figure 41: The UT dependence of the identified storms defined by their change in relativistic electron flux (top panel) and the driving solar wind structure. CIRs (middle panel) and CMEs (bottom panel).

[5.3]   Magnetospheric Response

The identified storms are magnetospheric responses to significant changes in the solar wind during active periods of the solar cycle. The orientation of the IMF, solar wind speed and solar wind density have all been observed to be correlated with increases in the energy and flux of trapped particles within the magnetosphere [*Paulikas and Blake*, 1978; *Lyatsky and Khazanov*, 2008; *Li et al.*, 2011b; *Reeves et al.*, 2011]. Geomagnetic storms, although observed to cause significant enhancements of the terrestrial plasma, have also been observed to reduce or have no effect on the flux of relativistic electrons at geosynchronous orbit [*Reeves et al.*, 2003].

Kilpua et al. [2015] presented observations that suggested that flux increase storms are caused by the occurrence of fast streams following the end of the solar wind structure which initiated the storm. Their analysis focused primarily on the effects of the solar wind speed and the separation of the sub-structures within the driving CME or CIR, for the different relativistic electron responses, and used a novel superposed epoch technique. However, the solar wind speed is not the only property of the solar wind that has been shown to be correlated with the increase in flux of the terrestrial plasma environment [e.g. *Lyatsky and Khazanov*, 2008]. In fact, *Li et al.* [2011b] suggested that it was enhanced geomagnetic activity driven by the orientation of the IMF rather than the solar wind speed which was more important in determining the effective enhancement of the magnetosphere by the solar wind. They also suggested that interpretation of the solar wind velocity being the key parameter was likely due to the high correlation between different parameters of the solar wind and favourable IMF conditions, with southward IMF often observed during periods of high speed solar wind.

[5.3.1] Flux vs. V_{SW} – All times

Following the work by *Paulikas and Blake* [1978] and *Reeves et al.* [2011] the relationship between the solar wind velocity and the geosynchronous electron flux will be briefly analysed. More specifically this relationship will be examined primarily during periods of enhanced geomagnetic activity. Figure 42 shows the distribution of the relativistic electron flux as observed by *Paulikas and Blake* [1978]: the data is coloured according to the average clock angle over that day with northward (CA<90°) IMF indicated by black points, 90°<CA<126° blue, 126°<CA<162° green and CA>162° red, thus indicating days where the IMF was the most southward. If the orientation of the IMF was the driving factor behind the enhancements in the geosynchronous relativistic electron flux it should follow that the red points would be confined to the highest flux and the black points to the lowest. However, as Figure 42 shows, points of all average clock angles can produce both high and low fluxes for varying levels of solar wind speed.
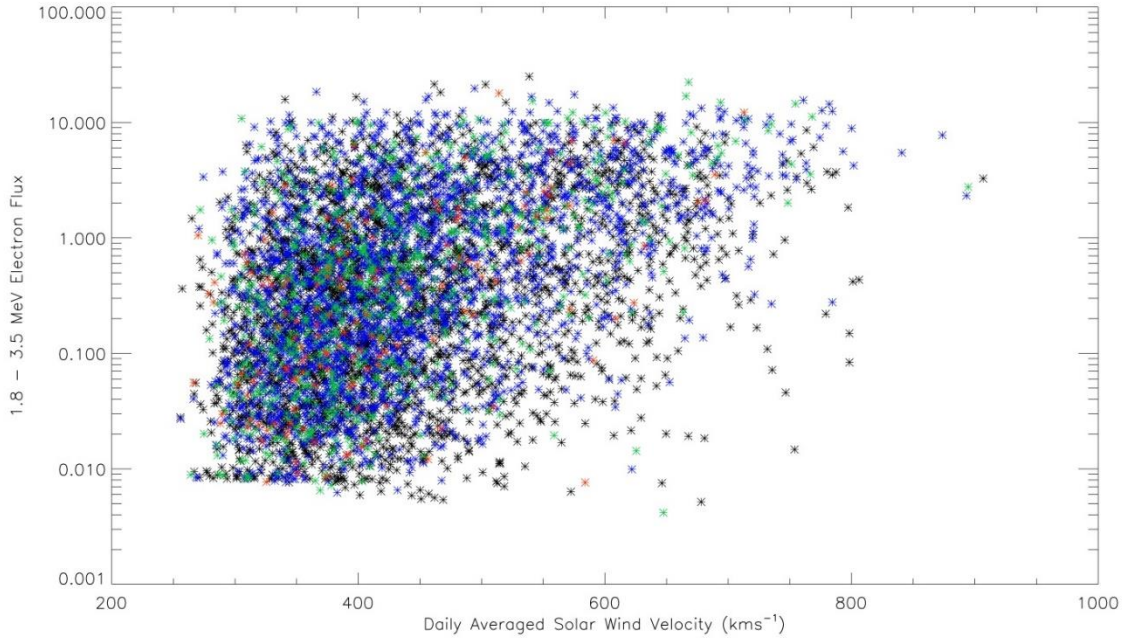
Figure 42: Reproduction of the solar wind velocity distribution originally reported by Paulikas and Blake [1978] and revisited by Reeves et al. [2011]. The data is coloured by the daily averaged clock angle. Northward (CA<90º) IMF is indicated by black points, 90º<CA<126º blue, 126º<CA<162º green and CA>162º red.

The average clock angle over the course of the day was calculated by using the average IMF B_Y and IMF B_z values over the day. This may not be the most accurate way of defining the amount of driving that the magnetosphere experiences during the day as the clock angle can vary rapidly and, as such, the average could be contaminated by sufficiently large IMF B_Y or B_Z components during the hour. Sustained southward IMF is thought to be a necessary condition for the enhancement of geomagnetic activity. The driving of the magnetosphere by the solar wind can also be characterised by the dayside reconnection rate (Equation 90), as defined by the functional form outlined by *Milan et al.* [2012], and is a function of the clock angle, solar wind speed and the IMF field strength.

$$\Phi_D = L_{eff}(V_x)V_xB_{yz} \sin^{\frac{9}{2}}\left(\frac{1}{2}\theta\right) \qquad (90)$$

$$L_{eff}(V_x) = 3.8R_E \left(\frac{V_x}{4 \times 10^5}\right) \qquad (91)$$

As such, the relativistic electron flux is plotted in Figure 43 as a function of both the number of consecutive minutes of southward IMF and the daily averaged dayside reconnection rate. The relationship between the daily averages of the clock angle and the consecutive minutes of southward IMF (i.e. the maximum duration of southward IMF per day) and dayside reconnection rates are plotted to evaluate the validity of the former as an indicator of favourable solar wind conditions and thus of enhancements in the relativistic electron flux.
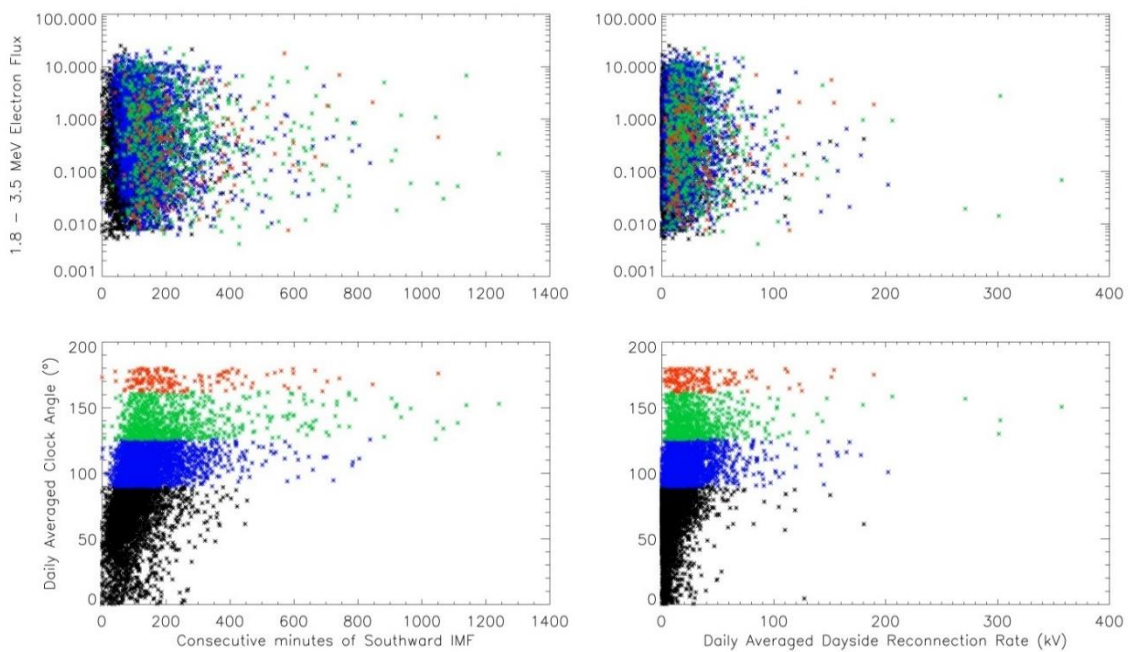
Figure 43: Relativistic electron flux plotted as functions of different proxies for the level of geomagnetic driving received by the magnetosphere. Consecutive minutes of southward IMF (left) are plotted against the electron flux (top) and the absolute value of the daily averaged clock angle (bottom). These parameters are also plotted against the daily averaged dayside reconnection rate (right). All are coloured by the daily averaged clock angle values, as defined for Figure 42, for clarity.

Figure 43 shows that for both increased duration of southward IMF and increased dayside reconnection rate the response of the relativistic electron flux at geosynchronous orbit can be extremely variable and does not seem to produce a coherent response as a function of the dayside driving. Li et al. [2011b] suggested that enhancements in the relativistic electron flux require enhanced geomagnetic activity, which in turn is driven by the southward orientation of the IMF.

This would suggest that the high flux days would most likely be associated with the days of high magnetosphere driving; however, this is not the case, with the highest driving, defined as either the dayside reconnection rate, sustained southward IMF or average clock angle, all showing a large range of flux response. The lower half of Figure 43 suggests that the daily averaged clock angle does indicate a greater level of magnetospheric driving, with both the dayside reconnection rate and consecutive minutes of southward IMF being greater for more southwardly average clock angles. Although there is a large range in both parameters, Figure 43 would suggest that the daily average clock angle may be used as a simple indicator of more favourable driving conditions although, due to the rapid variation of the clock angle on time scales much shorter than a day, any observed dependence upon this value would warrant further investigation at a higher time resolution.

[5.3.2] Flux vs. V_{SW} – Storm times

Figure 42 shows the relationship between the relativistic electron flux and the solar wind velocity for all levels of geomagnetic activity. During geomagnetic activity acceleration and loss processes are both enhanced and in competition with each other, which creates the potential for flux decreases as well as the more expected flux increases. *Kilpua et al.* [2015] found that flux increase storms are more likely to occur when the solar wind speed following the driving solar wind structure is high. Figure 44 shows the relationship between the solar wind velocity and the relativistic electron flux broken down by the phase of the storm and the response of the magnetosphere. As can be seen, flux increase storms and constant flux storms show a relationship similar to that of the overall triangular relationship observed in Figure 42. However, flux decrease storms show that the relationship between the solar wind velocity and the relativistic electron flux is more complex and that the relationship between the two is significantly different for these types of storm. The initial and main phase plots show extremely similar distributions, which is unsurprising given the relatively short duration of these storm phases, typically lasting several hours, which is less than the daily resolution of the data available. The data was selected for each of these phases as the daily average of the UT day on which they occur.

Flux increase storms show a clear relationship between the electron flux and the solar wind velocity and during initial and main phases, which appears more linear than the typical triangular distribution. The lack of the typical distribution during the initial and main phases of the storm could be due to the relatively fewer number of points during these phases of the storm when compared to the recovery phase. That being said the triangular distribution is observed during the initial and main phases of constant flux storms, which may suggest that the solar wind is more strongly coupled to the magnetosphere for flux increase storms than during the other types of storm. The points in Figure 44 are coloured by the daily average clock angle, black points (signifying northward IMF) are fewest during the main phase, as expected due to the necessity for southward IMF to cause the significant enhancement of the ring current, which occurs during this phase of the storm.
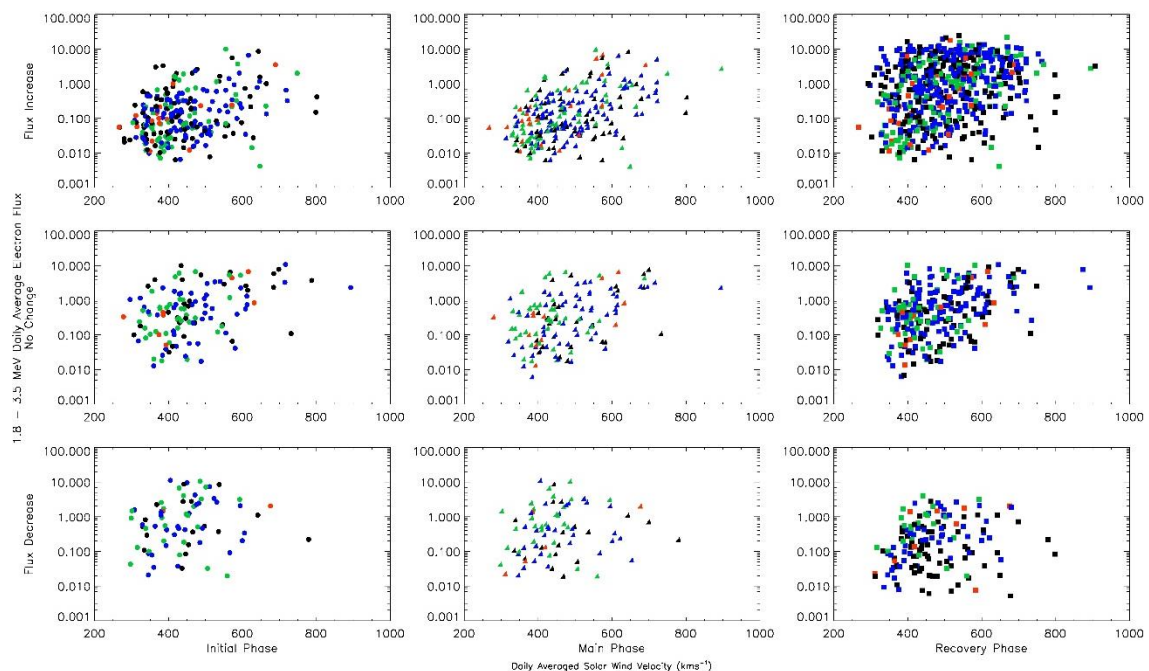
Figure 44: Relationship between the solar wind velocity and the relativistic electron flux containing only storm periods. The plots show flux increase (top) constant flux (centre) and flux decrease (bottom) storms broken down by the phase of the storm, initial phase (left), main phase (centre) and recovery phase (right). The electron flux response is coloured according to the average clock angle, as defined above.

It also appears that during the recovery phase the IMF orientation is more northward during the flux decrease storms and more southward during the flux increase storms, although there are many fewer points for the flux decrease storms as these types of storm are less likely to occur (18% of all storms compared to the 54% for flux increase storms). Figure 44 also shows that the flux decrease storms show a strikingly different relationship between the solar wind velocity and the electron flux compared to the flux increase and constant flux storms. *Kilpua et al.* [2015] suggested that it was the speed of the solar wind following the driving solar wind structure that played a key role in whether the storms enhanced or decreased the electron flux. It could therefore be expected that the solar wind speed would be significantly higher for the flux increase storms than for the flux decrease storms. Although Figure 44 shows that the flux increase storms have more points with higher solar wind velocity there are also a significant number of lower solar wind velocity days.

There does appear to be a significant difference in the ability of the solar wind to enhance the flux for the different types of storm. Higher velocity days during the recovery phase of flux decrease storms tend to produce lower fluxes than during other storm types. Additionally, low velocity days during the recovery phase of flux increase storms appear to produce higher fluxes than for other types of storm. Figure 45 confirms that this is the case. It also shows that the fluxes during the initial phase are higher across most solar wind velocities for flux decrease storms than for flux increase storms. This also agrees with the conclusion of *Kilpua et al.* [2015] that flux decrease storms generally have a higher flux of relativistic electrons before the storm than flux increase storms. The top plots of Figure 45 show the normalised distribution of the velocities during the phases of each type of storm. These distributions are remarkably similar for each phase and type of storm. The main difference is that during the recovery phase flux increase storms tend to have higher velocity during the recovery phase with the distribution peaking around 50 kms^{-1} higher than the flux decrease storms. The top right plot of Figure 45 also shows that there are more high solar wind velocity days for flux increase storms and fewer low solar wind velocity days during the recovery phase.

The bottom panels of Figure 45 show that this is not the full picture and that although there are more high velocity days, the average flux is greater for all velocities in the recovery phase of flux increase storms when compared to the other types of storm. This is not the case in the initial or main phase, which could suggest that the speed of the solar wind does not control whether the flux increases or decreases but rather that another factor is allowing the solar wind velocity to more effectively drive the magnetosphere during flux increase storms when compared to flux decrease storms in the recovery phase. This factor could also allow the solar wind velocity to more effectively control and enhance the electron flux during the initial phase of flux decrease storms.
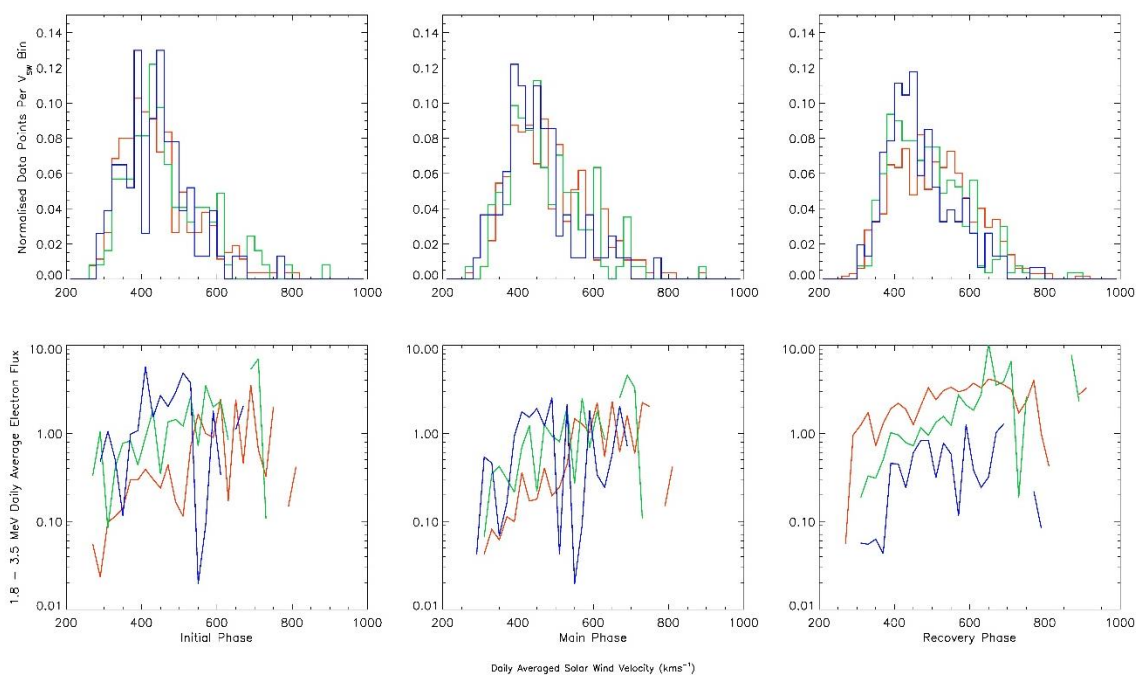
Figure 45: Normalised number of data points (top) and mean electron flux (bottom) per 20kms^{-1} solar wind velocity bins for flux increase (red), constant flux (green) and flux decrease (blue) storms.

[5.3.3] Flux vs. ρ_SW – All times

Lyatsky and Khazanov [2008] showed that the relativistic electron flux is also controlled by the solar wind density. Low solar wind densities produce a range of flux levels with the highest fluxes confined to the lowest solar wind density (Figure 46). Similarly to Figure 42, the colouring within Figure 46 depicts the daily averaged clock angle, with black signifying northward IMF and the other colours identifying bands of southward IMF from weak (blue) to strong (red). Again all strengths of solar wind density occur for all orientations of the IMF. The highest fluxes are confined to the lowest densities, while the lowest fluxes occur across a range of densities, with the highest densities exclusively producing low fluxes. *Lyatsky and Khazanov* [2008] used the cube root of the solar wind density to increase the observed correlation: here the solar wind density itself is used and although the linear correlation coefficient may not be as high, the same overall trends are observed.
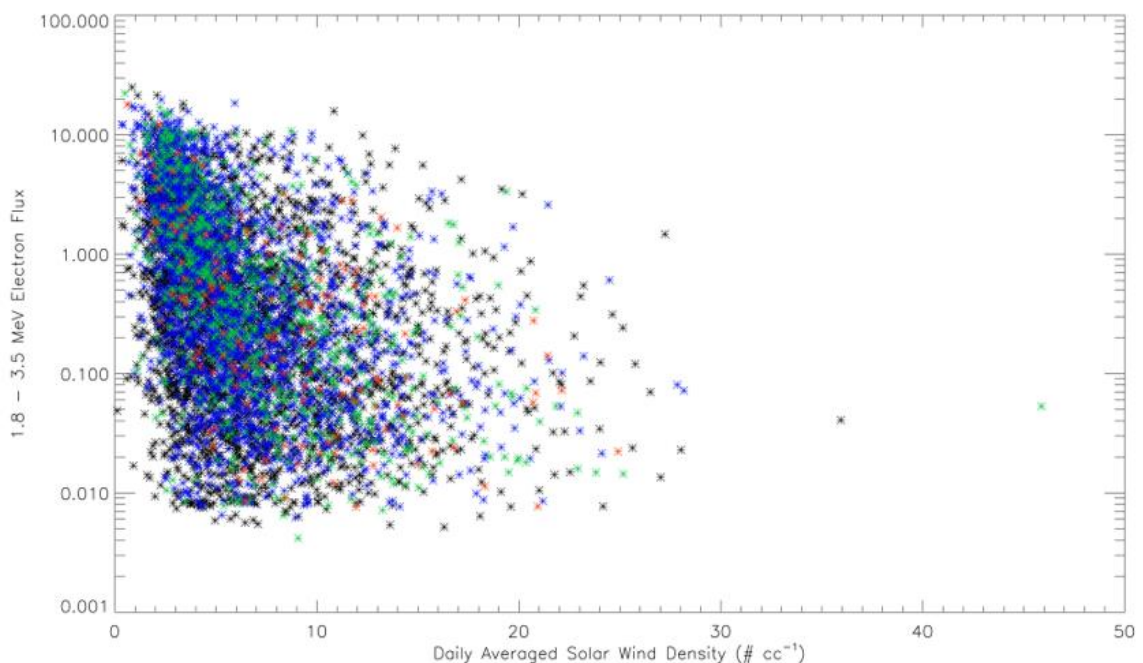
Figure 46: Solar wind density plotted against the electron flux for all times between 1994 and 2012

[5.3.4] Flux vs. ρ$_{SW}$ – Storm times

Lyatsky and Khazanov [2008] concluded that the observed solar wind density dependence of the relativistic electron flux was as significant as the solar wind velocity relationship and that it existed independently of the solar wind velocity. The solar wind density relationship was evaluated in the same way as the solar wind velocity relationship, above, for all storms as detected by *Kilpua et al.* [2015] in order to determine its effect on the occurrence of the different types of storm as defined by the change in the relativistic electron flux. Figure 47 shows that the characteristic low-density-high-flux relationship exists across the majority of storm types and phases. The main exception to this is during the recovery phase of flux decrease storms during which the low densities do not produce the highest fluxes. This is in contrast with the initial and main phases of the same storms, during which the relationship appears linear when compared to the typical non-linear relationship (Figure 46).
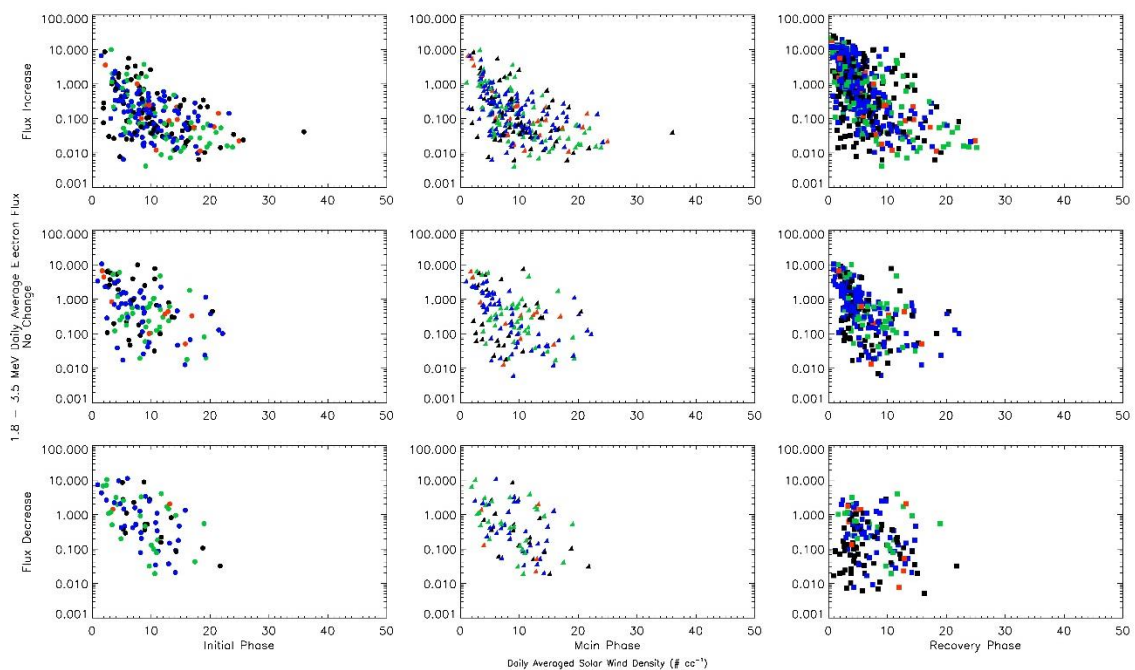
Figure 47: Relationship between the solar wind density and the relativistic electron flux containing only storm periods. The plots show flux increase (top) constant flux (centre) and flux decrease (bottom) storms broken down by the phase of the storm, initial phase (left), main phase (centre) and recovery phase (right). The electron flux response is coloured according to the average clock angle, as defined

Figure 48 shows the change in the solar wind density dependence of the electron flux from the initial phase to the recovery phase for each type of storm and is binned into equal sized density bins. The top row shows the number of days for each phase of the storm normalised for each storm type. For all three types of storm, the number of low density days increases dramatically during the recovery phase when compared to the other phases. There also tends to be more high solar wind density days during the recovery phase of flux decrease storms than during the recovery phase of the other two types of storm. As with the solar wind velocity relationship during the initial and main phases, flux decrease storms are better able to produce higher fluxes for the same solar wind density. However, during the recovery phase the flux decrease storms become significantly less able to produce high fluxes, specifically at the lowest densities. Again, this may suggest that, like the solar wind velocity, the solar wind density is not the ultimate controlling factor for the electron flux and that during flux decrease storms the solar wind is less able to enhance the electron flux than during flux increase or constant flux storms.
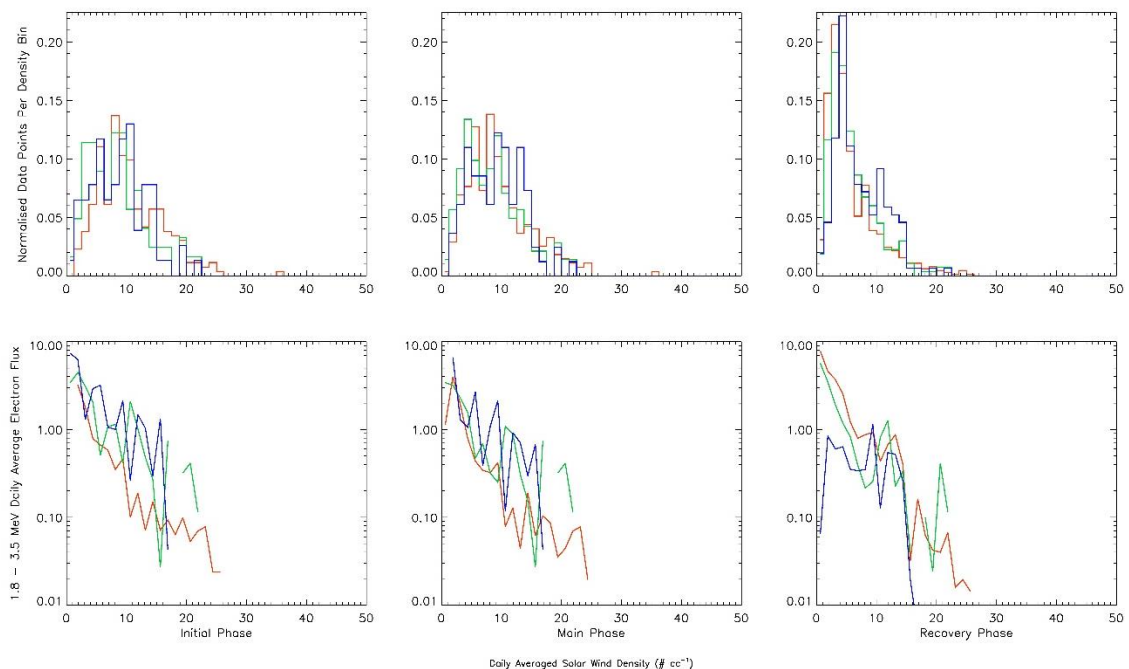
Figure 48: Normalised number of data points (top) and mean electron flux (bottom) per 1.25 #cc^{-1} solar wind density bins for flux increase (red), constant flux (green) and flux decrease (blue) storms.

[5.4]   Superposed epoch analysis

It appears that there are significant differences in both the solar wind velocity and the solar wind density relationships depending on whether a storm increases, decreases or has no effect on the relativistic electron flux at geosynchronous orbit. There are also significant differences between the recovery phase and the other two phases of the storm. The main reason for there being no real difference between the initial and main phases may be due to the short time period for which these phases last, usually less than a day, and as such using daily data will often use the same points for both phases as they occur on the same day. It is therefore important to evaluate the storms with a much greater time resolution.

Using a superposed epoch analysis technique is a good way of characterising the average parameters of multiple different storms. *Reeves et al.* [2003] defined the storm period for characterising the change in electron fluxes as a nine-day period broken down into a pre-storm (1-3 days before the day of the storm), the day of the storm (24 hours centred on the end of the main phase) and the post-storm (1-5 days after the day of the storm). The superposed epoch analysis was chosen to span the full duration of the storm (nine days) with the zero epoch at the end of the main phase. All of the following data is aligned with this epoch and averaged across all of the storms for each type of storm. The vertical lines on the superposed epoch analysis below indicating the start and end of the initial, main and recovery phases are indicative times taken from the average of the phase start times for each of the three types of storm.
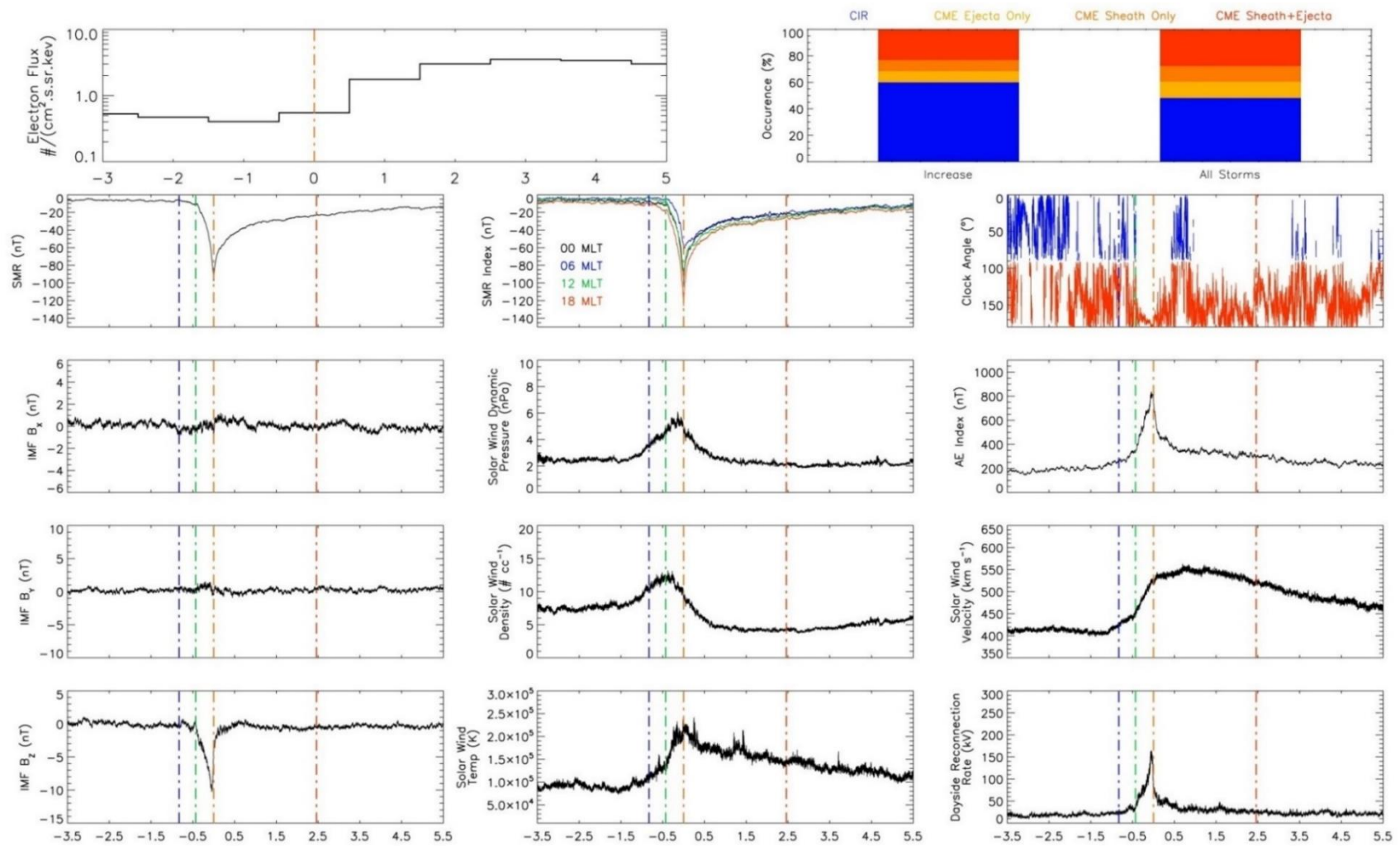
Figure 49: Superposed epoch analysis of solar wind parameters for flux increase storms. Vertical lines indicate the storm epochs, initial phase (blue to green), main phase (green to orange) and recovery phase (orange to red).
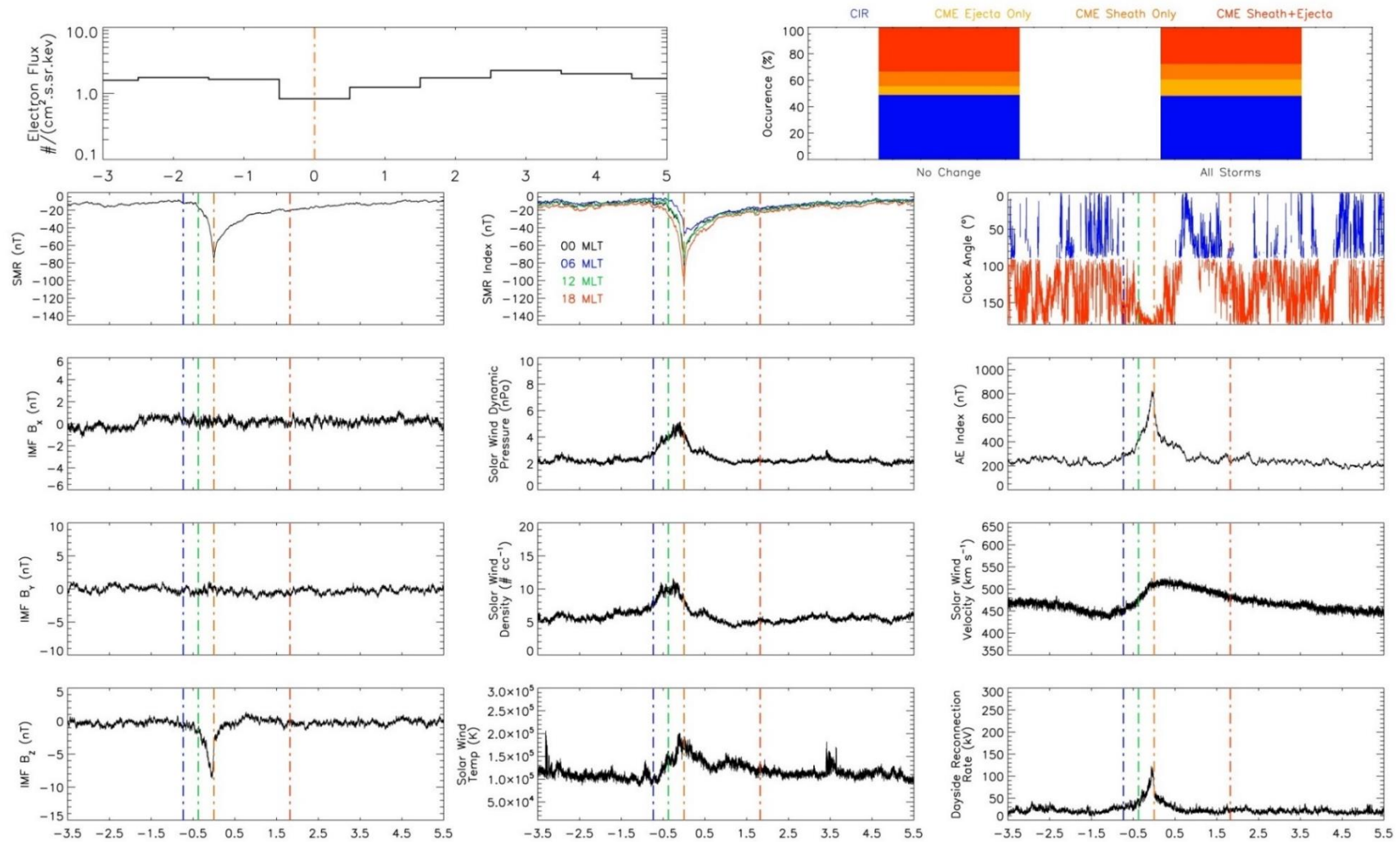
Figure 50: Superposed epoch analysis of solar wind parameters for storms that do not change the relativistic electron flux Vertical lines indicate the storm epochs, initial phase (blue to green), main phase (green to orange) and recovery phase (orange to red).
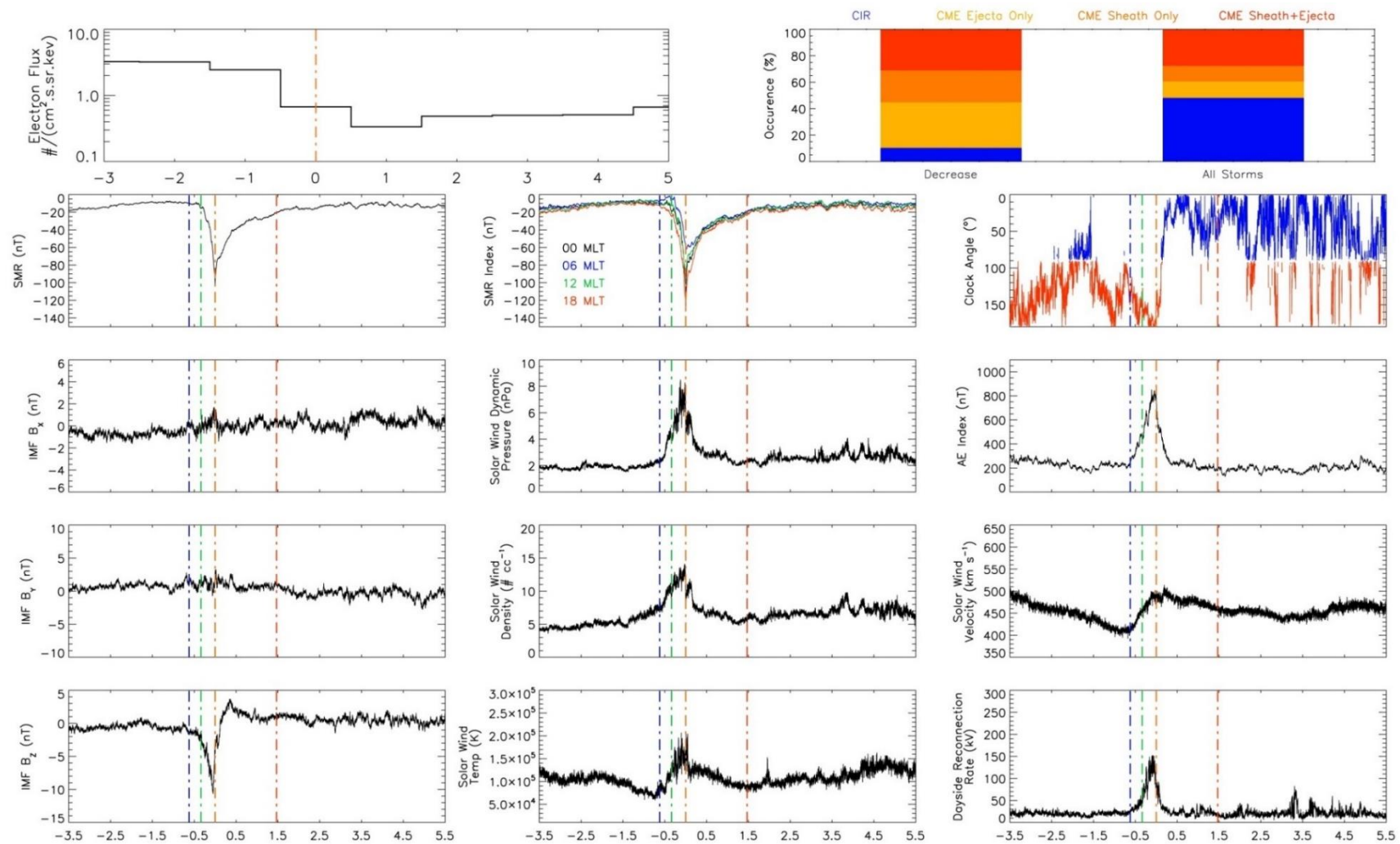
Figure 51: Superposed epoch analysis of solar wind parameters for storms that decrease the relativistic electron flux Vertical lines indicate the storm epochs, initial phase (blue to green), main phase (green to orange) and recovery phase (orange to red).

[5.4.1] Flux Change

Figure 49 to Figure 51 show the results of the superposed epoch analysis. There are a large number of plots that show several different parameters of both solar wind properties and geomagnetic indices. The top left panel shows the variation in daily average 1.8-3.5 MeV electron flux over the duration of the storm. It is important to note that because the data is the daily average, the epochs are slightly different to the other panels, with the day of the storm taken as the day on which the minimum SMR value for each storm occurred. The pre-storm and post-storm times are then evaluated with respect to that day. The panels showing the variation in the electron flux are combined to produce Figure 52, which clearly shows the expected variation and acts as a good verification of the event selection process. As previously mentioned by *Kilpua et al.* [2015], and clearly observable in Figure 52, flux decrease storms have, in general, enhanced fluxes prior to the storm whereas flux increase storms have depleted electron fluxes during this period. *Kilpua et al.* [2015] concluded that the pre-storm flux, when combined with the post-storm solar wind velocity, determined whether a storm would increase or decrease the flux.
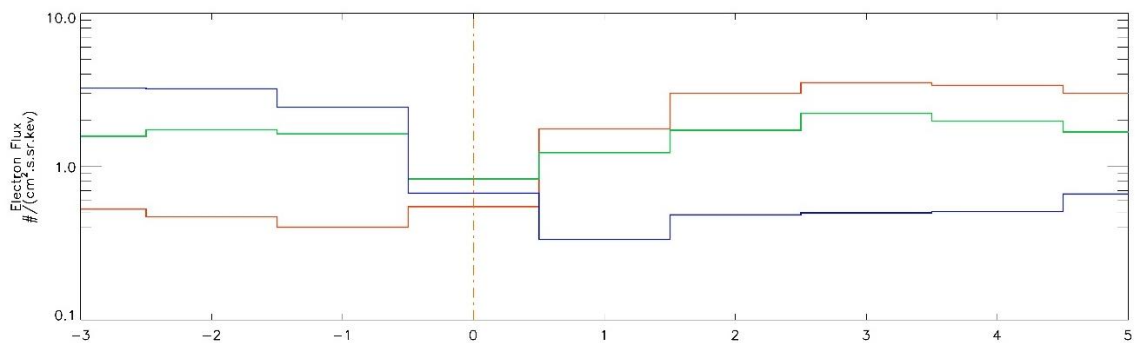
Figure 52: Variation in electron flux over the 9-day superposed epoch for flux increase (red), flux decrease (blue) and constant flux (green) storms.

This is due to the fact that fluxes which are already enhanced may not be further enhanced, which provides more scope for them to be depleted. Equally, fluxes which are already suppressed may not be able to be reduced further and so will more likely be enhanced.

This does raise several questions: at what level does the flux become so enhanced that it can no longer cause a flux increase? Is the flux saturated or does a high (low) initial flux inhibit the driving of acceleration (loss) processes within the inner magnetosphere? And what is the cause of these flux levels during the pre-storm period?

It would seem from Figure 52 that the electron flux is not the only controlling factor which determines the resultant flux change. This is shown by the lines for constant flux storms and flux decrease storms. Before the storm these fluxes are quite similar (within a factor of 1.5) where as in the post-storm region the flux for constant flux storms is around four times that of the average flux for flux decrease storm. Comparing the flux increase and constant flux storms the opposite trend can be seen suggesting that there is not simply a threshold at which the fluxes become sufficiently enhanced prior to the storm in order for it to determine the resultant flux change.

[5.4.2] Driver Types

The right hand plot of the top row in Figure 49 to Figure 51 shows the normalised breakdown of the occurrence of the solar wind structures that cause the storms to produce their respective changes in electron flux, compared with the normalised occurrence rates for all storms. As found previously [e.g. *Kilpua et al.*, 2015], flux increase storms tend to be more associated with CIRs (Figure 49), while those that decrease the flux are more associated with CMEs (Figure 51). Constant flux storms show a similar occurrence rate for both CIRs and CMEs when compared with the occurrence rate for all storms.

[5.4.3] SMR index

The second, third, fourth and fifth rows show a superposed epoch analysis using variables with one-minute time resolution. The left-hand plot shows the global SMR index over the duration of the storm with lines denoting the average phase times. Blue indicates the start of the initial phase, green the start of the main phase, orange the start of the recovery phase and red the end of the recovery phase.

It is interesting to note the obvious difference between the duration of the storm phases, with flux increase storms having the longest phases and decreasing the shortest as shown in Table 3. These phases are defined by their average duration of all the events for each of the different storm types.

Table 3: Average durations of the different storm phases depending on the change in the electron flux and associated standard error

Type of Storm	Average Duration of Storm Phase (hours)		
	Initial	Main	Recovery
Increase	9.57±0.65	10.34±0.67	59.06±2.95
No Change	8.65±0.81	8.99±0.77	43.73±3.61
Decrease	6.83±1.03	8.10±0.76	35.25±3.24

The minimum SMR value defining the strength of the storm is remarkably similar, with constant flux storms being slightly weaker, on average, than the other types. This suggests that the likelihood that a storm will change the electron flux is independent of the strength of the storm, as previously reported by *Reeves et al.* [2003]. The centre plot of the second row shows the SMR local time index, and as previously described [*Newell and Gjerloev*, 2012], there is a distinct asymmetry between the 06 and 18 indices, which is unsurprising as the majority of the current density, and hence stronger induced magnetic field, is carried by ions which travel along drift paths on the duskside. The difference between the SMR local time indices for 48 hours centred on the end of the main phase is plotted in Figure 53.

Figure 53 shows the change in the difference between the SMR18 and SMR06 indices over the 24 hours either side of the zero epoch time, where a value of 0 indicates that both indices are of equal strength. Positive values show that the SMR18 index is greater than the SMR06 index, whilst any negative values would indicate the opposite. The vertical lines on the graph (and similar later graphs) indicate the start of the initial phase, the start of the main phase and the start of the recovery phase, when viewed from left to right. These are only indicative start times and are taken from the average of the phase start times for each of the three types of storm. Figure 53 shows that the difference between the two indices increases during the initial and main phases, peaking roughly around 60nT for all three types of storm.

This is expected due to the drift paths of ions which drift through the dusk-side and hence induce a larger magnetic field (and thus produce a larger deflection in the north-south component of the magnetic field) than electrons which drift through the dawn-side. The difference is likely to increase during these periods as the magnetosphere is likely to be convection driven, thus only allowing ions to pass through the inner magnetosphere once before being lost to the magnetopause. At the end of the main phase and during the early recovery phase the difference between the two indices reduces rapidly as the dayside driving of the magnetosphere ceases and the convection strength reduces, allowing more ions to make complete drift paths and thus contribute to both the SMR18 and SMR06 indices. Although there is no real difference between the different types of storm during the initial and main phases there does appear to be a slight difference between the flux decrease storms and the flux increase and constant flux storms during the recovery phase. Initially all three types of storm show that the difference between the indices reduces rapidly over a period of around 6 hours, which is most likely due to the ongoing formation of a symmetric ring current. However, for flux decrease storms this continues while for the others it levels off. This suggests that for flux decrease storms there are more ions on the dawn-side or fewer on the duskside than for the other types of storm and may suggest a reduction in injection of particles to the inner magnetosphere.
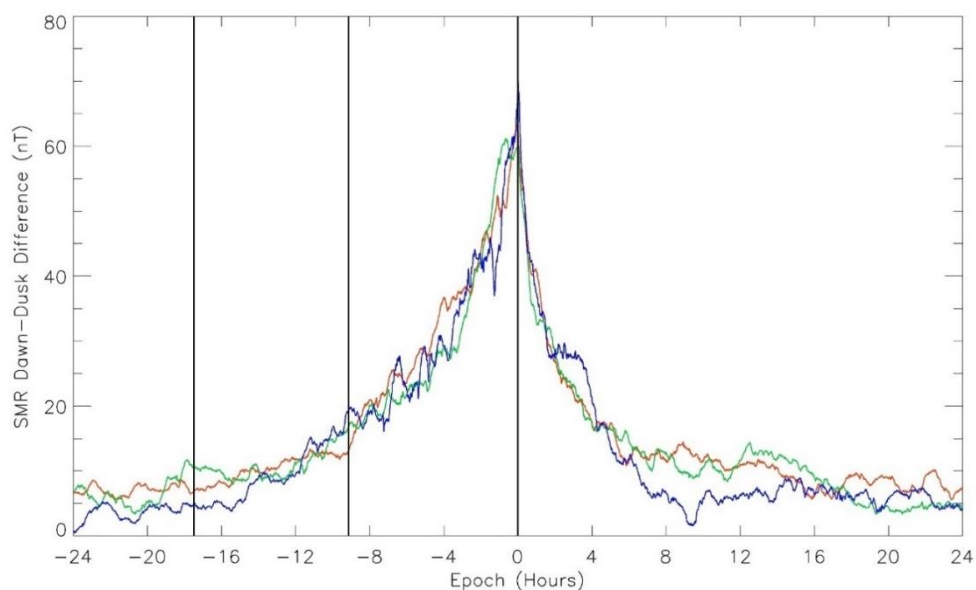
Figure 53: The difference between the dawn and dusk SMR indices over the 48 hours centred on the end of the storm main phase for flux increase (red), constant flux (green) and flux decrease (blue) storms

[5.4.4] Clock Angle

The right hand plot of the second row for the superposed epoch analysis (Figure 49 - Figure 51) shows the evolution of the clock angle over the duration of the storm epoch. The superposed clock angle is calculated from the average of the IMF B_Y and B_Z values over the duration of the storms. As previously mentioned, the clock angle is extremely variable over this duration and can change from extremely northward to extremely southward and back again on a timescale of hours. On initial inspection it appears that there are significant differences in the evolution of the clock angle over the duration of the different types of storm. During the pre-storm and initial phase, the clock angle for flux decrease storms is southward for the vast majority of this period and remains southward until the start of the recovery phase, during which it changes to significantly northward, which remains the dominant direction of the clock angle for the remainder of the storm period.

In contrast the flux increase storms have significantly more northward clock angle during the pre-storm and the clock angle remains northward until midway through the initial phase, whereas both other types of storm have southward IMF for the full duration of the initial phase. The clock angle for flux increase storms then turns southward and persists until the early recovery phase, during which it briefly turns northward, which is a necessary condition for the reduction in the magnetospheric driving and the start of the recovery phase. Interestingly the clock angle returns to a southward orientation for the remainder of the recovery phase, which lasts significantly longer than the recovery phases of the other types of storm (Table 3). Figure 54 shows this difference for the three types of storm more clearly. All types of storm have strongly southward IMF during the main phase, as expected, with the significant difference occurring in the early recovery phase where the clock angle turns northward much more rapidly for flux decrease storms than for flux increase or constant flux storms. Finally, the clock angle can be seen to change back to southward for flux increase storms at the end of the period plotted in Figure 54 while it remains northward for the other types of storm.
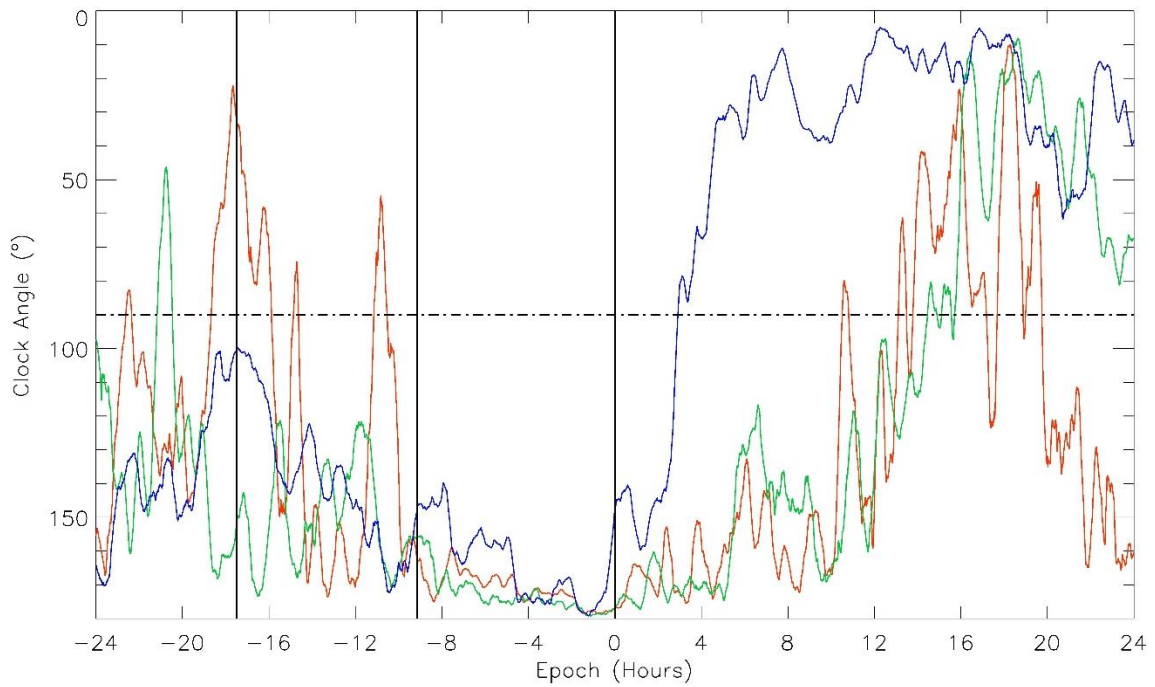
Figure 54: Evolution of the clock angle, smoothed for clarity, for flux increase (red), constant flux (green) and flux decrease (blue) storms for the 48 hours centred on the end of the main phase. The horizontal line denotes a clock angle of 90º.

[5.4.5] Solar Wind Dynamic Pressure

The middle panel of the third row shows the solar wind dynamic pressure. For all types of storm this increases through both the initial and main phases and then begins to decrease rapidly during the recovery phase. All storm types have a similar dynamic pressure evolution, however, flux decrease storms seem to have the strongest solar wind dynamic pressure. This may be a contributing factor to the ability of these storms to decrease the flux as an increase in solar wind dynamic pressure will lead to a reduction in the magnetopause standoff distance, which in turn leads to particles with lower drift altitudes being able to reach the magnetopause and be lost from the system, particularly during the main phase and early recovery phase.

[5.4.6] AE Index

In contrast to previous similar studies the evolution of the auroral electrojet (AE) index is also evaluated and is plotted on the right hand side of the third row (Figure 49 to Figure 51). This is a measure of the global electrojet activity produced by enhanced currents which flow in the ionospheric auroral zone [*Davis and Sugiura*, 1966]. These currents become enhanced during substorms and so the AE index can be used to indicate the prevalence of substorms over a certain period with higher values of the AE index indicating periods of high substorm activity. The AE index becomes enhanced during the initial and main phases of all the types of storm before dropping rapidly following the end of the main phase.

There are two significant differences between the types of storm. The first is that the AE index increases rapidly during the initial phase of flux decrease storms, and continues at the same rate during the main phase. This is different than for both the constant flux and flux increase storms, which both show a slight increase during the initial phase followed by a distinct change in gradient and a rapid increase to peak value of the AE index (which is almost identical for all types of storm) at the end of the main phase. The AE index decreases rapidly at the beginning of the recovery phase for all types of storm but does not reduce to the same level.

Figure 55 (a) shows more clearly the evolution for each type of storm. During flux decrease storms the AE index decreases to its pre-storm level almost immediately, whereas the AE index remains elevated following the initial decrease until around halfway through the recovery phase for constant flux storms, and for flux increase storms it remains elevated for the duration of the recovery phase. Figure 55 (b) gives an indication of the clock angle and therefore the orientation of the IMF. The AE index in graph (a) corresponds well to this orientation. The AE index remains higher for the flux increase and constant flux storms as the IMF remains southward for longer for these types of storms. Flux increase storms return to a southward orientation and the AE index remains elevated.

In contrast the constant flux storms change to a sustained northward IMF orientation and at the same time the AE index drops to the level of the flux decrease storms which have had a northward IMF orientation, and a lower AE index since approximately 3-4 hours following the zero epoch. This may provide an explanation for the resulting flux changes as it suggests that geomagnetic activity during flux increase storms continues to inject particles into the inner magnetosphere throughout the recovery phase when compared to flux decrease storms, and hence are more able to replace the electrons which may be lost during this phase. Additionally, during constant flux storms particles could be injected into the inner magnetosphere during the initial part of the recovery phase, which could replace any electrons previously lost (indicated by the enhanced AE index during the period), but it is then not possible to enhance the flux due to the drop off in injected particles midway through the recovery phase as indicated by the decrease in the AE index at this time. The observed decreases in the AE index appear to occur after the clock angle has turned northward, which may suggest that this is the ultimate cause of the differences between the different types of storm.
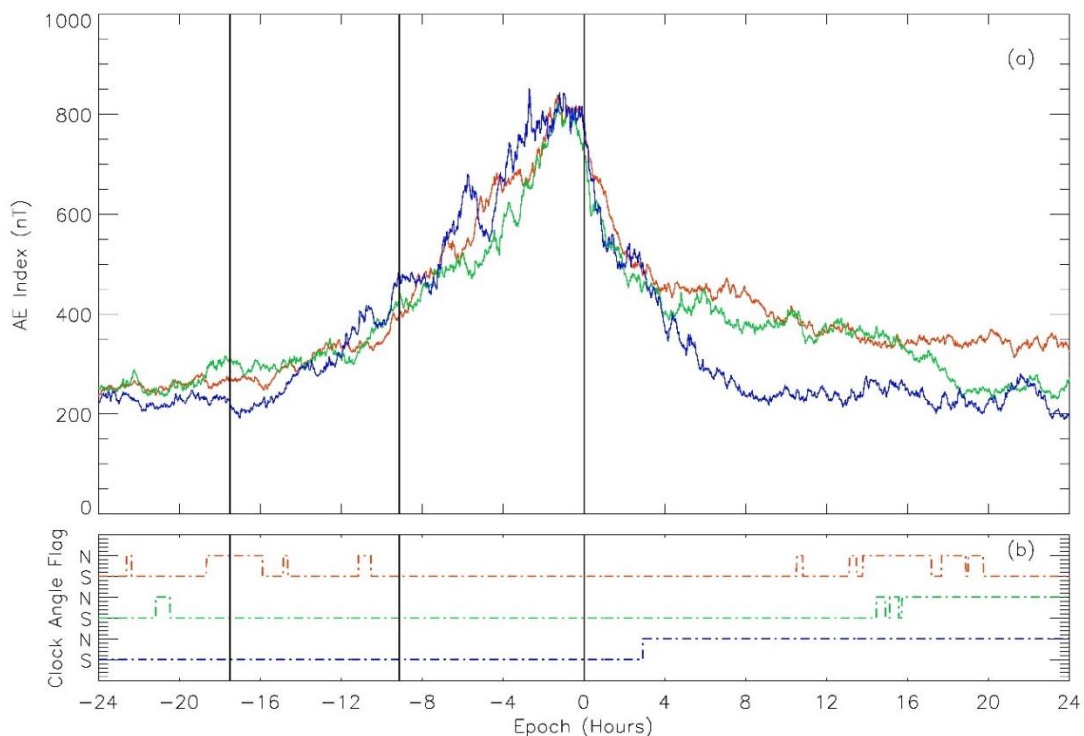
Figure 55: Top panel (a) shows the evolution of the AE index over the 48 hours centred on the end of the main phase for flux increase (red), constant flux (green) and flux decrease (blue) storms. The bottom panel (b) shows the clock angle flag indicating whether the IMF is in a northward or southward orientation for each of the three types of storms colour coded as in (a).

[5.4.7] Solar Wind Density

The centre plot of the fourth row shows the solar wind density over the duration of the storm period. There are significant differences between the three types of storm as suggested in sections [5.3.3] and [5.3.4]; on average, during the pre-storm time, flux decrease storms have the lowest density, flux increase storms have highest density and constant flux storms fall between these.

Figure 56 shows that during the initial and recovery phases the density increases for all storm types and peaks in the main phase. The location of this peak is different for each of the types of storm within the main phase; flux increase storms have a peak density at the start of the main phase, flux decrease storms have a peak density at the end of the main phase and constant flux storms have a peak close to the centre of the main phase. During the recovery and post-storm-phases the density returns to near the pre-storm levels but is again different for each type of storm: flux increase storms generally have the lowest densities over this duration, the densities being significantly lower than during the pre-storm period; constant flux storms show a slightly lower density following the storm than during the pre-storm period; and flux decrease storms have a density that is both higher than that of the flux increase and constant flux storms.
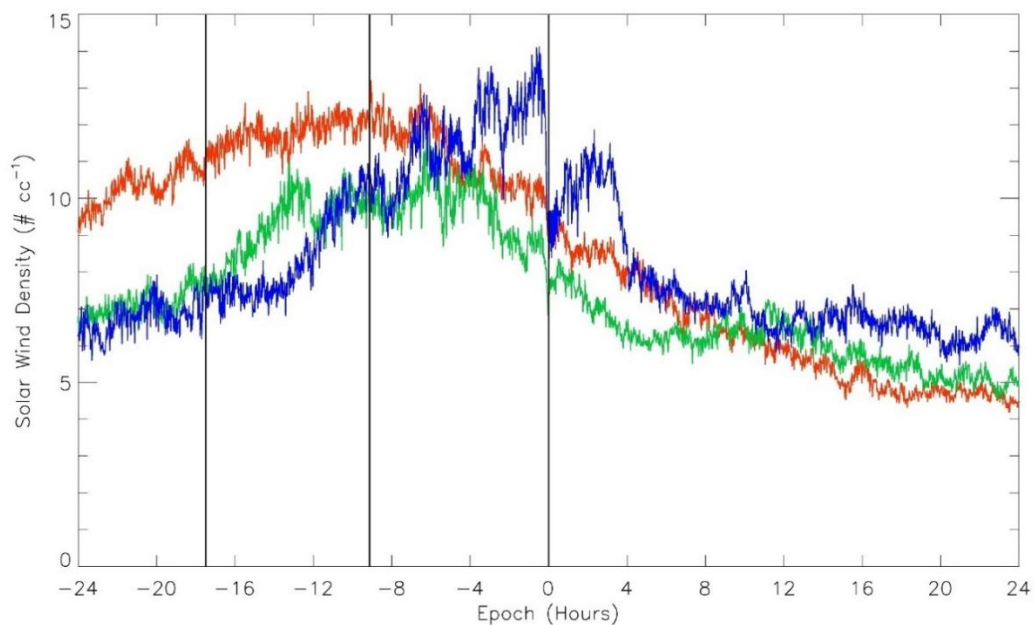
Figure 56: Evolution of the solar wind density over the 48 hours centred on the end of the main phase for flux increase (red), constant flux (green) and flux decrease (blue) storms

[5.4.8] Solar Wind Velocity

The right hand plot of the fourth row of the superposed epoch analysis (Figure 49 to Figure 51) shows the evolution of the solar wind velocity over the duration of the storm periods, with Figure 57 showing the variation in the solar wind velocity over the 48 hours centred on the end of the storm main phase. Again there are significant differences between the different types of storm as suggested by *Kilpua et al.* [2015] and as also observed above (sections [5.3.1] and [5.3.2]). The superposed epoch analysis provides another technique for observing the change in solar wind velocity for the different types of storm. Similarly to the solar wind density, the most significant differences are between the pre-storm and the recovery phase/post-storm periods.

Flux decrease storms have a higher solar wind velocity during the pre-storm phase which decreases through this period to its minimum value at the start of the initial phase. Constant flux storms have a similar evolution during this phase, apart from the fact that initial velocity is around 20 to 30 kms^{-1} lower than for flux decrease storms, and its minimum at the start of the initial phase is almost $50 kms^{-1}$ greater than for flux decrease storms; these differences produce a flatter evolution over the period. Flux increase storms have a similar flat distribution but at a much lower velocity, around $400 kms^{-1}$, than for either the constant flux or flux decrease storms during the pre-storm period (Figure 49 to Figure 51). Figure 57 shows that the solar wind evolution is remarkably similar for all types of storm through both the initial and main phases, increasing rapidly throughout the main phase. The solar wind velocity levels out following the end of the main phase and begins to fall back to a similar value to that of the pre-storm solar wind for all storms apart from flux increase storms, for which the average velocity continues to rise through the early recovery phase, peaking around halfway through this period before beginning to slowly decrease (Figure 57). The average solar wind velocity for flux increase storms still remains significantly higher than the pre-storm value throughout the post-storm period.
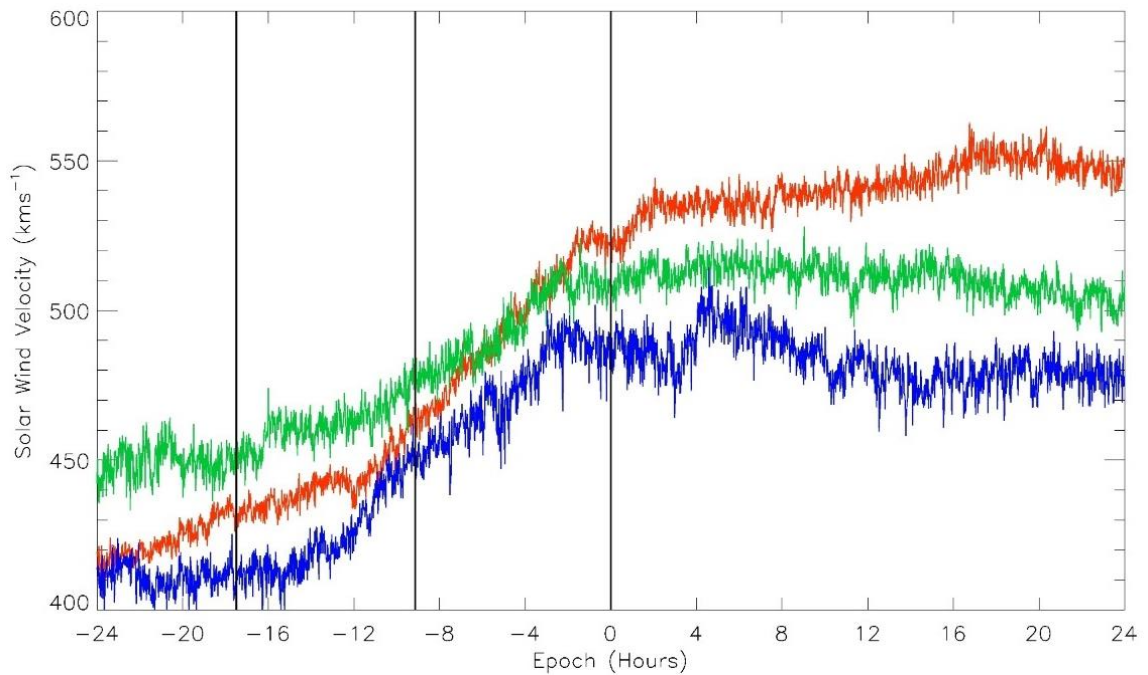
Figure 57: Evolution of the solar wind velocity over the 48 hours centred on the end of the main phase for flux increase (red), constant flux (green) and flux decrease (blue) storms

[5.4.9] IMF Strength

The left hand plot of the third row, of Figure 49 to Figure 51, shows the evolution of the IMF B_X component over the duration of the superposed storm period. All three types of storm show a very similar evolution with the IMF B_X component remaining close to zero for the duration. The most significant difference occurs during the post-storm region for flux decrease storms, during which the IMF B_X moves to more positive values than for the other types of storm. The left hand plot of the fourth row of the superposed epoch analysis (Figure 49 - Figure 51) shows the evolution of the IMF B_Y component. This is extremely similar for all of the different types of storm and there appears to be no significant variation in any of the plots, with the value remaining close to zero for the duration. Flux decrease storms appear to show that the IMF B_Y component tends to be slightly more negative towards the end of the post-storm period at the same time that the IMF B_X becomes more positive.

The left hand plot of the bottom row of the superposed epoch analysis shows the evolution of the IMF B_Z component. Figure 58 shows the evolution of the IMF B_Z component for the 48 hours centred on the end of the main phase. The first thing to note is that the field strength begins to decrease just over an hour (~65 minutes on average) prior to the end of the main phase for all types of storm, this is also observed in the magnetopause current index in chapter 4 (Section [4.5]). This, again, suggests that solar wind variations take around 1-2 hours to influence the inner magnetosphere.

The overall evolution of this parameter is similar for all three types of storm, with the field strength being close to zero during the pre-storm period, becoming significantly negative during the main phase and returning back to near zero during the recovery phase and post-storm period. The main difference between the types of storm occurs during the early recovery phase following the end of the dayside driving and the minimum value in the SMR index. For all three types of storm the IMF B_Z reduces rapidly at this point; however, for flux decrease storms the value of the parameter becomes strongly positive before returning to near zero whereas for flux increase storms this parameter stays southward for longer and only turns positive briefly before returning to slightly negative values for the remainder of the recovery phase. Constant flux storms follow the flux increase IMF B_Z evolution before turning more positive towards the middle of the recovery phase.
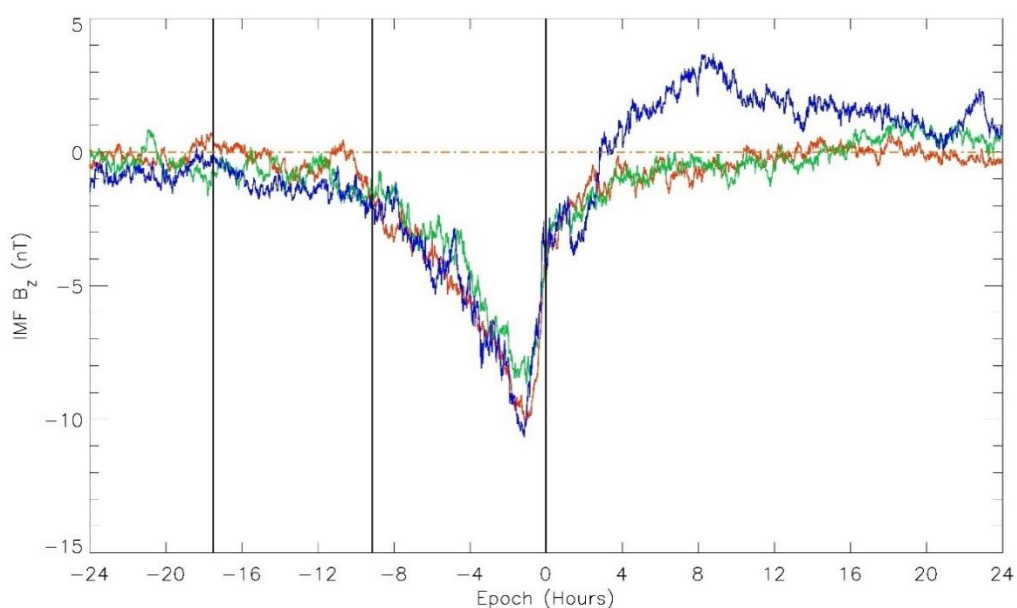
Figure 58: Evolution of the solar wind IMF B_Z component over the 48 hours centred on the end of the main phase for flux increase (red), constant flux (green) and flux decrease (blue) storms

[5.4.10]   Solar Wind Temperature

The centre plot of the bottom row shows the evolution of the solar wind temperature over the duration of the storm period. Again there is a similar evolution observed for all of the types of storm, with the temperature increasing through the initial and main phases before returning back to close to the pre-storm level through the recovery phase and into the post-storm period. The major difference is with flux increase storms and, like the solar wind velocity, the temperature reaches higher values than for flux decrease or constant flux storms and remains elevated throughout the recovery phase.

[5.4.11]   Dayside Reconnection Rate

The final plot in the superposed epoch analysis (bottom right) shows the dayside reconnection rate as defined by *Milan et al.* [2012] (Equations 90 & 91). Figure 59 shows that this parameter increases primarily during the main phase to a peak at the end of the main phase. This is to be expected, due to the selection of the zero epoch as being the minimum SMR value, which indicates the end of the strong driving by the solar wind just before the magnetosphere begins to recover and return back to its pre-storm state. The peak dayside reconnection rate is extremely similar for both flux increase and flux decrease storms and is slightly less for constant flux storms. This corroborates the conclusion of *Reeves et al.* [2003], who found that the type of storm did not depend on its strength. The main difference, most likely controlled by the field strength and clock angle, is during the early recovery phase. It can be seen in Figure 51 that the dayside reconnection rate returns to its pre-storm level almost immediately following the end of the main phase. In Figure 49 and Figure 50 the dayside reconnection rate, despite an initial rapid decrease, remains elevated longer into the recovery phase before returning to its pre-storm level. Comparing the three storms side by side (Figure 59) it is clear that the dayside reconnection rate is more enhanced during the recovery phase for flux increase storms than for the constant flux and flux decrease storms, especially between 4 and 12 hours following the end of the main phase.
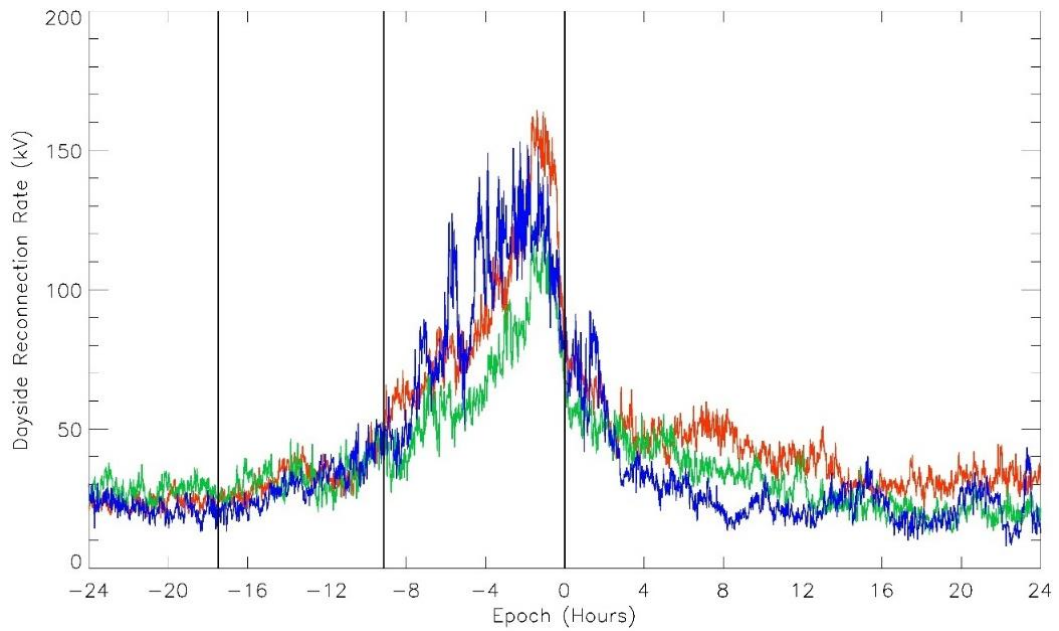
Figure 59: Evolution of the dayside reconnection rate over the 48 hours centred on the end of the main phase for flux increase (red), constant flux (green) and flux decrease (blue) storms

[5.5] Solar wind structures

Figure 54 shows that the clock angle evolution for flux decrease storms and the other types of storm is distinctly different in the early recovery phase. To determine the extent that this difference plays a role in the determination of the resultant flux change the ejecta and sheath plus ejecta storms will be examined by the orientation of the ejecta substructure. Ejecta associated with CMEs are magnetic clouds and as such typically have a period of northward IMF followed by a rotation to a southward orientation, or vice versa. The storms which had solar wind ejecta, as identified by *Kilpua et al.* [2015] were broken down into north-south (Figure 60) and south-north (Figure 61) ejecta types.

As shown in Figure 54 the clock angle for flux decrease storms turns northward rapidly following the end of the main phase, while for flux increase and constant flux storms it remains southward for a period of time following the end of the main phase before turning northward. It may therefore follow that south-north ejecta are more likely to cause an electron flux decrease than north-south ejecta.

The main phase occurs in the coherent southward IMF period for both storms as shown by the region bounded by the solid black lines in Figure 60 & Figure 61. Where this region of coherent southward IMF falls within the structure is important. Figure 60 shows that following the southward portion of the ejecta the clock angle becomes more random in its orientation, changing rapidly from northward to southward. In contrast the south-north ejecta (e.g. Figure 61) have a period of coherent northward IMF orientation for around half a day following the turning of the IMF from a southward orientation. It is interesting to note that the end of the main phase, which occurs at 3.5 days in both cases, occurs after the sustained strongly southward portion of the ejecta sub-structure, despite there being a preceding sheath in the case of Figure 61. It was found that approximately half of all ejecta and sheath plus ejecta CME structures had either north-south or south-north ejecta orientations.
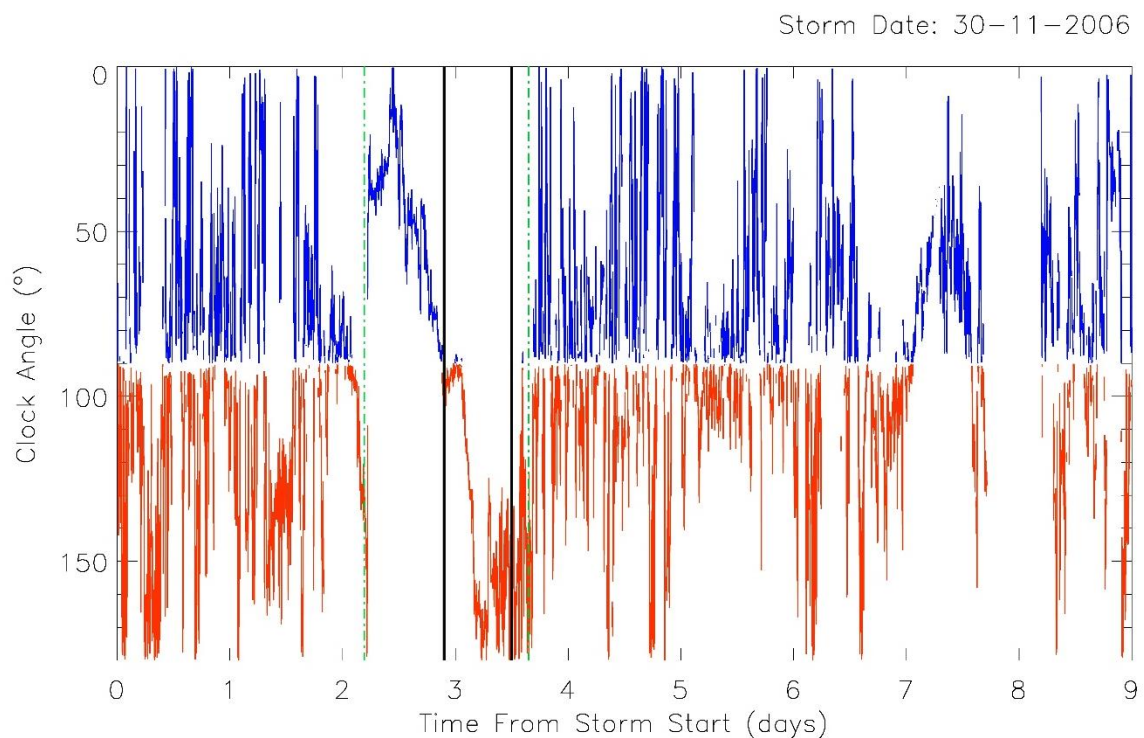
Figure 60: An example of a north-south ejecta type, the green dashed lines indicate the start and stop times of the ejecta substructure as identified by Kilpua et al. [2015]. The solid black lines indicate the start and stop times of the storm main phase.
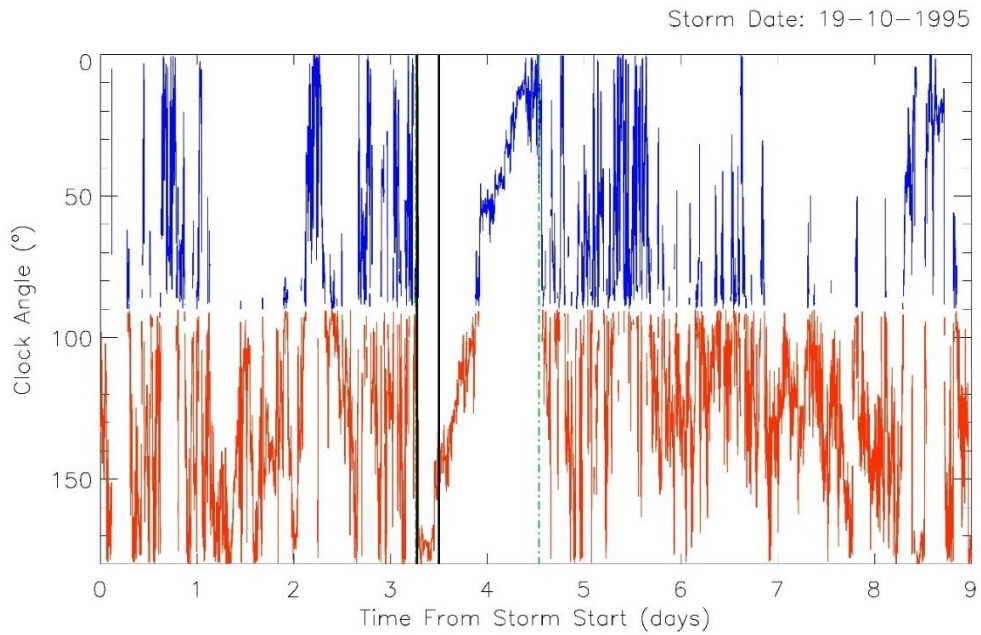
Figure 61: An example of a south-north ejecta type, the green dashed lines indicate the start and stop times of the ejecta substructure as identified by Kilpua et al. [2015]. The solid black lines indicate the start and stop times of the storm main phase.

Figure 62 shows the relative occurrence of each of the types of storm for the separate solar wind drivers and their respective ejecta orientations. The hypothesis that the N-S ejecta are more likely to cause flux increases than the S-N ejecta seems to be supported to a certain degree, especially for the ejecta only storm drivers. For sheath plus ejecta storms, the orientation of the ejecta does not seem to be as effective in dictating the change of the electron flux over the duration of the storm.
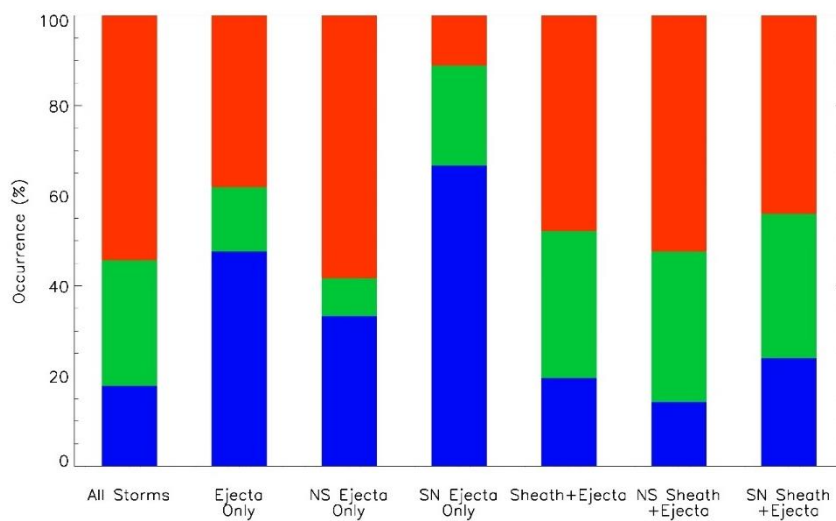
Figure 62: Flux increase (red), flux decrease (blue) and constant flux storms (green) are shown as a percentage of all storms on the far left. This can then be compared to the ejecta and sheath plus ejects substructures and also the orientation of the ejecta within each of these CME types.

In the above section the clock angle variation was extremely distinct for each of the three types during the entirety of the recovery and post-storm phases rather than just the early recovery phase. This may suggest that the duration of the recovery phase and post-storm period (5.5 days following the end of the main phase) may need to be examined for the true effect of the clock angle orientation to be determined.

For each individual storm the clock angle was calculated for the duration of the recovery phase and post-storm period (i.e. positive epochs in section [5.4]). The percentage that the clock angle was southward over this duration was then calculated and the storms were sorted into 10% bins. The relative abundance of each type of storm was then calculated for each southward percentage clock angle bin. The resultant graph is shown in Figure 63, and it can be clearly seen that both the number and relative abundance of flux decrease storms reduces as the amount of southward IMF in the recovery phase increases and that the opposite is true for flux increase storms.

The number of flux increase storms peaks around 60-70% southward IMF whereas the number of flux decrease storms peaks in the 30-40% bin with constant flux storms peaking in between the two. The relative abundance of each type of storm per bin shows this trend even more clearly starting with 100% flux decrease storms in the 10-20% bin, changing to 100% flux increase storms in the 80-90% bin. Constant flux storms peak around the 50-60% bin although they do not dominate for any amount of southward IMF clock angle. The reason for the constant flux storms may therefore not be exclusively determined by the amount of southward IMF during the recovery and post-storm periods. It's also interesting to note that the occurrence percentages are almost identical for the 40-50% bin and the relative abundance for all storms, as shown in the left hand bar of Figure 62.
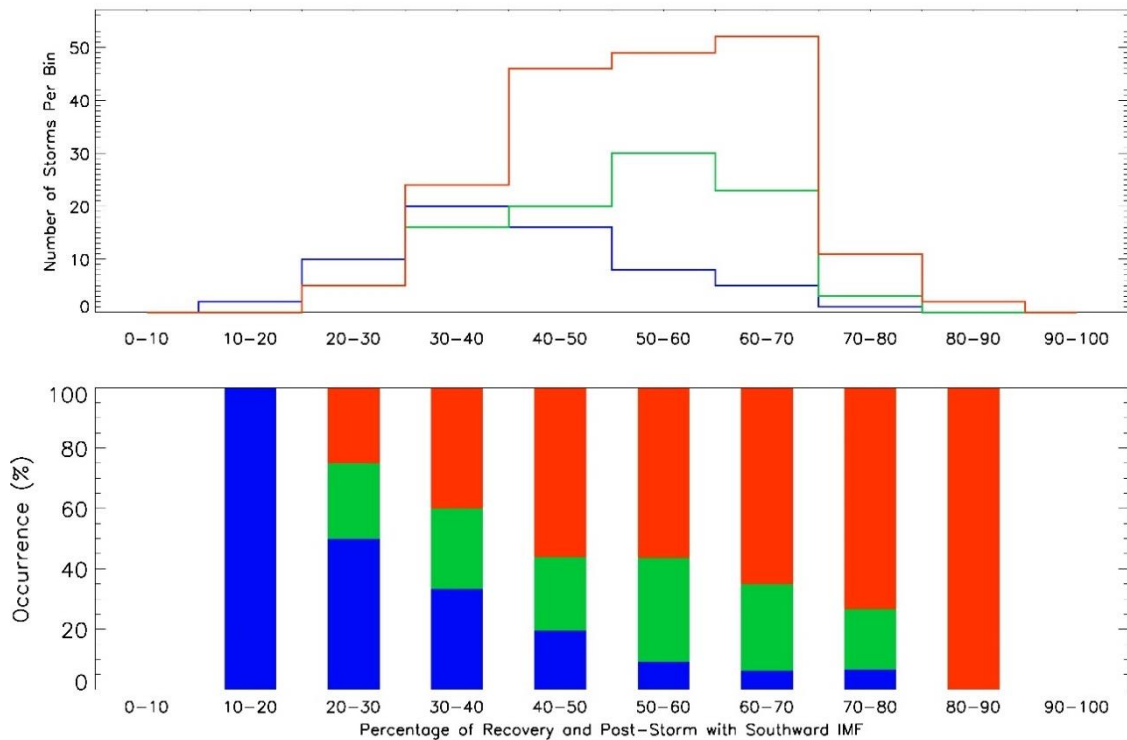
Figure 63: Number and relative occurrence of each type of storm broken down by the amount of southward IMF during the period following the end of the main phase.

[5.6]   Conclusion

Reeves et al. [2011], following the previous work done by *Paulikas and Blake* [1978], showed that the relativistic electron flux had a distinct solar wind velocity distribution. In this chapter this relationship was specifically evaluated for the different types of storm as defined by the change in relativistic electron flux. It is clear and that the solar wind velocity relationship (Figure 45) is not observed for flux decrease storms. and that high solar wind velocity during the recovery phase of these events does not produce the typical high fluxes.

Similarly, *Lyatsky and Khazanov* [2008] suggested it was in fact the solar wind density that controlled the flux of the relativistic electrons. Again it is shown here that by observing the change in the relativistic electron flux over the duration of geomagnetic storms the solar wind density (Figure 48) is unable to produce the typical response in the electron flux for flux decrease storms; i.e. low solar wind densities do not cause high fluxes during the recovery phase of flux decrease storms as might be expected.

Kilpua et al. [2015] showed that the electron flux change over the duration of storms differed depending on the type of driver, the solar wind speed and the pre-storm electron flux. However, it is shown here that this is not the full picture and as mentioned above it is not merely that the velocity of the solar wind is higher for flux increase storms but that higher fluxes are observed for all solar wind velocities. Using a superposed epoch analysis with additional indices, such as the AE index, IMF clock angle and dayside reconnection rate, it was shown that substorm activity is significantly lower during the recovery phase of the storm for flux decrease storms than for flux increase storms (Figure 55). This may suggest that the inner magnetosphere may not be refilled as efficiently during flux decrease storms as during flux increase storms, thus allowing loss processes to dominate.

These features suggest that the solar wind is not as influential on the earth's magnetosphere during the recovery phase of flux decrease storms when compared to flux increase storms. Driving of the magnetosphere by the solar wind is most efficient when the field lines of the Sun and the Earth have reconnected and solar wind particles are able to access the magnetosphere. This occurs preferentially during periods of southward IMF and this suggests that during the recovery phase of flux increase storms the IMF is significantly more southward than during the recovery phase of flux decrease storms (as shown in Figure 63). This may therefore be the reason why a storm is more likely to produce a particular flux change rather than any individual property of the solar wind. *Li et al.* [2011b] suggested that the solar wind velocity has been wrongly identified as the cause of electron flux enhancements and that instead enhancements occur via geomagnetic intensifications which, in turn, are driven by the favourable orientation of the IMF. The reason for the identification of the solar wind velocity and density as the parameters that produce flux enhancements may be due to the inter-correlation of solar wind parameters and the fact that high speed and low density solar wind is often observed during periods of favourable IMF orientation.

Miyoshi and Kataoka [2005] showed that CIR storms almost always produce flux enhancements while CME driven storms cause flux enhancements for only about half the time. Tanskanen et al. [2005] suggested that this is mainly due to continuous injections from the plasma sheet, attributed to substorm activity, during the recovery phase of CIR driven storms. This allows for the ring current to persist for a longer duration than during CME driven storms. The results presented in this chapter agree with this conclusion and support the assumption that the substorm injection of particles, driven by the continued favourable orientation of the IMF during the recovery and post-storm phases, determines whether the electron flux changes.

Although the clock angle orientation appears to be the key factor in determining the change in the electron flux, there are still many other questions regarding the exact processes involved and how they change. This is because substorms do not directly inject relativistic electrons but rather seed electrons which can generate wave modes, which in turn can enhance the relativistic electron flux. This will be discussed in more detail in the subsequent chapter. Additionally, only the electrons have been used as an indicator for the type of storm and so further questions arise regarding the evolution of the ion population both in the relative abundance of each species but also in the evolution of each species individually over these time periods. The following chapter will attempt to answer some of these questions by using the Cluster spacecraft to examine the evolution of the plasma and wave environment within the magnetosphere during these periods.

CHAPTER 6

Analysis of Storm Time Plasma and Field Variations

[6.1]   Introduction

The creation of an enhanced symmetric ring current, and the induced magnetic field associated with it, is the main feature of a geomagnetic storm. The particle environment within the magnetosphere varies dramatically during storms as a result of competition between source and loss processes, which are both significantly enhanced during storm times [*Li et al.*, 2007]. The relativistic electron fluxes at geosynchronous orbit, as observed by *Reeves et al.* [2003] are testament to this. The location and intensities of three identified wave modes will be evaluated and discussed in their relation to the observed change in particle fluxes over the duration of different types of storm.

As discussed in chapter 2, charge exchange, coulomb collisions and wave-particle interactions are important decay mechanisms in the erosion of the ring current during the recovery phase of geomagnetic storms. Each of these mechanisms dominate in different parts of the magnetosphere. Close to the neutral atmosphere, coulomb collisions are most important. Charge exchange causes ions with energies up to a few hundred keV to decay from the ring current. This becomes a less important factor as the particles' charge exchange cross section decreases with increasing energy [*Daglis et al.*, 1999]. Gyro-resonant wave-particle interactions can occur at almost any location within the magnetosphere if the driving conditions and plasma source populations are present. This being said there are more preferential locations [e.g. *Shprits et al.*, 2008] for the different types of wave modes.

Due to gradient-curvature drift the source population for the generation of wave modes will have a MLT dependence. Therefore, there will be preferred locations for the generation of each of the different types of wave. Both electrons and ions will resonate with different wave types due to the underlying conditions that vary with location [*Shprits et al.*, 2006a; *Shprits et al.*, 2008]. Negative gradients in phase space density can lead to a further mechanism for particle loss via outward radial diffusion, which can carry particles to the magnetopause where they are lost from the system [*Shprits et al.*, 2006b]. There is a very delicate balance between both acceleration and loss processes during storm times. As discussed these vary both with MLT and radial distance. Figure 64, reproduced from *Shprits et al.* [2008], shows an empirical model (based on observations) of areas in which each of the different loss process may be dominant.
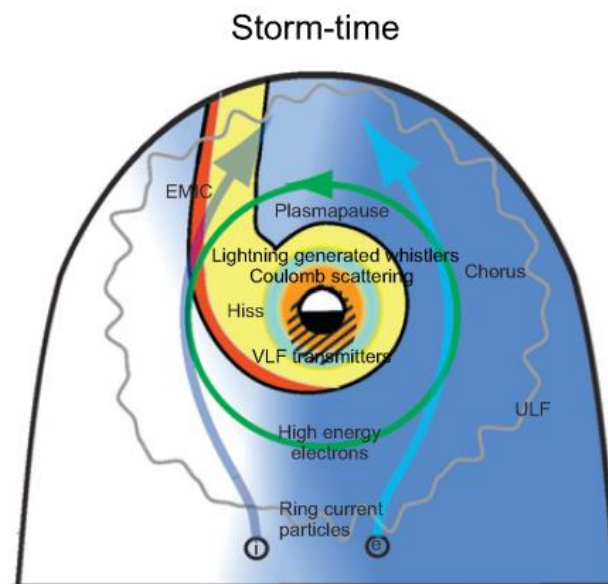
Figure 64: MLT and radial dependence of specific wave modes and other loss mechanisms during disturbed geomagnetic conditions. Reproduced from Shprits et al. [2008]

This chapter will thus concentrate on the wave power variations of these EMIC, hiss and chorus wave modes over the duration of storms and differences that arise due to the type of storm. The plasma environment for each of these types of storm will also be investigated in order to determine specific processes which may cause the observed variations.

[6.2]   Data Processing

Each of the Cluster instruments (see chapter 3) despite being upon the same spacecraft have slightly different data processing requirements and as such all have to be approached separately in order to remove bad data. The goal of the data processing was to create a series of data arrays which are all on the same time scale (1-minute resolution) over the duration of the identified storm periods. This section will briefly outline the techniques used for each of the different data products taken as recommended by the instrumentation user guides all of which can be found on the Cluster Science Archive for the suite of instruments which comprise the Cluster spacecraft.

The overall data processing is extremely similar for each instrument and in general comprises of the removal of bad or inappropriate data and the resampling of the remaining good quality data to a time resolution of one minute. A one-minute time resolution was chosen as it provides continuity with other data sets, primarily the SMR index, which are not produced at a higher resolution. Provided within the Cluster data products is a global quality flag, which indicates whether a measurement is of publishable quality. Flags with a value below 3 indicate that the data is poor, which may be due to a multitude of reasons but ultimately this data should not be, and in this work is not, used. Conversely flags with a value of three or greater are of good quality and can be used. Following this data processing, the data is resampled into a time resolution of one minute, by taking the average of multiple measurements where applicable. Additional caveats applicable to each instrument individually were accounted for as recommended in the respective user guides.

The region of interest in this chapter is the magnetosphere, specifically the plasma that is trapped on closed field lines and thus not directly connected to the solar wind. Determination of whether a field line is open or closed at any given minute was achieved by evaluating the magnetic field variations and the plasma properties as measured by each of the Cluster spacecraft.

[6.2.1] Determination of the Magnetosphere

The first challenge with this analysis is the determination of the closed field line region of the inner magnetosphere. It is important to define these regions using a robust methodology in order to avoid contamination of the data from regions such as the magnetopause. The technique used here is a combination of three data led identification algorithms. The first two identify all of the magnetopause crossings and from this the magnetosphere is defined. The third identifies the magnetospheric lobes, which have an open field configuration and so need to be removed.

[6.2.2] Magnetopause Crossings

Using the methodology of *Case and Wild* [2013] and *Raymer et al.* [2018 (In Prep)] the magnetopause crossings of the Cluster spacecraft can be determined from the magnetic field data and the plasma properties. *Case and Wild* [2013] use a modified *Ivchenko* [2000] algorithm due to the orbital configuration of the Cluster spacecraft. The main difference being that at high latitudes (at an angle of greater than 45° of the X-Y$_{GSM}$ plane) the orientation of the Earth's magnetic field is more radial than aligned along the Z$_{GSM}$ axis. As such at these latitudes the radial magnetic field strength is used rather than the Z component. The *Case and Wild* [2013] algorithm uses two three minute windows separated by a gap of 32 seconds (or 8 spins of the spacecraft) to compare the magnetic field. For the detection of a magnetopause crossing their algorithm requires that the average magnetospheric field strength is greater than 10 nT and at least 1.3 times greater than the average magnetosheath field strength. It also requires that the standard deviation of the magnetosheath window is greater than 4.5 and is no less than 2.5 times that of the magnetospheric window.

If a crossing is identified, then the windows are shifted by ten minutes. If not the windows are shifted by one spin (4 s) and the analysis re-run. Shifting the windows by 10 minutes following a successful magnetopause crossing identification mean that likelihood of detecting multiple crossings is reduced [*Case and Wild*, 2013].

The *Case and Wild* [2013] algorithm is used for all dayside crossings; however, *Raymer et al.* [2018 (In Prep)] found that the observed changes in the magnetic field are not as clear on the nightside as they are on the dayside. They have therefore produced a different algorithm that uses the plasma properties as well as the magnetic field data in order to better identify crossings, in this region. Similarly to *Case and Wild* [2013], two 3-minute windows separated by a gap are used to evaluate whether the spacecraft has left the magnetosphere. The *Raymer et al.* [2018 (In Prep)] algorithm detects a magnetospheric crossing if the average X_{GSM} plasma velocity in the magnetosphere is greater than -100 kms^{-1} and less than -100 kms^{-1} in the magnetosheath and that the difference between the two is more than 100 kms^{-1}. The magnetospheric plasma must also have an average density of less than 3 cm^{-3}, while the average plasma density of the magnetosheath window must be greater than 1 cm^{-3}. Finally, the standard deviation of the total magnetic field strength in the magnetosheath must greater than that in the magnetosphere. Only if all of these criteria are met will a magnetopause crossing be detected.

Using both of the above algorithms the magnetopause crossings for each spacecraft were detected. This defined the magnetosphere but included the lobe region of open magnetic field. Using the definition of the lobe plasma beta given by *Boakes et al.* [2014] it is possible to remove the data taken from within the lobes. This is done by setting a maximum threshold on the plasma beta as calculated from ratio of plasma pressure ($P = nkT$) to magnetic pressure (Equation 92).

$$\beta = \frac{P}{B^2/2\mu_0} \tag{92}$$

These values were determined from the Cluster measurements of the plasma number density (*n*) the plasma temperature (*T*) and the magnetic field strength (*B*). Once the plasma beta had been calculated the times when the spacecraft were in the lobes were removed from the times the spacecraft were in the magnetosphere. This left the times when the spacecraft were inside the magnetosphere and not in the lobes, or in other words the times when the spacecraft were on closed field lines.

Where pitch-angle distributions are known (particle fluxes) the data is split into trapped and precipitating populations. The loss cone angle is estimated from the ratio of the magnetic field strength at the position of the spacecraft, as measured by the spacecraft, and the magnetic field strength at the location of the field line footprints (both north and south, as determined by the magnetic field model), given by equation 93.

$$\alpha = \sin^{-1} \sqrt{\frac{B}{B_{max}}} \qquad (93)$$

"Precipitating" particle flux is defined as the flux in the pitch-angle bins including, and more field aligned than, the calculated loss cone angle. The "trapped" flux is thus the total flux in all of the remaining pitch-angle bins. The "precipitating" flux values are subsequently plotted at the location of the footprints in both hemispheres and the "trapped" flux is plotted at the location of the spacecraft in all three planes of GSM coordinates. For all parameters where pitch-angle distributions are not known the data plotted at the footprints is the same as the data plotted in the GSM planes.

[6.3]   Ion flux changes

In the previous chapter, the type of storm, as defined by the change in geosynchronous electron flux in the energy range between 1.8 and 3.5 MeV, was used as a differentiator for the different events. It was found that there is prolonged substorm activity in the recovery and post-storm phases when there is continuing favourable IMF orientation. If this is the case, ions as well as electrons should continue to be injected from the tail and therefore there should be a similar change in the ion fluxes for flux increase, flux decrease and constant flux storms.

Using the CODIF detector on the CIS instrument on board the Cluster spacecraft it is possible to separate the flux of ions by species. This was done and the average flux from multiple orbits from all four spacecraft were collated to produce a global picture of the trapped particle fluxes within the magnetosphere. Particles that fell into the field aligned pitch angle bins for the detector were plotted at the footprint of the trapped field lines to indicate the precipitation of the particles. It was then possible to bin the measured values by the type and phase of the storm, as well as the energy of the ions themselves. Figure 65 to Figure 67 show the flux of hydrogen, helium and oxygen in the 10 to 40 keV energy range. As can be seen from these figures there is a ring of high flux, more distinct on the duskside, between 3 and $6R_E$, shown in the xy-plane. This corresponds to the location of the radiation belts and ring current, although they can exist outside this region.
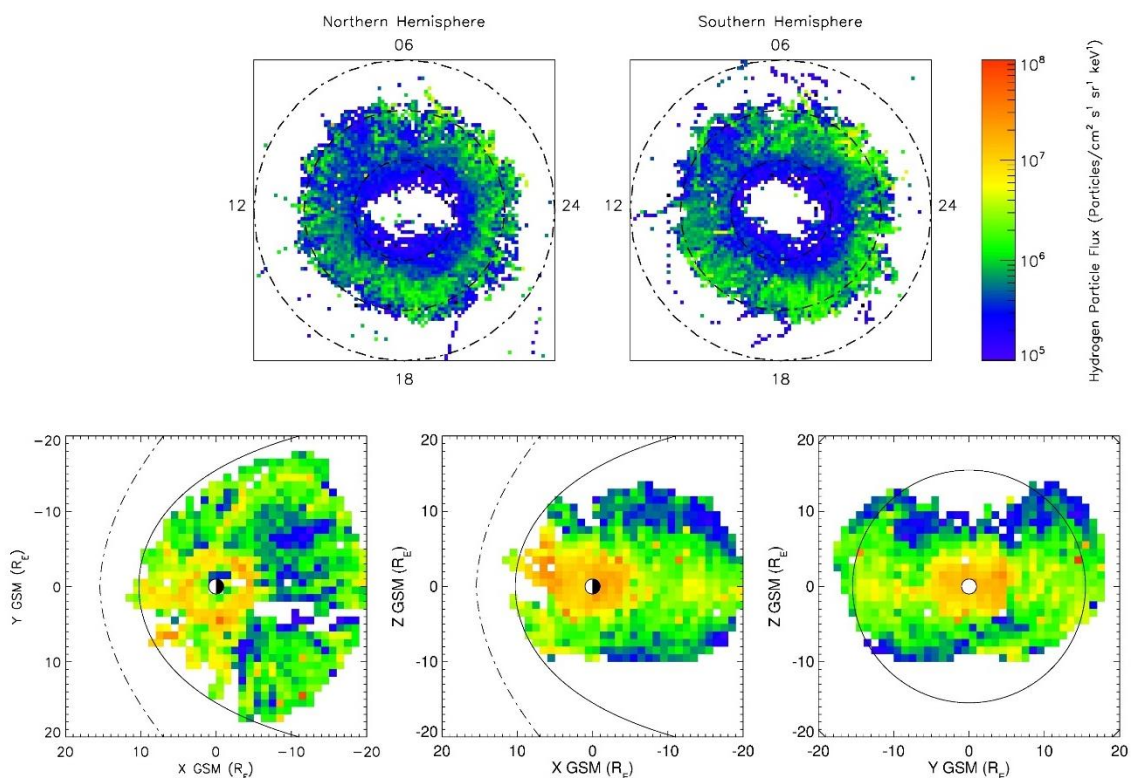
Figure 65: The distribution of precipitating (top) in both the northern and southern hemispheres and trapped (bottom) in the XY-, XZ- and YZ-GSM planes for the 10-40keV Hydrogen ions for all storm types and phases. Dashed rings on the top plots indicate successive 15 degrees of magnetic latitude. Solid line on the bottom plots indicate the Shue model magnetopause boundary and the dashed line indicates the bow shock.
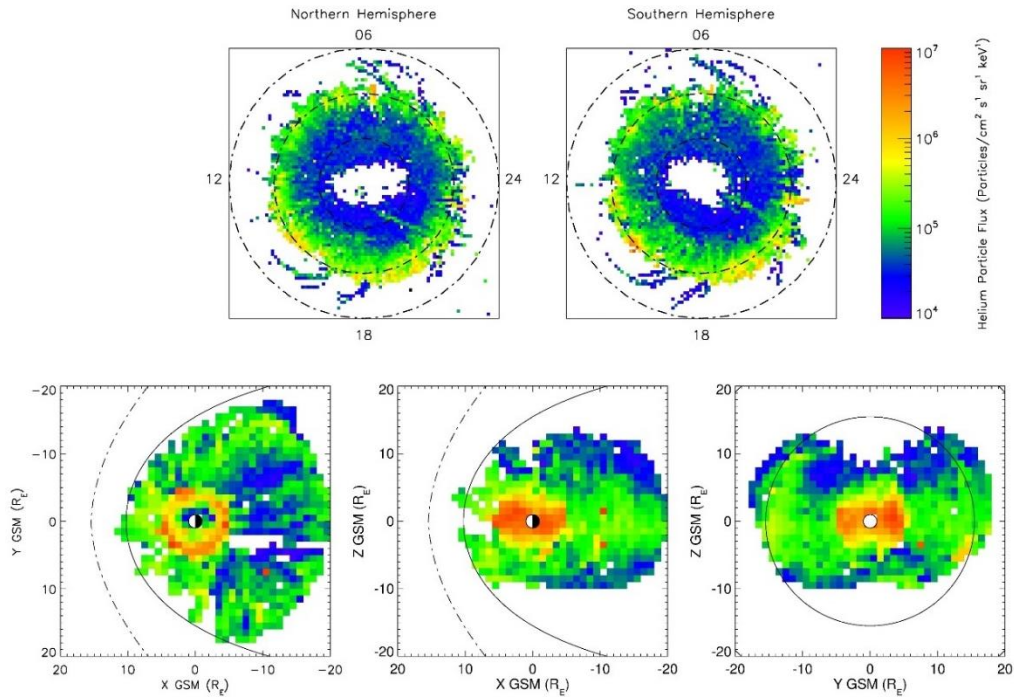
Figure 66: The distribution of precipitating (top) in both the northern and southern hemispheres and trapped (bottom) in the XY-, XZ- and YZ-GSM planes for the 10-40keV helium ions for all storm types and phases. Dashed rings on the top plots indicate successive 15 degrees of magnetic latitude. Solid line on the bottom plots indicate the Shue model magnetopause boundary and the dashed line indicates the bow shock.
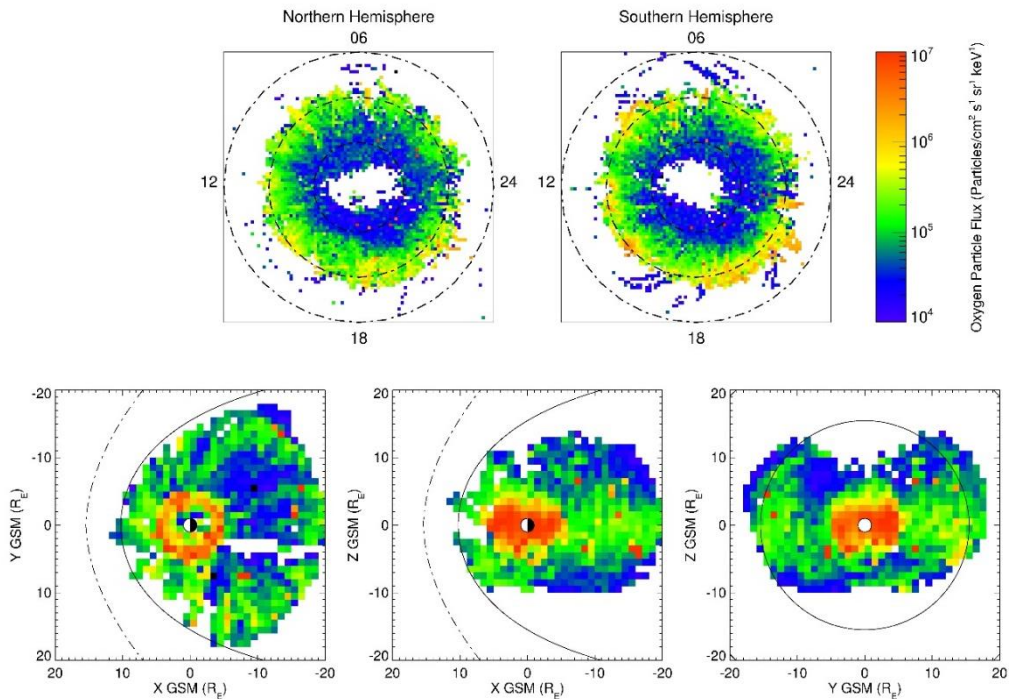
Figure 67: The distribution of precipitating (top) in both the northern and southern hemispheres and trapped (bottom) in the XY-, XZ- and YZ-GSM planes for the 10-40keV oxygen ions for all storm types and phases. Dashed rings on the top plots indicate successive 15 degrees of magnetic latitude. Solid line on the bottom plots indicate the Shue model magnetopause boundary and the dashed line indicates the bow shock.

Both Figure 68 and Figure 69 show the difference between the flux of ring current Hydrogen for flux increase and flux decrease storms respectively as defined by the change in electron flux as outlined in the previous chapter. As *Reeves et al.* [2003] observed flux increase storms happen approximately 50% of the time with the other two types, typically occurring around 25% of the time each. The spatial coverage for each type of storm therefore varies (as can be seen below). Additionally, the phases of the storms are of different lengths with the initial and main phases often not lasting for more than a few hours. The decision was thus taken to combine the measurements for both the initial and main phases to increase coverage. Physically this is appropriate as both phases occur during the driving of the magnetosphere on the dayside, following the arrival of either a CME or CIR. The difference between the two is that the ring current does not become enriched until the main phase, at which point there has been sufficient magnetic flux opened and transported to the tail that nightside reconnection begins. Unfortunately, even combining these two phases the data density (see Appendix) becomes small, once caveats and bad data have been removed, especially for flux decrease storms.

Figure 68 shows the difference between the flux of 10 – 40 keV hydrogen ions within the ring current region over the duration of a storm (i.e. post-storm minus pre-storm). The ring current region was defined as the region in space that exists between 3 and 6 R_E radially and ±4 R_E in the Z axis. A red region in Figure 68 shows a region in which the post-storm flux is greater than the pre-storm flux and a blue region shows the opposite. As can clearly be seen, especially in the xz and yz plane projections, there appears to be a distinct increase in flux from pre-storm to post-storm. Figure 69 shows the change in flux from pre- to post-storm for the flux decrease storms. As can be seen, there are more regions of flux decrease for flux decrease storms than for flux increase storms, as expected. There are regions of both flux increase and flux decrease for both Figure 68 and Figure 69, which indicates that although on average the ion fluxes may follow a similar pattern to the variations in relativistic electron flux, as defined by *Reeves et al.* [2003], locally dropout or enhancements can occur in either type of storm. This may indicate the presence of certain wave modes which could accelerate or scatter the ring current ions.
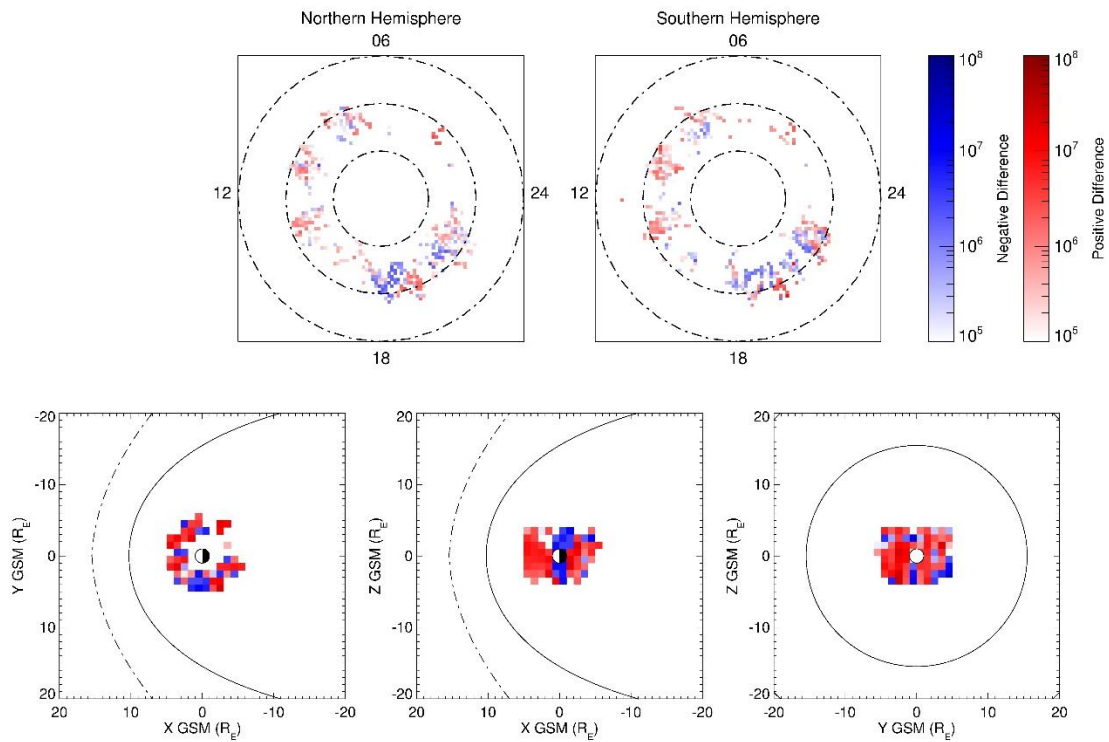
Figure 68: The difference in the distribution of precipitating (top) and trapped (bottom) 10-40 keV Hydrogen ions between pre- and post-storm periods for flux increase storms. Red regions indicate a flux increase whist blue regions indicate a flux decrease over the duration of a storm.
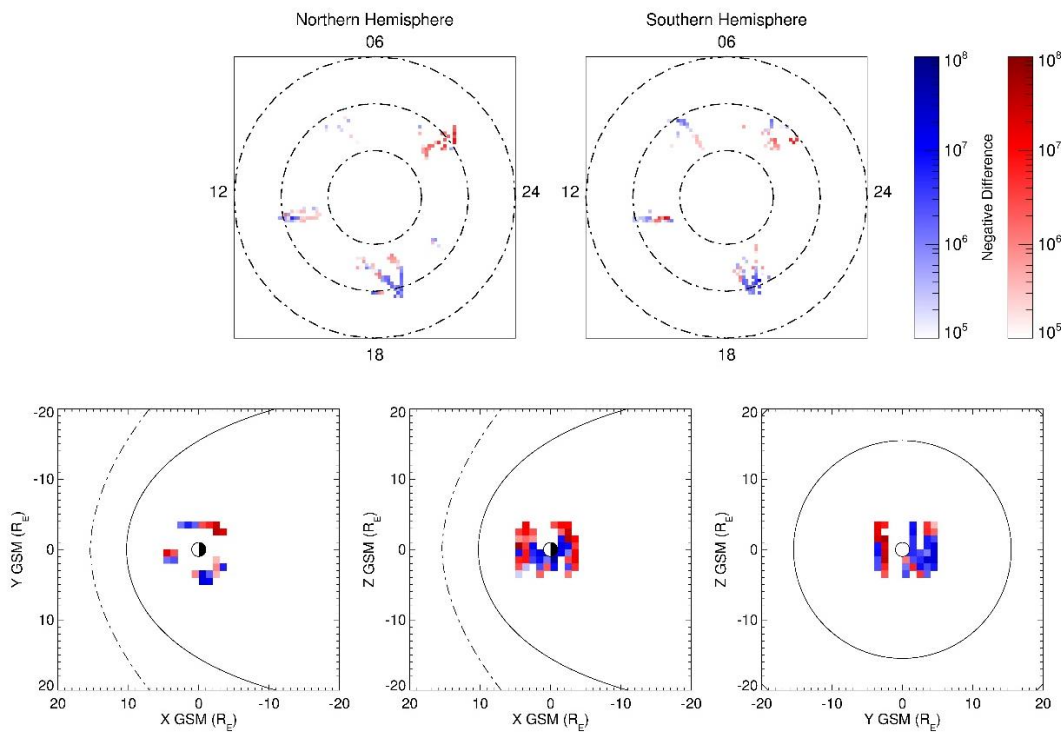
Figure 69: The difference in the distribution of precipitating (top) and trapped (bottom) 10-40 keV Hydrogen ions between pre- and post-storm periods for flux decrease storms. Red regions indicate a flux increase whist blue regions indicate a flux decrease over the duration of a storm

The ring current region was defined as the region in space that exists between 3 and $6R_E$ radially and $\pm 4R_E$ in the Z axis. The average flux for this was taken from this region for each phase of each type of storm in order to observe the average change in its value over the storm duration for each of the different ion species measurable by the CODIF detector. Figure 70 shows the results of this analysis.

As can be seen from Figure 70 the change in ion flux shows a similar trend to that of the electron flux change, albeit not as dramatically. The large dropout during the initial and main phase of the flux decrease storms is most likely due to the lack of data points during these phase which is most pronounced for flux decrease storms. The similarities between the change in hydrogen and helium flux over the duration of the storm with that of the change in electron flux are clearly observed. Flux increase storms, as defined by the change in electron flux, tend to show an increase of greater than a factor of 2 for all three ion populations shown. Constant flux storms, in which the electron flux remain within a factor of 2 from pre- to post-storm, also show that this is observed for the ion populations. Finally, flux decrease storms also show a decrease in the flux of all three major ion populations similar to that of the electron flux, as expected.

Oxygen ions of this energy have been shown to dominate the ring current during the main phase and early recovery phase due to injection from the plasma sheet following substorm driven ion outflows. For all types of storm, the flux of Oxygen ions is similar to that of the Hydrogen ions during the recovery phase before dropping off for flux decrease storms during the post storm period. This may support the hypothesis of Chapter 5 as continued injection of particles via substorms could lead to the continued outflow of Oxygen ions from the ionosphere, thus causing the observed increase into the post-storm period for flux increase storms.
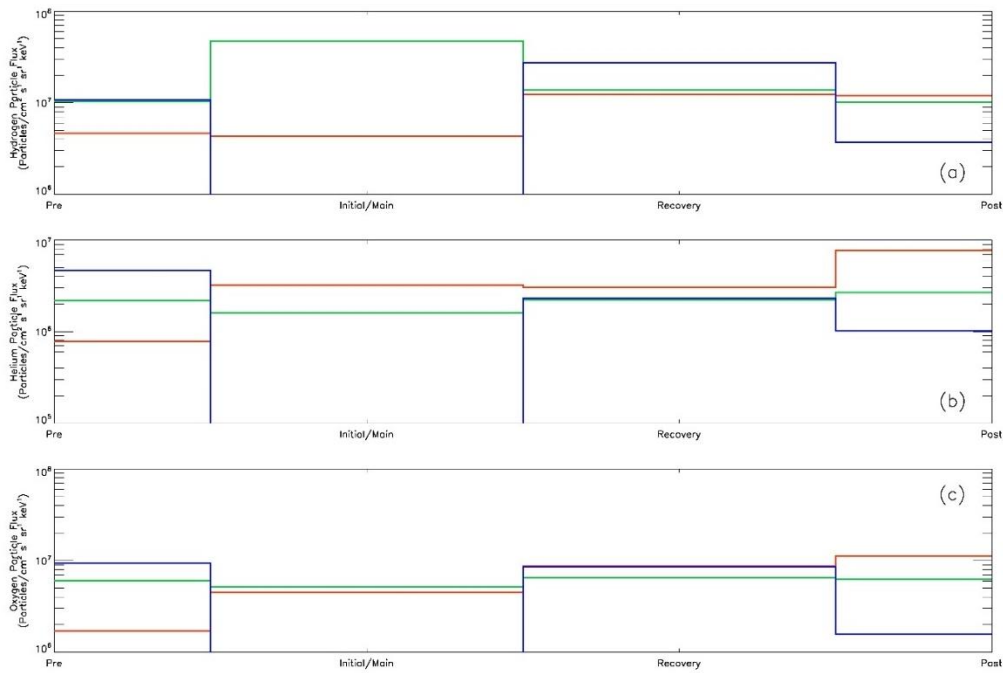
Figure 70: Change in average 10 – 40 keV ion fluxes within the ring current region for (a) Hydrogen, (b) Helium, and (c) Oxygen Ions over for storms between 2001 and 2011, broken down by storm phase and type of storm. Flux increase storms are shown in red, decrease in blue and constant flux storms in green.

[6.4]   Electron flux changes

The above analysis was also run on the electron flux as measured by the PEACE instrument on board the Cluster spacecraft for multiple energy levels. Figure 71 shows the result of this analysis. The low energy fluxes don't show the same flux change as the relativistic (>1MeV) fluxes (Figure 52), however as the energy increases the characteristic increase, decrease and no change become apparent. The higher energy electrons (Figure 71, plot (c)) are of a similar energy to seed electrons which, after injection via substorms, have the potential to drive the mechanisms required for the acceleration of electrons to relativistic energies [*Friedel et al.*, 2002]. The depletion in these electrons for flux increase storms between the recovery phase and post-storm period could be due to the mechanisms outlined by *Friedel et al.* [2002] and the acceleration of these electrons to higher energies. These mechanisms include the excitation of plasma waves including EMIC waves as well as whistler mode chorus and hiss, which are the specific modes of interest and are known to be excited during periods of enhanced geomagnetic activity [e.g. *Meredith et al.*, 2003b; *Meredith et al.*, 2003c; *Meredith et al.*, 2004; *Shprits et al.*, 2008; *Meredith et al.*, 2009].
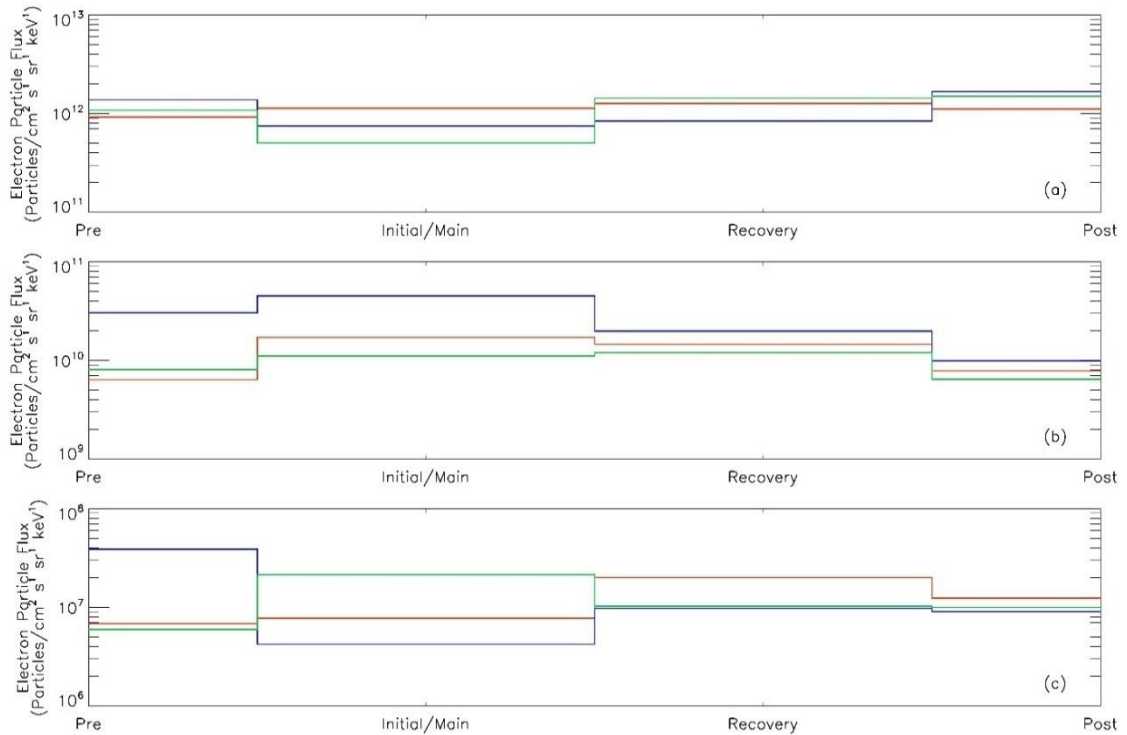
Figure 71: The evolution of the electron flux for (a) low energy (1 eV – 2 keV), (b) medium energy (2 – 10 keV) and (c) high energy (10 keV – 30 keV) for flux increase (red), decrease (blue) and constant flux (green) storms.

[6.5]   Wave mode occurrence

Figure 64 shows the theoretical distribution of the wave modes for geomagnetically active time periods. Using the wave power as measured by the STAFF instrument on board the Cluster spacecraft the theoretical distribution can be compared to direct observations.

[6.5.1] Chorus Waves

Whistler mode chorus waves are preferentially excited in the low density regions, outside the plasmasphere, of the dawnside magnetosphere via the injection of plasma sheet electrons during storm times [e.g. *Goldstein and Tsurutani*, 1984; *Miyoshi et al.*, 2003; *Santolik et al.*, 2003]. Gyro-resonant wave-particle interactions with these waves is thought to be an important mechanism for the acceleration of electrons to relativistic energies [e.g. *Horne et al.*, 2005; *Meredith et al.*, 2012; *Li et al.*, 2014].

It may therefore follow that flux increase storms which show both an increase in the relativistic electron fluxes as well as the plasma sheet electron fluxes should show more intense and widespread chorus emissions than flux decrease storms. However, chorus emissions have been linked to both acceleration, via stochastic energy diffusion [e.g. *Horne and Thorne*, 1998; *Summers et al.*, 1998; *Summers and Ma*, 2000a] and loss, via microburst precipitation [e.g. *Lorentzen et al.*, 2001; *O'Brien et al.*, 2004; *Thorne et al.*, 2005b]. Thus the opposite may be observed with more intense chorus emissions, and hence precipitation of relativistic electrons, observed during flux decrease storms. The figures below take the total power across this frequency range for every minute of each event. Once this is completed the relevant time periods are selected allowing for the separation of storm phases. These minutes are then binned in 1 R_E square bins and averaged based on the spacecraft position in each plane of the GSM co-ordinate system (XY shown).

[6.5.1.1]   Lower Band

Lower band chorus emissions exist in the frequency band between 0.2 and 0.5 f_{ce} peaking around 0.34f_{ce} [e.g. *Burtis and Helliwell*, 1976; *Santolik et al.*, 2004]. Figure 72 shows the location of the lower band chorus wave power as viewed in the GSM X-Y plane, for all of the identified storms across the full storm duration, including the pre and post-storm periods. Theoretically, both lower and upper band chorus emissions should occur in the lower density regions outside the plasmasphere, with lower band chorus most able to resonate with relativistic electrons [*Meredith et al.*, 2003b].

As Figure 72 shows the location of the more intense lower band chorus emissions is consistent with the theory and previous observations occurring predominantly in the outer magnetosphere on the dawn-side. The main difference between the model shown by *Shprits et al.* [2008], Figure 64, and the observation, Figure 72, is that the chorus emissions extend further into the dusk-side, although the intensity of the waves in this region is lower than on the dawn-side.

Meredith et al. [2003b] observed that the most intense chorus waves were located between 0300 and 1000 MLT in the equatorial plane and between 0600 and 1400 at mid-latitudes. Lower intensity chorus waves were also observed on the dusk-side between 1500 and 2100. Figure 72 shows this same pattern to the observations although due to the nature of the Cluster orbit it spends very little time in low latitude regions so it is not possible to say, from this figure, that the wave power observed between 0300 and 0600 is confined to the equatorial plane. However, the equivalent plot of the normalised wave power in the XZ plane (not shown) shows that for negative values of X_{GSM} the high intensity wave power is confined to ± 5 R_E in the Z axis whereas for positive values of X_{GSM} the peak intensities are closer to 10 R_E Z_{GSM}. As the wave intensity is much lower for negative values of X_{GSM} on the duskside it is likely that the peak in chorus emission near the equator in the XZ plane originates from the emission between 0300 and 0600 shown in Figure 72.
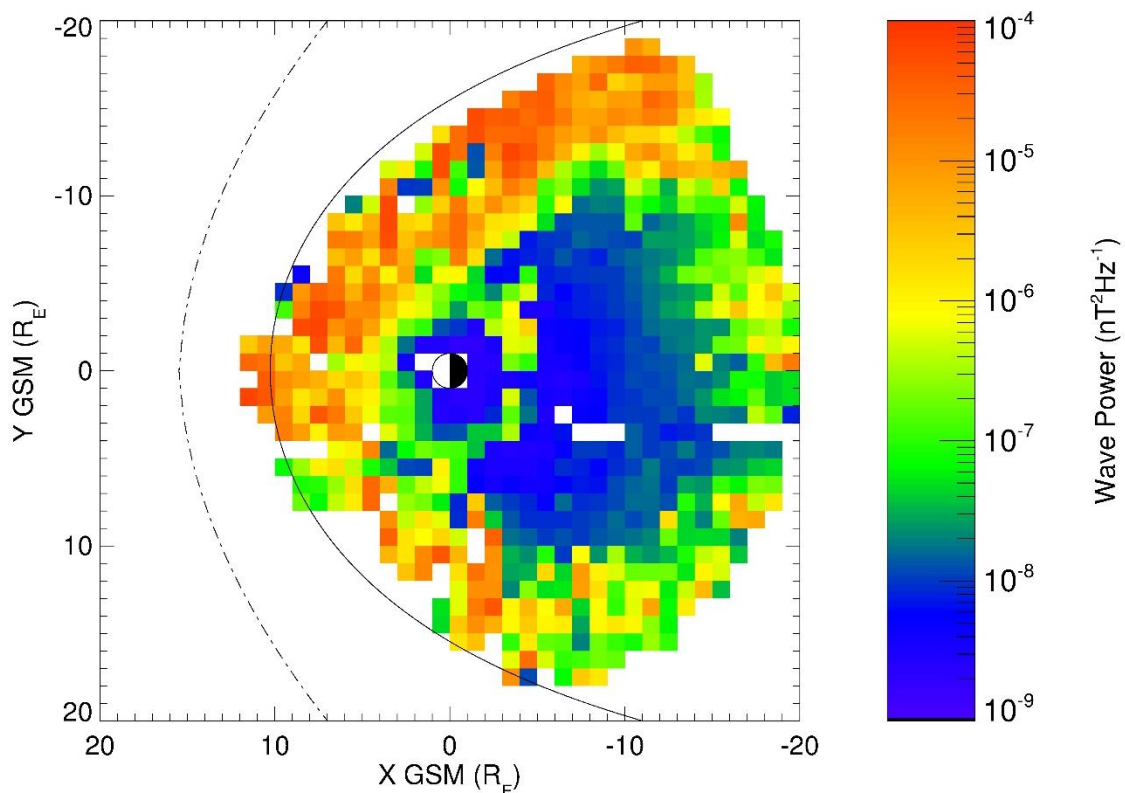
Figure 72: Location of lower band chorus emission as plotted by wave power for all identified storms across all of the storm phases shown for the XY-GSM plane.

Wave-particle interactions with chorus waves can accelerate seed electrons, which are provided by enhanced convection electric fields, up to relativistic energies [e.g. *Summers et al.*, 1998]. Therefore, it may follow that there would be more intense and widespread chorus emission during the recovery phase and post-storm period for flux increase storms than for flux decrease storms. Figure 73 shows the evolution of lower band chorus waves over the storm duration when compared between flux increase, flux decrease and constant flux storms. The most obvious point to make is that the data density is much lower for flux decrease and constant flux storms when compared to flux increase storms. This, however, is unsurprising due to flux increase storms being more common (~50% of all storms) than the other two (~25% each) [*Reeves et al.,* 2003]. In addition, as previously mentioned, the initial and main phases are much shorter than the pre-storm, recovery phase and post-storm periods. This duration is also short when compared to the Cluster spacecraft orbital period. When these factors are combined the data becomes extremly sparse for the initial and main phase for constant flux and flux decrease storms. Despite this there are still some interesting features to discuss.

The first point is that there is significant chorus intensity in all phases and all types of storm with the intensity of the lower band chorus waves apparently greater during flux increase storms than the other types for all phases. This can clearly be seen in Figure 74 when comparing the wave intensity between flux increase and flux decrease storms. This difference plot can only be completed for regions in which there are data for both types of storm and so needs to be evaluated in conjunction with Figure 73. For all phases Figure 74 shows that there is generally greater wave power during flux increase than flux decrease storms, during all phases, especially at lower radial distances. This is surprising as generally both the seed electron flux Figure 71 and the relativistic electron flux Figure 52 is lower during the pre-storm phase for flux increase storms than for both flux decrease and constant flux storms. Lower band chorus can gain energy from lower energy electrons near the loss cone. This would reduce the amount of seed electrons and increase the intensity of chorus waves, however, this would also likely cause a higher flux of relativistic electrons, which is not observed.

Figure 73 also shows that the intensity and spatial extent of lower band chorus waves is greater during the initial, main and recovery phases than the pre- and post-storm periods. The initial and main phase plots are extremely sparse for flux decrease and constant flux storms. For flux increase storms, however, the chorus wave intensities are high much closer to the Earth than for other phases potentially indicating the presence of a greater flux of seed electrons injected into the inner magnetosphere via substorms. Without a comparison with the other types of storm during these phases this cannot be said for sure.

Figure 74 shows that there is more intense wave activity during flux increase storms during the post storm phase in the inner magnetosphere, near geosynchronous orbit which could explain the increase in relativistic electron flux. Greater wave intensity could lead to the acceleration of the seed electrons to relativistic energies during the post storm period thus produce the observed variations.

During the recovery phase there is a reduction in the chorus wave intensity, when compared to the initial and main phase in the inner magnetosphere on the dawnside for flux increase storms. This could be due to the expansion of the plasmasphere during this phase and the removal of favourable conditions for the acceleration in the inner magnetosphere. This trend continues during the post-storm with the wave intensities at even greater radial distances. The location of the intense lower band chorus wave power increases in MLT coverage reaching further into the duskside from the pre-storm period through to the post-storm period. All of the observed data plotted in Figure 73 are on closed field lines and as such the trapped population of seed electrons may have drifted round to the duskside and exist in sufficient densities to cause the excitation of lower band chorus waves in this region of the magnetosphere.
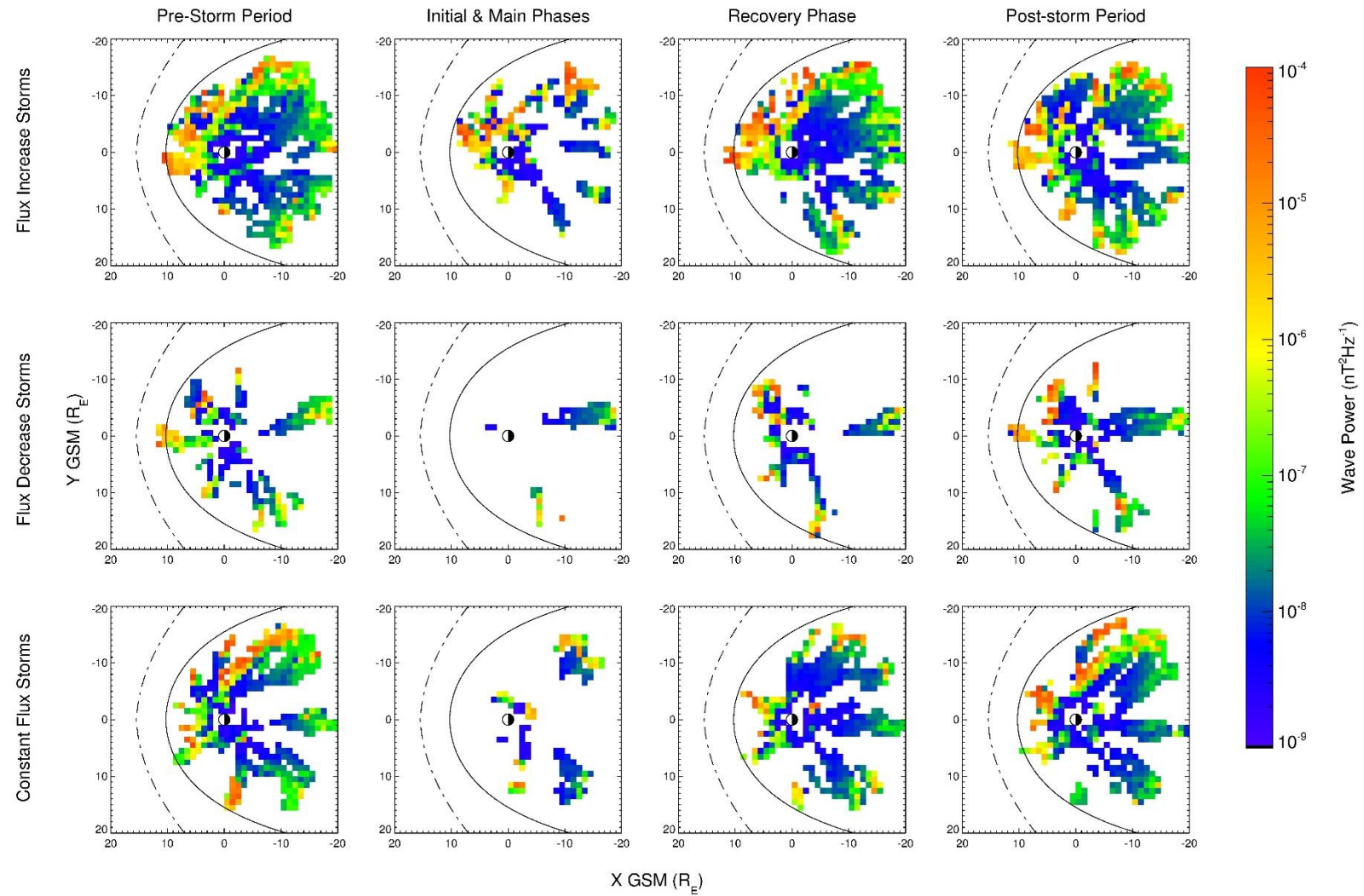
Figure 73: Location of lower band chorus emission as plotted by wave power broken down by the phase of the storm and the type of storm shown for the XY-GSM plane.
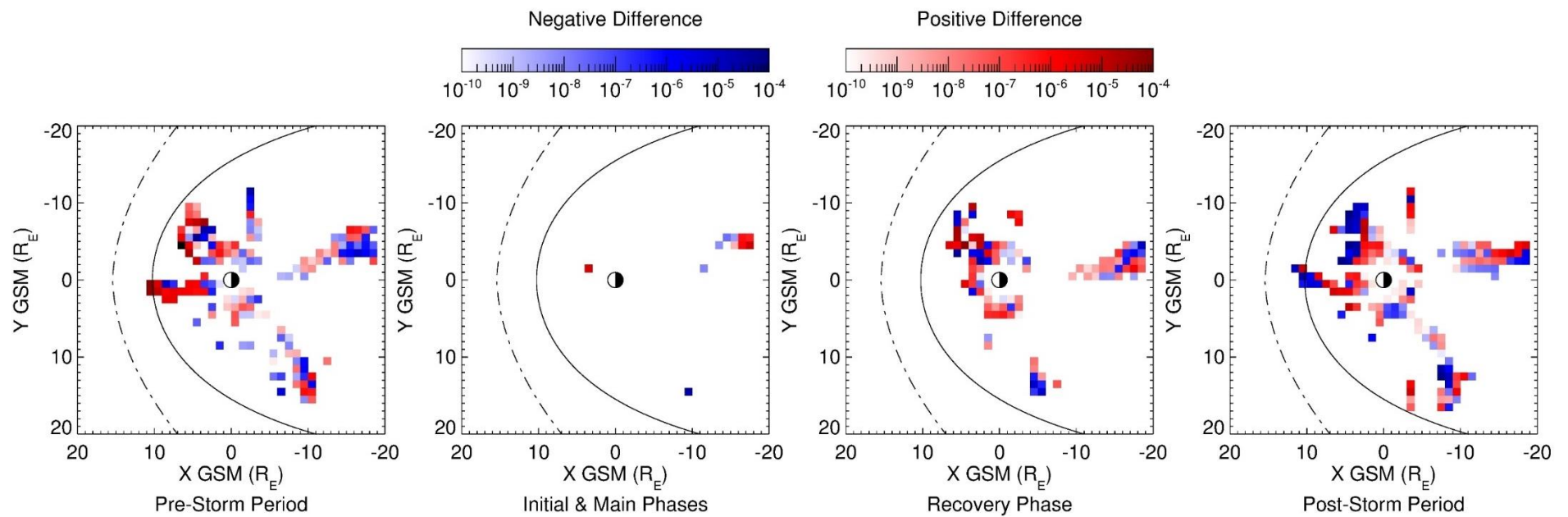
Figure 74: Difference in lower band chorus wave power between flux increase and flux decrease storms broken down by storm phase. Red regions indicate greater wave power during flux increase events and blue regions indicate greater wave power during flux decrease events.

[6.5.1.2]   Upper Band

Upper band chorus waves exist in the frequency band between $0.5f_{ce}$ and $0.8f_{ce}$ peaking around $0.53f_{ce}$ [e.g. *Burtis and Helliwell*, 1976; *Santolik et al.,* 2004]. Although upper band chorus waves are generally less intense and less able to interact with the electrons they can still cause significant electron acceleration and loss [e.g. *Lorentzen et al.,* 2001; *Summers et al.,* 2002; *Meredith et al.,* 2003b]. Figure 75 shows the spatial extent of upper band chorus mode waves and clearly shows a similar spatial coverage to lower band chorus mode waves. This is unsurprising as the mechanisms for their generation require the same population of electrons. Similarly to the lower band chorus emission, the wave power observed between 0300 and 0600 is confined to the equatorial plane with the emission post-dawn peaking at higher latitudes. The main difference between the upper and lower band chorus mode is the reduced intensity, typically an order of magnitude lower, with much fewer high intensity points. This is consistent with previous findings that upper band chorus is generally less intense than lower band chorus.

Figure 76 shows the breakdown of the location of upper band chorus based on type and phase of storm. Again the distribution is similar to that of the lower band chorus with fewer high intensity points. Flux increase storms again show the strongest chorus emission for each of the phases, although the difference between the flux increase and flux decrease storms (Figure 77) is less pronounced than for lower band chorus waves. There is a similar progression for the location from the initial and main phase through to the post-storm period. The more intense emission is located closer to Earth during the initial and main phase before moving out towards the magnetosphere and round towards the duskside. This suggests that the conditions for the generation of chorus waves becomes less favourable in the inner magnetosphere as the system recovers following the main phase of a storm. This could be due to the refilling of the plasmasphere and the increase in the electron density.

The observed local time dependence of both upper and lower whistler mode chorus waves (Figure 72 and Figure 75) is consistent with a first order cyclotron resonant generation mechanism with plasma sheet electrons, near the loss cone [*Horne and Thorne*, 2003], that are injected into the inner magnetosphere, where they subsequently gradient curvature drift through dawn towards the dayside. Diffusion of these electrons into the loss cone can provide the free energy for wave growth.
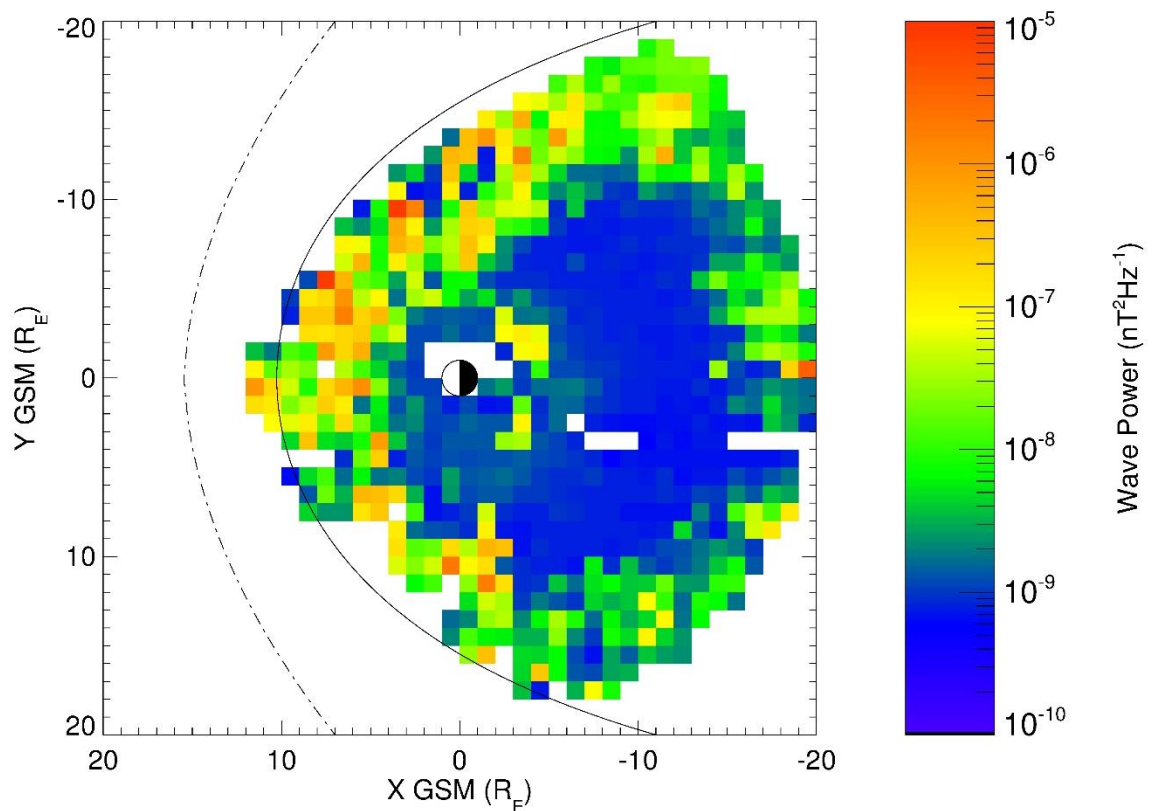
Figure 75: Location of upper band chorus emission as plotted by wave power for all identified storms across all of the storm phases shown for the XY-GSM plane.
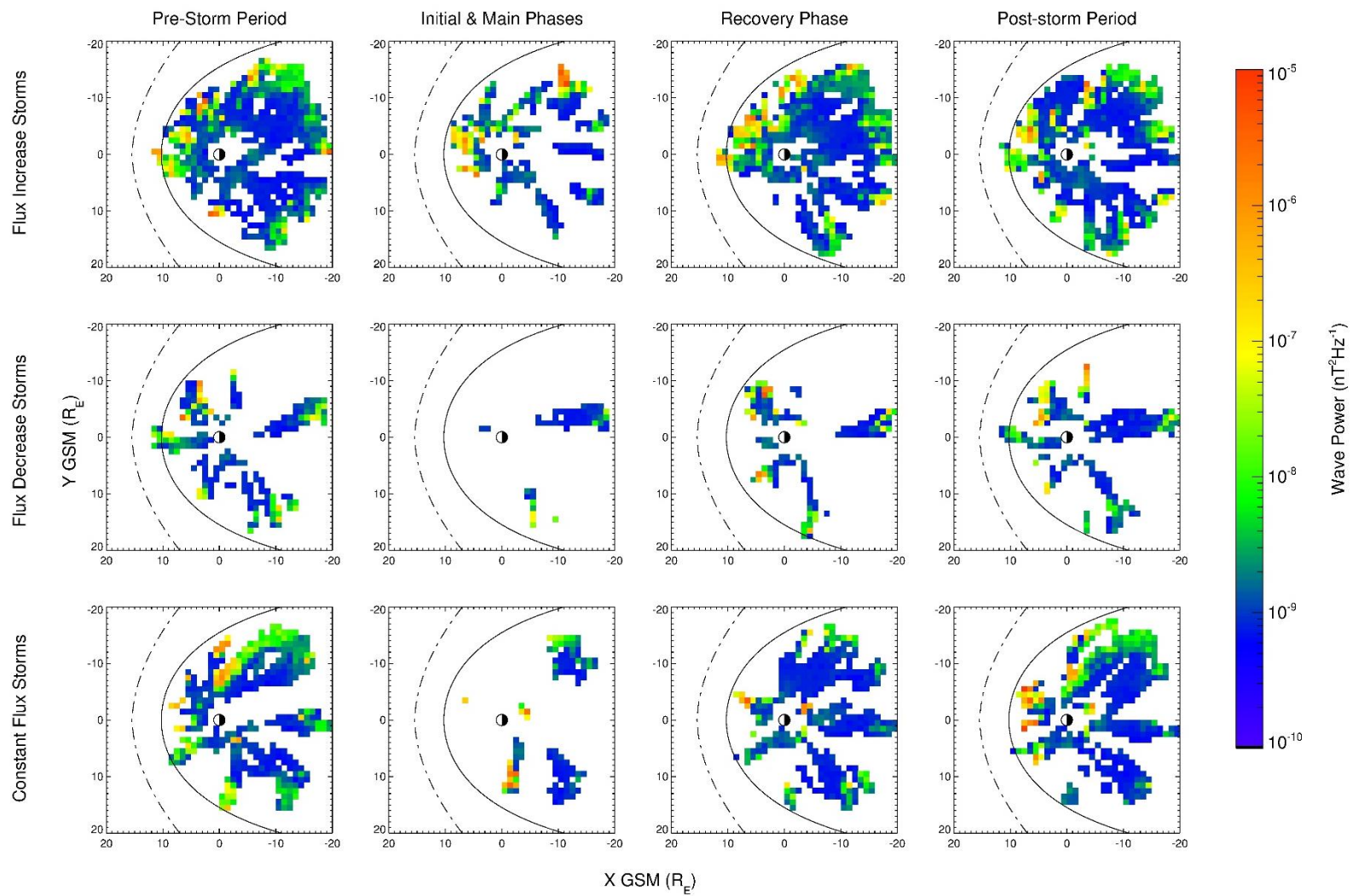
Figure 76: Location of upper band chorus emission as plotted by wave power broken down by the phase of the storm and the type of storm shown for the XY-GSM plane.
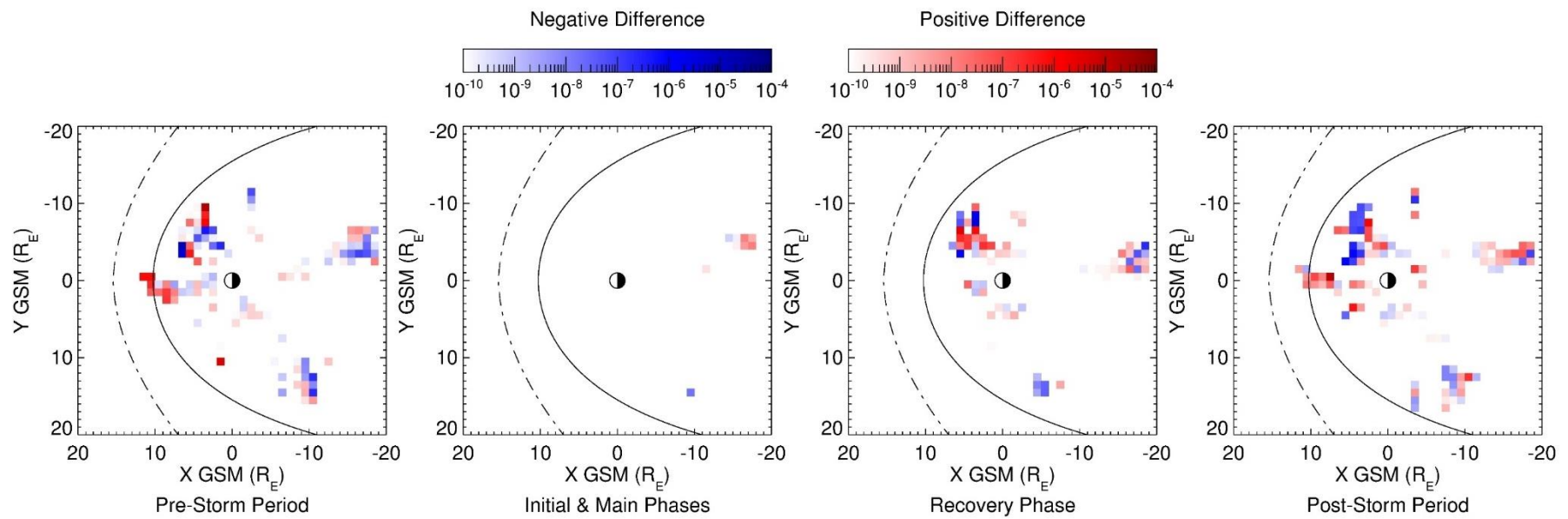
Figure 77: Difference in upper band chorus wave power between flux increase and flux decrease storms broken down by storm phase. Red regions indicate greater wave power during flux increase events and blue regions indicate greater wave power during flux decrease events.

[6.5.2] Hiss Waves

Whistler mode hiss waves, are confined to the high density regions such as the plasmasphere and dayside drainage plumes [e.g. *Thorne et al.*, 1973; *Meredith et al.*, 2004]. The source of hiss waves is thought to be just inside the plasmapause (L~4) and near the geomagnetic equator [*Muzzio and Angerami*, 1972]. These waves are often observed as broadband emission that have little to no structure, however, they can cause significant pitch-angle scattering of energetic electrons from the slot region [*Lyons and Thorne*, 1973; *Albert*, 1994; *Abel and Thorne*, 1998]. Hiss waves have shown to be efficient at redistributing high pitch angle electron distributions by causing significant pitch angle diffusion. It is thought that whistler mode hiss waves will dominate the loss processes inside the plasmasphere as it expands during the recovery phase causing a depletion of the relativistic electron flux due to the inability of chorus waves to accelerate electrons within the plasmasphere [*Meredith et al.*, 2006].

Figure 78 shows the location of the more intense emissions in the whistler mode hiss frequency band. As can be seen there is a ring of moderately intense emission centred on the Earth which most likely corresponds to the location of the plasmasphere. Interestingly, however, this is not the location of the most intense emission which is almost exclusively confined to the dayside from the outer plasmasphere to the magnetopause. The emissions also extend out towards dusk and dawn. Figure 79 shows the distribution of the electron density for all storms and all phases. The bottom left panel is the equivalent data projection as Figure 78. This shows that despite the extension of the intense emissions observed in Figure 78 it is almost perfectly aligned with the high density regions observed in Figure 79.
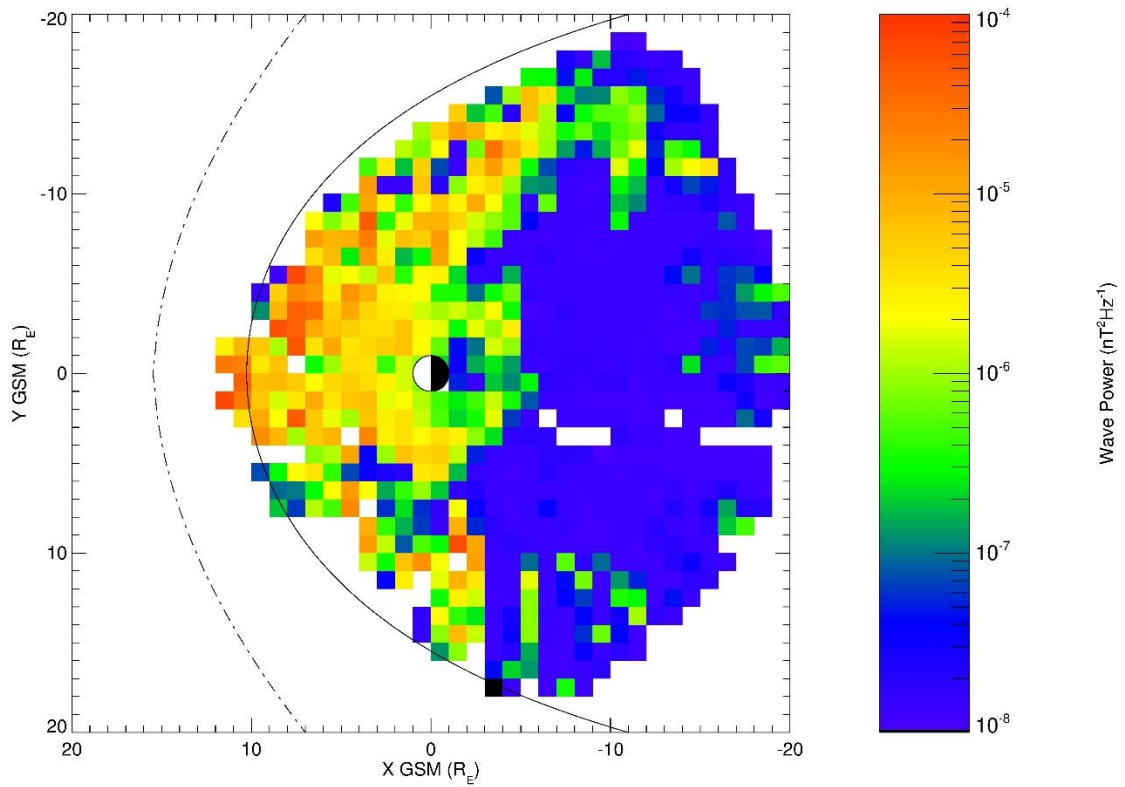
Figure 78: Location of whistler mode hiss emission as plotted by wave power for all identified storms across all of the storm phases shown for the XY-GSM plane.
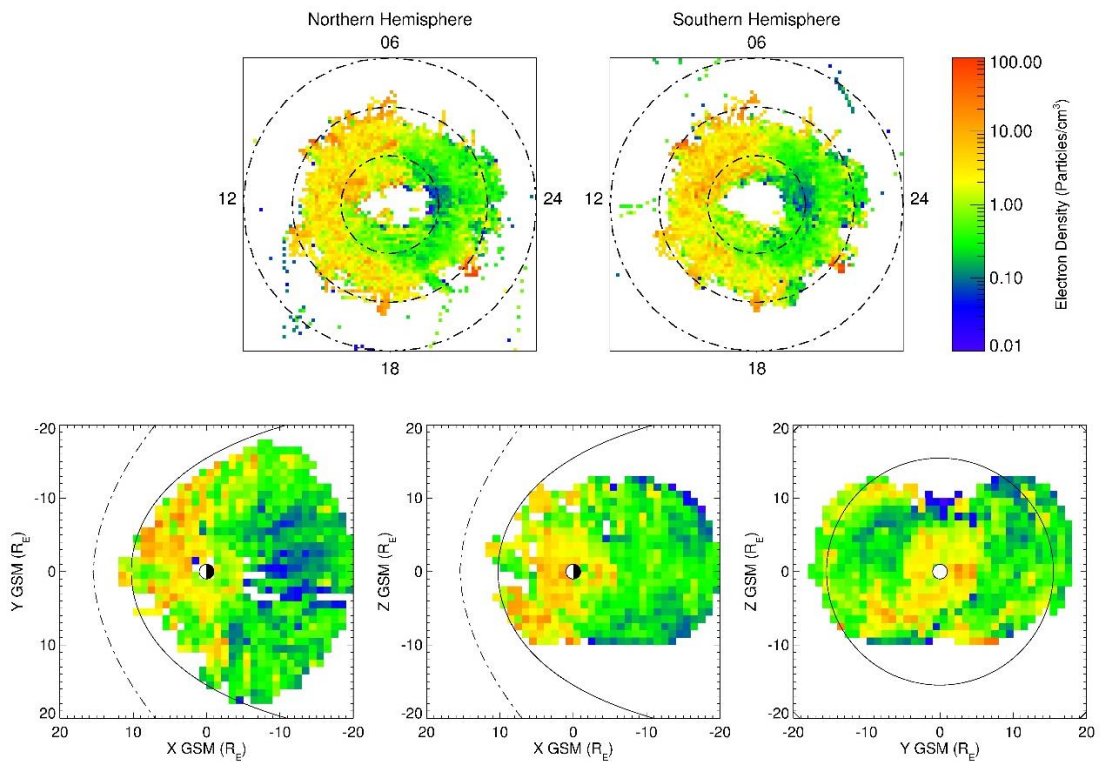
Figure 79: Distribution of the electron density, as measured by the PEACE instrument, plotted in the mapped co-ordinates for the Northern and Southern hemisphere (top) and the XY, XZ and YZ GSM planes (bottom) for all storm types and all phases

Figure 80 shows the location of the emissions in the whistler mode hiss frequency band broken down by the type and phase of the storm. Figure 64 shows that whistler mode hiss waves are confined to the inner magnetosphere during active periods before expanding out with the plasmasphere to cover a greater radial distance during more quiescent times. Figure 80 shows that the radial extent of the intense wave power in the whistler mode hiss frequency band is quite large for this time period stretching out to almost the magnetopause and again mirrors the location of the higher electron density regions for this period. During the more active period of the initial and main phase, for flux increase storms, the distribution of the intense whistler mode hiss waves has increased closer to the Earth and decreased at greater radial distances. The wave intensity then increases in the outer magnetosphere during the recovery phase for flux increase storms.

Wave power intensities appear to be the greatest during the recovery phase of flux increase storms. This is consistent with previous observations of the variations in hiss wave intensity with geomagnetic activity, which have suggested a cyclotron resonant generation mechanism fuelled by newly injected electrons [*Thorne et al.*, 1979; *Cornilleau-Wehrlin et al.*, 1993]. Chapter 5 showed that flux increase storms are more likely to occur when the IMF orientation remains favourable in the recovery phase and post-storm period. This is accompanied by extended periods of substorm activity during this time. This is likely to cause an increase in the injection of plasma sheet electrons during the recovery phase and into the post-storm period, as Figure 71(c) shows. It is therefore unsurprising to observe an increase in the wave power intensity across the whistler mode hiss frequency band for flux increase storms when compared to flux decrease and constant flux storms.

It might be expected that flux decrease storms would show more intense wave power in the pre-storm period as they have been shown to have a higher flux of electrons both at around 25keV (Figure 71(c)) and at relativistic energies (Figure 52, Section [5.4]) however this is not clearly observed in Figure 80.

This could be due to the lack of coverage due to the relatively few events compared to flux increase storms, however the points which correlate between the two types of storm show that the intensity of waves in the whistler mode hiss frequency band is at least of the same order if not slightly less intense suggesting that the high flux of electrons during the pre-storm period for flux decrease storms does not cause the same enhancements in wave power as is seen during the recovery phase of flux increase storms.

Hiss waves are thought to dominate the loss processes within the plasmasphere as it expands during the recovery phase causing a depletion of the relativistic electron flux due to the inability of chorus waves to accelerate electrons within the plasmasphere [*Meredith et al.*, 2006]. Figure 81 shows that the intensity of the wave power within the whistler mode hiss frequency band is lower during the recovery phase of flux decrease type storms than during the recovery phase of flux increase storms. This is indicated by the red regions of Figure 81 and is generally true of all of the storm phases not just the recovery phase.

As there is a lower flux of relativistic electrons during this period for flux decrease storms, low whistler mode hiss wave power intensity suggests that this is not due to an increase in loss via pitch-angle diffusion over flux increase storms. Rather it suggests that the acceleration mechanisms, which depend on the existence of the seed electrons [*Friedel et al.*, 2002], are less prevalent in the recovery phase of flux decrease storms in comparison to flux increase storms, as can be seen by the lower intensities in the whistler mode chorus wave powers for flux decrease storms in the recovery phase (Figure 73 & Figure 76). This would support the conclusion of Chapter 5, which suggests that flux increase storms occur when there is continued substorm activity, and hence injection of seed electrons into the inner magnetosphere, during the recovery phase.
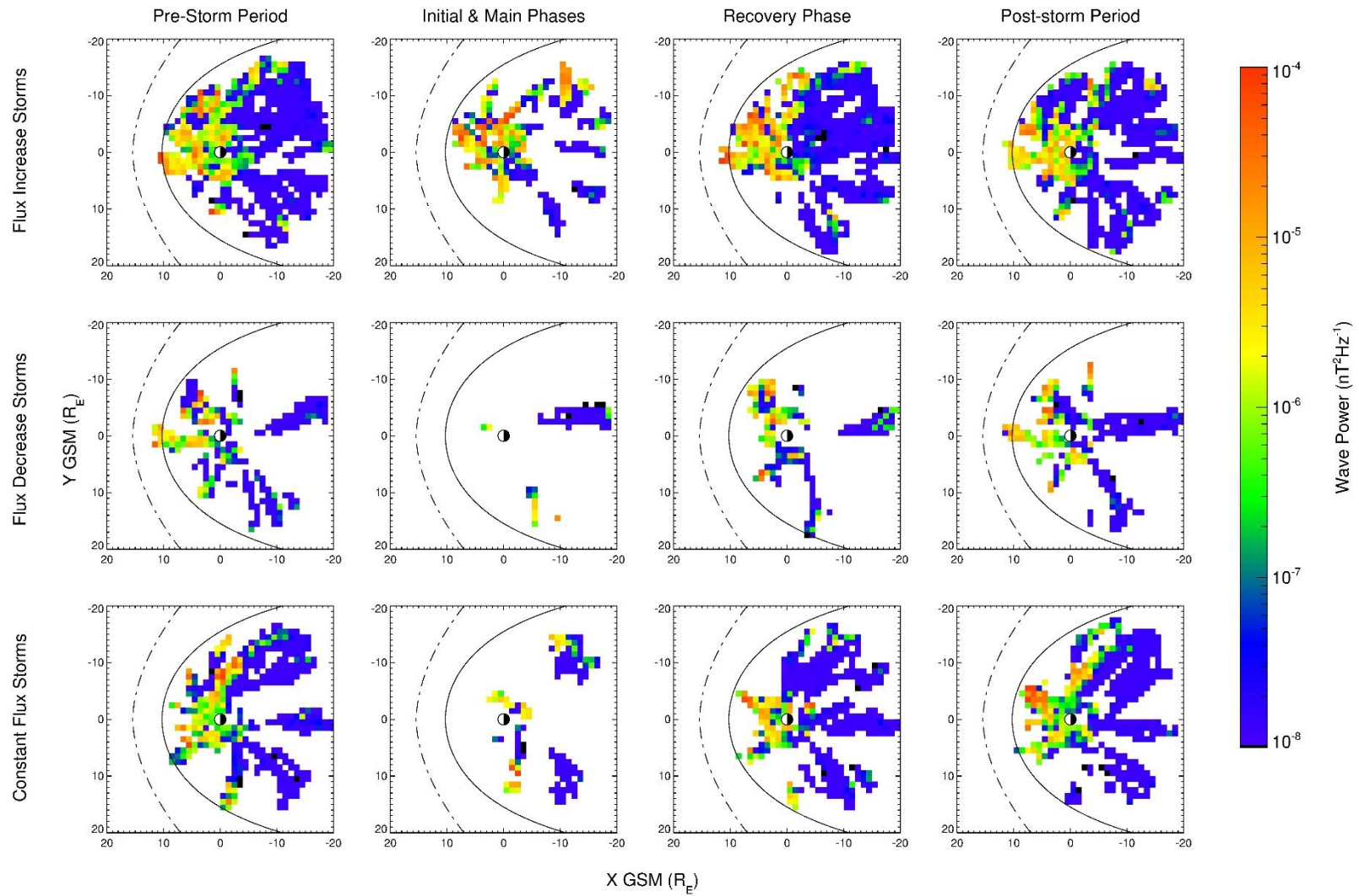
Figure 80: Location of whistler mode hiss emission as plotted by wave power broken down by the phase of the storm and the type of storm shown for the XY-GSM plane.
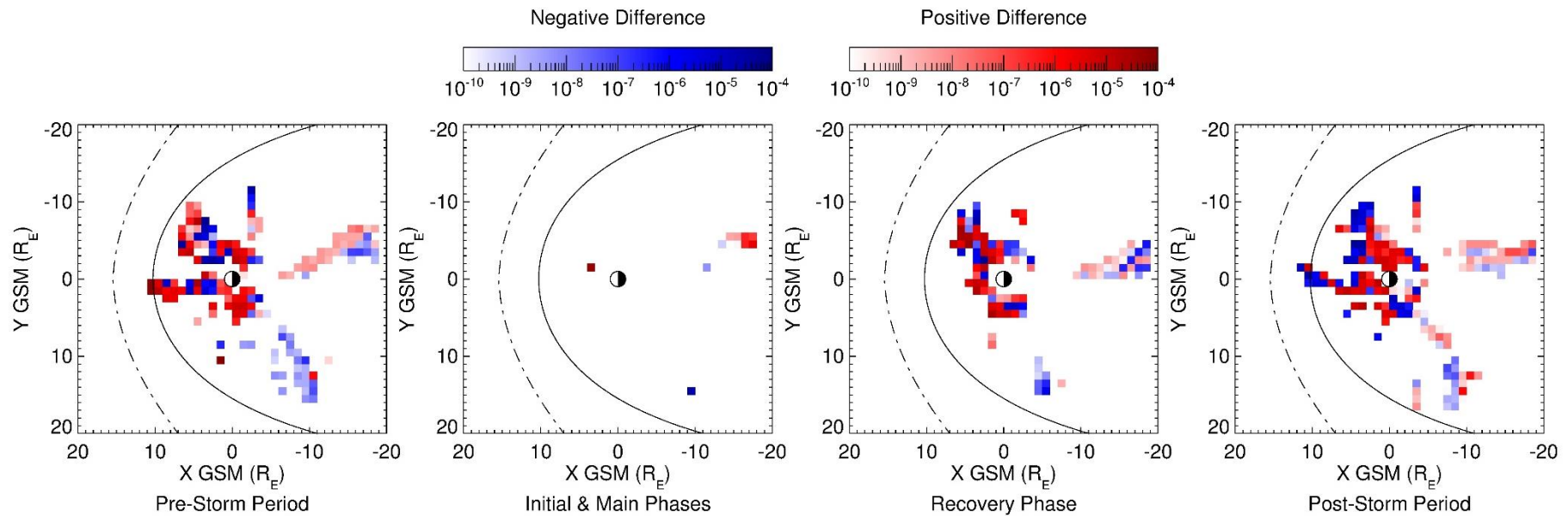
Figure 81: Difference in whistler mode hiss wave power between flux increase and flux decrease storms broken down by storm phase. Red regions indicate greater wave power during flux increase events and blue regions indicate greater wave power during flux decrease events.

[6.5.3] EMIC Waves

The generation of EMIC waves has previously been attributed to the temperature anisotropies in the ring current proton population [e.g. *Mauk and McPherron*, 1980; *Engebretson et al.*, 2007] in the high density regions of the magnetosphere such as the duskside plasmapause and dayside drainage plumes [e.g. *Thorne and Horne*, 1997; *Spasojević et al.*, 2003]. EMIC waves are most likely to occur during the recovery phase of storms when the plasmasphere expands and encounters the drift path of newly injected ions from the plasma sheet. It is this interaction between the higher energy ring current ions and the cold plasmaspheric ions that is thought to be key in the generation of EMIC waves as this can produce the required temperature anisotropies [*Horne and Thorne*, 1993; *Chen et al.*, 2009; *Halford et al.*, 2010]. *Cornwall et al.* [1970] suggested that during the recovery phase of storms EIMC waves should be able to interact with majority of the ion distribution, in the high density region just inside the plasmapause, as the phase velocity decreases. It has also been shown by *Horne and Thorne* [1993] that plasma density gradients, such as those observed at the plasmapause, can counteract the refraction of EMIC waves due to the magnetic field thus allowing their growth. EMIC waves may scatter ring current ions more effectively than collisional loss processes and can cause up to an additional 10nT/hr recovery in the Dst Index [*Kozyra et al.*, 1997]

Figure 82 shows the location and intensity of emissions in the EMIC wave frequency band. Intense emissions occur not only on the duskside but also principally on the dawnside. This is odd and does not reflect the picture outlined in Figure 64 [*Shprits et al.*, 2008] in which EMIC emission is confined to the duskside plasmapause and dayside plumes. However, *Anderson et al.* [1990] have reported EMIC wave emission outside of L=7 and *Daglis et al.* [1999] noted that EMIC waves have been observed on the dawn-side (0300-0900 MLT) albeit much less frequently than in the post-dawn sector (1000-1800 MLT). Figure 82 appears to agree with this description of the distribution of EMIC wave emission and shows a similar local time dependence. However, the intensity suggests that EMIC waves are more common between 0300 and 0900 than previously reported and are more widespread than the emissions that occur between 1000 and 1800 MLT.
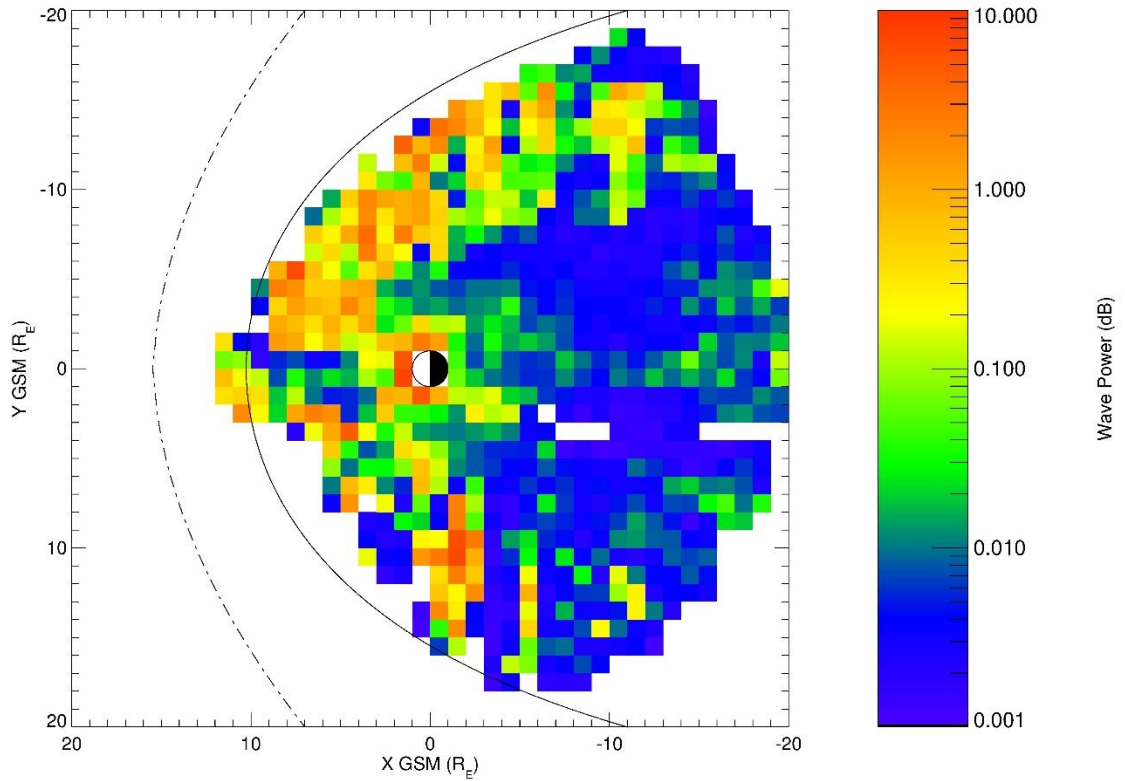
Figure 82: Location of EMIC emission as plotted by wave power for all identified storms across all of the storm phases shown for the XY-GSM plane.
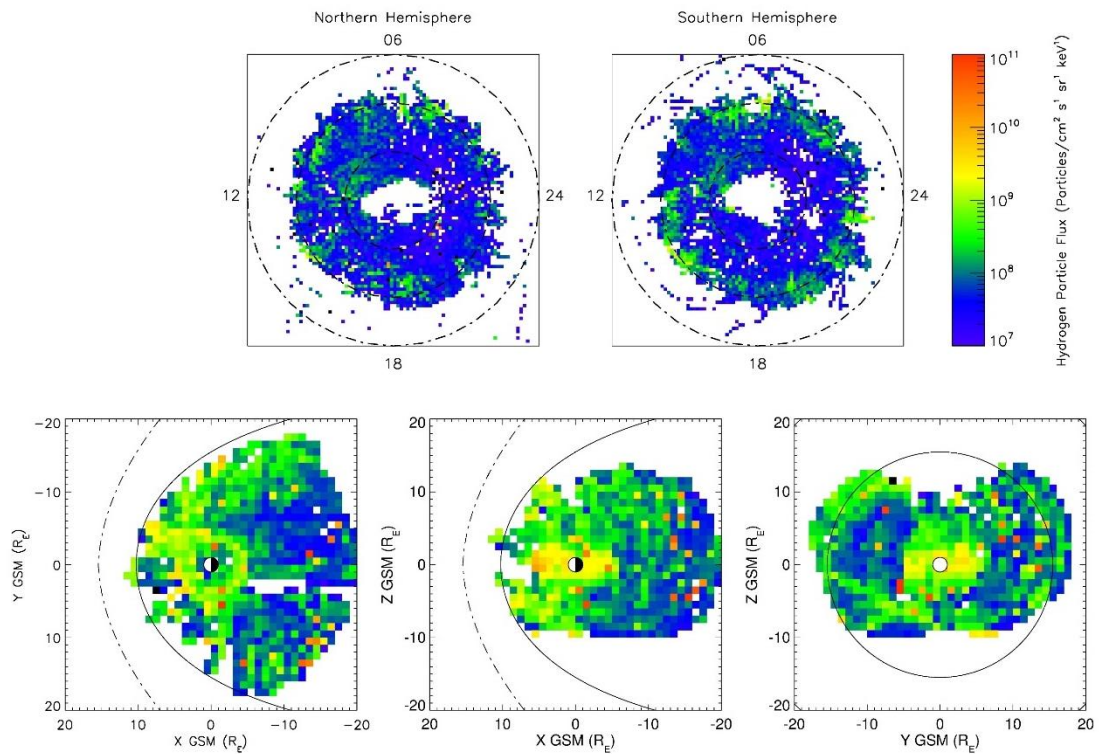
*Figure 83: Ring current proton flux plotted for precipitating (top) and trapped (bottom) particles for all storm types and all phases. The bottom left panel is the proton flux equivalent of Figure 82*

As mentioned above the location of EMIC waves will likely coincide with the location of ring current proton flux enhancements. Figure 83 shows the ring current proton flux across the magnetosphere for both precipitating and trapped particles. When this is compared to the enhancement in the EMIC wave frequency band Figure 82 there is a remarkable correlation in the outer magnetosphere ($> 5R_E$) and a similarly striking anti-correlation within $5R_E$ (from the observable ring of high flux in Figure 83 earthward). *Daglis et al.* [1999] noted that EMIC waves are modulated by the relative abundance of ion species, more specifically that a high abundance of O^+ ions can damp EMIC waves [*Kozyra et al.*, 1997]. This may explain the observed anti-correlation in the inner magnetosphere as this region is where the flux of O^+ is observed to be the greatest. Figure 84 shows that the relative abundance is high in the inner magnetosphere when compared to the abundance of H^+ ions, sometimes contributing over 50% to the combined flux. If the regions in which the O^+ abundance is low and the H^+ flux is high are compared to the location of intense EMIC wave activity, then the correlation is remarkably high suggesting that the O^+ ions may indeed damp the EMIC waves in the regions of high H^+ flux.
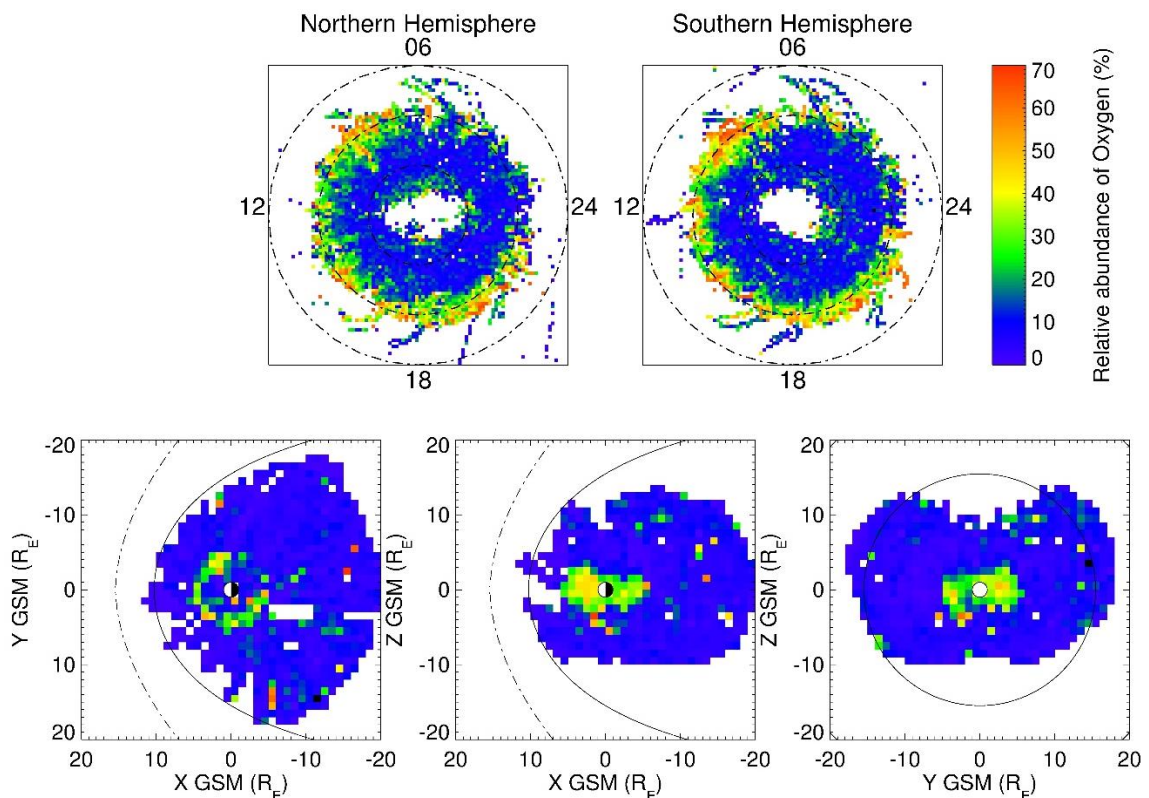
Figure 84: Relative abundance of O+ ions when compared to the abundance of H+ ions
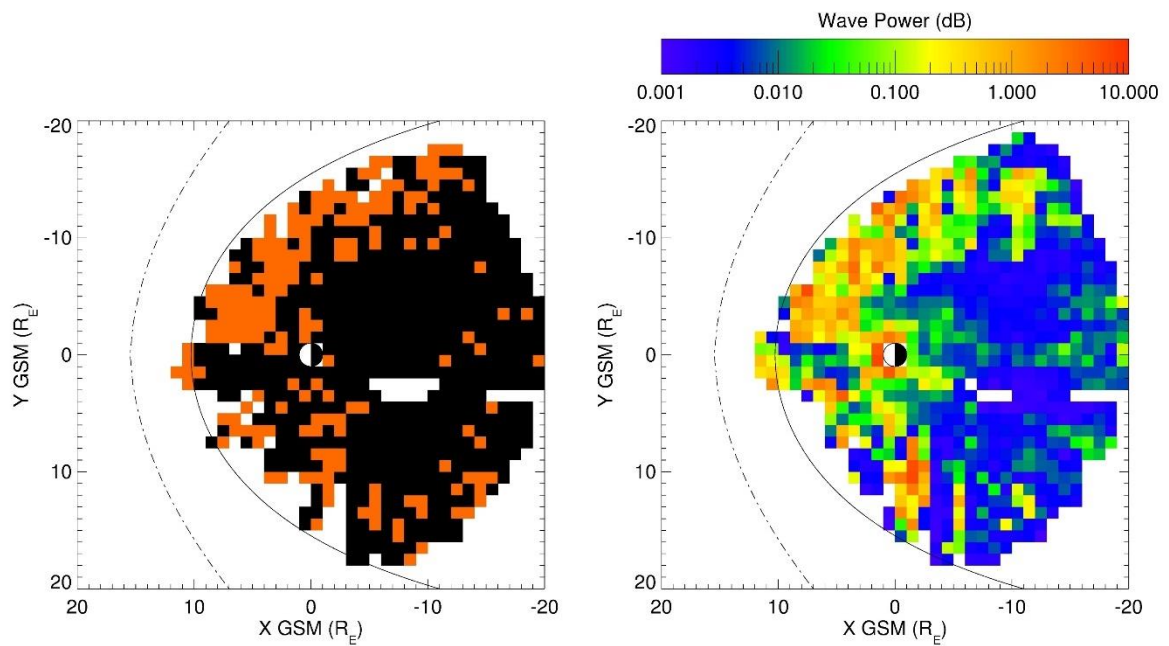
Figure 85: The location of high H+ flux and low O+ abundance (left) with the reproduced plot of EMIC wave emission location (right)

The left hand panel of Figure 85 shows the location of the bins in which the H+ flux is greater than 2.5×10^8 and where the O+ abundance is below 20%. The right hand panel is a reproduction of Figure 82 and shows the location of intense EMIC wave emission. The left hand panel reproduces the location of the intense emission remarkably well even reproducing some of the small scale features on the duskside. This again highlights the preference of the dawnside for the location of EMIC wave emission, although fails to indicate the high intensity region close to the Earth.

As mentioned above EMIC waves can provide an efficient loss mechanism and cause the more rapid decay of the ring current. Figure 36 shows that the ring current decays faster for flux decrease storms and therefore it may follow that EMIC wave intensity would be greater during these events. However, as has also been shown above that the hydrogen flux increases during flux increase type storms. If the above generation mechanism is correct it would suggest that the EMIC wave intensity would be greater and more widespread during these events as there is a greater flux of particles available to interact with the expanding plasmasphere. Figure 86 shows that this is generally the case for the pre- and post-storm period but is not the case during the recovery phase where the intensity of EMIC wave power seems to be greater for flux decrease storms.

Figure 87 more clearly shows that this is the case. There are much more red regions during the pre- and post-storm periods than during the recovery phase, which is predominantly blue. More intense EMIC waves would suggest more favourable conditions for the generation of waves. As the generation mechanism is dependent on freshly injected ions via substorms more intense EMIC wave power during the post-storm period during flux increase storms when compared to flux decrease storms may support the theory that flux increase storms are due to continued injection of plasma sheet particles into the post-storm period. Figure 86 shows the evolution of the EMIC wave power over the duration of each the different types of storm. The wave intensity again seems to be greatest for the increasing type storms appears to become slightly more intense during the initial and main phase. This is peculiar as the generation mechanisms suggest that the EMIC wave power should maximise during the recovery phase as the plasmasphere expands. The location of the power is also slightly strange as EMIC waves are thought be more common on the duskside. However, H^+ temperature anisotropies, thought to drive EMIC wave growth, have been shown to maximise on the dawn-side (0300-0900) [*Roux et al.*, 1982; *Lin et al.*, 2014].
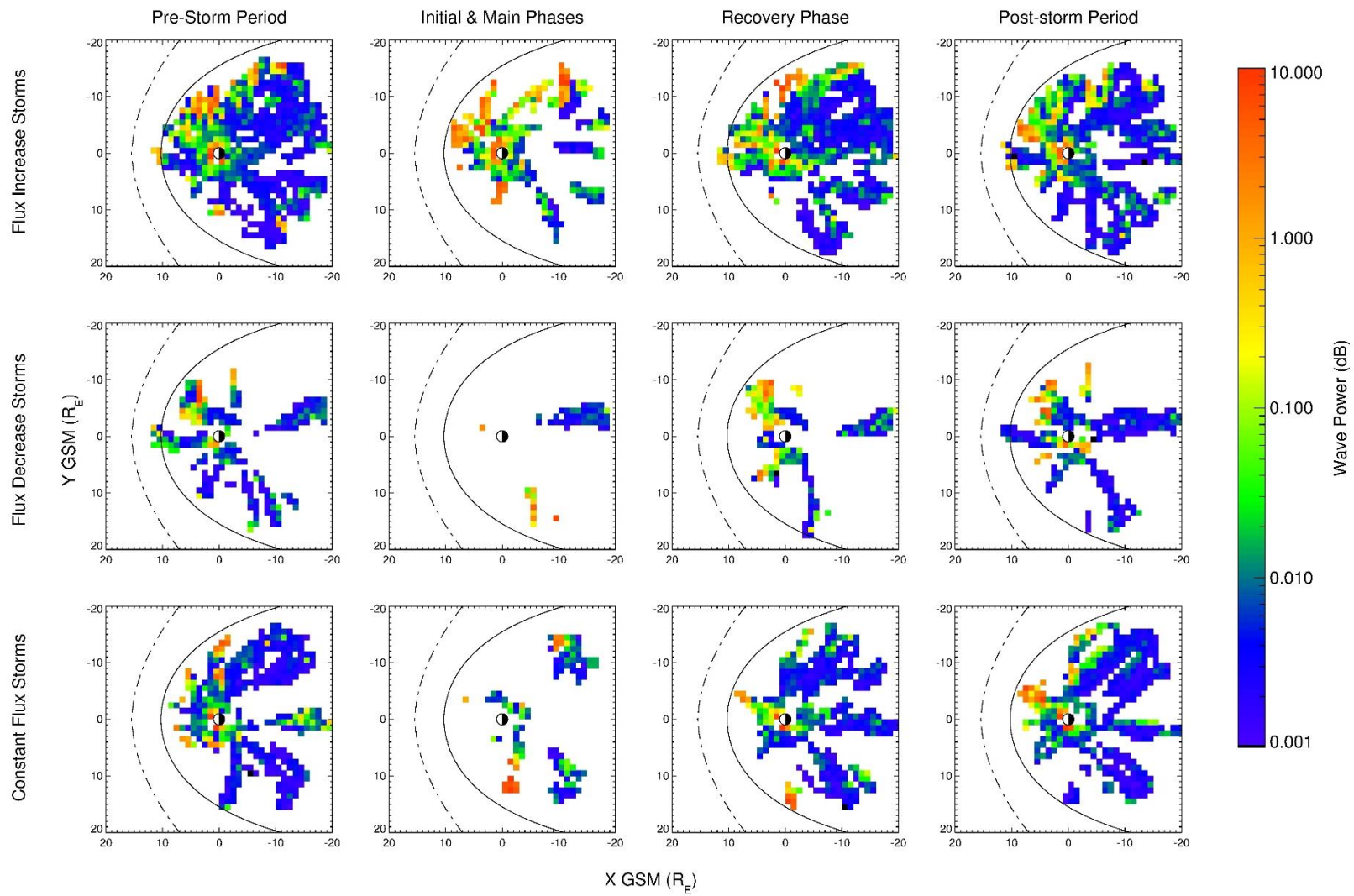
Figure 86: Location of EMIC emission as plotted by wave power broken down by the phase of the storm and the type of storm shown for the XY-GSM plane.
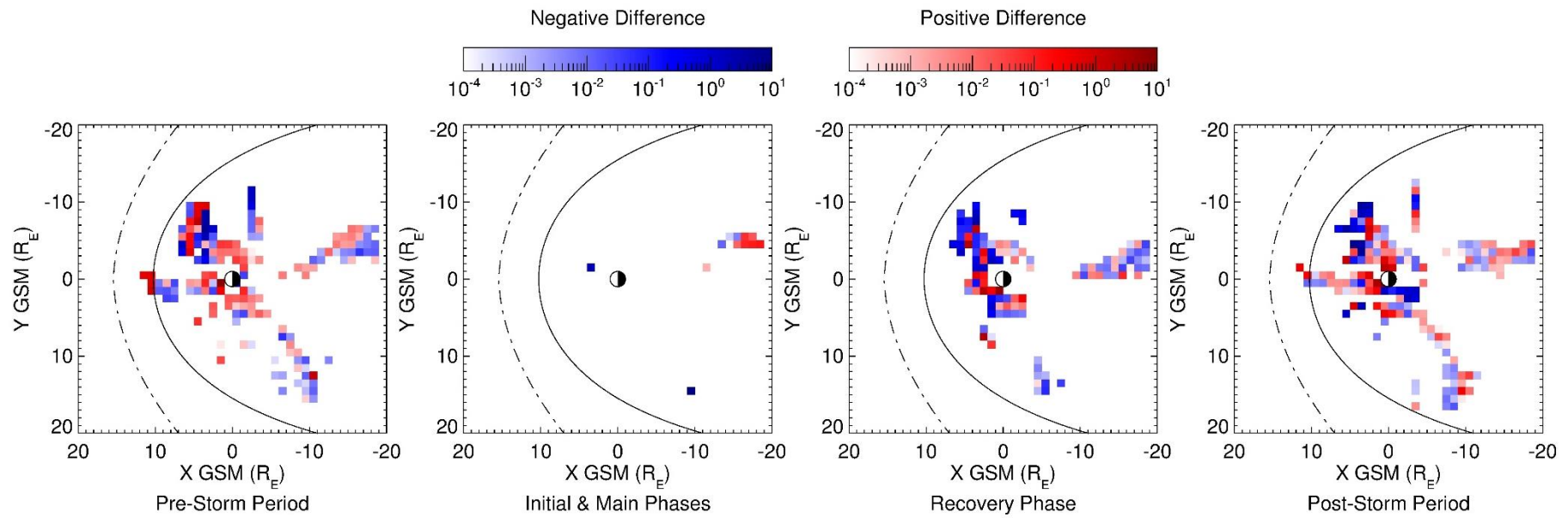
Figure 87: Difference in EMIC wave power between flux increase and flux decrease storms broken down by storm phase. Red regions indicate greater wave power during flux increase events and blue regions indicate greater wave power during flux decrease events.

Conclusion

The previous chapters have used indices to concentrate on the overall picture of the magnetosphere before, during and after geomagnetic storms. Although indices are invaluable in providing a global view of changes within the magnetosphere they are poor at providing information of the specific plasma species and their variations during active times. Using data from the Cluster spacecraft, specifically instruments that directly measure the plasma and field variations, it is possible to observed the change in individual particle species and wave modes across the magnetosphere for each of the different types of storm.

As discussed in the previous chapters the variation of the electron flux is well documented both in general [e.g. *Paulikas and Blake*, 1978; *Lyatsky and Khazanov*, 2008; *Reeves et al.*, 2011] and also specifically during storm times [e.g. *Reeves et al.*, 2003; *Kilpua et al.*, 2015]; however, the variation in the ion flux is less well documented. Chapter 5 suggests that increases in electron flux over the duration of a storm is likely caused by the continuing injection of plasma via substorms due to the favourable orientation of the IMF over this period. If this is the case, then it would follow that the flux of plasma sheet energy ions would follow the same trend. Figure 70 shows that this is the case for all three ion species in the energy range associated with the energies of the ring current [*Greenspan and Hamilton*, 2000]. The increase in O^+ during the recovery phase has been associated with substorm driven ion outflows and the subsequent injection from the plasma sheet into the inner magnetosphere. This would suggest that O^+ ion flux should increase more for increasing storms and less for decreasing storms if the observed change in the electron flux is caused by prolonged substorm activity during the recovery phase as appears to be the case from chapter 5.

The enhancement of ion fluxes supports the hypothesis that flux increase storms are due to the continued injection of plasma via substorms following the end of the main phase, as discussed following the analysis of chapter 5. This mechanism only explains the enhancement of plasma sheet energy ions and electrons and cannot directly cause enhancements or depletions within the relativistic electron population.

This therefore suggests the need for an enhancement mechanism to accelerate the electrons to relativistic energies. From previous research several wave modes were identified as potential mechanisms for both the acceleration of seed electrons to higher energies and loss of both seed and higher energy particles as both should be enhanced during active periods.

Whistler mode chorus waves are the prime candidate for the acceleration of electrons to higher energies. It was observed that the intensity of these waves are greater during recovery phase of flux increase storms when compared to flux decrease and constant flux storms. This suggests that these wave modes are the correct mechanism for creating the observed relativistic electron flux. Other wave modes such as whistler mode hiss waves and EMIC waves which require the injection of plasma sheet particles via substorms for their generation also appeared to be most intense during flux increase storms than any other type. This would suggest that the depletion of the particle flux during flux decrease storms is not caused by increased particle loss due to more intense EMIC and whistler mode hiss waves.

CHAPTER 7

Conclusion

[7.1]   Introduction

This chapter will briefly re-examine the conclusions from the three main data chapters before bringing each strand of work together and evaluating the results with respect to the aim of the study, which was outlined in the introductory chapter.

[7.2]   The Time Evolution of Magnetospheric Currents Derived from a New Storm Time Index

The SMR index was shown to be a good description of the Dcx index following the methodology outlined by *Wanliss and Showalter* [2006]. These indices are more accurate descriptors of the intensification of the terrestrial ring current due to the random and systematic errors which are present in the Dst index [e.g. *Karinen and Mursula*, 2005; *Asikainen et al.*, 2010; *Mursula et al.*, 2011]. However, both the Dcx and SMR indices still contain contributions from other current systems within the magnetopause (Section [4.4]). Following the method outlined by *Asikainen et al.* [2010] it has been shown that the magnetopause, tail and ring current contributions within the SMR index can be distilled from the overall index by using measurements of the isotropic boundary and the solar wind dynamic pressure and electric field.

Once the individual current indices had been produced it was possible to evaluate the average evolution of each of the constituent current systems over the storm duration using a superposed epoch analysis. This shows that the tail current decays quickly following the end of the main phase and the ring current remains enhanced for an extended period of time decaying slowly throughout the recovery phase.

The two step recovery, which is a common feature in the magnetic indices appears to be due to the more rapid recovery of the tail and magnetopause currents following the end of the main phase, rather than the composition of the ring current. The evolution of the current indices was also evaluated for each of the different types of storm and showed that the ring current decayed faster for flux decrease storms than either flux increase or constant flux storms. This suggests that the ions within the ring current show a similar behaviour to the relativistic electrons for each of the types of storm as defined by *Reeves et al.* [2003]. Additionally, the tail and ring current evolution was evaluated for different driving structures and it was found that CMEs with sheath substructures cause a greater enhancement in the tail current than CMEs without a sheath and CIRs. The ring current was also shown to most enhanced for sheath plus ejecta CMEs and least enhanced for CIR driven storms.

[7.3]   Analysis of the Cause of Storm Time Electron Flux Variations

Variations in the relativistic electron flux have been attributed to both the solar wind speed [e.g. *Paulikas and Blake*, 1978; *Reeves et al.*, 2011] and solar wind density [*Lyatsky and Khazanov*, 2008]. With regards to the change in the electron flux over the duration of a geomagnetic storm [*Reeves et al.*, 2003]. Using a superposed epoch analysis of geomagnetic indices and solar wind parameters along with examining the change in solar wind density and velocity it was shown that the orientation of the IMF appears to be the controlling factor governing the enhancement or depletion of the relativistic electron flux.

Figure 45 and Figure 48 show that the typical response in the electron flux is less apparent during the recovery phase of flux decrease storms when compared with flux increase storms for both the solar wind velocity and density. By comparing the IMF orientation over the durations of the recovery and post-storm period (Figure 63) it is clear that flux increase (decrease) storms occur preferentially when the IMF orientation is more southward (northward). A more favourable IMF orientation will lead to more substorms during the recovery phase of the storm and therefore the continued injection of plasma sheet particles into the inner magnetosphere.

Increased injection of plasma sheet particles will provide a continuous supply of seed electrons which are required for the enhancement of relativistic electrons [*Friedel et al.*, 2002]. Previous results have also hinted at the orientation of the IMF being the controlling factor governing the observed variation in the relativistic electron flux change rather than any one plasma parameter of the solar wind [e.g. *Miyoshi and Kataoka*, 2005; *Li et al.*, 2011a].

[7.4]   Analysis of Storm Time Plasma and Field Variations

Chapter 6 discussed the variation in ion fluxes and the prevalence of specific wave modes which are known to cause enhancements and depletions in the particle flux over the duration of a storm. Figure 70 shows that the ion fluxes mirror the storm type variations observed in the relativistic electron flux. This supports the hypothesis that flux increases are likely due to continuing injection of plasma sheet particles during the recovery phase as continued injections should also increase the ion flux, as observed. This mechanism will directly cause a variation in the enhancement of plasma sheet energy ions and electrons and cannot directly cause enhancements or depletions within the relativistic electron population. There is therefore a need for an enhancement mechanism to accelerate the electrons to relativistic energies.

All the identified wave modes appeared to be more intense during flux increase storms than flux decrease storms. This could imply that whistler mode chorus waves are the correct wave mode for the acceleration of seed electrons to relativistic energies. The greater intensity of whistler mode hiss and EMIC waves during flux increase storms suggests the presence of more seed particles needed for their generation. Coupling this with the relatively weak emission during flux decrease storms suggests that the observed depletion during these events is not due to enhance loss processes.

[7.5]   Conclusion

The difference between the types of geomagnetic storm has been the main focus of this work. By observing the variation in geomagnetic indices, solar wind parameters, particle fluxes and wave power a strong and new argument is presented for the cause of the observed variation in the relativistic electron flux originally reported by *Reeves et al.* [2003]. In addition, new geomagnetic indices have been produced which describe the variation in the tail, magnetopause and ring currents, as separated from the SMR index. The location of wave modes has been evaluated by direct measurement of field variations within the magnetosphere and has shown that although some wave modes, such as whistler mode chorus occur in the predicted location others are much more widespread.

The three aims of observing and comparing with theory the location and intensity of specific wave modes, presenting observations on the variations of ion species with different types of storm and the identification of the mechanism controlling the change in relativistic electron flux have all been achieved. Future work could increase the data coverage of wave mode observations by including additional spacecraft and extending the study to encompass more storms. In addition, case studies could be used to observe the specific wave mode responsible for the excitation of electrons to relativistic energies.

CHAPTER 8

Appendix

The below appendix plots show the typical data density for all storms both as a whole and broken down by type and phase. This is done for both individual measurements and the number of storms per bin.
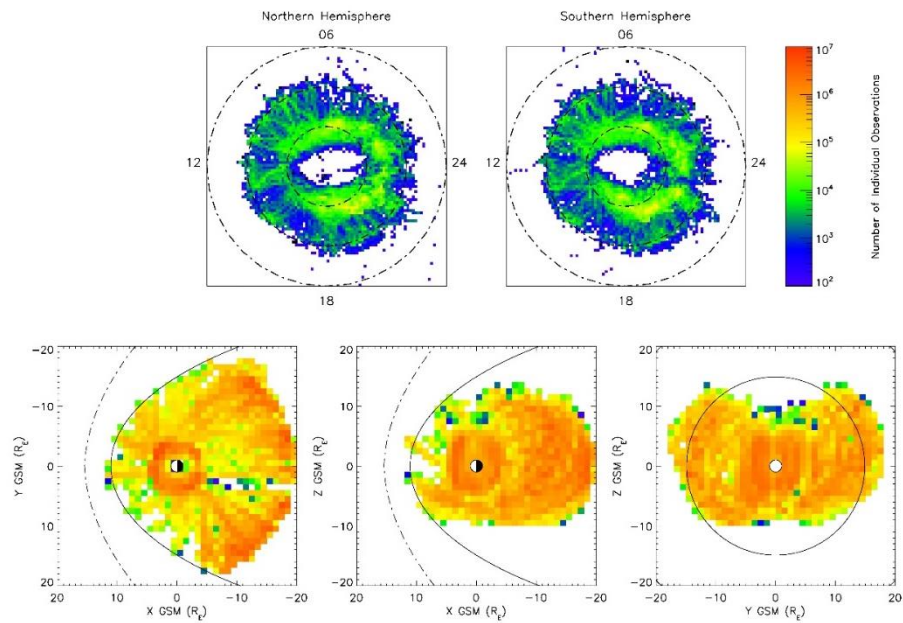
Figure App. 1: Total number of measurements used in for each location bin plotted for all storm types and phases.
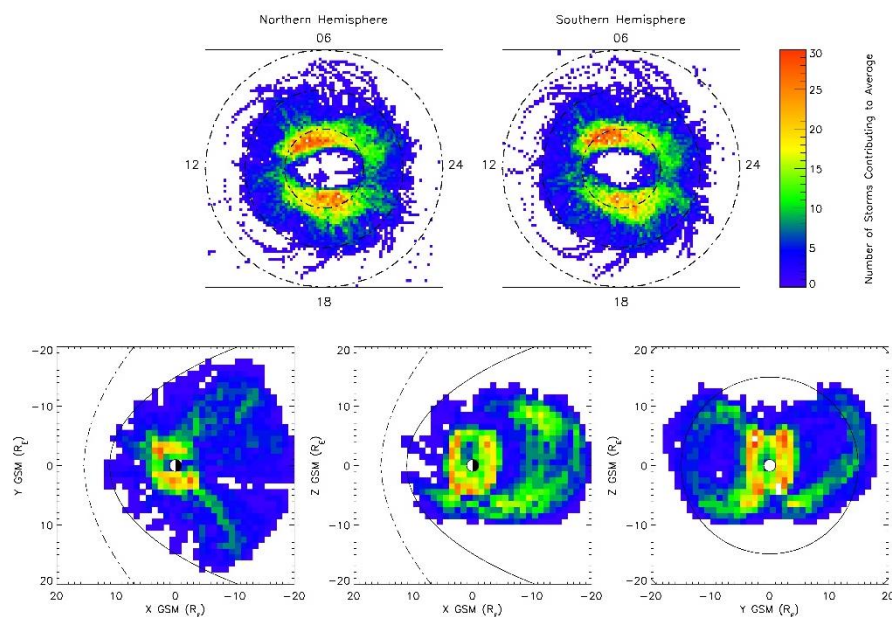
Figure App. 2: Total number of events used in for each location bin plotted for all storm types and phases
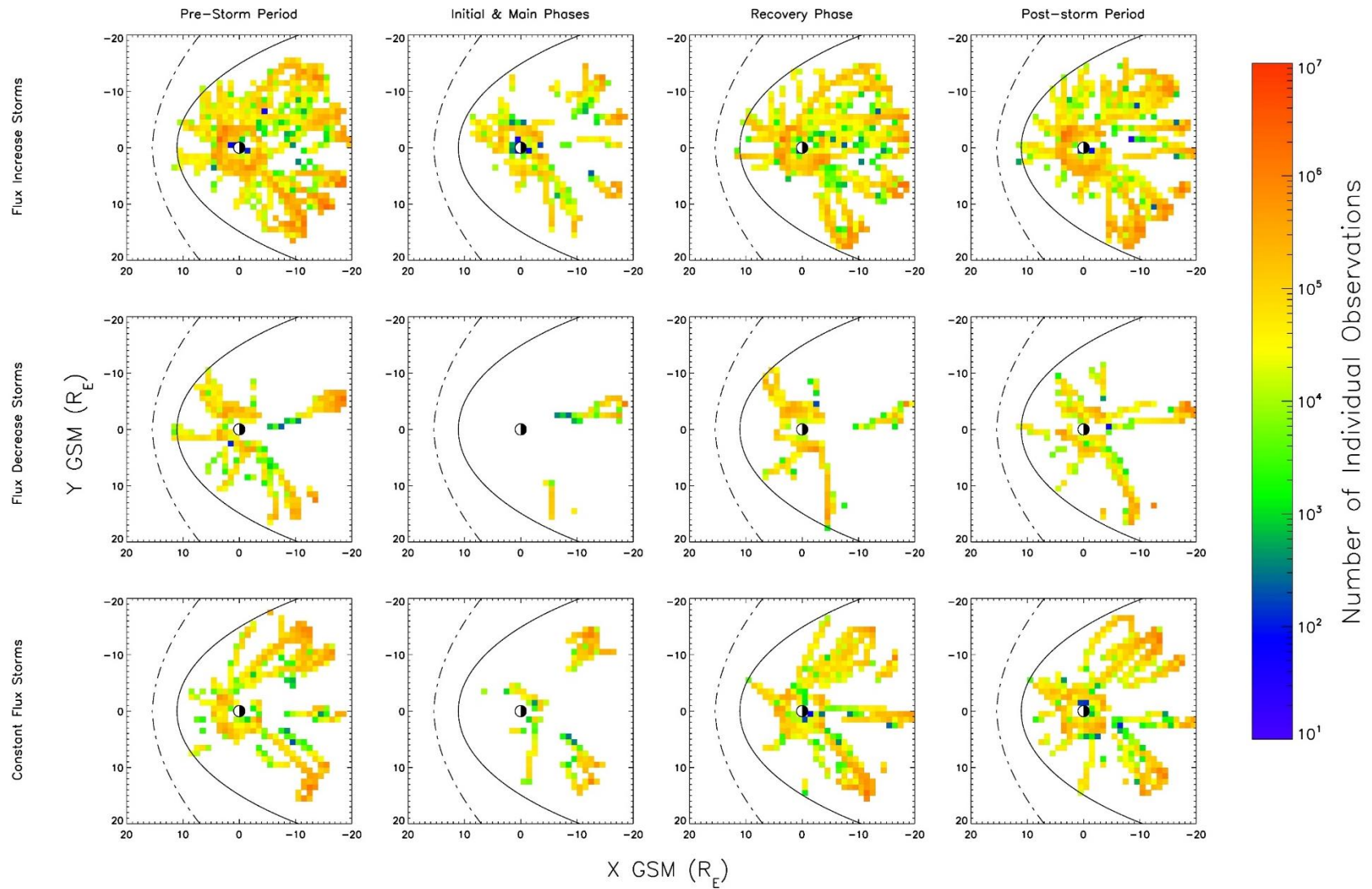
Figure App. 3: Total number of measurements used in for each XY location bin broken down by storm type and phase.
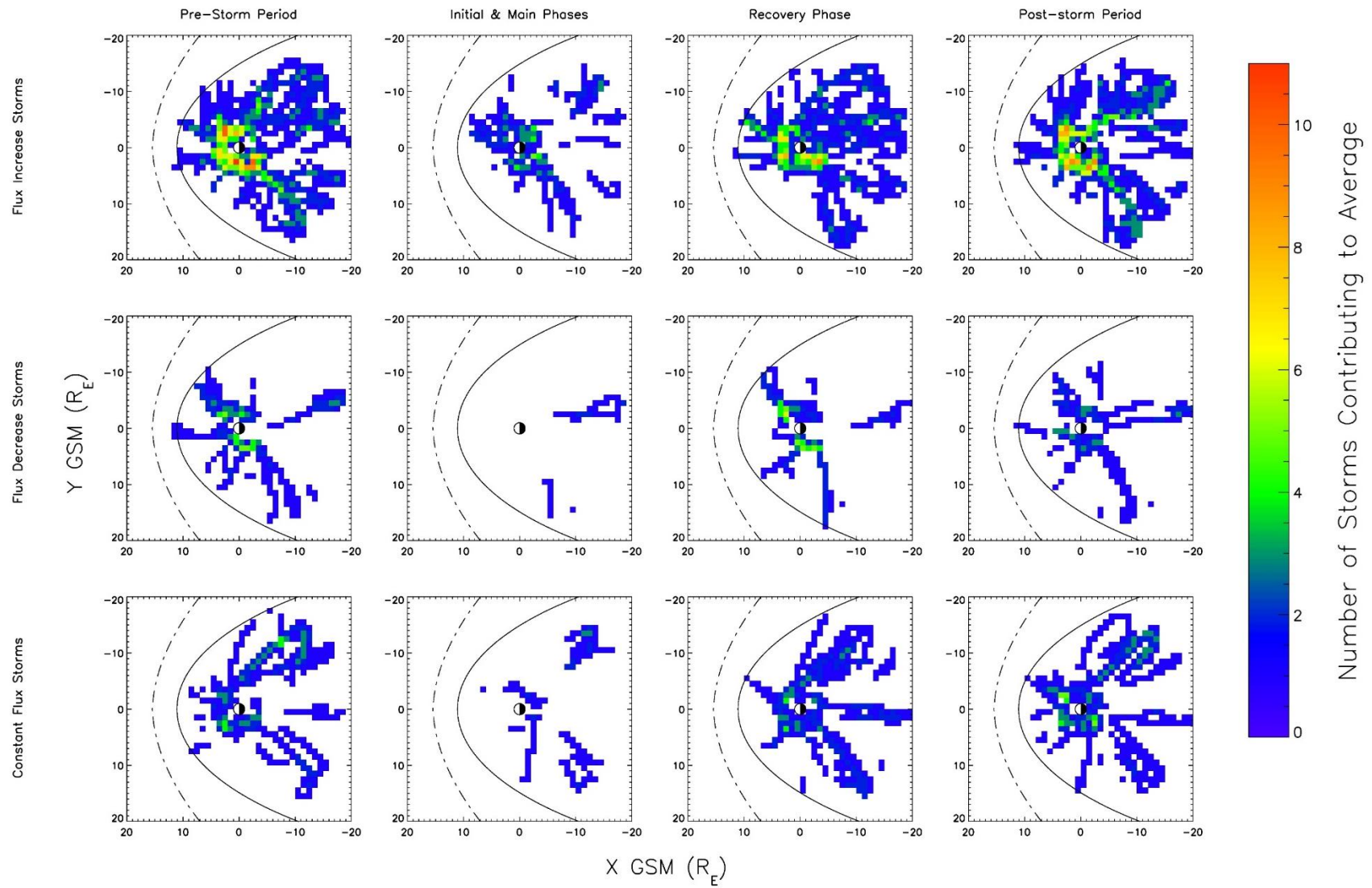
Figure App. 4: Total number of events used in for each XY location bin broken down by storm type and phase.

CHAPTER 9

Bibliography

Abel, B. and Thorne, R. M. (1998) 'Electron scattering loss in Earth's inner magnetosphere: 1. Dominant physical processes', *Journal of Geophysical Research: Space Physics*, 103(A2), pp. 2385-2396.

Akasofu, S.-I. (1981) 'Energy coupling between the solar wind and the magnetosphere', *Space Science Reviews*, 28(2), pp. 121-190.

Akasofu, S.-I. and Chapman, S. (1972) 'Solar-terrestrial physics'.

Albert, J. (1994) 'Quasi-linear pitch angle diffusion coefficients: Retaining high harmonics', *Journal of Geophysical Research: Space Physics*, 99(A12), pp. 23741-23745.

Albert, J. (2002) 'Nonlinear interaction of outer zone electrons with VLF waves', *Geophysical research letters*, 29(8).

Albert, J. (2003) 'Evaluation of quasi-linear diffusion coefficients for EMIC waves in a multispecies plasma', *Journal of Geophysical Research: Space Physics*, 108(A6).

Alfvén, H. (1942) 'Existence of electromagnetic-hydrodynamic waves', *Nature*, 150(3805), pp.405.

Anderson, B., Denton, R., Ho, G., Hamilton, D., Fuselier, S. and Strangeway, R. (1996) 'Observational test of local proton cyclotron instability in the Earth's magnetosphere', *Journal of Geophysical Research: Space Physics*, 101(A10), pp. 21527-21543.

Anderson, B., Takahashi, K., Erlandson, R. and Zanetti, L. (1990) 'Pc1 pulsations observed by AMPTE/CCE in the Earth's outer magnetosphere', *Geophysical Research Letters*, 17(11), pp. 1853-1856.

Anderson, B. R., Millan, R. M., Reeves, G. D. and Friedel, R. H. W. (2015) 'Acceleration and loss of relativistic electrons during small geomagnetic storms', *Geophysical Research Letters*, 42(23).

André, M., Li, K. and Eriksson, A. I. (2015) 'Outflow of low-energy ions and the solar cycle', *Journal of Geophysical Research: Space Physics*, 120(2), pp. 1072-1085.

André, M., Vaivads, A., Khotyaintsev, Y. V., Laitinen, T., Nilsson, H., Stenberg, G., Fazakerley, A. and Trotignon, J. (2010) 'Magnetic reconnection and cold plasma at the magnetopause', *Geophysical Research Letters*, 37(22).

André, N. and Lemaire, J. (2006) 'Convective instabilities in the plasmasphere', *Journal of atmospheric and solar-terrestrial physics*, 68(2), pp. 213-227.

Arnoldy, R. L. (1971) 'Signature in the interplanetary medium for substorms', *Journal of Geophysical Research*, 76(22), pp. 5189-5201.

Arnoldy, R. L. and Chan, K. (1969) 'Particle substorms observed at the geostationary orbit', *Journal of Geophysical Research*, 74(21), pp. 5019-5028.

Asikainen, T., Maliniemi, V. and Mursula, K. (2010) 'Modeling the contributions of ring, tail, and magnetopause currents to the corrected Dst index', *Journal of Geophysical Research: Space Physics*, 115(A12).

Asikainen, T. and Mursula, K. (2011) 'Recalibration of the long-term NOAA/MEPED energetic proton measurements', *Journal of Atmospheric and Solar-Terrestrial Physics*, 73(2), pp. 335-347.

Baker, D., Blake, J., Callis, L., Cummings, J., Hovestadt, D., Kanekal, S., Klecker, B., Mewaldt, R. and Zwickl, R. (1994) 'Relativistic electron acceleration and decay time scales in the inner and outer radiation belts: SAMPEX', *Geophysical research letters*, 21(6), pp. 409-412.

Baker, D., Jaynes, A., Li, X., Henderson, M., Kanekal, S., Reeves, G., Spence, H. E., Claudepierre, S., Fennell, J. F. and Hudson, M. (2014) 'Gradual diffusion and punctuated phase space density enhancements of highly relativistic electrons: Van Allen Probes observations', *Geophysical Research Letters*, 41(5), pp. 1351-1358.

Baker, D., Kanekal, S. and Blake, J. (2004) 'Characterizing the Earth's outer Van Allen zone using a radiation belt content index', *Space Weather*, 2(2).

Baker, D., Li, X., Pulkkinen, A., Ngwira, C., Mays, M., Galvin, A. and Simunac, K. (2013) 'A major solar eruptive event in July 2012: Defining extreme space weather scenarios', *Space Weather*, 11(10), pp. 585-591.

Baker, D., McPherron, R., Cayton, T. and Klebesadel, R. (1990) 'Linear prediction filter analysis of relativistic electron properties at 6.6 RE', *Journal of Geophysical Research: Space Physics*, 95(A9), pp. 15133-15140.

Baker, D., Pulkkinen, T., Li, X., Kanekal, S., Blake, J., Selesnick, R., Henderson, M., Reeves, G., Spence, H. E. and Rostoker, G. (1998a) 'Coronal mass ejections, magnetic clouds, and relativistic magnetospheric electron events: ISTP', *Journal of Geophysical Research: Space Physics*, 103(A8), pp. 17279-17291.

Baker, D., Pulkkinen, T., Li, X., Kanekal, S., Ogilvie, K., Lepping, R., Blake, J., Callis, L., Rostoker, G. and Singer, H. (1998b) 'A strong CME-related magnetic cloud interaction with the Earth's Magnetosphere: ISTP observations of rapid relativistic electron acceleration on May 15, 1997', *Geophysical Research Letters*, 25(15), pp. 2975-2978.

Balogh, A., Dunlop, M. W., Cowley, S. W. H., Southwood, D. J., Thomlinson, J. G., Glassmeier, K. H., Musmann, G., Lühr, H., Buchert, S., Acuña, M. H., Fairfield, D. H., Slavin, J. A., Riedler, W., Schwingenschuh, K. and Kivelson, M. G. (1997) 'The cluster magnetic field investigation', *Space Science Reviews*, 79(1-2), pp. 65-91.

Bame, S. J., McComas, D. J., Barraclough, B. L., Phillips, J. L., Sofaly, K. J., Chavez, J. C., Goldstein, B. E. and Sakurai, R. K. (1992) 'The Ulysses solar wind plasma experiment', *Astronomy and Astrophysics Supplement Series*, 92, pp. 237-265.

Banks, P., Nagy, A. and Axford, W. (1971) 'Dynamical behavior of thermal protons in the mid-latitude ionosphere and magnetosphere', *Planetary and Space Science*, 19(9), pp. 1053-1067.

Barker, A., Li, X. and Selesnick, R. (2005) 'Modeling the radiation belt electrons with radial diffusion driven by the solar wind', *Space Weather*, 3(10).

Baumjohann, W. (1986) 'Merits and limitations on the use of geomagnetic indices', *Solar Wind-Magnetosphere Coupling, edited by Y.Kamide and*, pp. 3-15.

Blake, J., Baker, D., Turner, N. E., Ogilvie, K. and Lepping, R. (1997) 'Correlation of changes in the outer-zone relativistic-electron population with upstream solar wind measurements', *Geophysical Research Letters*, 24(8), pp. 927-929.

Blake, J., Kolasinski, W., Fillius, R. and Mullen, E. (1992) 'Injection of electrons and protons with energies of tens of MeV into L< 3 on 24 March 1991', *Geophysical Research Letters*, 19(8), pp. 821-824.

Boakes, P. D., Nakamura, R., Volwerk, M. and Milan, S. E. (2014), 'ECLAT Cluster Spacecraft Magnetotail Plasma Region Identifications (2001–2009)', *Dataset Papers in Science*.

Boller, B. R., and H. L. Stolov (1970), 'Kelvin-Helmholtz instability and the semiannual variation of geomagnetic activity', *Journal of Geophysical Research: Space Physics*, 75(31), pp. 6073–6084.

Borovsky, J. E. and Denton, M. H. (2006) 'Differences between CME-driven storms and CIR-driven storms', *Journal of Geophysical Research: Space Physics*, 111(A7).

Borovsky, J. E., Thomsen, M. F. and Elphic, R. C. (1998) 'The driving of the plasma sheet by the solar wind', *Journal of Geophysical Research: Space Physics*, 103(A8), pp. 17617-17639.

Bortnik, J. and Thorne, R. (2007) 'The dual role of ELF/VLF chorus waves in the acceleration and precipitation of radiation belt electrons', *Journal of Atmospheric and Solar-Terrestrial Physics*, 69(3), pp. 378-386.

Bortnik, J., Thorne, R., O'Brien, T., Green, J., Strangeway, R., Shprits, Y. and Baker, D. (2006) 'Observation of two distinct, rapid loss mechanisms during the 20 November 2003 radiation belt dropout event', *Journal of Geophysical Research: Space Physics*, 111(A12).

Bossen, M., McPherron, R. and Russell, C. (1976) 'A statistical study of Pc 1 magnetic pulsations at synchronous orbit', *Journal of Geophysical Research*, 81(34), pp. 6083-6091.

Boteler, D. H., Pirjola, R. J. and Nevanlinna, H. (1998) 'The effects of geomagnetic disturbances on electrical systems at the Earth's surface', *Advances in Space Research*, 22(1), pp. 17-27.

Brautigam, D. and Albert, J. (2000) 'Radial diffusion analysis of outer radiation belt electrons during the October 9, 1990, magnetic storm', *Journal of Geophysical Research: Space Physics*, 105(A1), pp. 291-309.

Burtis, W. and Helliwell, R. (1976) 'Magnetospheric chorus: Occurrence patterns and normalized frequency', *Planetary and Space Science*, 24(11), pp. 1007IN11011-11010IN41024.

Burton, R. K., McPherron, R. L. and Russell, C. T. (1975) 'An empirical relationship between interplanetary conditions and Dst', *Journal of geophysical research*, 80(31), pp. 4204-4214.

Burton, R. K., Russell, C. T. and Chappell, C. R. (1970) 'The Alfvén velocity in the magnetosphere and its relationship to ELF emissions', *Journal of Geophysical Research*, 75(28), pp. 5582-5586.

Campbell, W. H. (2004) 'Failure of Dst index fields to represent a ring current', *Space Weather*, 2(8).

Cao, J. B., Ding, W. Z., Reme, H., Dandouras, I., Dunlop, M., Liu, Z. X. and Yang, J. Y. (2011) 'The statistical studies of the inner boundary of plasma sheet', *Annales geophysicae*, 29, p. 289.

Carovillano, R. L. and Siscoe, G. L. (1973) 'Energy and momentum theorems in magnetospheric processes', *Reviews of Geophysics*, 11(2), pp. 289-353.

Carpenter, D. L. (1962) 'Electron-density variations in the magnetosphere deduced from whistler data', *Journal of Geophysical Research*, 67(9), pp. 3345-3360.

Carpenter, D. L. (1966) 'Whistler studies of the plasmapause in the magnetosphere: 1. Temporal variations in the position of the knee and some evidence on plasma motions near the knee', *Journal of Geophysical Research*, 71(3), pp. 693-709.

Case, N. A., and Wlid, J. A. (2013) 'The location of the Earth's magnetopause: A comparison of modeled position and in situ Cluster data', *Journal of Geophysical Research*, 118, pp. 6127-6135.

Chapman, S. (1918) 'An outline of a theory of magnetic storms', *Proceedings of the Royal Society of London.Series A, Containing Papers of a Mathematical and Physical Character*, 95(666), pp. 61-83.

Chapman, S., Venkatesan, D. and Akasofu, S. I. (1963) 'THE MAIN PHASE OF GREAT MAGNETIC STORMS', *Journal of Geophysical Research (US)*, 68.

Chappell, C. (1982) 'Initial observations of thermal plasma composition and energetics from Dynamics Explorer-1', *Geophysical Research Letters*, 9(9), pp. 929-932.

Chen, F. F. (1974) *Introduction to plasma physics.* Plenum Press.

Chen, L., Li, W., Bortnik, J. and Thorne, R. M. (2012) 'Amplification of whistler-mode hiss inside the plasmasphere', *Geophysical Research Letters*, 39(8).

Chen, L., Thorne, R. M. and Horne, R. B. (2009) 'Simulation of EMIC wave excitation in a model magnetosphere including structured high-density plumes', *Journal of Geophysical Research: Space Physics*, 114(A7).

Chen, Y., Reeves, G. D. and Friedel, R. H. (2007) 'The energization of relativistic electrons in the outer Van Allen radiation belt', *Nature Physics*, 3(9), pp. 614-617.

Chen, Y., Reeves, G. D., Friedel, R. H. and Cunningham, G. S. (2014) 'Global time-dependent chorus maps from low-Earth-orbit electron precipitation and Van Allen Probes data', *Geophysical Research Letters*, 41(3), pp. 755-761.

Chisham, G. (1996) 'Giant pulsations: An explanation for their rarity and occurrence during geomagnetically quiet times', *Journal of geophysical research*, 101(A11), pp. 24755-24763.

Chiu, M. C., Von-Mehlem, U. I., Willey, C. E., Betenbaugh, T. M., Maynard, J. J., Krein, J. A., Conde, R. F., Gray, W. T., Hunt Jr, J. W. and Mosher, L. E. (1998) 'ACE spacecraft', *Space science reviews*, 86(1-4), pp. 257-284.

Clausen, L., Baker, J., Ruohoniemi, J. and Singer, H. (2011) 'EMIC waves observed at geosynchronous orbit during solar minimum: Statistics and excitation', *Journal of Geophysical Research: Space Physics*, 116(A10).

Cliver, E. W., Kamide, Y., Ling, A. G. and Yokoyama, N. (2001) 'Semiannual variation of the geomagnetic Dst index: Evidence for a dominant nonstorm component', *Journal of Geophysical Research: Space Physics*, 106(A10), pp. 21297-21304.

Cocke, W. J. and Cornwall, J. M. (1967) 'Theoretical simulation of micropulsations', *Journal of Geophysical Research*, 72(11), pp. 2843-2856.

Cornilleau-Wehrlin, N., Chauveau, P., Louis, S., Meyer, A., Nappa, J. M., Perraut, S., Rezeau, L., Robert, P., Roux, A. and De Villedary, C. (1997) 'The Cluster spatio-temporal analysis of field fluctuations (STAFF) experiment'. *The Cluster and Phoenix Missions.* Springer, pp 107-136.

Cornilleau-Wehrlin, N., Solomon, J., Korth, A. and Kremser, G. (1993) 'Generation mechanism of plasmaspheric ELF/VLF hiss: A statistical study from GEOS 1 data', *Journal of Geophysical Research: Space Physics*, 98(A12), pp. 21471-21479.

Cornwall, J. M., Coroniti, F. V. and Thorne, R. M. (1970) 'Turbulent loss of ring current protons', *Journal of Geophysical Research*, 75(25), pp. 4699-4709.

Cowley, S. W. H. and Lockwood, M. (1992) 'Excitation and decay of solar wind-driven flows in the magnetosphere-ionophere system', *Annales Geophysicae*, 10, pp. 103-115.

Credland, J., Mecke, G. and Ellwood, J. (1997) 'The Cluster mission: ESA's spacefleet to the magnetosphere'. *The Cluster and Phoenix Missions.* Springer, pp 33-64.

Daglis, I. A. (2001) 'Space storms, ring current and space-atmosphere coupling'. *Space storms and space weather hazards.* Springer, pp 1-42.

Daglis, I. A. and Axford, W. I. (1996) 'Fast ionospheric response to enhanced activity in geospace: Ion feeding of the inner magnetotail', *Journal of Geophysical Research: Space Physics*, 101(A3), pp. 5047-5065.

Daglis, I. A. and Kozyra, J. U. (2002) 'Outstanding issues of ring current dynamics', *Journal of Atmospheric and Solar-Terrestrial Physics*, 64(2), pp. 253-264.

Daglis, I. A., Thorne, R. M., Baumjohann, W. and Orsini, S. (1999) 'The terrestrial ring current: Origin, formation, and decay', *Reviews of Geophysics*, 37(4), pp. 407-438.

Dandouras, I. (2013) 'Detection of a plasmaspheric wind in the Earth's magnetosphere by the Cluster spacecraft', *Annales Geophysicae*. Copernicus GmbH, p. 1143.

Dandouras, I., Pierrard, V., Goldstein, J., Vallat, C., Parks, G. K., Rème, H., Gouillart, C., Sevestre, F., McCarthy, M. and Kistler, L. M. (2005) 'Multipoint Observations of Ionic Structures in the Plasmasphere by CLUSTER—CIS and Comparisons with IMAGE-EUV Observations and with Model Simulations', *Inner Magnetosphere Interactions: New Perspectives from Imaging*, pp. 23-53.

Darrouzet, F., Gallagher, D. L., André, N., Carpenter, D. L., Dandouras, I., Décréau, P. M., De Keyser, J., Denton, R. E., Foster, J. C. and Goldstein, J. (2009) 'Plasmaspheric density structures and dynamics: Properties observed by the CLUSTER and IMAGE missions', *Space science reviews*, 145(1-2), pp. 55-106.

Darrouzet, F., Pierrard, V., Benck, S., Lointier, G., Cabrera, J., Borremans, K., Ganushkina, N. Y. and Keyser, J. D. (2013) 'Links between the plasmapause and the radiation belt boundaries as observed by the instruments CIS, RAPID, and WHISPER onboard Cluster', *Journal of Geophysical Research: Space Physics*, 118(7), pp. 4176-4188.

Davis, T. N. and Sugiura, M. (1966) 'Auroral electrojet activity index AE and its universal time variations', *Journal of Geophysical Research*, 71(3), pp. 785-801.

Delcourt, D. (2002) 'Particle acceleration by inductive electric fields in the inner magnetosphere', *Journal of Atmospheric and Solar-Terrestrial Physics*, 64(5), pp. 551-559.

Dessler, A. J. and Parker, E. N. (1959) 'Hydromagnetic theory of geomagnetic storms', *Journal of Geophysical Research*, 64(12), pp. 2239-2252.

Draper, N. R. and Smith, H. (1998) 'Fitting a straight line by least squares', *Applied Regression Analysis, Third Edition*, pp. 15-46.

Dungey, J. W. (1961) 'Interplanetary magnetic field and the auroral zones', *Physical Review Letters*, 6(2), p. 47.

Echer, E., Gonzalez, W., Tsurutani, B. and Gonzalez, A. (2008) 'Interplanetary conditions causing intense geomagnetic storms (Dst≤− 100 nT) during solar cycle 23 (1996–2006)', *Journal of Geophysical Research: Space Physics*, 113(A5).

Elkington, S. R., Hudson, M. K. and Chan, A. A. (1999) 'Acceleration of relativistic electrons via drift-resonant interaction with toroidal-mode Pc-5 ULF oscillations', *Geophysical research letters*, 26(21), pp. 3273-3276.

Elkington, S. R., Hudson, M. K. and Chan, A. A. (2003) 'Resonant acceleration and diffusion of outer zone electrons in an asymmetric geomagnetic field', *Journal of Geophysical Research: Space Physics*, 108(A3).

Engebretson, M., Glassmeier, K. H., Stellmacher, M., Hughes, W. J. and Lühr, H. (1998) 'The dependence of high-latitude PcS wave power on solar wind velocity and on the phase of high-speed solar wind streams', *Journal of Geophysical Research: Space Physics*, 103(A11), pp. 26271-26283.

Engebretson, M., Keiling, A., Fornacon, K.-H., Cattell, C., Johnson, J., Posch, J., Quick, S., Glassmeier, K.-H., Parks, G. and Reme, H. (2007) 'Cluster observations of Pc 1–2 waves and associated ion distributions during the October and November 2003 magnetic storms', *Planetary and Space Science*, 55(6), pp. 829-848.

Engwall, E., Eriksson, A. I., Cully, C. M., André, M., Puhl-Quinn, P., Vaith, H. and Torbert, R. (2009) 'Survey of cold ionospheric outflows in the magnetotail', *Annales Geophysicae*. Copernicus GmbH, pp. 3185-3201.

Engwall, E., Eriksson, A. I., Cully, C. M., André, M., Torbert, R. and Vaith, H. (2009b) 'Earth's ionospheric outflow dominated by hidden cold plasma', *Nature Geoscience*, 2(1), pp. 24-27.

Escoubet, C. P., Schmidt, R. and Goldstein, M. L. (1997) 'Cluster-Science and mission overview'. *The Cluster and Phoenix Missions.* Springer, pp 11-32.

Evans, D. S. and Greer, M. S. (2000) *Polar Orbiting Environmental Satellite Space Environment Monitor-2: Instrument Description and Archive Data Documentation.* US Department of Commerce, National Oceanic and Atmospheric Administration, Oceanic and Atmospheric Research Laboratories, Space Environment Center.

Feldstein, Y. I. (1992) 'Modelling of the magnetic field of magnetospheric ring current as a function of interplanetary medium parameters', *Space Science Reviews*, 59(1-2), pp. 83-165.

Feldstein, Y. I., Levitin, A., Golyshev, S., Dremukhina, L., Vestchezerova, U., Valchuk, T. and Grafe, A. (1994) 'Ring current and auroral electrojets in connection with interplanetary medium parameters during magnetic storm', *Annales Geophysicae*. Springer, pp. 602-611.

Fok, M. C., Kozyra, J. U., Nagy, A. F., Cravens, T. E. (1991) 'Life-time of ring current particles due to Coulomb collisions in the plasmasphere', *Journal of Geophysical Research: Space Physics*, 96(A5), pp. 7861-7867.

Fraser, B., Singer, H., Hughes, W., Wygant, J., Anderson, R. and Hu, Y. (1996) 'CRRES Poynting vector observations of electromagnetic ion cyclotron waves near the plasmapause', *Journal of Geophysical Research: Space Physics*, 101(A7), pp. 15331-15343.

Friedel, R., Reeves, G. and Obara, T. (2002) 'Relativistic electron dynamics in the inner magnetosphere—A review', *Journal of Atmospheric and Solar-Terrestrial Physics*, 64(2), pp. 265-282.

Gary, S. P. and Wang, J. (1996) 'Whistler instability: Electron anisotropy upper bound', *Journal of Geophysical Research: Space Physics*, 101(A5), pp. 10749-10754.

Gazey, N., Lockwood, M., Grande, M., Perry, C., Smith, P., Coles, S., Aylward, A., Bunting, R., Opgenoorth, H. and Wilken, B. (1997) 'EISCAT/CRRES observations: Nightside

ionospheric ion outflow and oxygen-rich substorm injections', *Annales Geophysicae*. Springer, pp. 1032-1043.

Gjerloev, J. W. (2012) 'The SuperMAG data processing technique', *Journal of Geophysical Research: Space Physics*, 117(A9).

Glatzmaier, G. A. and Roberts, P. H. (1996) 'Rotation and Magnetism of Earth's Inner Core', *Science (New York, N.Y.)*, 274(5294), pp. 1887-1891.

Goldstein, B. E. and Tsurutani, B. T. (1984) 'Wave normal directions of chorus near the equatorial source region', *Journal of Geophysical Research: Space Physics*, 89(A5), pp. 2789-2810.

Goldstein, J., Sandel, B., Hairston, M. and Reiff, P. (2003) 'Control of plasmaspheric dynamics by both convection and sub-auroral polarization stream', *Geophysical research letters*, 30(24).

Gonzalez, W. D., Gonzalez, A. L. C. and Tsurutani, B. T. (1990) 'Dual-peak solar cycle distribution of intense geomagnetic storms', *Planetary and Space Science*, 38(2), pp. 181-187.

Gonzalez, W. D., Joselyn, J. A., Kamide, Y., Kroehl, H. W., Rostoker, G., Tsurutani, B. T. and Vasyliunas, V. M. (1994) 'What is a geomagnetic storm?', *Journal of Geophysical Research: Space Physics*, 99(A4), pp. 5771-5792.

Gonzalez, W. D., Tsurutani, B. T. and De Gonzalez, A. L. C. (1999) 'Interplanetary origin of geomagnetic storms', *Space Science Reviews*, 88(3-4), pp. 529-562.

Gonzalez, W. D., Tsurutani, B. T., Gonzalez, A. L. C., Smith, E. J., Tang, F. and Akasofu, S. I. (1989) 'Solar wind-magnetosphere coupling during intense magnetic storms (1978-1979)', *Journal of Geophysical Research: Space Physics*, 94(A7), pp. 8835-8851.

Gosling, J. T. (1990) 'Coronal mass ejections and magnetic flux ropes in interplanetary space', *Physics of Magnetic Flux Ropes*, pp. 343-364.

Gosling, J. T. and Pizzo, V. J. (1999) 'Formation and evolution of corotating interaction regions and their three dimensional structure'. *Corotating Interaction Regions.* Springer, pp 21-52.

Green, J. and Kivelson, M. (2001) 'A tale of two theories: How the adiabatic response and ULF waves affect relativistic electrons', *Journal of Geophysical Research: Space Physics*, 106(A11), pp. 25777-25791.

Green, J. C. and Kivelson, M. (2004) 'Relativistic electrons in the outer radiation belt: Differentiating between acceleration mechanisms', *Journal of Geophysical Research: Space Physics*, 109(A3).

Greenspan, M. E. and Hamilton, D. C. (2000) 'A test of the Dessler-Parker-Sckopke relation during magnetic storms', *Journal of Geophysical Research: Space Physics*, 105(A3), pp. 5419-5430.

Grew, R., Menk, F., Clilverd, M. and Sandel, B. (2007) 'Mass and electron densities in the inner magnetosphere during a prolonged disturbed interval', *Geophysical research letters*, 34(2).

Gustafsson, G., Boström, R., Holback, B., Holmgren, G., Lundgren, A., Stasiewicz, K., Åhlén, L., Mozer, F. S., Pankow, D. and Harvey, P. (1997) 'The electric field and wave experiment for the Cluster mission'. *The Cluster and Phoenix Missions.* Springer, pp 137-156.

Häkkinen, L. V. T., Pulkkinen, T. I., Nevanlinna, H., Pirjola, R. J. and Tanskanen, E. I. (2002) 'Effects of induced currents on Dst and on magnetic variations at midlatitude stations', *Journal of Geophysical Research: Space Physics*, 107(A1).

Halford, A., Fraser, B. and Morley, S. (2010) 'EMIC wave activity during geomagnetic storm and nonstorm periods: CRRES results', *Journal of Geophysical Research: Space Physics*, 115(A12).

Hamilton, D., Gloeckler, G., Ipavich, F., Stüdemann, W., Wilken, B. and Kremser, G. (1988) 'Ring current development during the great geomagnetic storm of February 1986', *Journal of Geophysical Research: Space Physics*, 93(A12), pp. 14343-14355.

Hietala, H., Kilpua, E. K. J., Turner, D. L. and Angelopoulos, V. (2014) 'Depleting effects of ICME-driven sheath regions on the outer electron radiation belt', *Geophysical Research Letters*, 41(7), pp. 2258-2265.

Hirahara, M., Nakamura, M., Terasawa, T., Mukai, T., Saito, Y., Yamamoto, T., Nishida, A., Machida, S. and Kokubun, S. (1994) 'Acceleration and heating of cold ion beams in the plasma sheet boundary layer observed with Geotail', *Geophysical research letters*, 21(25), pp. 3003-3006.

Hirahara, M., Seki, K., Saito, Y. and Mukai, T. (2004) 'Periodic emergence of multicomposition cold ions modulated by geomagnetic field line oscillations in

the near- Earth magnetosphere', *Journal of Geophysical Research: Space Physics*, 109, pp. n/a-n/a. doi: 10.1029/2003JA010141.

Horne, R., Glauert, S. and Thorne, R. (2003a) 'Resonant diffusion of radiation belt electrons by whistler-mode chorus', *Geophysical research letters*, 30(9).

Horne, R. and Thorne, R. (2003) 'Relativistic electron acceleration and precipitation during resonant interactions with whistler-mode chorus', *Geophysical research letters*, 30(10).

Horne, R. B. (2002) 'The contribution of wave-particle interactions to electron loss and acceleration in the Earth's radiation belts during geomagnetic storms'.

Horne, R. B., Meredith, N. P., Thorne, R. M., Heynderickx, D., Iles, R. H. and Anderson, R. R. (2003b) 'Evolution of energetic electron pitch angle distributions during storm time electron acceleration to megaelectronvolt energies', *Journal of Geophysical Research: Space Physics*, 108(A1).

Horne, R. B. and Thorne, R. M. (1993) 'On the preferred source location for the convective amplification of ion cyclotron waves', *Journal of Geophysical Research: Space Physics*, 98(A6), pp. 9233-9247.

Horne, R. B. and Thorne, R. M. (1994) 'Convective instabilities of electromagnetic ion cyclotron waves in the outer magnetosphere', *Journal of Geophysical Research: Space Physics*, 99(A9), pp. 17259-17273.

Horne, R. B. and Thorne, R. M. (1998) 'Potential waves for relativistic electron scattering and stochastic acceleration during magnetic storms', *Geophysical Research Letters*, 25(15), pp. 3011-3014.

Horne, R. B., Thorne, R. M., Shprits, Y. Y., Meredith, N. P., Glauert, S. A., Smith, A. J., Kanekal, S. G., Baker, D. N., Engebretson, M. J. and Posch, J. L. (2005) 'Wave acceleration of electrons in the Van Allen radiation belts', *Nature*, 437(7056), pp. 227-230.

Hutchinson, J. A., Wright, D. and Milan, S. (2011) 'Geomagnetic storms over the last solar cycle: A superposed epoch analysis', *Journal of Geophysical Research: Space Physics*, 116(A9).

Huttunen, K. E. J. and Koskinen, H. E. J. (2004) 'Importance of post-shock streams and sheath region as drivers of intense magnetospheric storms and high-latitude activity', *Annales Geophysicae*, 22, pp. 1729-1738.

Iles, R., Fazakerley, A., Johnstone, A., Meredith, N. and Bühler, P. (2002) 'The relativistic electron response in the outer radiation belt during magnetic storms', *Annales Geophysicae*. pp. 957-965.

Ipavich, F., Galvin, A., Gloeckler, G., Hovestadt, D., Klecker, B. and Scholer, M. (1984) 'Energetic (> 100 keV) O+ ions in the plasma sheet', *Geophysical research letters*, 11(5), pp. 504-507.

Johnstone, A. D., Alsop, C., Burge, S., Carter, P. J., Coates, A. J., Coker, A. J., Fazakerley, A. N., Grande, M., Gowen, R. A. and Gurgiolo, C. (1997) 'PEACE: A plasma electron and current experiment'. *The Cluster and Phoenix Missions.* Springer, pp 351-398.

Jordanova, V., Farrugia, C., Quinn, J., Thorne, R., Ogilvie, K., Lepping, R., Lu, G., Lazarus, A., Thomsen, M. and Belian, R. (1998) 'Effect of wave-particle interactions on ring current evolution for January 10–11, 1997: Initial results', *Geophysical research letters*, 25(15), pp. 2971-2974.

Jordanova, V., Kistler, L., Farrugia, C. and Torbert, R. (2001) 'Effects of inner magnetospheric convection on ring current dynamics', *AGU Spring Meeting Abstracts*.

Jordanova, V., Kistler, L., Kozyra, J., Khazanov, G. and Nagy, A. (1996) 'Collisional losses of ring current ions', *Journal of Geophysical Research: Space Physics*, 101(A1), pp. 111-126.

Karinen, A. and Mursula, K. (2005) 'A new reconstruction of the D st index for 1932-2002', *Annales Geophysicae*, 23, pp. 475-485.

Karinen, A. and Mursula, K. (2006) 'Correcting the Dst index: Consequences for absolute level and correlations', *Journal of Geophysical Research: Space Physics*, 111(A8).

Karinen, A., Mursula, K., Takalo, J. and Ulich, T. (2001) 'An erroneous Dst index in 1971', *Solspa 2001, Proceedings of the Second Solar Cycle and Space Weather Euroconference*. 2002. pp. 443-446.

Kennel, C. F. and Petschek, H. (1966) 'Limit on stably trapped particle fluxes', *Journal of Geophysical Research*, 71(1), pp. 1-28.

Kilpua, E. K. J., Hietala, H., Turner, D. L., Koskinen, H. E. J., Pulkkinen, T. I., Rodriguez, J. V., Reeves, G. D., Claudepierre, S. G. and Spence, H. E. (2015) 'Unraveling the

drivers of the storm time radiation belt response', *Geophysical Research Letters*, 42(9), pp. 3076-3084.

Kim, H. J. and Chan, A. A. (1997) 'Fully adiabatic changes in storm time relativistic electron fluxes', *Journal of Geophysical Research: Space Physics*, 102(A10), pp. 22107-22116.

Kistler, L., Ipavich, F., Hamilton, D., Gloeckler, G., Wilken, B., Kremser, G. and Stüdemann, W. (1989) 'Energy spectra of the major ion species in the ring current during geomagnetic storms', *Journal of Geophysical Research: Space Physics*, 94(A4), pp. 3579-3599.

Kistler, L., Klecker, B., Jordanova, V., Möbius, E., Popecki, M., Patel, D., Sauvaud, J., Rème, H., Di Lellis, A. and Korth, A. (1999) 'Testing electric field models using ring current ion energy spectra from the Equator-S ion composition (ESIC) instrument', *Annales Geophysicae*. Springer, pp. 1611-1621.

Kivelson, M. G. and Russell, C. T. (1995) *Introduction to space physics.* Cambridge university press.

Koons, H. C. and Roeder, J. L. (1990) 'A survey of equatorial magnetospheric wave activity between 5 and 8 RE', *Planetary and Space Science*, 38(10), pp. 1335-1341.

Kotova, G. (2007) 'The Earth's plasmasphere: state of studies (a review)', *Geomagnetism and Aeronomy*, 47(4), pp. 409-422.

Kozyra, J., Cravens, T., Nagy, A., Fontheim, E. and Ong, R. (1984) 'Effects of energetic heavy ions on electromagnetic ion cyclotron wave generation in the plasmapause region', *Journal of Geophysical Research: Space Physics*, 89(A4), pp. 2217-2233.

Kozyra, J., Jordanova, V., Borovsky, J., Thomsen, M., Knipp, D., Evans, D., McComas, D. and Cayton, T. (1998) 'Effects of a high-density plasma sheet on ring current development during the November 2–6, 1993, magnetic storm', *Journal of Geophysical Research: Space Physics*, 103(A11), pp. 26285-26305.

Kozyra, J., Jordanova, V., Home, R. and Thorne, R. (1997) 'Modeling of the contribution of electromagnetic ion cyclotron (EMIC) waves to stormtime ring current erosion', *Magnetic storms*, pp. 187-202.

Kozyra, J. U., Leimohn, M. W., Ridley, A., Thomsen, M. F. and Borovsky, J. (2000) 'Storm geoeffectiveness and ring current modeling of the September 1999 campaign storms'. *S-RAMP*. Sapporo: 2000. p. 176.

Lagrange, J.-L. (1772) 'Essai sur le probleme des trois corps', *Prix de l'académie royale des Sciences de paris*, 9, p. 292.

Legrand, J.-P. and Simon, P. A. (1991) 'A two-component solar cycle', *Solar Physics*, 131(1), pp. 187-209.

Lemaire, J. (2001) 'The formation of the light-ion trough and peeling off the plasmasphere', *Journal of Atmospheric and Solar-Terrestrial Physics*, 63(11), pp. 1285-1291.

Lemaire, J. and Schunk, R. (1992) 'Plasmaspheric wind', *Journal of atmospheric and terrestrial physics*, 54(3-4), pp. 467-477.

Lepping, R. P., Acũna, M. H., Burlaga, L. F., Farrell, W. M., Slavin, J. A., Schatten, K. H., Mariani, F., Ness, N. F., Neubauer, F. M. and Whang, Y. C. (1995) 'The WIND magnetic field investigation', *Space Science Reviews*, 71(1-4), pp. 207-229.

Li, L., Cao, J., Zhou, G. and Li, X. (2009) 'Statistical roles of storms and substorms in changing the entire outer zone relativistic electron population', *Journal of Geophysical Research: Space Physics*, 114(A12).

Li, W., Ni, B., Thorne, R., Bortnik, J., Green, J., Kletzing, C., Kurth, W. and Hospodarsky, G. (2014) 'Calculation of whistler-mode wave intensity using energetic electron precipitation', *General Assembly and Scientific Symposium (URSI GASS), 2014 XXXIth URSI*. IEEE, pp. 1-4.

Li, W., Shprits, Y. and Thorne, R. (2007) 'Dynamic evolution of energetic outer zone electrons due to wave-particle interactions during storms', *Journal of Geophysical Research: Space Physics*, 112(A10).

Li, W., Thorne, R., Bortnik, J., Shprits, Y., Nishimura, Y., Angelopoulos, V., Chaston, C., Le Contel, O. and Bonnell, J. (2011a) 'Typical properties of rising and falling tone chorus waves', *Geophysical Research Letters*, 38(14).

Li, X., Baker, D., Elkington, S., Temerin, M., Reeves, G., Belian, R., Blake, J., Singer, H., Peria, W. and Parks, G. (2003) 'Energetic particle injections in the inner magnetosphere as a response to an interplanetary shock', *Journal of atmospheric and solar-terrestrial physics*, 65(2), pp. 233-244.

Li, X., Baker, D., O'Brien, T., Xie, L. and Zong, Q. (2006) 'Correlation between the inner edge of outer radiation belt electrons and the innermost plasmapause location', *Geophysical research letters*, 33(14).

Li, X., Baker, D., Temerin, M., Larson, D., Lin, R., Reeves, G., Looper, M., Kanekal, S. and Mewaldt, R. (1997) 'Are energetic electrons in the solar wind the source of the outer radiation belt?', *Geophysical research letters*, 24(8), pp. 923-926.

Li, X., Baker, D., Temerin, M., Reeves, G., Friedel, R. and Shen, C. (2005) 'Energetic electrons, 50 keV to 6 MeV, at geosynchronous orbit: Their responses to solar wind variations', *Space Weather*, 3(4).

Li, X., Roth, I., Temerin, M., Wygant, J., Hudson, M. and Blake, J. (1993) 'Simulation of the prompt energization and transport of radiation belt particles during the March 24, 1991 SSC', *Geophysical Research Letters*, 20(22), pp. 2423-2426.

Li, X., Temerin, M., Baker, D. and Reeves, G. (2011b) 'Behavior of MeV electrons at geosynchronous orbit during last two solar cycles', *Journal of Geophysical Research: Space Physics*, 116(A11).

Li, X. and Temerin, M. A. (2001) 'The electron radiation belt', *Space Science Reviews*, 95(1-2), pp. 569-580.

Liao, J., Kistler, L., Mouikis, C., Klecker, B. and Dandouras, I. (2012) 'Solar cycle dependence of the cusp O+ access to the near-Earth magnetotail', *Journal of Geophysical Research: Space Physics*, 117(A10).

Liemohn, M., Kozyra, J., Jordanova, V., Khazanov, G., Thomsen, M. and Cayton, T. (1999) 'Analysis of early phase ring current recovery mechanisms during geomagnetic storms', *Geophysical research letters*, 26(18), pp. 2845-2848.

Liemohn, M., Kozyra, J., Thomsen, M., Roeder, J., Lu, G., Borovsky, J. and Cayton, T. (2001) 'Dominant role of the asymmetric ring current in producing the stormtime Dst', *Journal of Geophysical Research: Space Physics*, 106(A6), pp. 10883-10904.

Lin, R. L., Zhang, J. C., Allen, R., Kistler, L., Mouikis, C., Gong, J. C., Liu, S. Q., Shi, L. Q., Klecker, B. and Sauvaud, J. A. (2014) 'Testing linear theory of EMIC waves in the inner magnetosphere: Cluster observations', *Journal of Geophysical Research: Space Physics*, 119(2), pp. 1004-1027.

Lorentzen, K., Blake, J., Inan, U. and Bortnik, J. (2001) 'Observations of relativistic electron microbursts in association with VLF chorus', *Journal of Geophysical Research: Space Physics*, 106(A4), pp. 6017-6027.

Lorentzen, K., McCarthy, M., Parks, G., Foat, J., Millan, R., Smith, D., Lin, R. and Treilhou, J. (2000) 'Precipitation of relativistic electrons by interaction with electromagnetic ion cyclotron waves', *Journal of Geophysical Research: Space Physics*, 105(A3), pp. 5381-5389.

Lui, A. T., McEntire, R. and Krimigis, S. (1987) 'Evolution of the ring current during two geomagnetic storms', *Journal of Geophysical Research: Space Physics*, 92(A7), pp. 7459-7470.

Lyatsky, W. and Khazanov, G. V. (2008) 'Effect of geomagnetic disturbances and solar wind density on relativistic electrons at geostationary orbit', *Journal of Geophysical Research: Space Physics*, 113(A8).

Lyatsky, W., Tan, A. and Khazanov, G. (2006) 'A simple analytical model for subauroral polarization stream (SAPS)', *Geophysical research letters*, 33(19).

Lyons, L. R. and Thorne, R. M. (1973) 'Equilibrium structure of radiation belt electrons', *Journal of Geophysical Research*, 78(13), pp. 2142-2149.

Mathie, R. and Mann, I. (2000a) 'A correlation between extended intervals of ULF wave power and storm-time geosynchronous relativistic electron flux enhancements', *Geophysical research letters*, 27(20), pp. 3261-3264.

Mathie, R. and Mann, I. (2000b) 'Observations of Pc5 field line resonance azimuthal phase speeds: A diagnostic of their excitation mechanism', *Journal of Geophysical Research: Space Physics*, 105(A5), pp. 10713-10728.

Mathie, R. and Mann, I. (2001) 'On the solar wind control of Pc5 ULF pulsation power at mid-latitudes: Implications for MeV electron acceleration in the outer radiation belt', *Journal of Geophysical Research: Space Physics*, 106(A12), pp. 29783-29796.

Mauk, B. (1986) 'Quantitative modeling of the "convection surge" mechanism of ion acceleration', *Journal of Geophysical Research: Space Physics*, 91(A12), pp. 13423-13431.

Mauk, B. and McPherron, R. (1980) 'An experimental test of the electromagnetic ion cyclotron instability within the Earth's magnetosphere', *The Physics of Fluids*, 23(10), pp. 2111-2127.

McComas, D. J., Bame, S. J., Barker, P., Feldman, W. C., Phillips, J. L., Riley, P. and Griffee, J. W. (1998) 'Solar wind electron proton alpha monitor (SWEPAM) for the Advanced Composition Explorer'. *The Advanced Composition Explorer Mission.* Springer, pp 563-612.

McPherron, R., Baker, D. and Crooker, N. (2009) 'Role of the Russell–McPherron effect in the acceleration of relativistic electrons', *Journal of Atmospheric and Solar-Terrestrial Physics*, 71(10), pp. 1032-1044.

Meier, M.-M., Belian, R. D., Cayton, T. E., Christensen, R. A., Garcia, B., Grace, K. M., Ingraham, J. C., Laros, J. G. and Reeves, G. D. (1996) 'The energy spectrometer for particles (ESP): Instrument description and orbital performance', *AIP Conference proceedings*, pp. 203-210.

Meredith, N. P., Cain, M., Horne, R. B., Thorne, R. M., Summers, D. and Anderson, R. R. (2003a) 'Evidence for chorus-driven electron acceleration to relativistic energies from a survey of geomagnetically disturbed periods', *Journal of Geophysical Research: Space Physics*, 108(A6).

Meredith, N. P., Horne, R., Johnstone, A. D. and Anderson, R. R. (2000) 'The temporal evolution of electron distributions and associated wave activity following substorm injections in the inner magnetosphere', *Journal of Geophysical Research*, 105(A6), pp. 12,907-912,917.

Meredith, N. P., Horne, R. B. and Anderson, R. R. (2001) 'Substorm dependence of chorus amplitudes: Implications for the acceleration of electrons to relativistic energies', *Journal of Geophysical Research: Space Physics*, 106(A7), pp. 13165-13178.

Meredith, N. P., Horne, R. B., Glauert, S. A. and Anderson, R. R. (2007) 'Slot region electron loss timescales due to plasmaspheric hiss and lightning-generated whistlers', *Journal of Geophysical Research: Space Physics*, 112(A8).

Meredith, N. P., Horne, R. B., Glauert, S. A., Thorne, R. M., Summers, D., Albert, J. M. and Anderson, R. R. (2006) 'Energetic outer zone electron loss timescales during

low geomagnetic activity', *Journal of Geophysical Research: Space Physics*, 111(A5).

Meredith, N. P., Horne, R. B., Iles, R. H., Thorne, R. M., Heynderickx, D. and Anderson, R. R. (2002) 'Outer zone relativistic electron acceleration associated with substorm-enhanced whistler mode chorus', *Journal of Geophysical Research: Space Physics*, 107(A7).

Meredith, N. P., Horne, R. B., Sicard-Piet, A., Boscher, D., Yearby, K. H., Li, W. and Thorne, R. M. (2012) 'Global model of lower band and upper band chorus from multiple satellite observations', *Journal of Geophysical Research: Space Physics*, 117(A10).

Meredith, N. P., Horne, R. B., Thorne, R. M. and Anderson, R. R. (2003b) 'Favored regions for chorus-driven electron acceleration to relativistic energies in the Earth's outer radiation belt', *Geophysical Research Letters*, 30(16).

Meredith, N. P., Horne, R. B., Thorne, R. M. and Anderson, R. R. (2009) 'Survey of upper band chorus and ECH waves: Implications for the diffuse aurora', *Journal of Geophysical Research: Space Physics*, 114(A7).

Meredith, N. P., Horne, R. B., Thorne, R. M., Summers, D. and Anderson, R. R. (2004) 'Substorm dependence of plasmaspheric hiss', *Journal of Geophysical Research: Space Physics*, 109(A6).

Meredith, N. P., Thorne, R. M., Horne, R. B., Summers, D., Fraser, B. J. and Anderson, R. R. (2003c) 'Statistical analysis of relativistic electron energies for cyclotron resonance with EMIC waves observed on CRRES', *Journal of Geophysical Research: Space Physics*, 108(A6).

Milan, S. E., Gosling, J. S. and Hubert, B. (2012) 'Relationship between interplanetary parameters and the magnetopause reconnection rate quantified from observations of the expanding polar cap', *Journal of Geophysical Research: Space Physics*, 117(A3).

Milan, S. E., Hutchinson, J., Boakes, P. and Hubert, B. (2009) 'Influences on the radius of the auroral oval', *Annales Geophysicae*. Copernicus GmbH, pp. 2913-2924.

Milan, S. E., Provan, G. and Hubert, B. (2007) 'Magnetic flux transport in the Dungey cycle: A survey of dayside and nightside reconnection rates', *Journal of Geophysical Research: Space Physics*, 112(A1).

Millan, R. M., Lin, R., Smith, D., Lorentzen, K. and McCarthy, M. (2002) 'X-ray observations of MeV electron precipitation with a balloon-borne germanium spectrometer', *Geophysical research letters*, 29(24).

Miyoshi, Y. and Kataoka, R. (2005) 'Ring current ions and radiation belt electrons during geomagnetic storms driven by coronal mass ejections and corotating interaction regions', *Geophysical research letters*, 32(21).

Miyoshi, Y. and Kataoka, R. (2008) 'Flux enhancement of the outer radiation belt electrons after the arrival of stream interaction regions', *Journal of Geophysical Research: Space Physics*, 113(A3).

Miyoshi, Y., Kataoka, R., Kasahara, Y., Kumamoto, A., Nagai, T. and Thomsen, M. (2013) 'High-speed solar wind with southward interplanetary magnetic field causes relativistic electron flux enhancement of the outer radiation belt via enhanced condition of whistler waves', *Geophysical Research Letters*, 40(17), pp. 4520-4525.

Miyoshi, Y., Morioka, A., Misawa, H., Obara, T., Nagai, T. and Kasahara, Y. (2003) 'Rebuilding process of the outer radiation belt during the 3 November 1993 magnetic storm: NOAA and Exos-D observations', *Journal of Geophysical Research: Space Physics*, 108(A1).

Möbius, E., Hovestadt, D., Klecker, B., Scholer, M., Ipavich, F., Carlson, C. and Lin, R. (1986) 'A burst of energetic O+ ions during an upstream particle event', *Geophysical research letters*, 13(13), pp. 1372-1375.

Moldwin, M. B., Downward, L., Rassoul, H. K., Amin, R. and Anderson, R. R. (2002) 'A new model of the location of the plasmapause: CRRES results', *Journal of Geophysical Research: Space Physics*, 107(A11).

Mursula, K., Holappa, L. and Karinen, A. (2008) 'Correct normalization of the Dst index', *Astrophysics and Space Sciences Transactions*, 4(2), pp. 41-45.

Mursula, K., Holappa, L. and Karinen, A. (2011) 'Uneven weighting of stations in the Dst index', *Journal of Atmospheric and Solar-Terrestrial Physics*, 73(2), pp. 316-322.

Mursula, K. and Karinen, A. (2005) 'Explaining and correcting the excessive semiannual variation in the Dst index', *Geophysical Research Letters*, 32(14).

Muzzio, J. and Angerami, J. J. (1972) 'Ogo 4 observations of extremely low frequency hiss', *Journal of Geophysical Research*, 77(7), pp. 1157-1173.

Nakamura, R., Isowa, M., Kamide, Y., Baker, D. N., Blake, J. B. and Looper, M. (2000) 'SAMPEX observations of precipitation bursts in the outer', *Journal of geophysical research*, 105(A7), pp. 15,875-815,885.

Newell, P. T. and Gjerloev, J. W. (2012) 'SuperMAG-based partial ring current indices', *Journal of Geophysical Research: Space Physics*, 117(A5).

Newell, P. T., Sotirelis, T., Liou, K., Meng, C.-I., and Rich, F. J. (2007), 'A nearly universal solar wind–magnetosphere coupling function inferred from 10 magnetospheric state variables', *Journal of Geophysical Research: Space Physics*, 112(A1)

Newell, P., Sotirelis, T. and Wing, S. (2009) 'Diffuse, monoenergetic, and broadband aurora: The global precipitation budget', *Journal of Geophysical Research: Space Physics*, 114(A9).

Newell, P. T., Liou, K., Sotirelis, T. and Meng, C. I. (2001) 'Polar Ultraviolet Imager observations of global auroral power as a function of polar cap size and magnetotail stretching', *Journal of Geophysical Research: Space Physics*, 106(A4), pp. 5895-5905.

Ni, B., Thorne, R. M., Shprits, Y. Y. and Bortnik, J. (2008) 'Resonant scattering of plasma sheet electrons by whistler-mode chorus: Contribution to diffuse auroral precipitation', *Geophysical Research Letters*, 35(11).

Nishimura, Y., Bortnik, J., Li, W., Thorne, R. M., Lyons, L. R., Angelopoulos, V., Mende, S., Bonnell, J., Le Contel, O. and Cully, C. (2010) 'Identifying the driver of pulsating aurora', *Science*, 330(6000), pp. 81-84.

Nosé, M., Lui, A., Ohtani, S., Mauk, B., McEntire, R., Williams, D., Mukai, T. and Yumoto, K. (2000) 'Acceleration of oxygen ions of ionospheric origin in the near-Earth magnetotail during substorms', *Journal of Geophysical Research: Space Physics*, 105(A4), pp. 7669-7677.

Nurunnabi, A., West, G. and Belton, D., (2013) 'Robust locally weighted regression for ground surface extraction in mobile laser scanning 3D data', *ISPRS Workshop Laser Scanning,* pp. 217-222.

O'Brien, T., Looper, M. and Blake, J. (2004) 'Quantification of relativistic electron microburst losses during the GEM storms', *Geophysical research letters*, 31(4).

O'Brien, T., Lorentzen, K., Mann, I., Meredith, N., Blake, J., Fennell, J., Looper, M., Milling, D. and Anderson, R. (2003) 'Energization of relativistic electrons in the presence of ULF power and MeV microbursts: Evidence for dual ULF and VLF acceleration', *Journal of Geophysical Research: Space Physics*, 108(A8).

O'Brien, T., McPherron, R., Sornette, D., Reeves, G., Friedel, R. and Singer, H. (2001) 'Which magnetic storms produce relativistic electrons at geosynchronous orbit?', *Journal of Geophysical Research: Space Physics*, 106(A8), pp. 15533-15544.

O'Brien, T. P. and McPherron, R. L. (2000) 'An empirical phase space analysis of ring current dynamics: Solar wind control of injection and decay', *Journal of Geophysical Research: Space Physics*, 105(A4), pp. 7707-7719.

O'Brien, T., Shprits, Y. and Moldwin, M. (2008) 'Eigenmode analysis of pitch-angle diffusion of energetic electrons in the outer zone', *Journal of Atmospheric and Solar-Terrestrial Physics*, 70(14), pp. 1738-1744.

Obana, Y., Menk, F. W. and Yoshikawa, I. (2010) 'Plasma refilling rates for L= 2.3–3.8 flux tubes', *Journal of Geophysical Research: Space Physics*, 115(A3).

Ogilvie, K. W., Chornay, D. J., Fritzenreiter, R. J., Hunsaker, F., Keller, J., Lobell, J., Miller, G., Scudder, J. D., Sittler Jr, E. C. and Torbert, R. B. (1995) 'SWE, a comprehensive plasma instrument for the Wind spacecraft', *Space Science Reviews*, 71(1-4), pp. 55-77.

Olson, J. V. and Lee, L. (1983) 'Pc1 wave generation by sudden impulses', *Planetary and Space Science*, 31(3), pp. 295-302.

Onsager, T., Green, J., Reeves, G. and Singer, H. (2007) 'Solar wind and magnetospheric conditions leading to the abrupt loss of outer radiation belt electrons', *Journal of Geophysical Research: Space Physics*, 112(A1).

Onsager, T., Rostoker, G., Kim, H. J., Reeves, G., Obara, T., Singer, H. and Smithtro, C. (2002) 'Radiation belt electron flux dropouts: Local time, radial, and particle-energy dependence', *Journal of Geophysical Research: Space Physics*, 107(A11).

Orsini, S., Candidi, M., Stokholm, M. and Balsiger, H. (1990) 'Injection of ionospheric ions into the plasma sheet', *Journal of Geophysical Research: Space Physics*, 95(A6), pp. 7915-7928.

Owens, H. D. and Frank, L. A. (1968) 'Electron omnidirectional intensity contours in the earth's outer radiation zone at the magnetic equator', *Journal of Geophysical Research*, 73(1), pp. 199-208.

Park, C. (1970) 'Whistler observations of the interchange of ionization between the ionosphere and the protonosphere', *Journal of Geophysical Research*, 75(22), pp. 4249-4260.

Paulikas, G. A. and Blake, J. B. (1978) *Effects of the solar wind on magnetospheric dynamics: Energetic electrons at the synchronous orbit.* Wiley Online Library.

Petschek, H. E. (1964) 'Magnetic field annihilation', *NASA Special Publication*, 50, pp. 425.

Pierrard, V., Goldstein, J., André, N., Jordanova, V. K., Kotova, G. A., Lemaire, J. F., Liemohn, M. W. and Matsui, H. (2009) 'Recent progress in physics-based models of the plasmasphere', *Space science reviews*, 145(1-2), pp. 193-229.

Pierrard, V., Khazanov, G., Cabrera, J. and Lemaire, J. (2008) 'Influence of the convection electric field models on predicted plasmapause positions during magnetic storms', *Journal of Geophysical Research: Space Physics*, 113(A8).

Prigancová, A. and Feldstein, Y. I. (1992) 'Magnetospheric storm dynamics in terms of energy output rate', *Planetary and space science*, 40(4), pp. 581-588.

Pulkkinen, A., Bernabeu, E., Thomson, A., Viljanen, A., Pirjola, R., Boteler, D., Eichner, J., Cilliers, P. J., Welling, D., Savani, N. P., Weigel, R. S., Love, J. J., Balch, C., Ngwira, C. M., Crowley, G., Schultz, A., Kataoka, R., Anderson, B., Fugate, D., Simpson, J. J. and MacAlester, M. (2017), 'Geomagnetically induced currents: Science, engineering, and applications readiness', *Space Weather*, 15, pp. 828–856,

Rasinkangas, R. and Mursula, K. (1998) 'Modulation of magnetospheric EMIC waves by Pc 3 pulsations of upstream origin', *Geophysical research letters*, 25(6), pp. 869-872.

Raymer, K. M., S. E. Milan, S. M. Imber, and T. Nagai, (2018), 'Magnetospheric and upstream solar wind influences on the shape and location of the Earth's magnetopause', Unpublished manuscript, University of Leicester, Leicester, Leicestershire.

Reeves, G. and Henderson, M. (2001) 'The storm-substorm relationship- Ion injections in geosynchronous measurements and composite energetic neutral atom images', *Journal of geophysical research*, 106, pp. 5833-5844.

Reeves, G. D., McAdams, K. L., Friedel, R. H. W. and O'Brien, T. P. (2003) 'Acceleration and loss of relativistic electrons during geomagnetic storms', *Geophysical Research Letters*, 30(10).

Reeves, G. D., Morley, S. K., Friedel, R. H. W., Henderson, M. G., Cayton, T. E., Cunningham, G., Blake, J. B., Christensen, R. A. and Thomsen, D. (2011) 'On the relationship between relativistic electron flux and solar wind velocity: Paulikas and Blake revisited', *Journal of Geophysical Research: Space Physics*, 116(A2).

Reme, H., Bosqued, J. M., Sauvaud, J. A., Cros, A., Dandouras, J., Aoustin, C., Bouyssou, J., Camus, T., Cuvilo, J. and Martz, C. (1997) 'The Cluster ion spectrometry (CIS) experiment'. *The Cluster and Phoenix Missions.* Springer, pp 303-350.

Riedler, W., Torkar, K., Rüdenauer, F., Fehringer, M., Pedersen, A., Schmidt, R., Grard, R. J. L., Arends, H., Narheim, B. T. and Troim, J. (1997) 'Active spacecraft potential control'. *The Cluster and Phoenix Missions.* Springer, pp 271-302.

Roberts, W., Horwitz, J., Comfort, R., Chappell, C., Waite, J. and Green, J. (1987) 'Heavy ion density enhancements in the outer plasmasphere', *Journal of Geophysical Research: Space Physics*, 92(A12), pp. 13499-13512.

Rostoker, G., Skone, S. and Baker, D. N. (1998) 'On the origin of relativistic electrons in the magnetosphere associated with some geomagnetic storms', *Geophysical research letters*, 25(19), pp. 3701-3704.

Roux, A., Perraut, S., Rauch, J., Villedary, C. d., Kremser, G., Korth, A. and Young, D. (1982) 'Wave-particle interactions near ΩHe+ observed on board GEOS 1 and 2: 2. Generation of ion cyclotron waves and heating of He+ ions', *Journal of Geophysical Research: Space Physics*, 87(A10), pp. 8174-8190.

Russell, C. T., Lu, G. and Luhmann, J. G. (2000) 'Lessons from the ring current injection during the September 24, 25 storm', *Geophysical Research Letters*, 27(9), pp. 1371-1374.

Russell, C. T. a. and McPherron, R. L. (1973) 'Semiannual variation of geomagnetic activity', *Journal of geophysical research*, 78(1), pp. 92-108.

Sandel, B., Goldstein, J., Gallagher, D. and Spasojevic, M. (2003) 'Extreme ultraviolet imager observations of the structure and dynamics of the plasmasphere', *Space Science Reviews*, 109(1-4), pp. 25-46.

Santolik, O., Gurnett, D. and Pickett, J. (2004) 'Multipoint investigation of the source region of storm-time chorus', *Annales Geophysicae*. pp. 2555-2563.

Santolik, O., Gurnett, D., Pickett, J., Parrot, M. and Cornilleau-Wehrlin, N. (2003) 'Spatio-temporal structure of storm-time chorus', *Journal of Geophysical Research: Space Physics*, 108(A7).

Sauvaud, J. A., Louarn, P., Fruit, G., Stenuit, H., Vallat, C., Dandouras, J., Reme, H., André, M., Balogh, A. and Dunlop, M. (2004) 'Case studies of the dynamics of ionospheric ions in the Earth's magnetotail', *Journal of Geophysical Research: Space Physics*, 109(A1).

Schiller, Q., Li, X., Blum, L., Tu, W., Turner, D. L. and Blake, J. (2014) 'A nonstorm time enhancement of relativistic electrons in the outer radiation belt', *Geophysical Research Letters*, 41(1), pp. 7-12.

Schulz, M. and Lanzerotti, L. J. (1974) *Particle diffusion in the radiation belts.* vol. 7. Springer Science & Business Media.

Sckopke, N. (1966) 'A general relation between the energy of trapped particles and the disturbance field near the Earth', *Journal of Geophysical Research*, 71(13), pp. 3125-3130.

Seale, R. and Bushnell, R. (1987) *TIROS-N/NOAA AJ space environment monitor subsystem. Technical memo.* National Oceanic and Atmospheric Administration, Boulder, CO (USA). Space Environment Lab. Available.

Seki, K., Hirahara, M., Hoshino, M., Terasawa, T., Elphic, R. C., Saito, Y., Mukai, T., Hayakawa, H., Kojima, H. and Matsumoto, H. (2003) 'Cold ions in the hot plasma sheet of Earth's magnetotail', *Nature*, 422(6932), pp. 589-592. doi: 10.1038/nature01502.

Seki, K., Nagy, A., Jackman, C. M., Crary, F., Fontaine, D., Zarka, P., Wurz, P., Milillo, A., Slavin, J. A. and Delcourt, D. C. (2015) 'A review of general physical and chemical processes related to plasma sources and losses for solar system magnetospheres', *Space science reviews*, 192(1-4), pp. 27-89.

Selesnick, R. and Blake, J. (2000) 'On the source location of radiation belt relativistic electrons', *Journal of Geophysical Research: Space Physics*, 105(A2), pp. 2607-2624.

Sergeev, V. and Gvozdevsky, B. (1995) 'MT-index-a possible new index to characterize the magnetic configuration of magnetotail', *Annales Geophysicae*. Springer, pp. 1093-1103.

Sergeev, V., Malkov, M. and Mursula, K. (1993) 'Testing the isotropic boundary algorithm method to evaluate the magnetic field configuration in the tail', *Journal of Geophysical Research: Space Physics*, 98(A5), pp. 7609-7620.

Sergeev, V. and Tsyganenko, N. (1982) 'Energetic particle losses and trapping boundaries as deduced from calculations with a realistic magnetic field model', *Planetary and Space Science*, 30(10), pp. 999-1006.

Shprits, Y., Li, W. and Thorne, R. (2006a) 'Controlling effect of the pitch angle scattering rates near the edge of the loss cone on electron lifetimes', *Journal of Geophysical Research: Space Physics*, 111(A12).

Shprits, Y. and Thorne, R. (2004) 'Time dependent radial diffusion modeling of relativistic electrons with realistic loss rates', *Geophysical research letters*, 31(8).

Shprits, Y., Thorne, R., Friedel, R., Reeves, G., Fennell, J., Baker, D. and Kanekal, S. (2006b) 'Outward radial diffusion driven by losses at magnetopause', *Journal of Geophysical Research: Space Physics*, 111(A11).

Shprits, Y., Thorne, R., Horne, R., Glauert, S., Cartwright, M., Russell, C., Baker, D. and Kanekal, S. (2006c) 'Acceleration mechanism responsible for the formation of the new radiation belt during the 2003 Halloween solar storm', *Geophysical Research Letters*, 33(5).

Shprits, Y., Thorne, R., Reeves, G. and Friedel, R. (2005) 'Radial diffusion modeling with empirical lifetimes: Comparison with CRRES observations', *Annales Geophysicae*. pp. 1467-1471.

Shprits, Y. Y., Subbotin, D. A., Meredith, N. P. and Elkington, S. R. (2008) 'Review of modeling of losses and sources of relativistic electrons in the outer radiation belt II: Local acceleration and loss', *Journal of Atmospheric and Solar-Terrestrial Physics*, 70(14), pp. 1694-1713.

Simnett, G. M. (2000) 'The relationship between prominence eruptions and coronal mass ejections', *Journal of Atmospheric and Solar-Terrestrial Physics*, 62(16), pp. 1479-1487

Siscoe, G. L. and Huang, T. S. (1985) 'Polar cap inflation and deflation', *Journal of Geophysical Research: Space Physics*, 90(A1), pp. 543-547.

Skoug, R. M., Thomsen, M. F., Henderson, M. G., Funsten, H. O., Reeves, G. D., Pollock, C. J., Jahn, J. M., McComas, D. J., Mitchell, D. G. and Brandt, P. C. (2003) 'Tail-dominated storm main phase: 31 March 2001', *Journal of Geophysical Research: Space Physics*, 108(A6).

Smith, C. W., L'Heureux, J., Ness, N. F., Acuña, M. H., Burlaga, L. F. and Scheifele, J. (1998) 'The ACE magnetic fields experiment'. *The Advanced Composition Explorer Mission.* Springer, pp 613-632.

Smith, E., Frandsen, A., Tsurutani, B., Thorne, R. and Chan, K. (1974) 'Plasmaspheric hiss intensity variations during magnetic storms', *Journal of Geophysical Research*, 79(16), pp. 2507-2510.

Smith, P. H., and Bewtra, N. K. (1978) 'Charge exchange lifetimes for ring current ions', *Space Science Reviews*, 22(3), 301–318

Spasojević, M., Goldstein, J., Carpenter, D., Inan, U., Sandel, B., Moldwin, M. and Reinisch, B. (2003) 'Global response of the plasmasphere to a geomagnetic disturbance', *Journal of Geophysical Research: Space Physics*, 108(A9).

Strangeway, R. J. (2000) 'Singly charged oxygen as a proxy for Dst', *The First S-RAMP Conference Abstract Book. Sapporo*, p. 178.

Su, Z., Xiao, F., Zheng, H., He, Z., Zhu, H., Zhang, M., Shen, C., Wang, Y., Wang, S. and Kletzing, C. (2014) 'Nonstorm time dynamics of electron radiation belts observed by the Van Allen Probes', *Geophysical Research Letters*, 41(2), pp. 229-235.

Sugiura, M. (1963) 'Hourly values of equatorial Dst for the IGY'.

Sugiura, M. (1980) 'What do we expect in magnetic activity in the current solar cycle?', *Eos, Transactions American Geophysical Union*, 61(43), pp. 673-675.

Sugiura, M. and Chapman, S. (1961) *The average morphology of geomagnetic storms with sudden commencement.* DTIC Document. Available.

Sugiura, M., Kamei, T., Berthelier, A. and Menvielle, M. (1991) *Equatorial Dst Index: 1957-1986.* ISGI Publications Office.

Summers, D., Ma, C., Meredith, N., Horne, R., Thorne, R., Heynderickx, D. and Anderson, R. (2002) 'Model of the energization of outer-zone electrons by whistler-mode chorus during the October 9, 1990 geomagnetic storm', *Geophysical research letters*, 29(24).

Summers, D. and Ma, C. (2000a) 'A model for generating relativistic electrons in the Earth's inner magnetosphere based on gyroresonant wave-particle interactions', *Journal of Geophysical Research: Space Physics*, 105(A2), pp. 2625-2639.

Summers, D. and Ma, C. (2000b) 'Rapid acceleration of electrons in the magnetosphere by fast-mode MHD waves', *Journal of Geophysical Research: Space Physics*, 105(A7), pp. 15887-15895.

Summers, D. and Thorne, R. M. (2003) 'Relativistic electron pitch-angle scattering by electromagnetic ion cyclotron waves during geomagnetic storms', *Journal of Geophysical Research: Space Physics*, 108(A4).

Summers, D., Thorne, R. M. and Xiao, F. (1998) 'Relativistic theory of wave-particle resonant diffusion with application to electron acceleration in the magnetosphere', *Journal of Geophysical Research: Space Physics*, 103(A9), pp. 20487-20500.

Svalgaard, L. (2011) 'Geomagnetic semiannual variation is not overestimated and is not an artifact of systematic solar hemispheric asymmetry', *Geophysical Research Letters*, 38(16).

Tanskanen, E. I., Slavin, J. A., Tanskanen, A. J., Viljanen, A., Pulkkinen, T. I., Koskinen, H. E., J., Pulkkinen, A. and Eastwood, J. (2005), Magnetospheric substorms are strongly modulated by interplanetary high-speed streams, *Geophysical Research Letters*, 32(16)

Taylor, J. R., Lester, M. and Yeoman, T. K. (1994) 'A superposed epoch analysis of geomagnetic storms', *Annales Geophysicae*, 12, pp. 612-624.

Thorne, R., Church, S. and Gorney, D. (1979) 'On the origin of plasmaspheric hiss: The importance of wave propagation and the plasmapause', *Journal of Geophysical Research: Space Physics*, 84(A9), pp. 5241-5247.

Thorne, R., Li, W., Ni, B., Ma, Q., Bortnik, J., Chen, L., Baker, D., Spence, H. E., Reeves, G. and Henderson, M. (2013) 'Rapid local acceleration of relativistic radiation-belt electrons by magnetospheric chorus', *Nature*, 504(7480), pp. 411-414.

Thorne, R., Shprits, Y., Meredith, N., Horne, R., Li, W. and Lyons, L. (2007) 'Refilling of the slot region between the inner and outer electron radiation belts during geomagnetic storms', *Journal of Geophysical Research: Space Physics*, 112(A6).

Thorne, R. M. (2010) 'Radiation belt dynamics: The importance of wave-particle interactions', *Geophysical Research Letters*, 37(22).

Thorne, R. M. and Horne, R. B. (1994) 'Landau damping of magnetospherically reflected whistlers', *Journal of Geophysical Research: Space Physics*, 99(A9), pp. 17249-17258.

Thorne, R. M. and Horne, R. B. (1997) 'Modulation of electromagnetic ion cyclotron instability due to interaction with ring current O+ during magnetic storms', *Journal of Geophysical Research: Space Physics*, 102(A7), pp. 14155-14163.

Thorne, R. M., Horne, R. B., Glauert, S., Meredith, N. P., Shprits, Y. Y., Summers, D. and Anderson, R. R. (2005a) 'The influence of wave-particle interactions on relativistic electron dynamics during storms', *Inner Magnetosphere Interactions: New Perspectives From Imaging*, pp. 101-112.

Thorne, R. M. and Kennel, C. (1971) 'Relativistic electron precipitation during magnetic storm main phase', *Journal of Geophysical research*, 76(19), pp. 4446-4453.

Thorne, R. M., Ni, B., Tao, X., Horne, R. B. and Meredith, N. P. (2010) 'Scattering by chorus waves as the dominant cause of diffuse auroral precipitation', *Nature*, 467(7318), pp. 943-946.

Thorne, R. M., O'Brien, T., Shprits, Y., Summers, D. and Horne, R. B. (2005b) 'Timescale for MeV electron microburst loss during geomagnetic storms', *Journal of Geophysical Research: Space Physics*, 110(A9).

Thorne, R. M., Smith, E. J., Burton, R. K. and Holzer, R. E. (1973) 'Plasmaspheric hiss', *Journal of Geophysical Research*, 78(10), pp. 1581-1596.

Tsurutani, B. T., Gonzalez, W. D., Tang, F., Lee, Y. T., Okada, M. and Park, D. (1992) 'Reply to LJ Lanzerotti: Solar wind ram pressure corrections and an estimation of the efficiency of viscous interaction', *Geophysical Research Letters*, 19(19), pp. 1993-1994.

Tsurutani, B. T. and Smith, E. J. (1974) 'Postmidnight chorus: A substorm phenomenon', *Journal of Geophysical Research*, 79(1), pp. 118-127.

Tsurutani, B. T. and Smith, E. J. (1977) 'Two types of magnetospheric ELF chorus and their substorm dependences', *Journal of Geophysical Research*, 82(32), pp. 5112-5128.

Tsyganenko, N. A. (1996) 'Effects of the solar wind conditions in the global magnetospheric configurations as deduced from data-based field models', *International Conference on Substorms*. p. 181.

Tu, W., Li, X., Chen, Y., Reeves, G. and Temerin, M. (2009) 'Storm-dependent radiation belt electron dynamics', *Journal of Geophysical Research: Space Physics*, 114(A2).

Turner, D., Angelopoulos, V., Li, W., Bortnik, J., Ni, B., Ma, Q., Thorne, R., Morley, S., Henderson, M. and Reeves, G. (2014) 'Competing source and loss mechanisms due to wave-particle interactions in Earth's outer radiation belt during the 30 September to 3 October 2012 geomagnetic storm', *Journal of Geophysical Research: Space Physics*, 119(3), pp. 1960-1979.

Turner, N. E., Baker, D., Pulkkinen, T. and McPherron, R. (2000) 'Evaluation of the tail current contribution to Dst', *Journal of Geophysical Research: Space Physics*, 105(A3), pp. 5431-5439.

Tverskaya, L., Pavlov, N., Blake, J., Selesnick, R. and Fennell, J. (2003) 'Predicting the L-position of the storm-injected relativistic electron belt', *Advances in Space Research*, 31(4), pp. 1039-1044.

Ukhorskiy, A., Anderson, B., Takahashi, K. and Tsyganenko, N. (2006) 'Impact of ULF oscillations in solar wind dynamic pressure on the outer radiation belt electrons', *Geophysical research letters*, 33(6).

Usanova, M., Mann, I., Rae, I., Kale, Z., Angelopoulos, V., Bonnell, J., Glassmeier, K. H., Auster, H. and Singer, H. (2008) 'Multipoint observations of magnetospheric *compression-related EMIC Pc1 waves by THEMIS and CARISMA', Geophysical Research Letters, 35(17).*

Vasyliunas, V. M., Kan, J. R., Siscoe, G. L., and Akasofu, S.-I. (1982), 'Scaling relations governing magnetosphere energy transfer', *Planetary and Space Science*, 30, pp. 359–365

Vennerstrøm, S. (1999) 'Dayside magnetic ULF power at high latitudes: A possible long-term proxy for the solar wind velocity?', *Journal of Geophysical Research: Space Physics*, 104(A5), pp. 10145-10157.

Vijaya Lekshmi, D., Balan, N., Tulasi Ram, S. and Liu, J. (2011) 'Statistics of geomagnetic storms and ionospheric storms at low and mid latitudes in two solar cycles', *Journal of Geophysical Research: Space Physics*, 116(A11).

Walsh, B., Foster, J., Erickson, P. and Sibeck, D. (2014) 'Simultaneous ground-and space-based observations of the plasmaspheric plume and reconnection', *Science*, 343(6175), pp. 1122-1125.

Wang, D., Yuan, Z., Yu, X., Deng, X., Zhou, M., Huang, S., Li, H., Wang, Z., Qiao, Z. and Kletzing, C. (2015) 'Statistical characteristics of EMIC waves: Van Allen Probe observations', *Journal of Geophysical Research: Space Physics*, 120(6), pp. 4400-4408.

Wanliss, J. A. and Reynolds, M. A. (2003) 'Measurement of the stochasticity of low-latitude geomagnetic temporal variations', *Annales geophysicae*, 21, pp. 2025-2030.

Wanliss, J. A. and Showalter, K. M. (2006) 'High-resolution global storm index: Dst versus SYM-H', *Journal of Geophysical Research: Space Physics*, 111(A2).

Weigel, R. S., Vassiliadis, D. and Klimas, A. J. (2002) 'Coupling of the solar wind to temporal fluctuations in ground magnetic fields', *Geophysical Research Letters*, 29(19).

Weigel, R., Klimas, A. and Vassiliadis, D. (2003) 'Precursor analysis and prediction of large-amplitude relativistic electron fluxes', *Space Weather*, 1(3).

Welling, D.T., André, M., Dandouras, I., Delcourt, D., Fazakerley, A., Fontaine, D., Foster, J., Ilie, R., Kistler, L., Lee, J. H., Leimohn, M. W., Slavin, J. A., Wang, C-P., Wiltberger, M., Yau, A. (2015), 'The Earth: Plasma Sources, Losses, and Transport Processes', *Space Science Reviews*, 192(1-4), pp. 145-208.

Williams, D. (1985) 'Dynamics of the Earth's ring current: Theory and observation', *Space Science Reviews*, 42(3-4), pp. 375-396.

Yermolaev, Y. I., Nikolaeva, N. S., Lodkina, I. G. and Yermolaev, M. Y. (2009) 'Specific interplanetary conditions for CIR-, Sheath-, and ICME-induced geomagnetic

storms obtained by double superposed epoch analysis', *arXiv preprint arXiv:0911.3315*.

Yuan, C. and Zong, Q. G. (2012) 'Quantitative aspects of variations of 1.5–6.0 MeV electrons in the outer radiation belt during magnetic storms', *Journal of Geophysical Research: Space Physics*, 117(A11).

Zeilik, M. and Gregory, S. (1997) 'Introductory Astronomy and Astrophysics – Fourth Edition', Brooks Cole

Zhao, H., Li, X., Baker, D., Fennell, J., Blake, J., Larsen, B., Skoug, R., Funsten, H., Friedel, R. and Reeves, G. (2015) 'The evolution of ring current ion energy density and energy content during geomagnetic storms based on Van Allen Probes measurements', *Journal of Geophysical Research: Space Physics*, 120(9), pp. 7493-7511.

Zwickl, R. D., Doggett, K. A., Sahm, S., Barrett, W. P., Grubb, R. N., Detman, T. R., Raben, V. J., Smith, C. W., Riley, P. and Gold, R. E. (1998) 'The NOAA real-time solar-wind (RTSW) system using ACE data', *Space Science Reviews*, 86(1-4), pp. 633-648.